UNIVERSIDADE FEDERAL DE MINAS GERAIS
ESCOLA DE ENGENHARIA
PROGRAMA DE PÓS-GRADUAÇÃO EM ENGENHARIA QUÍMICA

TARCIZO DA CRUZ COSTA DE SOUZA

HYBRID n-SiO_2 / MWCNTs DEVELOPMENT AND ITS APPLICATION IN REACTIVE POWDER CONCRETE

Thesis

BELO HORIZONTE - MG
2021

TARCIZO DA CRUZ COSTA DE SOUZA

HYBRID n-SiO_2 / MWCNTs DEVELOPMENT AND ITS APPLICATION IN REACTIVE POWDER CONCRETE

Thesis

Tese apresentada ao Programa de Pós-Graduação em Engenharia Química da Escola de Engenharia da Universidade Federal de Minas Gerais, como requisito parcial para obtenção do Grau de Doutor em Engenharia Química.
Linha de Pesquisa: Tecnologias limpas, materiais e nanotecnologia
Orientador: Prof. Dr. Manuel Houmard.
Coorientador: Prof. Dr. Luiz Orlando Ladeira.

BELO HORIZONTE – MG
2021

S729h

Souza, Tarcizo da Cruz Costa de.
Hybrid n-SiO_2 / MWCNTs development and its application in reactive powder concrete [recurso eletrônico] / Tarcizo da Cruz Costa de Souza. – 2021.
1 recurso online (xx, 220 f. : il., color.) : pdf.

Orientador: Manuel Houmard.
Coorientador: Luiz Orlando Ladeira.

Tese (doutorado) – Universidade Federal de Minas Gerais, Escola de Engenharia.

Bibliografia: f. 205-220.
Exigências do sistema: Adobe Acrobat Reader.

1. Engenharia química - Teses. 2. Silica - Teses. 3. Nanotubos de carbono - Teses. 4. Concreto - Teses. 5. Pozolanas - Teses. I. Houmard, Manuel. II. Ladeira, Luiz Orlando. III. Universidade Federal de Minas Gerais. Escola de Engenharia. IV. Título.

CDU: 66.0(043)

Ficha catalográfica: Biblioteca Profº Mário Werneck, Escola de Engenharia da UFMG.

UNIVERSIDADE FEDERAL DE MINAS GERAIS
ESCOLA DE ENGENHARIA
PROGRAMA DE PÓS-GRADUAÇÃO EM ENGENHARIA QUÍMICA

FOLHA DE APROVAÇÃO

"HYBRID N-SIO2 / MWCNTS DEVELOPMENT AND ITS APPLICATION IN REACTIVE POWDER CONCRETE"

Tarcizo da Cruz Costa de Souza

Tese submetida à Banca Examinadora designada pelo Colegiado do Programa de Pós-Graduação em Engenharia Química da Escola de Engenharia da Universidade Federal de Minas Gerais, como parte dos requisitos à obtenção do título de **DOUTOR EM ENGENHARIA QUÍMICA**.

49ª TESE APROVADA EM 19 DE FEVEREIRO DE 2021 POR:

Documento assinado eletronicamente por **Manuel Noel Paul Georges Houmard**, **Professor do Magistério Superior**, em 19/02/2021, às 18:21, conforme horário oficial de Brasília, com fundamento no art. 5º do Decreto nº 10.543, de 13 de novembro de 2020.

Documento assinado eletronicamente por **Luiz Orlando Ladeira**, **Professor do Magistério Superior**, em 19/02/2021, às 18:34, conforme horário oficial de Brasília, com fundamento no art. 5º do Decreto nº 10.543, de 13 de novembro de 2020.

Documento assinado eletronicamente por **Eduardo Henrique Martins Nunes**, **Professor do Magistério Superior**, em 19/02/2021, às 18:34, conforme horário oficial de Brasília, com fundamento no art. 5º do Decreto nº 10.543, de 13 de novembro de 2020.

Documento assinado eletronicamente por **Jose Marcio Fonseca Calixto**, **Professor Magistério Superior - Voluntário**, em 19/02/2021, às 18:35, conforme horário oficial de Brasília, com fundamento no art. 5º do Decreto nº 10.543, de 13 de novembro de 2020.

Documento assinado eletronicamente por **Roberto Braga Figueiredo**, **Professor Titular-Livre Magistério Superior**, em 19/02/2021, às 18:36, conforme horário oficial de Brasília, com fundamento no art. 5º do Decreto nº 10.543, de 13 de novembro de 2020.

Documento assinado eletronicamente por **Alice Gonçalves Osorio**, **Usuário Externo**, em 19/02/2021, às 18:37, conforme horário oficial de Brasília, com fundamento no art. 5º do Decreto nº 10.543, de 13 de novembro de 2020.

Documento assinado eletronicamente por **Péter Ludvig**, **Usuário Externo**, em 19/02/2021, às 18:37, conforme horário oficial de Brasília, com fundamento no art. 5º do Decreto nº 10.543, de 13 de novembro de 2020.

A autenticidade deste documento pode ser conferida no site https://sei.ufmg.br/sei/controlador_externo.php?acao=documento_conferir&id_orgao_acesso_externo=0, informando o código verificador **0559660** e o código CRC **37ED2F07**.

Referência: Processo nº 23072.206518/2021-40 SEI nº 0559660

AGRADECIMENTOS

Dentro do meu particular, da minha forma de sentir e dar fé da minha crença, agradeço a DEUS por me permitir capacidade.

Aos meus pilares, sem os quais não teria condição de percorrer todo o caminho da minha pós-graduação (e de nossas vidas) e chegar ao ponto de propor uma Tese, Cecília minha amada esposa e Eduardo Isaac nosso amado filho, muito obrigado!

Aos meus pais, Lourdes e José de Souza, o tempo vai nos mostrando que os exemplos e a forma de educar renderam a formação dos filhos. Muito obrigado!

Aos familiares e amigos, antes do agradecimento, meus pedidos de desculpas pelas ausências que a dedicação ao período acadêmico me imporam. Sem a pretensão de compensar, obrigado!

Ao Prof. Calixto, que foi meu professor, depois orientador no mestrado e coordenador no CTNano/UFMG, e que agora o tenho como um grande amigo, muito obrigado por tudo que fez e faz por mim.

Prof. Luiz Orlando Ladeira, se me permite, como são antagônicas a sua simplicidade e a sua genialidade. Muito obrigado pela oportunidade de trabalhar e conviver contigo.

Ao Prof. Manuel Houmard, que me acompanhou como orientador nessa trajetória, meus agradecimentos por acreditar no meu trabalho e por me ajudar no amadurecimento acadêmico. Tenha certeza de que me dediquei bastante a cada comentário seu.

Para as já engenheiras, Amanda Brasil e Ana Cristina Melo, que à época atuaram comigo como estudantes de iniciação científica, meus agradecimentos por toda a ajuda e dedicação.

Aos meus colegas do CTNano/UFMG, a todos, meus agradecimentos pela convivência, pelo apoio e gentilezas. Em especial, registro meus agradecimentos a Enga. Raquel Kênia, ao Eng. Carlos Martins, ao Físico Tiago Campolina e ao mestre Sérgio Oliveira.

Ao Programa de Pós-graduação em Engenharia Química da UFMG, meus agradecimentos pela acolhida. A Fernanda, muito obrigado pela atenção.

Agradeço de forma especial a Professora Andréa Costa, atual coordenadora do Programa. Pela atenção comigo, desde a banca no processo de seleção, passando pelo período como aluno e no final da caminhada como coordenadora, meus sinceros agradecimentos.

A Professora Alice Osório e aos professores Péter Ludvig, Eduardo Nunes e Roberto Braga, muito obrigado por fazerem parte da banca para avaliação do meu trabalho. Foi uma honra.

Aos patrocinadores do CTNano/UFMG, as empresas InterCement e Petrobrás, obrigado pela parceria dedicada à pesquisa e inovação. Agradecimento especial ao Eng. Seiiti Suzuki da InterCement.

Agradeço ao Centro de Microscopia da UFMG pelas análises realizadas. Aos técnicos que lá atuam, muito obrigado pela atenção e perícia nos preparos e análises das minhas amostras.

Agradeço ao Eng. Samuel Lima, técnico do Laboratório de Difração de Raios X do DEMET, que sempre foi atencioso com minhas demandas.

Agradeço a gentileza das empresas Tecnosil e Grace, por cederem materiais para a pesquisa.

To my beloved wife Cecilia,
and our son Eduardo Isaac.
I dedicate.

“...Mas é preciso ter força, é preciso ter raça,
É preciso ter gana sempre...”
Milton Nascimento / Fernando Brant

“They did not know it was impossible, so they did it!".
Mark Twain

"Ne sachant pas que c'était impossible, ils l´ont fait!.”
Jean Cocteau

RESUMO

A Nanotecnologia tem se mostrado um campo científico importante na produção de materiais avançados, que por sua vez, são objetos de estudo da Engenharia Química. Conforme a bibliografia, nanomateriais possuem propriedades singulares e sua aplicação pode resultar em mudanças benéficas em compósitos cimentícios como o concreto. Nanotubos de carbono e nanosílica são nanomateriais muito estudados em concretos, devido a melhorias de desempenho. Considerando isto e possíveis aplicações em concretos especiais, como o concreto de pós reativos (*RPC*), esse trabalho apresenta o desenvolvimento de um material híbrido, composto de sílica nanoestruturada (n-SiO_2) suportando nanotubos de carbono de paredes múltiplas (*MWCNTs*), para melhoria da tenacidade à fratura em *RPC* sem fibras. *MWCNTs* foram modulados e sintetizados usando o método de deposição química da fase vapor por catálise (*CCVD*), tendo metano como fonte de carbono e ferro como catalisador. No desenvolvimento desse trabalho as influências do suporte e do método de incorporação do catalisador nas características dos *MWCNTs* foram avaliadas. Para controlar as propriedades de diferentes n-SiO_2, essas foram produzidas pelo método sol-gel. Inicialmente foram produzidos cinco tipos de n-SiO_2, e sobre cada uma, sintetizados *MWCNTs.* Posteriormente, três métodos de incorporação de catalisador ao suporte foram avaliados. Após as caracterizações em cada etapa e baseado nos resultados obtidos o material híbrido foi produzido com características adequadas dos *MWCNTs* para ganhos de tenacidade nos *RPCs*. Considerando variações na quantidade e utilizando várias técnicas, a proporção adequada do híbrido foi previamente determinada mediante avaliações do efeito pozolânico em soluções e em pastas de cimento. Por fim, o desempenho mecânico dos RPCs, com e sem a utilização do híbrido, foi avaliado. Em conjunto com avaliações da microestrutura, os resultados comprovaram a hipótese inicial do efeito pozolânico em torno dos *MWCNTs*, influenciando então na microestrutura e refletindo no desempenho da tenacidade. Durante o ensaio de flexão, verificou-se que a incorporação de 2% (em massa) do híbrido promoveu aumentos na tenacidade da ordem de 100%.

Palavras-chave: Sílica nano-estruturada; Sol-gel; Nanotubos de carbono; Concreto de pós reativos; Efeito pozolânico; Tenacidade.

ABSTRACT

Nanotechnology has been proved to be an important scientific field to produce advanced materials, which in turn, are objects of Chemical Engineering studies. The literature review indicates that nanomaterials possess singular properties, and their development and application can promote beneficial changes in cement-based composites, such as concrete. Carbon nanotubes and nano-silica are nanomaterials widely studied in cementitious composites, due to their capacity to improve performance. Considering these aspects and possible applications in special concretes, such as reactive powder concrete (RPC), this work presents the development of a hybrid material, composed of nanostructured silica (n-SiO_2) supporting multi-walled carbon nanotubes (MWCNTs), to improve fracture toughness in RPC without fibers. MWCNTs were modulated and synthesized using the catalytic chemical vapor deposition method (CCVD), having methane as a carbon source and iron as a catalyst. Along with the study, the influences of the support and the method of catalyst incorporation on the characteristics of the MWCNTs were evaluated. To control the properties of different n-SiO_2, these materials were produced by the sol-gel method. Five types of n-SiO_2 were produced initially, and MWCNTs were synthesized on each one. Later, three methods of catalyst incorporation were evaluated. Finally, after the characterizations at each stage and based on the results, the hybrid material was produced with adequate MWCNTs characteristics to achieve toughness gains for the RPCs. Considering variations in quantity and using specific techniques, the appropriate proportion of the hybrid was previously determined by assessing the pozzolanic effect in solutions and cement pastes. Finally, the mechanical performance of the RPCs, with and without the use of the hybrid, was evaluated. Together with the microstructural evaluations, the results confirmed the initial hypothesis of the pozzolanic effect around the MWCNTs, improving the microstructure and reflecting on their mechanical behavior. During bending tests, it was verified that the incorporating of 2% bwoc of hybrid promoted increases in toughness in the order of 100%.

Keywords: Nano-structured silica; Sol-gel; Carbon nanotubes; Reactive powder concrete, Pozzolanic effect; fracture toughness.

LIST OF FIGURES

LIST OF TABLES

LIST OF ABBREVIATIONS

BSE – Backscattered electron

bwoc – by weight of cement

C-S-H – Calcium silicate hydrate (cement chemist notation)

C_2S – Dicalcium silicate (belite, cement chemist notation)

C_3A – Tricalcium aluminate (cement chemist notation)

C_3S – Tricalcium silicate (alite, cement chemist notation)

C_4AF – Tetracalcium aluminoferrite (cement chemist notation)

CH – Calcium hydroxide (cement chemist notation)

CaO – Calcium oxide

$Ca(OH)_2$ – Calcium hydroxide

CCD - Charge Coupled Device

CO_2 – Carbon dioxide

CNFs – Carbon nanofibers

CNTs – Carbon nanotubes

CVD – Chemical vapor deposition

CCVD – Catalytic Chemical vapor deposition

DTG – Derivative thermogravimetric analysis

E_a – Activation Energy [J]

EDS – Energy dispersive spectroscopy

Fe_2O_3 – Hematite

FeO – Wüstite

FTIR – Fourier transform infrared (spectroscopy)

H – Water (cement chemist notation)

HPC – High-performance concrete

KBr – Potassium bromide

Mg – Magnesium

MgO – Magnesium oxide

MWCNTs – Multi-walled carbon nanotubes

N_2 – Nitrogen

OPC – Ordinary Portland Cement

pH – Potential of hydrogen

RPC – Reactive powder concrete

S – Silicon dioxide (cement chemist notation)

SEM – Scanning electron microscopy

SF – Silica fume

SiC – Silicon carbide

SiO_2 – Silicon dioxide (silica)

SSA – Specific surface area

SWCNTs – Single-walled carbon nanotubes

TPBT – Three points bending test

TEOS – Tetraethylorthosilicate

TEM – Transmission electron microscopy

TGA – Thermogravimetric analysis

UHPC – Ultra-high-performance concrete

w/c – Water to cement ratio

w/w – weight per weight

XRD – X-ray diffraction

TABLE OF CONTENTS

1. INTRODUCTION

1.1. CONTEXTUALIZATION

Based on the possibilities to develop advanced materials, the application of Nanotechnology has been highly effective in recent years, becoming an important field in the Materials Science area. The technical literature in Materials Science has been showing a considerable increase in the number of studies that address the application of nanomaterials. The results are technological solutions that correspond to the important demands of society.

According to Palmer (2009), nanotechnology has generated great expectations in the development of advanced composites due to the singular properties of such small materials (10^{-9} m). Rahman and Padavettan (2012) emphasized that the properties of matter at the nanoscale differ from the properties of atoms and molecules which allow the development of new composite materials with specific features. Thus, the production of new materials can be an object of Chemical Engineering study.

For materials and cementitious composites used in the construction industry, Kalra and Saxena (2017) mentioned that Nanotechnology can improve their behavior. The same observation was made by Han *et al*. (2017b) that describes the possibility to develop high-performance cementitious composites with unique mechanical properties, durability, and multifunctional features.

New technologies demand new materials and, from this point of view, the nanomaterials, with their specific properties, can promote the viability of innovative techniques. Concerning the required advances in the construction industry, due to the need for better performance, durability, and extended service life of structures, reactive powder concrete (RPC), which is a construction material with a high packing of its components, can be a viable alternative to apply such small materials. This concrete was first developed by Richard and Cheyrezy (1995) to obtain ductile ultra-high performance concrete and has been widely used in long-span, ultra-rise, and complex civil engineering infrastructures (DONG *et al.*, 2020). According to these authors, despite their excellent

mechanical properties, the propagation of cracks plays a crucial role to obtain safe RPC structures.

An alternative, considering the features of the RPC and the possible synergy with nanomaterials is its application as a repair material. Lee; Wang; Chiu (2007) proposed the use of RPC as a retrofit material and the results showed that this type of concrete presented excellent repair and retrofit potential in terms of performance. Considering these aspects, the possibility to achieve high-performance in a short time is an important factor, mainly in terms of fracture capacity, a characteristic that the cementitious materials are deficient.

To increase the fracture toughness in cementitious materials (as in RPC), the incorporation of fibers is a common alternative. In RPC matrix, the fracture mechanisms occur in such a way that to inhibit the crack propagation, fibers in the micro- and nanoscale are important, as mentioned by Liu *et al*. (2019). Thus, in cementitious composites, reinforcement is a necessary condition to achieve high-performance.

One of the most employed nanomaterials in cement composites is the nano-silica. This material has the potential to change the cement hydration process and promote the so-called pozzolanic effect, which converts a less resistant hydrated phase (calcium hydroxide) into another (calcium silicate hydrate – C-S-H) that gives the matrix mechanical strength (HOU *et al*., 2013). This effect refines the pore structure makes the final matrix more homogeneous, according to Hou *et al*. (2015).

In the last years, since its discovery by Iijima (1991), carbon nanotubes have been a nanomaterial with greater interest due to their exceptional physical properties, and one of these is their high mechanical strength. This is a characteristic that enables carbon nanotubes to be an excellent reinforcement material in concrete (FRAGA; MARÍA; GARCÍA, 2014).

Taking into account the characteristics of these nanomaterials and their effect on composite materials, nano-silica and carbon nanotubes synergy can promote significant modifications in the material matrix, like concrete, improving its performance in terms of mechanical strength and lifetime.

As will be discussed in the text, the greatest difficulty for the use of carbon nanotubes (CNTs) in materials composites consists of their adequate dispersion. A suitable dispersion is essential to get a homogeneous CNTs distribution in the matrix and consequently a high support load transfer and mitigation of cracks propagation, according to Lu; Ouyang; Xu (2016). Carbon nanotubes are hydrophobic and have a high tendency to agglomerate when mixed in aqueous solutions or pastes. To promote their dispersion, some methods are used, such as acidic functionalization, use of surfactants, ultrasonication, microwave, and mechanical stirring, but sometimes these procedures promote an undesired CNTs degradation and/or an incompatibility with the composite preparation, like in concrete. Returning to the point of the CNTs reinforcement capacity, this is associated with its diameter and length, and preserve these characteristics is very important to achieve effective internal crack propagation reduction in concrete under loading or thermal actions.

To minimize the dispersion problem and facilitate the CNTs application, an alternative is the CNTs synthesis directly on the desired materials support (*in situ* synthesis), allowing the CNTs to be anchored on it without a possible clump formation (NASIBULIN *et al.*, 2009; LUDVIG *et al*., 2011; OTHMAN; KINLOCH; WILKINSON, 2013).

In this context, this work presents the development of a hybrid material composed of nanostructured silica (n-SiO_2) and carbon nanotubes (CNTs), with specific features. It was applied in reactive powder concrete to improve fracture toughness at an early age. Beyond this, studies with the CNTs incorporation in RPC contributes to the better development of this material in terms of toughness gain. As cited by Liu *et al*. (2019), the number of investigations related to CNT modification of RPC is small.

To control the n-SiO_2 features, the sol-gel process was used to produce silica particles with morphology suitable to grow CNTs and develop the role of pozzolanic material. Concerning the CNTs synthesis, using the nanostructured silica as a support, the Catalytic Chemical Vapor Deposition (CCVD) method was employed, resulting in this hybrid material with specified characteristics (diameter and length of the CNTs) suitable to be employed in the RPC.

To obtain the desired hybrid, with the necessary properties, the CNTs synthesis method was developed in three stages. Firstly, the influence of the silica support was evaluated with changes in its morphology. Later, the influence of the iron-based catalyst incorporation method was tested. Finally, after the consideration of the adequate route to produce the hybrid, the third stage corresponded to the production on large scale. In all development processes, the manufactured materials were properly characterized by specific technics, evaluating the influence of the adopted choices.

With the chosen material (the hybrid), a program of tests to evaluate the possible pozzolanic effect was carried out, considering variation in the quantity used in the cementitious matrix. The results of these evaluations indicated an adequate amount of the hybrid concerning the pozzolanic effect and the local formation of C-S-H involving the CNTs.

To test the material (the hybrid) with the desired effects, RPCs were manufactured with and without the incorporation of the hybrid. The objective was to verify the mechanical performance in terms of toughness behavior at an early age. With variations in the content and form of addition of the hybrid, the RPCs samples were evaluated. In the end, the results showed an increase in the toughness after the maximum tensile stress was reached. This result is following by other studies that evaluated the influence of micro and nanomaterials in RPC matrices, proving that the developed hybrid (n-SiO_2/CNTs) achieved the desired objective.

1.2. THESIS STRUCTURE

This Thesis is structured in seven chapters. Chapter 1 introduces the aborded theme, shows an overview of the new demands of cementitious materials employed in the Construction Industry, and the possibilities that Nanotechnology can provide in terms of high-performance materials. Thus, having in view these aspects, the proposal of the research is presented considering a hybrid material development with desired adequate features to improve the performance of reactive powder concrete in terms of fracture toughness. Chemicals and

physicals methods were used to develop the hybrid and an extensive description is presented.

Chapter 2 shows the general objective of this research and also details other specific objectives aimed at achieving the general objective.

Chapter 3 describes an overview of the points related to high-performance concretes, mainly reactive powder concrete, and its deficiencies concerning the fracture toughness capacity. Later, the use of nanomaterials in cementitious materials is aborded, showing the implications of these in their performance. The pozzolanic effect provided by nano-silica and the improvement in the mechanical performance arising from using carbon nanotubes is particularly presented. Next, a literature review literature about the n-SiO_2 and CNTs production, by the sol-gel and catalytic chemical vapor deposition methods, respectively is presented. In this context, the originality of the developed hybrid is revealed,

Chapter 4 shows the proposed methodology used in the Thesis to achieve the objectives and validate the main hypothesis raised, the improvement in toughness behavior in RPC by CNTs linked in the hydrated cement matrix, and the additional C-S-H formation over then. To provide a consistent evaluation, with corroborative results, different procedures were used, mainly in the pozzolanic evaluation. Beyond, the methods used to evaluate the effect of the hybrid in mechanical behavior were based on the literature review.

In Chapter 5 the obtained results are presented, and a wide discussion is provided. Initially, the discussions address important aspects of the n-SiO_2 and the CNTs properties, desired and obtained, in the route used in the synthesis of the n-SiO_2/CNTs hybrid. Next, the evaluation of the hybrid in terms of the pozzolanic effect is described, comparing the behavior due to changes in the employed quantity in the matrix. Using the optimal amount and a variation over this amount, the effects of the n-SiO_2/CNTs hybrid in RPC (without fibers) were evaluated in terms of mechanical behavior, and the results were discussed comparing with a reference RPC without the use of the hybrid and fibers.

In Chapter 6 the conclusions are presented considering the obtained results in each stage of the study, as well as their correlations with the objectives initially proposed.

Finally, Chapter 7 presents some suggestions for future works to have a better understanding of the behavior of the hybrid in the performance of the cement-based materials. Uses of RPC in other conditions are also described.

After the content of Chapter 7, are listed the intellectual and scientific production during the time that this Thesis was developed.

2. OBJECTIVE

2.1. GENERAL OBJECTIVE

The main objective of this work is to develop a hybrid material composed of nanostructured silica particles and carbon nanotubes to be applied in reactive powder concrete to promote gains in terms of toughness.

2.2. SPECIFIC OBJECTIVES

- Synthesis, by the sol-gel method, of nanostructured silica oxides (n-SiO_2) with specific features to be used as suitable support in the production of carbon nanotubes (CNTs) by the catalytic chemical vapor deposition method (CCVD).

- Evaluation of the pozzolanic effect promoted by the produced hybrid, and its influence in the cement hydration at an early age.

- Production of reactive powder concretes with the addition of the selected n-SiO_2/CNTs hybrid composite, and evaluation of the mechanical performance at an early age.

- Investigation, at an early age, that this hybrid material acts in the conversion of calcium hydroxide (CH) in additional calcium silicate hydrate (C-S-H), involving carbon nanotubes and reinforcing the material structure at the micro and nano-scales.

3. LITERATURE REVIEW

At present, concrete, as well as other materials such as silicon, oil, and gas, is one of the pillars of our developed societies, and in the last decades, its consumption and mechanical performance have increased considerably (van DAMME, 2018). The increase in consumption may be related to the great availability of raw materials and their relatively low cost. However, the exploration of these raw materials is associated with the impact on mineral resources, which are non-renewable natural resources. On the other hand, the development of concrete technology has been constant, aiming to achieve better performance with reduced use of mineral resources (van Damme, 2018).

Based on this scenario, high-performance concretes (HPC) and ultra-high performance concretes (UHPC) have been studied to allow the design of durable concrete structures (SHI *et al*., 2015).

An alternative to this scenario may be provided by Nanotechnology. This fact becomes clearer when the possibilities inherent to the use of nanomaterials in concrete matrices, as shown in the reviews made by Kalra and Saxena (2017); Norhasri; Hamidah; Fadzil (2017); and Paul *et al*. (2018).

Concrete is a quasi-brittle material and susceptible to cracking. To supply the deficiencies of the concrete concerning the tensile stress, the use of fibers can be mechanically effective, as reported by Hambach *et al*. (2016). These authors discuss the use of aligned carbon fibers, 3% in volume, in cement paste to promote material with high performance, reaching a flexural strength gain of 1,340%. However, considering the concrete technology, these authors also discuss that there are still challenges to produce concretes with a good fiber alignment by extrusion, for example.

Currently, many researchers are working on the application of nanomaterials, like carbon nanotubes, to increase the mechanical performance in cementitious materials, and important results are reported in the review work of Rashad (2017). The use of other nanosized materials, such as silicon dioxide (SiO_2) nanoparticles, has been also intensively investigated for the production of high-performance concrete (SINGH *et al.*, 2013; ZHANG *et al.*, 2017). Due to its

pozzolanic capacity, SiO_2 reacts with $Ca(OH)_2$ to produce additional calcium silicate hydrated (C-S-H), the cement hydrated phase that provides strength to the cementitious matrices.

Taking into account all these aspects, the literature review of this Thesis was structured to present a theoretical basis that enables the development and implementation of a hybrid material, composed of nanostructured silica (n-SiO_2) and carbon nanotubes (CNTs), mainly to increase the toughness performance, at an early age, of Reactive Powder Concrete without macro fibers.

On the foregoing, it is understood that the concrete termed as Reactive Powder Concrete (RPC), according to Richard and Cheyrezy (1995), may be appropriate for such interest.

3.1. REACTIVE POWDER CONCRETE

Considered as the most used man-made material in the world (Ferro *et al*. 2014), concrete has applications in different areas of the infrastructure of modern society: from roads, bridges, buildings, nuclear reactors, hydroelectric power plants, tunnels, dams, to simple residences. Due to the necessity to develop infrastructure with adequate performance and long service life, concrete technology has evolved to compensate its low tensile strength and toughness. Despite having high compressive strength, the concrete is a quasi-brittle material, with a porous structure containing micro (< 2 nm) and mesopores (2-50 nm), and macropores (> 50 nm).

For durability and performance, these characteristics have negative effects on the use of concrete. Thus, traditional technologies, as reinforcing concrete with steel bars, and recent technologies, as the use of fibers or pre-tensioning and post-tensioning concrete, seek to make up for the deficiency of the material, resulting in HPC and UHPC.

Usually employed in precast industries, Ultra-High Performance Concrete (UHPC) is a type of concrete with high compressive resistance, approximately 3–16 times higher than conventional concretes, according to Wang *et al*. (2015). It

also exhibits good toughness and excellent durability according to Shi *et al.* (2015). Due to its features, the Reactive Powder Concrete (RPC) is considered a type of UHPC.

RPC is a concrete developed using concepts of microstructural engineering, with ultra-fine powders and low water/cementitious material ratio (lower than 0.20), to ensure a highly dense matrix and particle size homogeneity. When fibers, pressure, and heat treatment are used, the material can reach compressive strength in the range between 200 and 800 MPa, fracture energy in the range between 1,200 and 4,000 $J.m^{-2}$, and ultimate tensile strain in the order of 1% (RICHARD; CHEYREZY, 1995; YAZICI *et al.*, 2008; CWIRZEN; PENTTALA; VORNANEN, 2008). The values of these properties are much higher compared to conventional concrete.

Concerning the granulometry of its components, RPC is more similar to a mortar with the addition of fibers. Tutikian, Isaia, and Helene (2011) mention, that despite the high strength and performance, the term concrete prevails. These authors also comment that this kind of concrete has elevated cement consumption (of the order of 1,000 $kg.m^{-3}$) and higher mixing time, due to the absence of coarse aggregates in the blending.

Richard and Cheyrezy (1995), developers of this technology, mention that the basic principles of RPC are:

- Enhancement of homogeneity by the elimination of coarse aggregates;
- Enhancement of the particles packing by the granular mixture optimization, and application of pressure before and during setting;
- Enhancement of the microstructure by post-set heat treatment;
- Enhancement of the ductility by incorporating small-sized steel fibers;
- Maintenance of mixing and casting procedures as close as possible to the existing practice.

Some typical compositions of RPC (RPC 200 and RPC 800) are presented in Table 3.1. The corresponding mechanical properties for the two types of concrete are shown in Table 3.2.

Table 3.1 – Typical RPC compositions and proportions (by weight of cement).

	RPC 200				RPC 800	
	Non-fibered		Fibered		Silica aggregates	Steel aggregates
Portland Cement	1	1	1	1	1	1
Silica Fume	0.25	0.23	0.25	0.23	0.23	0.23
Sand 150 – 600 μm	1.1	1.1	1.1	1.1	0.5	-
Crushed quartz d_{50}=10 μm	-	0.39	-	0.39	0.39	0.39
Superplasticizer	0.016	0.019	0.016	0.019	0.019	0.019
Steel fiber L=12 mm	-	-	0.175	0.175	-	-
Steel fiber L=3 mm	-	-	-	-	0.63	0.63
Steel aggregates <800 μm	-	-	-	-	-	1.49
Water	0.15	0.17	0.17	0.19	0.19	0.19
Compacting pressure	-	-	-	-	50 MPa	50 MPa
Heat treatment temperature	20°C	90°C	20°C	90°C	250-400°C	250-400°C

Source: Richard and Cheyrezy (1995)

Table 3.2 – Mechanical properties of RPC types.

	RPC 200	RPC 800
Compressive strength	170 to 230 MPa	490 to 680 MPa* 650 to 810 MPa**
Flexural strength	30 to 60 MPa	45 to 141 MPa
Fracture Energy**	20,000 to 40,000 $J.m^{-2}$	1,200 to 20,000 $J.m^{-2}$
Ultimate Strain	5,000 x 10^{-6} to 7,000 x 10^{-6} $m.m^{-1}$	-
Young´s modulus	50 to 60 GPa	65 to 75 GPa

Source: Richard and Cheyrezy (1995)

* using quartz sand.

** using steel aggregate.

Richard and Cheyrezy (1995) highlight other important features and considerations about RPC: coarse aggregates are replaced by fine sand (600 μm maximum) with a mean particle diameter of about 250 μm; cement with low C_3A content has better results; heat treatment should be only applied when crushed quartz is used, and the tensile strength is not significantly increased with the application of pressure treatment.

The optimization of the mix proportion, in terms of the particle size distribution of the granular materials, is a concept widely employed in the mix design of UHPC and RPC, according to Shi *et al*. (2015). According to van Damme (218), the most popular method employed is *Andreasen and Andersen's* distribution model,

Andreasen (1930). The mathematical model of this method is described by Equation 3.1:

$$PD = \frac{D^q - D_{min}^q}{D_{max}^q - D_{min}^q}, \quad (3.1)$$

where PD is the fraction of the total solids being smaller than size D. D is the particle size (μm), D_{max} and D_{min} is the maximum and minimum particle size (μm) respectively, and q is the distribution modulus. Yu, Spiesz, and Brouwers (2014) point out that mixtures with coarse particle sizes are obtained with higher values of q (> 0.5), while lower q values (q < 0.25) result in concrete mixes that are rich in fine particles.

Regarding the workability and extrusion property, Mounanga *et al.* (2012) developed and studied five RPC especially designed for the manufacture of tubular elements to be used in chemically aggressive environments. The results showed a behavior favorable to extrusion in four of these concretes. The extrusion tests gave a homogeneous, continuous, and visible crack-free extrudate from these concrete pastes. Thus, this work shows that RPC can be used in systems with a quickly demolding process, for example.

Pressure and temperature are used to improve RPC performance. The effects of high-pressure/temperature in the curing process on RPC, as well as in its microstructure were studied by Helmi *et al.* (2016). These authors relate significant effects on the macro scale physical and mechanical properties: pressure treatment followed by heat curing increased the capillary pore volume and then accelerated the pozzolanic effect.

Despite their exceptional mechanical performance, crack propagation is a crucial point to be inhibited in RPC. In this sense, several investigations were conducted using fiber elements seeking to improve fracture toughness and fracture energy to reduce brittle failure. Han *et al.* (2016), Dong *et al*. (2019), and Dong *et al*. (2020), for example, worked with super-fine stainless wire (SSW) and obtained important gains in terms of toughness, both at the age of 3 and 28 days after the production. In these studies, a point highlighted by all authors is that the SSW presence prevents the rapid spread of narrow, short, and tortuous failure cracks. The concepts related to crack zone propagation and crack inhibition are

shown in Figure 3.1. In Figure 3.1a, the area of the crack propagation has fibers in the matrix (crack resistance zone); Figure 3.1b shows the fracture process zone, with the advance in the macro- and micro-zones. With the continuous advance, the cracks create the failure zone and reach more internal regions of the RPC matrix, as presented in Figure 3.1c.

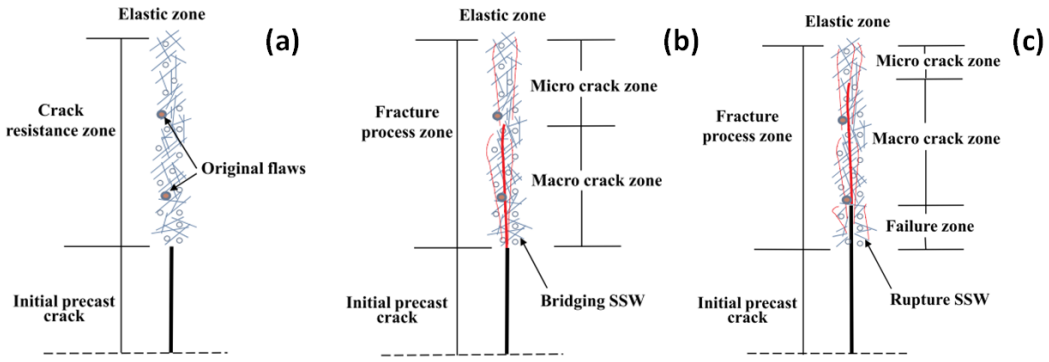

Figure 3.1 – Fracture mechanisms of fine fibers reinforced RPC.
Adapted from: Dong *et al*. (2020).

From the concepts presented in Figure 3.1, to reinforce RPC compact matrices, macro, micro, and nanosized fibers should be used to better reduce the crack propagation process.

Concerning the use of nanomaterials, Han *et al.* (2017a) used nano SiO_2-coated TiO_2 (NSCT) as reinforcement and filler to modify RPC. These authors used the same mixed proportion adopted by Richard and Cheyrezy (1995). However, the water-cement ratio (w/c) was equal to 0.3, the plasticizer content was adjusted in function of the NSCT amount, and part of the cement was replaced by fly ash. The results show an increase in flexural and compressive strength. With 5% bwoc of NSCT, the flexural strength increased 74% after 3 days of cure, and 87% after 28 days of cure when compared to the RPC without NSCT. With 3% bwoc of NSCT, the gains also were significant, in the same order of magnitude: 83%, and 75% respectively. On the other hand, for the same cure times, the compressive strength did not have expressive gains: around 10% for the content of 3% and 5% bwoc of NSCT. Despite the significative gains, a low performance of the reference RPC (without NSCT) was observed.

Zhang *et al.* (2018) incorporated boron nitride nanoparticles in RPC, varying the particle size and content, to evaluate the strength and durability. Comparing with the mix proportions used by Richard and Cheyrezy (1995), the w/c ratio (0.38), superplasticizer content (1.1 – 2.6 % bwoc), and silica fume proportions (0.31) were modified. The mechanical performance at the curing ages of 3 and 28 days showed gains in compressive and tensile strength. Improvements in the chloride penetration resistance were also observed. The authors attributed these gains to the nucleation effect in the cement hydration process, consisting of the filling and bridging of the voids promoted by the nanomaterial.

Long *et al*. (2016) investigated the application of nanomaterials in the workability, hydration process, pore structure, and mechanical behavior of RPC. Nanoparticles of nano-silica (SiO_2), nano-calcium carbonate ($CaCO_3$), nano-aluminum oxide (Al_2O_3), and nano-iron oxide (n-Fe_2O_3) were used. The test results showed a decrease in the flowability when larger amounts of nanoparticles were used and an increase in the relative density of fresh RPC. With the optimal content for each nanoparticle around 1.5-2.0% bwoc, significant gains in flexural and compressive strength were achieved. These strength gains were higher in the early cure ages compared with later ages. Reduction in the pore volume and average pore diameter were also observed.

3.2. CARBON NANOTUBES AND NANO-SILICA IN CEMENTITIOUS MATERIALS

Nanomaterials can promote significant changes and effects in cementitious matrices, mainly in terms of durability, mechanical performance, and microstructure. This is what the current technical literature has shown in various review papers (NORHASRI; HAMIDAH; FADZIL, 2017; PAUL *et al.*, 2018; RECHES, 2018).

The idea of the development of a “nano concrete” is approached according to the concepts:

> "Nano particle works in concrete by improving the bulk properties or also known as packing model structure. Ultra or nano particles can perform a super filler effect by refining the intersectional zone in cement and producing more density concrete. By acting as good filler, their manipulation or alteration in the cement matrix system occurs to provide a new nanoscale structure." (NORHASRI; HAMIDAH; FADZIL, 2017)

Thus, the nanoparticles act as elements that can improve the filler effect and the packing model structure. Important characteristics that allow obtaining structures with high performance and durability, without the need for macrostructural elements like microfibers and rebars. According to Li *et al*. (2017), adding nanofibers (like CNTs) in cement-based materials to develop crack-free concretes with improved ductility is a strategy that has gained considerable attention worldwide during recent years.

Despite the potential and possible advantages of nanomaterials in cementitious matrices, the challenge is to promote an adequate dispersion of these particles. Nanomaterials have a high specific surface area and, for this reason, they are highly subordinated to attraction forces like van der Waals interactions. This may cause their agglomeration and consequently lead to a low efficiency concerning its potentials improvements. Geometrical and superficial parameters play a major part in the agglomeration process, and obviously, these parameters are critical to achieving a proper dispersion both in water and cementitious matrices (KORAYEM *et al*., 2017).

Topics 3.2.1 – 3.2.3, discuss, particularly, the influence of carbon nanotubes (CNTs) and nano-silica (nano-SiO_2) in cement-based materials. Emphasis is given to the possible benefits of these nanomaterials in terms of mechanical performance and durability. Aspects related to the hydration process and mechanical performance are also addressed.

3.2.1. Carbon nanotubes effects

Carbon nanotubes are constantly mentioned in the scientific literature as an exceptional material to reinforce composites (polymeric or cementitious) to

improve specific properties (COLEMAN *et al.*, 2006; HAN *et al*., 2015; RASHAD, 2017; REALES; TOLEDO FILHO, 2017).

In general, the influences of CNTs in cement-based materials are related to modifications in the microstructure, cement hydration process, rheological behavior, mechanical performance, durability, as well as singular features: piezo resistivity and self-healing behavior.

As mentioned by Reales and Toledo Filho (2017), CNTs are inert and do not have a chemical influence on the reactions occurring during the cement hydration process. However, due to its size, they can modify the kinetics of some of these reactions, favoring the nucleation. CNTs can also alter the dissolution mechanism in the cement hydration kinetics. Working with single-walled carbon nanotubes (SWCNT), Makar and Chan (2009) mention that:

> "The combination of accelerated hydration reactions increased the production of calcium hydroxide, and the formation of hydration products around the nanotubes indicates that the SWCNT nucleated the hydration reactions, possibly through polarization or adsorption effects. The nucleation of the C–S–H on the SWCNT slowed the formation of a coating of C–S–H on the surface of the OPC[1] grains, resulting in enhanced dissolution and nucleation and growth hydration activity as compared with both the as-delivered and sonicated OPC samples." (MAKAR; CHAN 2009)

These authors also explain that CNTs produce higher hydration rates, affecting the early hydration process. The same effect was observed by MAKAR *et al.* (2005) working with the addition of 0.02% bwoc of CNTs in cement pastes.

Cui *et al*. (2015) added functionalized MWCNTs (0.25 - 1.0% bwoc) dispersed by dry mixing in cement. The results showed that MWCNTs accelerated the hydration of cement after 3 hours: the higher the MWCNTs amount, the higher the effect. However, some aspects, as the use of chemical dispersants with determined specification and the type of CNTs, can change this trend, as quoted by Mendonza Reales *et al.* (2016).

[1] Ordinary Portland Cement

In a review work written by Shi *et al*. (2019), it is mentioned that the effect of CNTs on the hydration process of cement is still not clear. Moreover, still according to these authors, some researchers considered that the presence of CNTs could accelerate the hydration process of cement-based materials, while other researchers considered that the incorporation of CNTs did not affect it.

The MWCNTs influence in C-S-H gel was studied by Li *et al*. (2020). Using an MWCNTs/C-S-H composite (with variations in Ca/Si ratio) and applying various analysis techniques, the researchers verified an increase in the interlayer spacing of the C-S-H when the amount of functionalized MWCNTs increased. According to the authors, the reason was a decrease in Ca^{2+} concentration in the interlayer due to the adsorption of Ca^{2+} by the functionalized groups of the MWCNTs, and changes in the attraction effect between the silicon chains and Ca^{2+}.

The study performed by Li *et al*. (2020) showed an increase in the proportion of gel pores and large capillary pores was observed in cement composites. However, the proportion of small capillary pores decreased with the increase of MWCNT content. Li *et al*. (2020) also emphasized that Ca^{2+} was adsorbed by the functioned MWCNTs and react with SiO^- groups to form silicon chains, reducing the proportion of capillary pores. Figure 3.2 illustrates the concepts of the pore structure of the C-S-H gel.

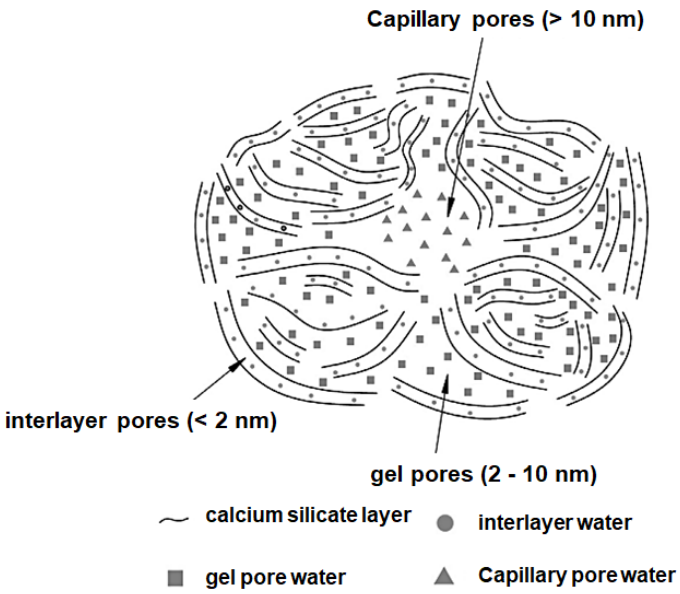

Figure 3.2 – Scheme of the pore structure of C-S-H gel.
Adapted from: Li *et al*. (2020).

Considering cement-based materials with a low w/c ratio (condition of the RPC), Jung *et al*. (2019) studied the MWCNTs influence on the mechanical performance and the microstructure of cement composites (cement pastes and mortars), with w/c equal to 0.28 and the employment of superplasticizer (SP) equal to 0.4 bwoc. It was verified that cement hydrates were formed around the CNTs inside the hardened cement porous structure and promoted connections between the cement hydrates.

According to the review paper of Rashad (2017):

> "It is safe to conclude that the addition of CNTs to cement matrix accelerated the hydration of cement as reported by approximately 78% of the quoted studies. Accelerating cement hydration has some benefits such as earlier finishing of surfaces, reduction of the hydraulic pressure on forms, further effective plugging of leaks counter to hydraulic pressure, earlier removing forms, reduction of curing time and compensation for the effect of low temperature on strength development." (RASHAD, 2017).

About the mechanical performance, scientific literature has published an extensive number of papers abording the influence of CNTs on compressive strength, tensile strength, and parameters related to ductility. According to Shi *et al*. (2019), CNTs are nano-structured fibrous material with excellent mechanical properties and they have broad prospects in the applications in cement-based materials.

Up to the year 2015, the review of Han *et al.* (2015) was the reference of results about CNTs incorporation in cement-based materials. In summary, considering the variations of dispersion and application methods, this work presents average gains in compressive strength in the order of 25%, and tensile strength (considering the flexural strength) gains in the order of 30%. Concerning ductility, gains in the order of 150% are related, as well as for the toughness modulus. To fracture energy, gain in the order of 14% is reported.

In 2017, Rashad (2017) published a very complete review work with a detailed organization of results in terms of CNTs contents and type of cement-based material. Despite great variations of the parameters evaluated, type of preparation, type of CNTs, and functionalization methods employed, the results

presented in this work showed in general, gains in terms of compressive and tensile strength and ductility of cement pastes, mortars, and concretes containing CNTs. The best results are achieved when the CNT content is around 0.1 – 0.2% bwoc.

Another important point reported in the literature, concerning the CNTs influence on the cement-based material performance, is the aspect ratio of CNTs. These nanomaterials may have a high aspect ratio, and in terms of reinforcement capacity, such characteristic is beneficial to improve mechanical performance.

Evaluating twelve different types of MWCNTs, in the ratios of 0.1, 0.5, and 0.8% bwoc, in cement pastes with w/c equal to 0.2 and a proportion of 0.75% of SP (bwoc), Cui *et al.* (2017) verified that the compressive strength with large-diameter MWCNTs was higher than the one of composites with small-diameter. However, Manzur; Yazdani; Emon (2014), working with mortars with w/c ratios in the range 0.485 – 0.6, reported the opposite. These studies suggest that different behaviors can be observed due to the cement composite porosity, which is a function of the w/c ratio. Still, according to Cui *et al.* (2017), long MWCNTs are better for improving flexural strength than short.

Abu Al-Rub; Ashour; Tyson (2012), for example, worked with MWCNTs with different aspect ratios and concentrations in cement paste composites with w/c 0.4 and superplasticizer ratio of 0.4% bwoc. These authors used long and short MWCNTs, with aspect ratios around 160 and 2500, respectively. To the long MWCNTs, the concentrations adopted were 0.04 and 0.1%, and to short were 0.04%, 0.1%, and 0.2% bwoc. In conclusion, nanocomposites with a low concentration of long MWCNTs have a comparable mechanical performance to the nanocomposites with a higher concentration of short MWCNTs. Besides that, they also report that the addition of short MWCNTs with a concentration of 0.2% (bwoc) gives better results than the other concentrations studied at the curing age of 28 days. Concerning early ages (age up to 7 days), all specimens showed higher ductility than the plain cement (reference) samples.

Still, about the influence of CNTs aspect ratio in cementitious composites behavior, an important and systematized work was developed by Ramezani; Kim;

Sun (2019). The authors did a review in literature considering a large database and a consistent statistical analysis. In summary, the conclusions are:

> "The analyses revealed that short and small-diameter CNTs could be beneficial for increasing compressive strength. Conversely, relatively long and large-diameter CNTs were more effective in increasing flexural strength. In general, an average CNT length of 10–20 μm and an average diameter of 20–32.5 nm resulted in the highest overall mechanical performance." (RAMEZANI; KIM; SUN, 2019).

Concerning the use of CNTs in RPC, on the perspective to promote singular properties in this type of concrete, recent scientific work presents important results. These results reflected, in the composite material, the particular properties that the CNTs possess.

Investigating the application of four types of MWCNTs (functionalized or not and with cure in water or oven), Ruan *et al.* (2018) used the RPC proportion proposed by Richard and Cheyrezy (1995) with the substitution of 20% of cement by Fly Ash, a water/cement ratio of 0.3 and a water reducer (surfactant) amount of 1.5% by the weight of anhydrous cement (bwoc). According to the authors, the surfactant (superplasticizer) was necessary to improve the workability of the mixture, due to the low w/c ratio. The amounts of MWCNTs were 0, 0.25, and 0.50% bwoc. In water curing, the four types of MWCNTs, in the amount of 0.25%, presented gains of flexural strength in the order of 16 – 27%. About the fracture energy in RPC, a gain of around 42% was obtained with the use of MWCNTs functionalized with -COOH chemical groups. About the compressive strength, the composition with 0.5% of MWCNTs functionalized with -OH chemical groups presented the highest gain, around 18% with respect to the reference material (without CNTs).

Studying the effect of the heat treatment cure, these authors relate gains in flexural strength around 24 – 31% with the amount of 0.25 and 0.50wt% of MWCNTs (with a -COOH functionalization), respectively. For compressive strength behavior, an increase of 31 and 17% was obtained for the amount of 0.25 and 0.50wt% of MWCNTs (with a -OH functionalization), respectively. The authors highlight that in many cases, the mechanical properties of RPC with heat treatment are better than using a water immersed cure. This is because the heat

treatment improves the bond between the MWCNTs and the RPC cement hydrated matrix.

Liu *et al.* (2019), studied the effect of different types of MWCNTs, in agreement with steel fibers, on the improvement of toughness in RPC, and this mechanism was discussed. Using a mix proportion similar to employed by Richard and Cheyrezy (1995), however adopting a cement slag addition, with w/c ratio equal to 0.24 and SP ratio equal to 0.045, these authors mentioned that the effect of MWCNTs on the fracture energy adsorption was significant, due to the effective energy adsorption capacity of MWCNTs with high aspect ratios. The mechanism to transfer the internal stress and improving the RPC performance was the connection between MWCNTs and the cement hydrated products. This connection allows a reduction in crack development at the nanoscale and improves the initial cracking tensile strength of the RPC matrix. A important point of this work was a proposed method to evaluate the toughness: the use of the areas under the load-displacement curve obtained in the three-point bending test.

A constant discussion in the literature is the fact that CNTs have a high difficulty staying dispersed during the preparation of cementitious composites (SOBOLKINA *et al.*, 2012; PARVEEN; RANA; FANGUEIRO 2013; KORAYEM *et al.*, 2017). This problem restrains their homogeneous distribution in the matrix and consequently leads to lower efficiency in the internal stress distribution. Non-uniformly distributed CNTs cannot form a fine and continuous network within a matrix to support load transfer or to mitigate crack propagation, as quoted by Sobolkina *et al.* (2012).

Since CNTs are hydrophobic, they have a great tendency to agglomerate in the presence of water. For an effective application of these nanomaterials in cementitious matrices, some methods are employed, such as acidic functionalization (chemical methods), use of surfactants, as well as the use of ultrasound, microwaves, and mechanical stirring (KORAYEM *et al.*, 2017; MENDONZA REALES et al., 2018).

In general, the performance of cementitious matrices with CNTs is conditioned to the dispersion method employed during the preparation. This is because the vast majority of researchers use the physical mixture method, where CNTs are

functionalized and dispersed by mechanical or chemical methods. High-performance results often depend on the use of these mechanisms, as reported by Parveen *et al.* (2015).

However, such processes may cause undesired degradation of the CNTs properties and difficulty in the preparation of the composite (KIM *et al.*, 2005; PARVEEN; RANA; FANGUEIRO, 2013).

To minimize the dispersion problem of CNTs in composite materials, some researchers have implemented a synthetic route to grow CNTs using a ceramic material as support, allowing the carbon nanotubes to be anchored on it, reducing the possibility of agglomeration during application. This method, called as “in situ” process, has presented effective and significant results (with gains compatible or superior to the physical mixture method) with the use of cement clinker as support, reducing the dispersion problem of CNTs in cementitious matrices (NASIBULIN *et al*., 2009; LUDVIG *et al*., 2011; SUN *et al*., 2013; PAULA *et al*., 2014; SOUZA *et al*., 2020).

3.2.2. Nano-silica effects

According to Zhang *et al.* (2017), nano-silica (nano-SiO_2) is a type of nanoparticle with the most extensive applications in concrete and ultra-high performance concrete (UHPC) due to its high reactivity, high specific surface area, and pozzolanic activity during the cement hydration process.

The addition of nano-SiO_2 in cement-based materials can modify the cement hydration process, mainly at the early stage of hydration (LAVERGNE *et al*., 2019). Land and Stephan (2012) observed that the hydration heat of ordinary Portland cement blended with nano-SiO_2 during the main period increases significantly due to the larger surface area of silica, which can promote the nucleation effect. They report that:

> "Nucleation seeding is a new approach to control the kinetics of cement hydration. It is known that nano-silica has an accelerating effect on cement hydration. In this case, the acceleration should depend on the particle's surface area. The acceleration of cement hydration clearly correlates with the total surface size of the added particles." (LAND; STEPHAN, 2012)

Thus, these modifications change the microstructure of the hydrated cement matrices and modify performance. Still as reported by Land and Stephan (2012), the aim of the application of ultra-fine additives like nano-SiO_2 in cementitious systems is to improve the characteristics of the plastic and hardened material. This is because nano-scaled silica particles have a filler effect, according to Said *et al*. (2012), filling up the voids between the cement grains.

Using the technique of isothermal calorimetry, Lavergne *et al*. (2019) verified significant differences in the cement hydration process between cement pastes without nano-silica and with 1.5, 3, and 5% bwoc of nano-SiO_2. Even varying the w/c ratio (0.35 to 0.45) the difference remained, indicating that there is a significant contribution of this amorphous material in the cement hydration process.

The acceleration in cement hydration reactions may be related to the elevated specific surface area of nano-silica, according to Qing *et al.* (2007). With the presence of silanol groups on its surface, nano-silica has the capacity of attracting cations (Na^+, K^+, and Ca^{2+}), conform quoting by Oertel *et al.* (2014). According to Singh *et al*. (2013), when the nano-SiO_2 is added to cement grains in presence of water, the Ca^{+2} ions in solution react with $H_2SiO^{2-}_4$ groups converting it into additional calcium-silicate-hydrate (C-S-H). These, in turn, are spread in the solution and serve as seeds for the formation of more compact C-S-H phases. Besides, nano-SiO_2 promotes a reduction in setting time, shortening the duration of dormant and induction periods of hydration, and decreases the formation of calcium hydroxide in the first hours of the process (BJÖRNSTRÖM *et al.*, 2004).

Considering the effect of nano-SiO_2 in the context of UHPC, it is necessary to take into account the influence of a large amount of superplasticizer employed to produce this type of concrete. As a result, the hydration process is retarded, as quoted by Yu, Spiesz, and Brouwers (2014). However, also conform to these

authors, this delay is compensated by the further effects of nano-SiO_2 on structural improvement.

The main effect of nano-SiO_2 in the cement hydration process is the pozzolanic effect. The pozzolanic effect can be understood as a reaction transforming CH ($Ca(OH)_2$) in additional C-S-H, the phase responsible for the mechanical strength in hardened cementitious matrices. With the application of nano-SiO_2, this reaction can be described by Equations 3.2 to 3.4:

$$nano - SiO_2 + H_2O \rightarrow H_2SiO_4^{2-} \quad (3.2)$$

$$Ca(OH)_2 + H_2O \rightarrow Ca^{2+} + OH^- \quad (3.3)$$

$$H_2SiO_4^{2-} + Ca^{2+} \rightarrow C - S - H\ (additional) \quad (3.4)$$

Other materials have the potential to improve the pozzolanic effect. However, according to Hou *et al.* (2013), nano-SiO_2 has a higher capacity due to the unsaturated Si-O bonds on the particle surface, which speeds up the pozzolanic reaction. This is very important in producing ultra-high performance concrete and the key to the process is the nano-silica high specific surface area (HOU *et al.*, 2013; YU; SPIESZ; BROUWERS 2014; SHI *et al.*, 2015; ZHANG *et al.*, 2017; WU; HENRI; SHI 2017; BALAPOUR; JOSHAGHANI; ALTHOEY 2018).

In general, the additional formation of C-S-H by pozzolanic effect due to the presence of nano-SiO_2 can be summarized schematically as shown in Figure 3.3.

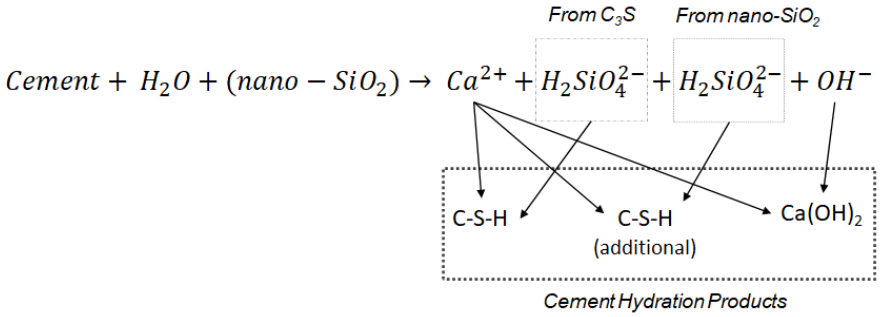

Figure 3.3 – Pozzolanic effect with nano-SiO_2 application in cement-based materials. Adapted from Singh *et al.* (2013)

Concerning the workability (capacity to flow) of cement-based materials with the addition of nano-SiO_2, the scientific literature relates that due to their high specific surface area, there is a higher water demand to retain the workability (ZHANG *et al*., 2017; PAUL *et al*., 2018). According to Berra *et al.* (2012), this may be due to instantaneous interactions between the nano-SiO_2 and the liquid phase of the cementitious mixtures, mainly dissolved alkalis, forming gels characterized by high water retention capacities. Kong *et al*. (2013) investigated the influence of precipitated nano-SiO_2 on the rheological behavior of cement pastes. They verified that the agglomeration of this nanomaterial reduces the workability. Due to difficulty in packing the particles, and consequently, the filler effect, less free water is released to improve the mixture fluidity. The amount of nano-SiO_2 can also influence the behavior in the fresh state. Even working with low replacement ratios (0.75 and 1.50% of the binder weight) of nano-SiO_2 particles with different specific surface areas in high-performance concrete (HPC), Khaloo; Mobini; Hosseini (2016) verified a reduction in the flow spray, with trend intensified when increasing this nanomaterial content. Because of these aspects, when nano-SiO_2 is used in reactive powder concrete (RPC), the correct superplasticizer admixture dosage is particularly important to guarantee proper workability and applicability of the concrete.

Regarding the performance modifications with the use of nano-SiO_2 in high-performance concretes (HPC), expressive gains in terms of compressive and tensile strength, and durability have been shown in the literature. These results are related to the effects, previously cited, that the nano-SiO_2 causes in cement-based materials, modifying the microstructure to improve the cement matrices, ensuring more strength. The conclusions of recent review papers highlight the following (Singh *et al*., 2013; Zhang *et al*., 2017; Balapour; Jhoshaghani; Althoey, 2018):

- The addition of nano-silica or partial cement substitution by nano-SiO_2 improves the compressive and tensile strength. It is mainly due to the filler and pozzolanic effects, which promote changes in the microstructure and results also in additional C-S-H formation;
- Flexural strength and flexural fatigue are enhanced in HPC with the addition of a small amount of nano-SiO_2;

- The increase in nano-SiO_2 quantity can promote a decrease in performance in terms of mechanical behavior: dosages smaller than 5% bwoc are more adequate. The fracture parameters increase gradually with the amount of nano-SiO_2 increasing up to a maximum content of 5%. Values higher than that resulting in a decrease in performance;
- Nano-SiO_2 promotes changes in the hydration of cement and generates a large formation of C-S-H gel. This change decreases the porosity inside the hydrated cement paste and in the interfacial transition zone (ITZ) between the aggregates and the cementitious matrix. This result effectively increases the mechanical strength and durability performance.

3.2.3. CNTs and nano-SiO_2 synergistic effects

As discussed in the previous topics, both CNTs and nano-SiO_2 have the potential to improve the performance of cement-based materials. Consequently, it is possible to infer that the use of these two nanomaterials can enhance, in a singular way, the mechanical behavior of cementitious matrices. The main objective of using together CNTs and silica materials is the possibility to improve the dispersion, as discussed by Zhang *et al*. (2006) and Bourlinos *et al.* (2007), and the performance of CNTs in the cementitious matrices (MUDIMELA *et al*., 2009; NASIBULIN *et al*., 2009; LUDVIG *et al*., 2011; ALREKABI *et al*., 2016).

In a recent paper, Kim *et al*. (2019) evaluated the effects of covalently synthesized CNTs and silica fume (SF). An aminated SF was synthesized together with CNTs and this hybrid was used in cement paste (w/c ratio equal to 0.5). The results of nanoindentation showed stiffness and compressive strength increases of the composite C-S-H phase. However, as reported by the authors, no gain in the tensile strength was achieved.

Yakovlev *et al.* (2017) investigated the influence of so-called “complex nano dispersed systems with multi-walled carbon nanotubes and dispersed nano-silica” in cement pastes. Through the technics employed, the results showed a structured binding matrix along with a perfect dense shell of hydrated new

products on the surface of the solid phases. It is worth mentioning that the authors used a sonication process and surfactant to disperse the nanomaterials.

One advantage of the combined use of CNTs and nano-SiO_2 can be the modification in the cement hydration process with the addition of a superplasticizer. This admixture can modify and retard the cement hydration process. It was reported by Sikora *et al.* (2019) that, in the presence of a silica shell on the MWCNT/nano-SiO_2 by physical mixture, the hydration rate of cement is higher than the one of pure cement and cement incorporated with inaccessible MWCNTs. In the same work, the reported compressive strength gain was around 20% compared to the control samples.

Replacing cement by fly ash (40% bwoc) together with MWCNTs (0.08 % bwoc) and nano-SiO_2 (2 % bwoc) in self-compact concrete (SCC), Aydin; Nasl; Kotan (2018) reported modifications in the rheological behavior (increase in viscosity), acceleration of the cement hydration process in the early ages, and improvements on flexural toughness of 20%.

The interaction between CNTs and cement hydrated matrice is crucial in optimizing the reinforcement of CNTs in cement composites. With this concept, Li *et al*. (2017) evaluated the effects of nano-SiO_2 (manufactured by sol-gel method with a mean particle diameter of 14 nm) on the interactive behaviors of CNTs by physical mixture in the cement pastes with different w/c ratio. Using various analysis methods, the authors reported that the nano-SiO_2 did not affect the dispersion of MWCNTs suspension, but promoted the nucleation of C-S-H around MWCNTs. It was also possible to verify that the nano-SiO_2 is adsorbed on the surface of MWCNTs and accelerates the formation of hydration products of the cement. The simultaneous insertion of nano-SiO_2 and MWCNTs improved the interfacial adhesion between MWCNTs and cement matrices, leading to higher loss modulus and improved the energy dissipation ability (66% higher than the control sample).

In general, according to the consulted bibliography, the synergic application of CNTs and SiO_2 in cement-based materials promotes similar effects provided by the separated materials. However, improvements in terms of dispersion and nucleation effects are reported. All these modifications reflect improvements in

terms of mechanical performance, mainly in terms of ductility, a deficit feature of the cement-based materials.

3.3. SYNTHESIS OF CNTs BY CCVD METHOD

Carbon nanotubes (CNTs) have attracted great interest in academic and industrial areas owing to their unique and novel physicochemical properties when compared to other macros-, micros-, and nanomaterials (LIN *et al*., 2011; SHUKRULLAH *et al*., 2016).

Kumar (2011) highlights the exceptional properties of this nanomaterial:

- “CNT is 100 times stronger than stainless steel and six times lighter”;
- “CNT is as hard as diamond and its thermal capacity is twice that of pure diamond”;
- “CNT’s current-carrying capacity is 1000 times higher than copper”;
- “CNT is thermally stable up to 4000K”;
- “CNT can be conductor or semiconductor, depending on their diameter and chirality”

However, still according to this author, it is important to note that all those superlative features were predicted for an atomically-perfect ideal CNTs, which is not the actual reality. Concerning the characteristics mentioned, the scientific literature specifies reference values conform to some types of CNTs (SHAH; TALI, 2016).

The structure of carbon nanotubes is based on graphene. According to Bhushan (2007), it is a monoatomic and polyaromatic layer of carbon atoms in hybrid bonds type sp^2, arranged in hexagons. CNTs are quasi-one-dimensional nanostructures, Gohier *et al.* (2008), produced through a range of growth processes, with specific nature in agreement to the targetted applications (SHUKRULLAH *et al*., 2016).

The three major techniques for the production of CNTs are arc discharge, laser ablation, and chemical vapor deposition (CVD) (TAN *et al*., 2013). Still, according

to these last authors, the CVD technique shows advantages for the growth of CNTs due to its low growth temperature, good controllability, and easiness of scaling up production at a relatively low cost.

According to Kumar (2011), Tan *et al*. (2013), and Shah; Tali (2016), the CVD method consists of a procedure where a carbon source (generally a hydrocarbon), inside a reactor with controlled temperature, is directed to one point where transition metal nanoparticles (predominantly metal with 3d valence like Fe, Co, and Ni) denominated catalyst, are located and are used as a point of decomposition of the hydrocarbon source. This process occurs due to the high solubility and diffusion rate of carbon over the catalyst at high temperatures. Usually, ceramic materials are used as support for metal catalysts. Sometimes, when a catalyst is used, the term catalytic chemical vapor deposition (CCVD) is employed.

It is reported by Gupta *et al*. (2013), that there are two types of CNTs: the single-walled carbon nanotubes (SWNTs) and the multi-walled carbon nanotubes (MWNTs). However, other types are cited in the literature, like double-walled carbon nanotubes (DWCNT´s) and few-walled carbon nanotubes (FWCNTs), which cover nanotubes with sidewalls of 2-5 layers and diameters ranging from 3 to 8 nm (DOUVEN *et al*. 2011; CUNHA *et al.*, 2018).

To describe the two main types of CNTs, Gupta *et al*. (2013) quote that SWCNTs can be seen as single-layer graphene rolled into a cylinder form, one-atom-thick, usually with a small number (40–50) of carbon atoms along the circumference and a length along the cylinder axes of some microns. The MWCNTs consist of multiple rolled layers (concentric tubes) of graphene and are typically 100 times longer than they are wide and have outer diameters mostly in the tens of nanometers. These authors still reported that, although it is easier to produce significant quantities of MWCNTs than SWCNTs, their structures are less understood than SWCNTs because of their greater complexity and variety. Figure 3.4 illustrates the graphene structure and types of carbon nanotubes structures.

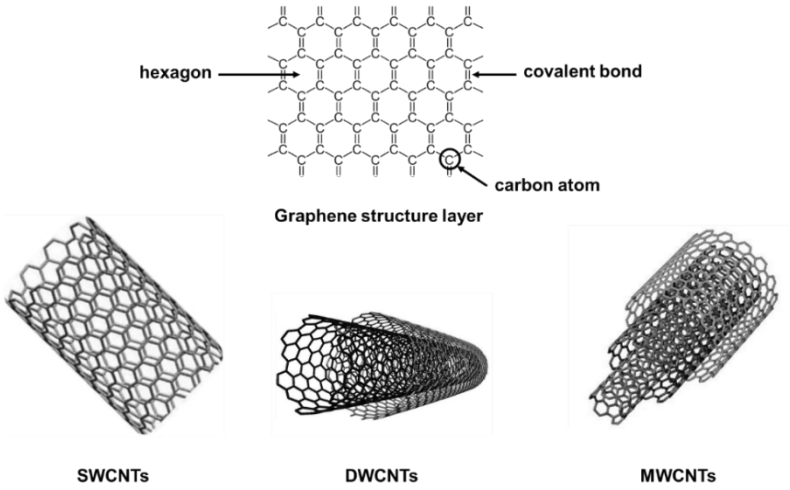

Figure 3.4 – Schematic models of a graphene sheet and some types of carbon nanotubes.

In the CCVD process, the catalyst nanoparticle can remain anchored to the substrate (support) or not. In the first condition, the synthesis model is called ‘‘base-growth’’. In the second mode, the growth follows a ‘‘tip-growth’’ mechanism, when the particle lifts off the substrate and is observed at the top of the CNTs (GOHIER *et al.*, 2008).

According to Hong *et al.* (2012), the growth mode is related to the catalyst particle size. Working with three different catalysts (cobalt, nickel, and iron), the ‘‘tip-growth’’ mode was observed for large catalyst particles (> 5 nm), the ‘‘base-growth’’ mode for smaller ones (< 5 nm). This was related to the catalyst cluster formation process.

However, as shown by Song *et al.* (2004), the difference in growth mode can also be explained in terms of adhesion force and interaction between the catalyst and the material support. While a weak contact favors the “tip-growth” mechanism, a strong interaction promotes the “base-growth”. Figure 3.5 presents a schematic illustration of the CCVD method for a horizontal reactor, and the CNTs growth modes.

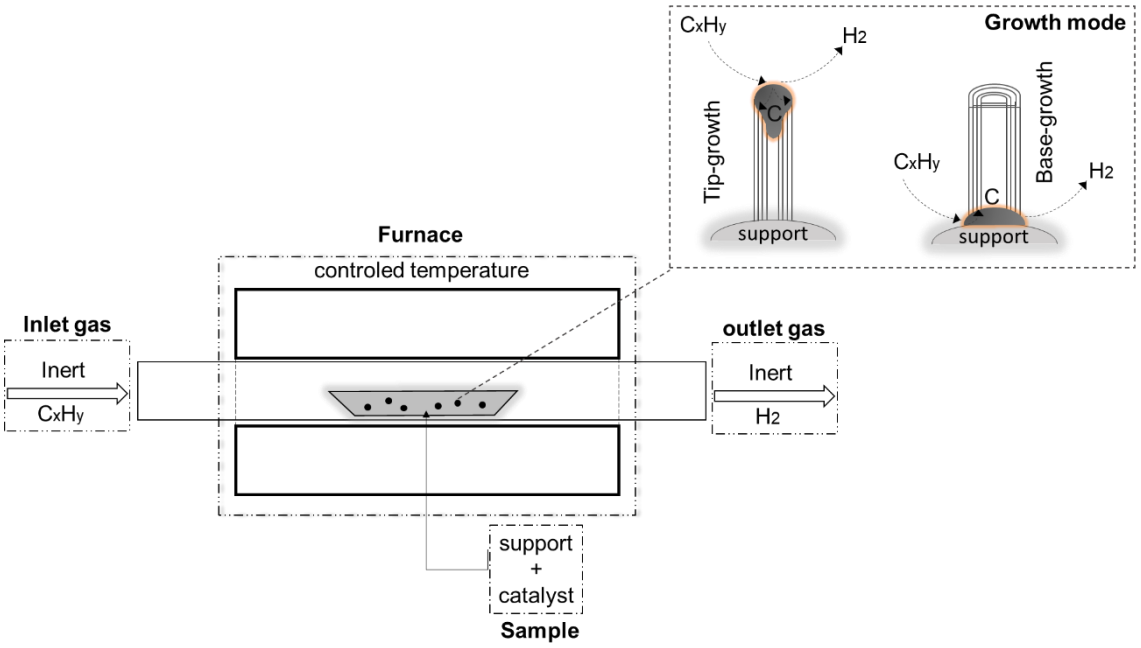

Figure 3.5 – Schematic illustration of the catalytic chemical vapor deposition method and CNT growth mode.

Due to its features, the advantages of the catalytic chemical vapor deposition method, conformed Shah and Tali (2016), are:

- to be a simple, economical, and scalable technique for mass production of carbon nanotubes;
- to be able to use plenty of hydrocarbons in any form (solid, liquid, or gas) and various kind of substrates;
- to be able to grow CNTs in different forms like aligned or entangled, straight or coiled nanotubes, or the desired architecture of nanotubes on predefined cites of a patterned substrate.

In the CCVD method, the structural characteristics of CNTs are directly dependent on some aspects, as the type and geometry of the reactor, process conditions, type, and nature of the gas carbon source, reactants proportions, catalyst activity, precursor flow rate, growth temperature, and the activation energy (DUPUIS, 2005; JOURDAIN; BICHARA, 2013; SHUKRULLAH *et al.*, 2016).

The molecular structure of the carbon source influences the morphology of the synthesized CNTs (JOURDAIN; BICHARA, 2013; SHAH; TALI, 2016). In the

literature about the CCVD method, the majority of the works use hydrocarbons as a carbon precursor. Kumar and Ando (2010) cite that the most used are methane, ethylene, acetylene, benzene, and xylene. These authors still mentioned that linear hydrocarbons, such as methane, ethylene, and acetylene, decompose thermally in carbon atoms or linear dimers/trimers of carbon and generally produce aligned CNTs. On the other hand, cyclic hydrocarbons such as benzene, xylene, cyclohexane, and fullerene produce relatively curved CNTs.

The choice of carbon precursor should take into account the process as a whole, including the type of reactor employed, pressure in the system, process time, type of catalyst used, and the working temperature. About the temperature, a common range is between 500 to 1000°C, according to Bhushan (2007).

Considering the CNTs growth modes, an important consideration should be given to the catalyst and the substrate employed in the CCVD process. The importance of using an adequate catalyst, with suitable size, is related to two main factors: i) metal-based particles with nanometer-size are required to promote the hydrocarbon decomposition for the CNTs growth (Kumar and Ando, 2010), and ii) the catalyst-particle size dictates the nanotube diameter size: generally nanotubes with smaller diameters are synthesized when the size of the catalyst particle has few nanometers (KUMAR, 2011; SHAH; TALI, 2016).

As previously cited, the transition metal Fe, Ni, and Co are the most appropriated and commonly used in the supported CCVD method. Oxides with these metals are commonly deposited in ceramic substrates (also oxides) to grow CNTs with specific features. According to Kumar and Ando (2010), the substrate material, surface morphology, and textural properties greatly affect the yield and quality of the resulting CNTs. An adequate interaction between the catalyst and the support prevents catalyst agglomeration to form large clusters that can results in CNTs with inadequate qualities (WRIGHT *et al*., 2003). van der Wal; Ticich; Curtis (2001) also emphasize these aspects and report that in addition to these physical interactions, the support can also interact chemically with the catalyst particle and drastically affect its catalytic activity.

Regarding the purpose of this work, the use of nanostructured SiO_2 (n-SiO_2) and CNTs in RPC, some considerations on the use of silica as support for catalyst in the CNTs synthesis by CCVD method are addressed.

Mesoporous nano-SiO_2 is commonly referred to as a good support material for CNTs synthesis by the CCVD process, according to Ramesh *et al*. (2005); Escobar *et al*. (2007); and Othman; Kinloch; Wilkinson (2013). Especially when the SiO_2 has high specific physical parameters (pore volume, pore size, and specific surface area) and it improves the interaction with the catalyst material necessary to grow the CNTs by CCVD (WANG *et al.*, 2007). Thus, the n-SiO_2 production with tailored structural properties is desired and the sol-gel method adequate.

3.4. SYNTHESIS OF SiO_2 BY SOL-GEL METHOD

According to Hiratsuka; Santilli; Pulcinelli (1995), the sol-gel method is a secular knowledge of chemistry. From the 1960 and 1970 decades, it has presented alternatives to the synthesis of vitreous materials applied in several areas of Materials Science, such as multi-component glasses, optical fibers, and additions for polymeric composites. The use and interest in vitreous materials, mostly silica (SiO_2), are reported from the beginning of the civilization, as quoting by Hench and Vasconcelos (1990). These authors still report that the traditional processes for obtaining this oxide, in its pure form, involve the melting of natural quartz, which often has unwanted impurities.

Currently, technological development demands the use of materials with specific features allowing full functionality of apparatus or technological processes that use them. In this sense, a material that has a high demand for application in various areas of technology is silica with high purity. Applications in electronic devices, insulating devices, catalysis, pharmaceuticals, photonic crystals, chemical sensors, biosensors, imaging markers, corrosive, and protection additions for advanced materials use SiO_2 with high purity (DUBEY; RAJESH; MORE, 2015; GUO *et al.*, 2017).

Other works mention applications of SiO_2 obtained by sol-gel methods, like aerogels, monodisperse silica; thin films application; ceramics matrices; membranes; adsorption; and support to carbon nanomaterials (PRIMEAU; VAUTEY; LANGLET 1997; RAO; BHAGAT 2004; TOMITA; KAWASAKI; OKADA 2004; RAMESH *et al*., 2005; HOUMARD *et al*., 2014; CASTRICUM *et al*., 2015; SHIMOGAKI *et al.,* 2015; MOTA *et al*., 2017; PIÑERO *et al*., 2018).

Besides the issue of material quality, another important point for any of the mentioned applications is the production of a material with controlled physical properties, particularly the pore volume and size (RAHMAN; PADAVETTAN, 2012). In this aspect, the sol-gel process can provide control conditions allowing the production of nano-scale materials (10^{-9} m) (DUBEY; RAJESH; MORE, 2015).

The sol-gel process allows producing silica particles with high superficial surface area, in the thousands of $m^2.g^{-1}$, for example, until diameter porous size in the order of few nanometers (SINGH *et al*., 2014).

According to Guo *et al*. (2017), the sol-gel method is simple and efficient to synthesize SiO_2 nanoparticles with uniform size. This relates to an approach called bottom-up, where a chemical route is used to produce nanoparticles of silica from the atomic or molecular scale (RAHMAN; PADAVETTAN, 2012).

As quoted by Hiratsuka; Santilli; Pulcinelli (1995), in the definition of the term sol-gel, the term sol defines a dispersion of colloidal particles stable in a fluid. The term gel defines a system formed by a rigid structure of colloidal particles or polymeric chains that immobilizes the liquid phase in their interstices. Brinker and Scherer (1990) mention that colloids are elements that can be used for the generation of polymers or ceramic materials. Still according to these authors, in the sol-gel process, the precursors for preparing a colloid consisting of a metal or a non-metal element bonded with several other elements.

Livage *et al*. (1989) describe that the chemistry of the sol-gel process is based on inorganic polymerization reactions and the precursors generally used are solutions of inorganic salts or alkoxides dissolved in organic solvents. In both cases, these authors present the reactions described in the sequence:

- Hydrolysis of the precursor leading to the formation of M-OH bonds. For inorganic precursors, the hydroxylation is obtained by changing the pH of the solution, leading to the protonation of anionic oxo-ions:

$$MO_n^{x-} + H^+ \rightleftharpoons HMO_n^{(x-1)-}$$

or the deprotonation of cationic aquo-ions:

$$M(OH_n)_n^{z+} \rightleftharpoons [M(OH)(OH_2)_{n-1}]^{(z-1)+} + H^+$$

The hydroxylation of alkoxides is performed by hydrolysis after the addition of water:

$$M(OR)_n + H_2O \rightleftharpoons M(OH)(OR)_{n-1} + ROH$$

- Condensation, or polycondensation, follows the hydroxylation reaction, generating water molecules:

olation: $M\begin{matrix}/^{OH}\\ \backslash_{OH_2}\end{matrix} + \begin{matrix}^{H_2O}\backslash\\ {}_{OH}/\end{matrix}M \rightarrow M\begin{matrix}/^{OH}\backslash\\ \backslash_{OH}/\end{matrix}M + 2.H_2O$

$$M - OH + HO - M \rightarrow M - O - M + H_2O$$

or alcohol molecules (oxolation):

$$M - OH + RO - M \rightarrow M - O - M + ROH$$

Still, according to Livage *et al*. (1989), hydroxyl or oxygen bridges are formed in both cases, leading to the condensation of species. At the end of the process, all metallic atoms are bonded to oxygen and a network of hydrated oxide is obtained.

In general, for the SiO_2 synthesis, the sol-gel method involves the hydrolysis and condensation of metal alkoxides ($Si(OR)_4$), as the tetraethylorthosilicate (TEOS, $Si(OC_2H_5)_4$) or inorganic salts such as sodium silicate (Na_2SiO_3), in the presence of acid or alkali as catalyst (RAHMAN; PADAVETTAN, 2012). Figure 3.6 presents a schematic diagram of the process using the TEOS precursor.

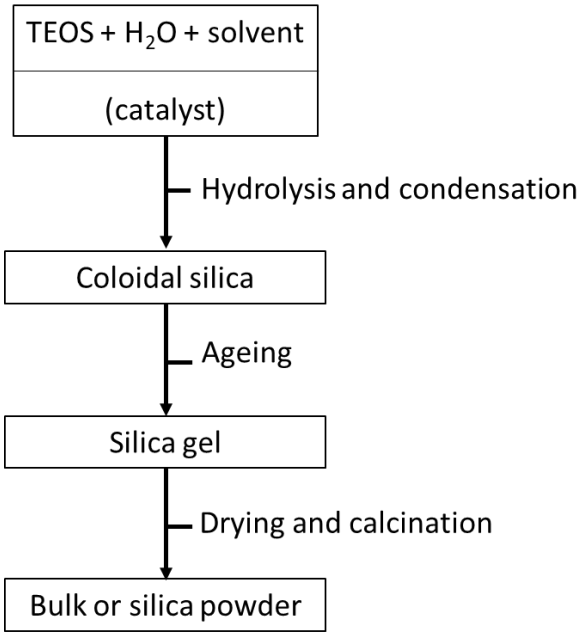

Figure 3.6 – Typic steps of SiO_2 synthesis by the sol-gel method.
Adapted from (RAHMAN; PADAVETTAN, 2012)

The typical reaction for this process, using the TEOS precursor, is presented below:

$$Si(OC_2H_5)_4 + H_2O \xrightarrow{hydrolysis} Si(OC_2H_5)_3{-}OH + C_2H_5OH$$

$$\equiv Si - O - H + H - O - Si \equiv \xrightarrow{\text{water } condensation} \equiv Si - O - Si \equiv + H_2O$$

$$\equiv Si - OC_2H_5 + H - O - Si \equiv \xrightarrow{alcohol\ condensation} \equiv Si - O - Si \equiv + C_2H_5OH.$$

The hydrolysis of the TEOS molecules forms silanol groups and the condensation/polymerization reactions between these groups, or between silanol and ethoxy groups, create siloxane bonds (Si-O-Si), which in turn form a tridimensional silica structure (RAHMAN; PADAVETTAN, 2012).

3.5. CONSIDERATIONS ABOUT THE LITERATURE REVIEW

The current technical development scenario favors the emergence of new building construction techniques and solutions. However, its viability and effective implementation are associated with the development of new materials, which provide high-performance functions and durability.

Thus, Nanotechnology is an emergent field and can contribute to making real new solutions. This is due to the particular characteristics that nanomaterials usually have, allowing them to produce composites with high performance and with non-conventional features. Based on these aspects, carbon nanotubes are already a reality to the ability to structurally reinforce composite materials.

As previously mentioned, due to their properties, CNTs are hydrophobic and their employment in cement-based materials has difficulties for adequate dispersion. A viable solution, appropriate to the civil construction processes, may be the “in situ” synthesis by the CCVD method. By this method, as already reported in the literature, the CNTs dispersion is facilitated, and higher performances of cementitious composites are achieved.

Besides the dispersion, the CNTs morphology is also an important aspect. The reviewed literature reports modifications in mechanical behavior according to the physical properties of the CNTs. Gains in tensile strength and fracture parameters are reported with long MWCNTs, but short MWCNTs are important during the cement hydration process. Thus, to obtain a material with adequate morphology, the MWCNTs synthesis process needs to be controlled, mainly in terms of the catalyst interaction with the substrate support.

In this context, the use of nanostructured silica (n-SiO_2) as support for CNTs growth has a huge interest. Indeed, its surface features could favor the catalyst interaction and favor the growth of CNTs with the desired quality and morphology. This feature should also favor its pozzolanic activity leading to efficient conversion of CH in additional C-S-H, which is the main cement hydrated phase responsible for the concrete strength. Besides, through the pozzolanic reaction, occurring over the n-SiO_2/CNTs hybrid synthesized in this work, the CNTs anchorage in the

concrete structure could be improved favoring its mechanical purpose, mainly in terms of fracture toughness. Thus, the control of the silica morphology appears to be important for the final concrete properties targeted in this research.

Taking into account these aspects, the sol-gel method was considered adequate to produce silica with a tailored porous structure to promotes the pozzolanic effect and to control the MWCNTs growth process by the CCVD method. As reported in the literature, it is possible by the sol-gel method to control parameters such as the specific surface area, volume porosity, and pore size distribution. These aspects are important for the objective of this work, in terms of pozzolanic effect and microstructural reinforcement, improving the fracture parameters of a brittle concrete.

4. METHODOLOGY

In agreement with the proposed objectives, the methodologies adopted in this Thesis were the production of hybrid material with nano-structured silica (n-SiO_2) and carbon nanotubes (CNTs) with desired features. The CNTs were synthesized directly over the nanostructured silica particles, because this concept promotes an effective bonding between these two nanomaterials, thus inhibiting the pronounced effect of the agglomeration when applied in cementitious materials. Furthermore, according to the literature review, the aspect ratio of the *MWCNTs* is a relevant characteristic in terms of stress transfer inside the cementitious matrix and in terms of the cement hydration process. Concerning this last point, nano-structured silica has a relevant contribution, as related in the literature. Thus, considering all these aspects, this hybrid material was incorporated in reactive powder concrete to improve, mainly, the fracture toughness.

Concerning the structural reinforcement capacity at the microstructure level, the hypothesis of a pozzolanic effect with the generation of additional C-S-H around the n-SiO_2 particles and involving the CNTs, during the cement hydration process was evaluated. The process was analyzed at an early age: after 3 days of cement hydration. Thus, the evaluated hypothesis, based on the mechanical properties of the CNTs and the pozzolanic effect of the n-SiO_2, was creating regions in the microstructure of the concrete matrix with high performance in terms of strength, reflecting in the macro behavior in terms of fracture toughness. Figure 4.1 illustrates this concept and the effect on the RPC matrix. In the figure, (1A) represents the RPC matrix after the mixing process, and (1B) the hydrated matrix. With the addition of the hybrid, in (2A), the RPC matrix after the mixing process, and (2B) when hydrated, with local reinforcement.

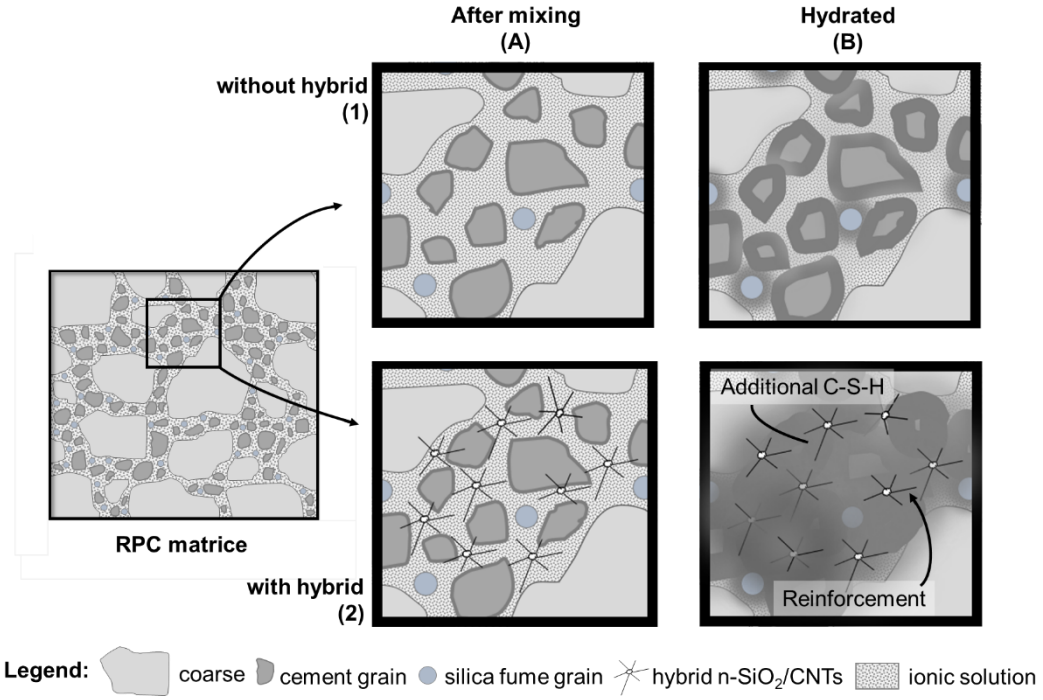

Figure 4.1 – Concepts related to the proposed hypothesis in RPC matrice.

Considering that the pozzolanic effect is more pronounced in the presence of silica with a high specific surface area and considering the possibilities that the sol-gel method can promote in terms of SiO_2 synthesis with controlled parameters, it was considered adequate to use this method to produce the desired material, as previously mentioned. Furthermore, a support material to CNTs synthesis with adequate length and morphology also needs to have adequate characteristics.

Thus, once again, the sol-gel method can be used to fabricate this material. These arguments justify the use of the sol-gel method to produce the hybrid material, with the necessary characteristics of the desired effects in RPC matrice.

To validate the discussed hypothesis, chemical and physical characterizations were employed, and the described following steps were adopted to achieving the delimited objectives.

For the development of the hybrid (SiO_2/CNTs), three stages were performed.

Initially, the features support (SiO_2) influencing the CNTs growth process was verified. Five nanostructured silica were synthesized by the sol-gel method

controlling the process parameters to obtain materials with different physical properties, like porosity, specific surface area, and pore size. In the same way, also using the sol-gel method, an iron-based catalyst was synthesized to obtain hematite particles with an equivalent diameter in the nanometric scale. After this, using the CCVD method, the carbon nanotube (CNT) synthesis processes were performed in each one of the five prepared samples. The resulted hybrids were then properly characterized.

The chosen carbon source was methane (CH_4), due to its hydrogen/carbon ratio, which provides carbon to CNTs, beyond H_2 for the catalyst reduction. Besides that, natural gas (rich in CH_4) can be used in the future for large-scale production of the hybrid.

In the second stage, considering the silica support with better results in terms of CNTs quality and quantity, the CNTs synthesis was again performed, but changing the catalyst incorporation method in this silica support. Therefore, three different catalyst incorporation methods were used: by deposition, by impregnation, and one based on a modified sol-gel method. The details of the processes are explained in the text, topic 4.1. Again, the CNT syntheses were performed by the CCVD method. The three obtained (n-SiO_2/CNTs) hybrids samples were then properly characterized.

After the characterizations and upon the obtained results in these first two stages, an embased choice was made and resulted in the suitable support and catalyst method incorporation to CNTs synthesis. Based on this consideration, the SiO_2/CNTs hybrid was produced in sufficient quantity to be incorporated in the cementitious composites and carry out the tests. This was considered the third stage in the production of the hybrid.

Considering the possible influence of the hybrid on the early cement hydration process and to evaluate an adequate amount of this hybrid in the RPC matrix, pozzolanic tests and cement hydration assessments were performed. These were the previous step before the incorporation of the hybrid in the reactive powder concretes (RPCs) to the mechanical evaluations.

Initially, a specific analysis was performed to evaluate indirectly the possible pozzolanic effect of the hybrid, by the denominated chemical method. Later, evaluations were carried out by thermogravimetric analysis, x-ray analysis, and N_2 adsorption to verify the effects of the hybrid in the cement hydration process on a global scale. Lastly, the hydrated microstructure was then evaluated by EDS-SEM analysis to verify the effect of the hybrid (according to its concentration) locally. After all these steps, the adequate content of the hybrid was defined to be used in the reactive powder concretes (RPCs).

Finally, RPCs were produced and the macro performance evaluations, in terms of mechanical behavior, were carried out. Additionally, the adopted content of hybrid from the previous analysis, a lower content also was used considering, proportionally, the optimum CNTs proportion (by weight of cement) described by the literature review (≈ 0.25 wt%). Figure 4.2 schematizes the synthesis procedure used in this work.

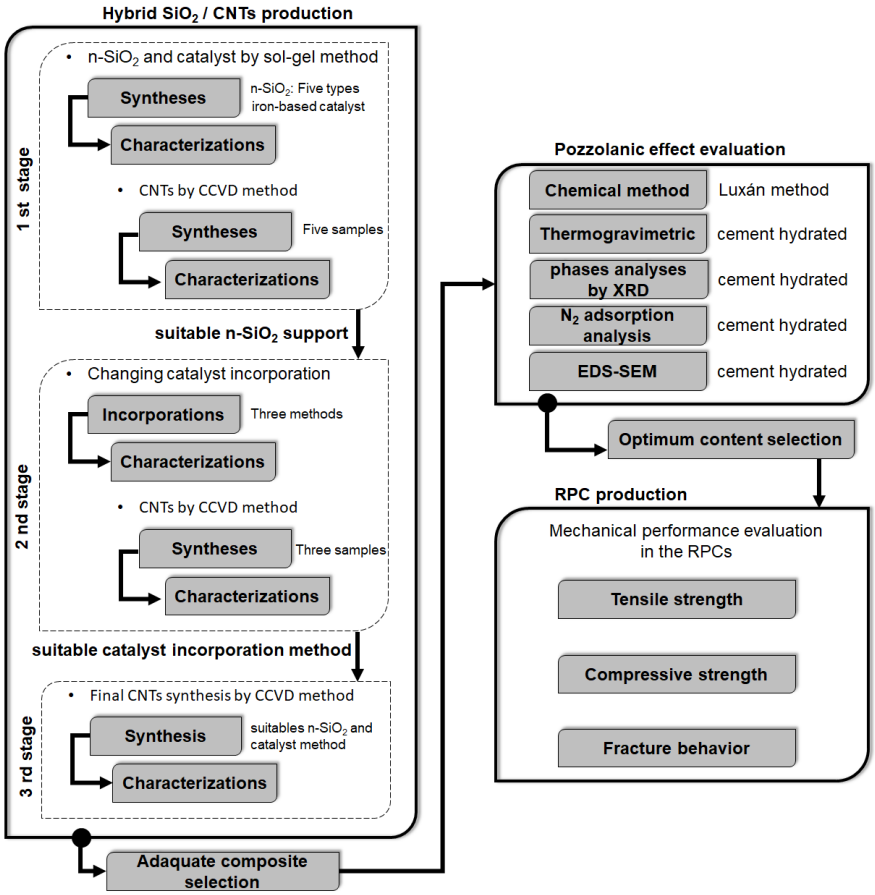

Figure 4.2 – Scheme of the adopted procedures in the development and production of the hybrid and its application in RPC.

4.1. PRODUCTION OF THE HYBRID n-SiO_2/CNTs

As previously mentioned, considering the importance of catalyst/support interaction in CNT synthesis by the CCVD method, and the development of the hybrid, to achieve an adequate interaction between the CNTs and the support, three routes were used to associate the substrate and the catalyst.

The first was the deposition (DEP) method, where an iron-based catalyst particle was synthesized and prepared separately, and later deposited over the nanostructured silica. In this route, the support (substrate) modification was considered through changes in its physical properties. Thus, five silica substrates were synthesized by the sol-gel method controlling the synthesis parameters and consequently changing the physical parameters of the resulted material. The objective was to obtain suitable support and evaluate its influence in CNT morphology.

The second route used was the impregnation (IMP) method. In this case, the catalyst was incorporated from salt impregnation over one type of nanostructured silica, seeking an adhesion by surface interactions. The n-SiO_2 choice was based on the results of the previous route, DEP, where the silica support with suitable features was obtained.

And finally, the third method adopted was based on a modification of the sol-gel method (MSG) by a co-condensation, where the catalyst was incorporated together with the same type of n-SiO_2 chosen in the first route, using an iron precursor. The objective was to insert the iron directly in the Si-O-Si chain, holding the catalyst in the silica structure.

Given the above mentioned, the procedures adopted to nanostructured silica (n-SiO_2), catalyst, and hybrid syntheses are presented in the sequence. Appropriate sample quantities were prepared to carry out the necessary characterizations.

4.1.1. First stage – Suitable n-SiO_2 support evaluation

4.1.1.1. n-SiO_2 syntheses by sol-gel method

Based on Houmard *et al*. (2014) and Mota *et al*. (2017), five nanostructured silica (n-SiO_2) substrates were prepared by the sol-gel method. The hydrolysis and condensation of tetraethylorthosilicate (TEOS) were performed in the presence of absolute ethanol (EtOH) and deionized water (pH around 6.5). Among the five types of n-SiO_2 prepared, three were synthesized using nitric acid (HNO_3) as an acidic catalyst in the process, one using sodium hydroxide (NaOH) as a basic catalyst, and one without the use of catalyst. Table 4.1 presents the reagents specifications used in the syntheses.

Table 4.1 – Specification of the reagents used for the silica syntheses.

Reagent	Supplier	Molecular formula	Purity (%)
TEOS	Aldrich™	$Si(OC_2H_5)_4$	98
Ethanol	Neon™	C_2H_5OH	>99.5
Nitric acid	Synth™	HNO_3	65
Sodium hydroxide	Synth™	NaOH	99

Initially, to each n-SiO_2 sample, a solution with deionized water, ethanol, and the catalyst was prepared at room temperature, and then the silica precursor (TEOS) was added. The as-prepared sols were kept under vigorous stirring (500 rpm) at room temperature (≈ 25°C) for 30 min. Table 4.2 shows the molar ratio (TEOS:EtOH:H_2O:x) for the five types of n-SiO_2 prepared, and the theoretical potential of hydrogen (pH) for each one, where “x” is the proportion of catalyst in molar ratio. The proportions were calculated to produce approximately 25 g of n-SiO_2.

Table 4.2 – Reagent proportions, catalysts, and pH used in n-SiO_2 syntheses by the sol-gel.

Sample (TEOS:EtOH:H_2O: x)	Catalyst	Calculated pH in solution*
1:4:4:0.005	HNO_3	2
1:4:4:0.0005	HNO_3	3
1:4:4:0.00005	HNO_3	4
1:4:4:0	-	≈ 6.5**
1:4:4:0.00005	NaOH	10

* Theorical value.

** pH close to the water used in the synthesis.

After this, to accelerate the sol-gel reactions, the prepared solutions were kept in air at 90 °C, in a muffle furnace, in a closed bottle (500 mL) until the total gelation of the sol and then dried at 90 °C, again in a muffle oven. After these steps, the granulated material obtained for each sample was ball milled for 24 h at 50 rpm using a milling jar of porcelain. The powdered material was subsequently washed in deionized water, and then dried again at 90 °C in a muffle furnace for 24 h.

4.1.1.2. Iron-based catalyst synthesis

Considering that the metal catalyst particle size is a relevant factor to CNTs synthesis by the catalyst chemical vapor deposition (CCVD) method, as discussed in topic 3.3, iron-based catalyst synthesis was also performed through the sol-gel method, to prepare nano-sized particles of hematite (α-Fe_2O_3). The process was based on the work of Akbar *et al*. (2004), with adjustments to allow the production of more material.

A volume of 200 mL of iron precursor solution, in the molar concentration of 0.1 M, was prepared using iron nitrate nonahydrate (Table 4.3) dissolved in deionized water (pH ≈ 6.5). To promote a suitable mixture, this solution was placed under constant stirring (300 rpm) for 10 min. The gelation process was performed using 800 mL of a solution, also in the molar concentration of 0.1 M of citric acid (Table 4.3) with deionized water (pH ≈ 6.5) as a solvent. This solution was prepared under constant magnetic stirring (500 rpm) for 10 min. Table 4.3 presents the reagent specifications.

Table 4.3 – Reagent specifications used in the iron-based catalyst synthesis.

Reagent	Supplier	Molecular formula	Grade (%)
Iron nitrate nonahydrate	Synth™	$Fe(NO_3)_3.9H_2O$	98
Citric acid	Synth™	$C_6H_8O_7$	98

After these two steps, the iron solution was dropwise added to the citric acid solution under continuous stirring (200 rpm) for about 2h. After this, the temperature was kept at 90 °C for around 24 h. The dried gel formed was

collected and later calcined for 4 h at 400°C in the atmosphere air using a muffle furnace, to promote the crystallization of the hematite phase. Finally, the resultant powder was collected and subjected to ball-milled for 24 h at 50 rpm using a milling jar of porcelain. After this procedure, the powder was removed from the jar by washing with ethanol; the resulting solution was brought to a muffle furnace at 100°C for evaporation. The resulting material was a red powder with reduced granulometry and was considered as hematite (Fe_2O_3), as proven after the characterizations.

4.1.1.3. Support/catalyst preparation and CNTs synthesis

In each of the five nanostructured silica, produced as previously described, the iron-based catalyst was incorporated to obtain 1.5% of iron (Fe) atoms by the weight of silica, w/w. Considering the preparation of 5 g of support (n-SiO_2), 75 mg of Fe was required. Considering the molar ratio of 0.7 of Fe in the hematite molar mass, the amount of iron-based catalyst incorporated was 107 mg. The powders (n-SiO_2 and Fe_2O_3) were mixed in a jar ball-miller (50 rpm) to promote the catalyst deposition over the silica support.

Thus, using the five prepared silica samples, the CNTs syntheses were realized by the CCVD method. The processes were performed using a horizontal reactor with a 100 mm diameter quartz tube, 1,200 mm in length, and a furnace with 200 mm of the heated zone. Figure 4.3 illustrates the equipment used to grow the CNTs. Argon was used as a purge and flow gas and, methane as the carbon precursor.

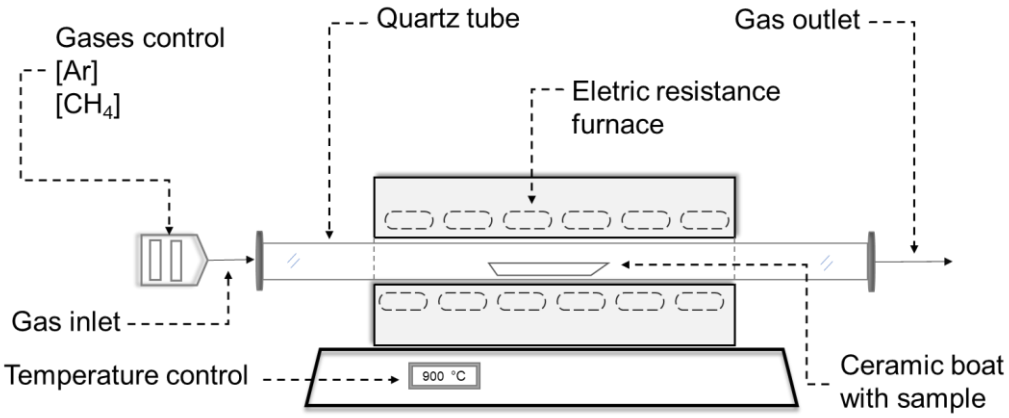

Figure 4.3 – Scheme CCVD reactor used to CNTs syntheses in the first and second stage.

To each sample, the powders (silica and hematite) were placed in a ceramic (SiC) boat and inserted in the central part of the quartz tube reactor and the system sealed. Later, the reactor was initially heated at a rate of 6°C.min^{-1} up to 900°C. After 10 min, the reactor was purged with inert gas, argon (99.9%), in a gas stream of 200 ml.min^{-1}, for an additional 20 min. Then, a flow of argon and methane (99.9%/99.995%), respectively 100 and 50 ml.min^{-1}, the gas mixture was provided, for 20 min. After this, the reactor was cooled down to room temperature under argon flow at 100 ml.min^{-1}. The resultant material was then collected.

4.1.2. Second stage – Suitable catalyst incorporation method

After the definition of the silica support, as presented in topic 5.3.4, and to evaluate the influence of the catalyst incorporation method, in this second stage the CCVD process was performed changing the catalyst incorporation method to verify possible modifications in the quality of the MWCNTs. A reduction in the iron-based catalyst content was also adopted, to reduce the production of undesirable carbon deposition structures.

4.1.2.1. Catalyst incorporation by the deposition method

The iron-based catalyst was incorporated to obtain 1.0% of iron (Fe) atoms (in mass) by weight of n-SiO_2 (sample 1:4:4:0 - Table 4.2). Considering the preparation of 5 g silica, 50 mg of Fe was required. The same route previously used to produce the hematite was employed and considering the molar ratio of 0.7 of Fe in the hematite molar mass, the amount of iron-based catalyst incorporated was 71 mg. The powders (n-SiO_2 and Fe_2O_3) were mixed in a jar ball-miller (50 rpm) to promote the catalyst deposition over the silica support. After these steps, the resultant material was calcined for 3 h at 300°C in the air using a muffle furnace, to promote the crystallization of the hematite phase. Samples prepared by this method were named SiO_2-dep.

4.1.2.2. Catalyst incorporation by impregnation method

Considering the reference nanostructured silica n-SiO_2 (sample 1:4:4:0 - Table 4.2), the iron-based catalyst was deposited by the impregnation method, according to Dunes; Mackenzie; Harris (2009) and Zhou *et al.* (2017), using an iron nitrate solution (iron 1wt% of silica) in ethanol. Considering that nitrate salt ($Fe(NO_3)_3$. $9H_2O$ Neon/>99.5%) has a molecular mass equal to 404 $g.mol^{-1}$ and that the molar ratio 0.139 of Fe, 360 mg of nitrate salt and 5 g of silica support were placed in a beaker (300 mL) together with 200 mL of ethanol (C_2H_5OH Neon/>99.5%). The content was kept under constant stirring (300 rpm) at 200°C in a hotplate (IKA RCT basic) until the complete evaporation of the liquid, approximately 24 h. After this, the as-prepared material was calcined in a muffle furnace at 300°C for 3 h to promote the crystallization of the hematite phase. Samples prepared samples by this method were identified as SiO_2-imp.

4.1.2.3. Catalyst incorporation by co-condensation sol-gel method

Taking into account the reference nanostructured silica (sample 1:4:4:0 - Table 4.2) and its preparation method, this route was performed to produce the n-SiO_2 with iron atoms embedded in the silica structure. Considering the production of 5 g of n-SiO_2, initially, 360 mg of iron nitrate salt ($Fe(NO_3)_3$. $9H_2O$ Neon/>99.5%) was previously dissolved in 6 mL of deionized water used in the sol-gel method and kept in continuous stirring for 30 min. The amount of deionized water was corrected since the salt is already hydrated. Using this aqueous solution with the iron salt, 18.6 mL of TEOS, and 19.4 mL of ethanol, the same sol-gel procedure previously described (topic 4.1.1.1) was performed to produce the n-SiO_2 with iron atoms embedded in its structure. Samples produced in this way were named SiO_2-msg.

4.1.2.4. CNT syntheses

After all these procedures and the sample preparations by the three routes, the CNTs syntheses were performed again by the CCVD method. The same horizontal reactor previously described and illustrated in Figure 4.3 was used, however, with 1200 mm of the heated zone. It was due to changes in the physical laboratory conditions. Thus, before the synthesis process, tests were done to achieve similar conditions to the previous arrangement in the reactor. This justifies the changes in the gas flows, as described in the sequence.

To each sample, the powders (calcined n-SiO_2 loaded with catalyst) were placed in a ceramic (SiC) boat and inserted in the central part of the quartz tube reactor. After the insertion, the reactor was initially heated at a rate of 6°C.min^{-1} up to 900°C. After 10 min, the reactor was purged with inert gas, argon (99.9%), in a gas stream of 200 mL.min^{-1}, for an additional 20 min. Then, a flow of argon and methane (99.9%/99.995%), respectively 200 and 100 mL.min^{-1}, and the gas mixture was provided, for 40 min. After this, the reactor was cooled down to room temperature under argon flow at 200 mL.min^{-1}. The resultant materials were then collected.

4.1.3. Third stage – Large scale CNT synthesis by CCVD method

After the first two stages and the appropriate characterizations in the produced hybrids, adequate silica support and the catalyst incorporation method were selected to be used in the final hybrid (n-SiO_2/CNTs) production. Based on these results, the nanostructured silica (n-SiO_2 1:4:4:0 - Table 4.2) and the catalyst incorporation method by impregnation (IMP) were selected.

Using the same procedure previously mentioned by the silica sol-gel synthesis (topic 4.1.1) and considering the production of around 40 g of the hybrid to be used in RPC samples, 45 g of the n-SiO_2 were produced. To incorporate the iron-based catalyst, with the 1.0 % of Fe, 3.24 g nitrate salt ($Fe(NO_3)_3$. $9H_2O$ Neon/>99.5%) were placed in a beaker (5,000 mL) together with 1,600 mL of ethanol (C_2H_5OH Neon/>99.5%) and the silica. The content was kept under constant stirring at 200°C in a hotplate (IKA RCT basic) until the complete evaporation of the liquid, which took approximately 36 h. After that, the as-prepared material was calcined in a muffle furnace at 300°C for 3 h to promote the crystallization of the hematite phase.

Due to the greater amount of material to produce and apply in the RPC samples, a CCVD reactor with a greater capacity was used. The reactor was a batch type, with a horizontal and rotative quartz tube: 2,000 mm in length, 100 mm in diameter, with a heated zone of 1,500 mm. Figure 4.4 shows the equipment used in this stage.

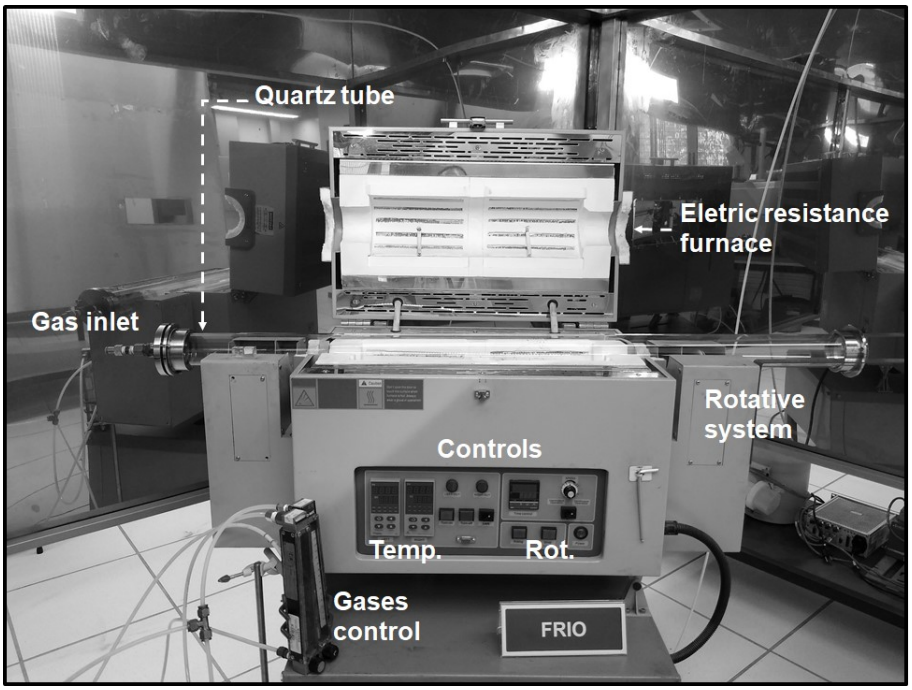

Figure 4.4 – CCVD batch reactor used for CNTs synthesis in the third stage.

Previous tests were performed to achieve similar conditions in terms of the morphology of the hybrid produced in the second stage. These tests resulted in time and flow changes. After that, the MWCNT synthesis was conducted.

The powder, silica with catalyst impregnated, was placed inside the quartz tube. The reactor was then initially heated at a rate of 6°C.min^{-1} up to 900°C. After 15 min, the reactor was purged with inert gas, argon (99.9%), in a gas stream of 500 mL.min^{-1}, for an additional period of 40 min. Then, a mixed flow of argon and methane (99.9%/99.995%), respectively 500 and 555 mL.min^{-1}, was provided, for 98 min. After this, the reactor was cooled down to room temperature under argon flow at 200 mL.min^{-1}. The resultant material was then collected.

4.2. CHARACTERIZATIONS METHODS OF SILICAS, CATALYST, AND HYBRIDS

Considering the importance of knowing the produced materials, the characterizations of the silica supports (n-SiO_2), iron-based catalyst (Fe_2O_3), and final material (the hybrid) were performed. The objectives were to evaluate the microstructure, the physical and chemical features at each step of the fabrication.

The techniques employed to characterize the materials are presented in the sequence.

4.2.1. N_2 adsorption and condensation analysis

Sol-gel samples, silica, and iron catalyst were examined by Nitrogen (N_2) adsorption and desorption to evaluate the mesoporosity and the specific surface area (SSA). For the analyses, 5 mg of the material was used. Nitrogen sorption was carried out using a Quantachrome Nova 1200e apparatus within an experimental error of 5%. To n-SiO_2/CNTs hybrid sample produced in the third stage, the SSA was evaluated also using a Belsorp (MicroBel Corp) apparatus considering the multipoint BET method.

Before these analyses, the samples were degassed under vacuum at 300°C for 3 h and then for 24 h at 100°C. Specific surface areas were determined according to Brunauer; Emmett; Teller (1938) by the multipoint BET method and the mean pore diameter (d_p) was estimated by Equation 4.1, where V_{mes} is the mesoporous volume, assessed from the collected N_2 adsorption isotherms. For evaluating the pore size distribution of samples, the BJH model was adopted, according to Barret; Joyner; Halenda (1951).

$$d_p = \frac{4V_{mes}}{SSA} \tag{4.1}$$

4.2.2. Infrared analysis

To evaluate the functional groups present in the sol-gel n-SiO_2 and n-SiO_2/catalyst samples, Fourier-Transform Infrared Spectroscopy (FTIR) was performed using a Perkin Elmer FTIR Spectrometer Frontier using the Transmittance mode. For the analyses, an amount of 1 mg of each powder was pretreated at 100°C for 2 h, mixed with 100 mg of KBr, and then compacted in pellets of approximately 1-mm thick. The spectra were taken from 4000 to 650 cm^{-1} at a resolution of 4 cm^{-1} and 128 scans.

4.2.3. DLS analysis

The Dynamic Light Scattering (DLS) technique was employed, using a particle size analyzer Anton Paar model Litesizer 500™, to evaluate the equivalent diameter of the nanostructured silica particles in the five samples produced. Before the analyses, 1 g of each sample was placed in a beaker (200 mL) with 100 mL deionized water and later sonicated for 5 minutes at ambient temperature (≈ 25°C). Immediately after this process, an aliquot (1 mL) was added to a quartz cuvette cell (light path length 10 mm) and inserted into the equipment. The analyses were carried out at 25°C and in the transmittance mode (70%).

4.2.4. SEM analysis

To evaluate the microstructure of the n-SiO_2 and n-SiO_2/CNTs samples, Scanning Electron Microscopy (model SEM-FIB - Quanta FEG 3D FEI), with a secondary electron detector, was used. The n-SiO_2 samples were deposited on a double-sided carbon tape attached to a stub and then sputter-coated with carbon to metallization. Similarly, n-SiO_2/CNTs samples were deposited on a double-sided carbon tape attached to a stub, but without metallization. The SEM micrographs were carried out at 5 kV.

Concerning the hybrids synthesized according to the method related to the second stage, to evaluate the diameters of the synthesized MWCNTs, a size distribution was measured for each sample, using various SEM micrographics. The measurements were carried out with the aid of ImageJ software (Rueden; Schindelin; Hiner (2017)) only from structures with fiber shape.

4.2.5. TEM analysis

Transmission Electron Microscopy (model TEM - Tecnai G2-20 - SuperTwin FEI) was used to evaluate the morphologies of the catalyst (Fe_2O_3), n-SiO_2, and hybrids n-SiO_2/CNTs. For such analysis, suspensions in ethanol with a

concentration of 1:100 were prepared for the samples and sonicated for 5 min. Few drops of these suspensions were then put onto the copper TEM grid. TEM micrographs were performed at 200 kV.

For the sol-gel catalyst particles (hematite), TEM images were used to obtain the diameter distribution, some micrographs were used for this, and the analysis was made using the ImageJ software measuring the equivalent diameter of the particles. Energy dispersive spectroscopy (EDS) analysis was carried out to evaluate the catalyst composition.

For the hybrids synthesized according to the method described in the third stage (topic 4.1.3), the size distribution of the diameters of the synthesized MWCNTs was measured for each sample, using various TEM micrographics. Again, the measurements were carried out with the aid of ImageJ software.

4.2.6. XRD analysis

The crystalline structures of the iron-based catalyst, the n-SiO_2/catalyst, and n-SiO_2/CNTs hybrids were evaluated by X-ray diffraction (XRD) using a Panalytical instrument (Empyream), with the use of CuKα radiation source (λ = 1.54 Å and an accelerator detector operating at 40 kV and 40 mA. The 2θ scan range was set for 3-89° using a step size of 0.06° with a time per step of 1 s.

4.2.7. Thermal analysis

To quantify the yield of CNTs after the CCVD process and the degradation temperature of the carbon structures formed, thermogravimetric analyses were carried out using an equipment TGA - Perkin Elmer STA 8000™. The heating program run from 30 to 900°C, with a heating rate of 10°C.min^{-1} in an oxidizing atmosphere (N_2 and 20±0.5% O_2 – 99.999% purity) with a gas flow rate of 50 mL.min^{-1}. The procedure to evaluate the yield of CNTs by thermogravimetric was employed in agreement with Trigueiro *et al*. (2007).

To better characterize the hybrids synthesized in the second step, the degradation kinetics of the carbon structures formed in quasi-isothermal conditions was evaluated. A differential thermal analysis using Perkin Elmer STA 8000 equipment was employed to evaluate the activation energy (E_a). E_a was calculated using the Arrhenius Equation (4.2).

$$k = A.e^{\frac{-E_a}{R.T}} \quad (4.2)$$

where k is the kinetic rate for carbon oxidation (s^{-1}), A is the frequency factor (s^{-1}), R is the universal gas constant ($J.mol^{-1}.K^{-1}$), and T the temperature (K).

First, in an inert atmosphere (N_2), the temperature of the sample was heated up to 200°C and maintained for 30 min. The temperature then was quickly elevated to 500°C; after that, it was heated up to 700°C at a low heating rate of $1°C.min^{-1}$ in an oxidizing atmosphere. This procedure is based on Santangelo *et al.* (2011).

4.2.8. Raman analysis

To verify the quality of the CNTs synthesized, Raman analyses were carried out under ambient conditions using the equipment WiTec Alpha 300™, and the results are associated with sp^2 bonds between carbon atoms in a hexagonal lattice. The Raman spectra were recorded from 280 to 5070 cm^{-1} with a 457 nm and set to a power of 1 mW with 6 accumulations of 10 s each. For the hybrids produced in the first stage (support evaluation), six Raman spectra were recorded for each sample. For the hybrids produced in the second stage (catalyst incorporation method), fourteen spectra were recorded for each sample. For the hybrids produced in the third stage, six spectra were recorded.

4.3. MATERIALS EMPLOYED IN THE CEMENTITIOUS COMPOSITES

As previously mentioned (topic 3.1), Reactive Powder Concrete (RPC) is a special type of concrete that uses microstructural engineering concepts: ultra-fine powders and a low water/cement ratio. To produce this composite, specific raw materials and a plasticizer (admixture) were selected, to keep the correspondence with the materials employed by Richard and Cheyrezy (1995). In terms of the proposal of this work, the hybrid n-SiO_2/CNTs were added to the mix in different proportions.

A cement classified as type CP-V, in conformity with NBR 16667 ABNT (2018), and provided by InterCement S.A. was used. A silica fume (SF), denominated Microsilica, in conformity with NBR 13956, ABNT (2012) was kindly provided by Tecnosil®. An admixture (superplasticizer) denominated ADVA® 518, kindly provided by GCP Applied Technologies®, and specifications in conformity with NBR 11768, ABNT (2011), was used. As aggregate, sands denominated as “Areia Normal – Padrão IPT”, purchased from Instituto de Pesquisas Tecnológicas (IPT) – São Paulo were used. To reach information and characterizations of these materials, specific techniques were used, according to the following. The results are presented in topic 5.6.

4.3.1. Cement

Cement was characterized according to normative Brazilian standard codes. The results were provided by the company InterCement S.A and present information about the physicochemical features. According to Brazilian specifications, the main results are the Blaine fineness, the chemical composition, the water content for normal consistency, the setting time, the loss on ignition, and compressive strength at specific ages.

To complete the information, the cement phases and granulometric distribution were evaluated, as detailed in the sequence.

Cement crystalline phases were characterized by X-ray diffraction (XRD) using

again, the Panalytical instrument (Empyream). The adopted analysis parameters were: CuKα radiation source and an accelerator detector operating at 40 kV and 40 mA. The 2θ scan range was set for 3-89° using a step size of 0.06° with a time per step of 1 s. The software Qualx 2.0, Altomare *et al.* (2015), was used for the cement phase identifications and quantifications.

To obtain the cement granulometric distribution a laser particle size analyzer (CILAS 1064) equipment was used. To the analysis, 1 g of cement was diluted in 100 mL of isopropyl alcohol and kept in an ultrasonic dispersion for 60 s. After this, the sample was inserted into the equipment and the data was recorded twice during 60 s. The presented results corresponding to an average of these two analyses.

4.3.2. Silica Fume

Some physical and chemical silica fume (SF) characterizations were provided by the supplier and are presented in topic 5.6.1.2. To complete the information, the SF diffraction pattern and granulometric distribution were evaluated, as detailed in the sequence.

To obtain the SF granulometric distribution the laser particle size analyzer (CILAS 1064) equipment was also employed. To the analysis, 1 g of silica fume was diluted in 100 mL of isopropyl alcohol and kept in an ultrasonic dispersion for 60 s. After this, the sample was inserted into the equipment and the data was recorded twice during 60 s. The presented results corresponding to an average of these two analyses.

4.3.3. Superplasticizer

The superplasticizer employed was a polycarboxylate-based high-range water reducer. Considering that the admixture efficiency is related to the kind and amount of the polymeric chains, to verify the real solid content (polymer) present, thermogravimetric analysis was chosen. Using the equipment TGA - Perkin Elmer

STA 8000™, an aliquot of approximately 22 mg was dropped in the alumina sample holder and evaluated following the heating program run from 30 to 900°C, with a heating rate of 10°C.min^{-1} in an oxidizing atmosphere (N_2 and 20±0.5% O_2 – 99.999% purity) with a gas flow rate of 50 mL.min^{-1}. More details about the superplasticizer are presented in topic 5.6.1.3, according to the supplier information.

4.3.4. Sand

The sand employed is produced from controlled grinding and granulometric distribution. Information and characterizations are presented in topic 5.6.1.4, according to the supplier.

4.4. POZZOLANIC EFFECT EVALUATION

The possible pozzolanic effect of the synthesized hybrid was evaluated by five methods. By the electrical conductivity in solution according to Luxan; Madruga; Saavedra (1989); by the thermogravimetric analysis, according to Dweck *et al.* (2009), where indirectly $Ca(OH)_2$ and calcium silicate hydrate content are measured, through the evaluation of crystalline phases present by XRD analysis, and completed by N_2 adsorption and EDS-SEM evaluation.

As mentioned in the Literature Review, the use of nano-silica in cement-based materials presents beneficial effects in the range of 2 – 5% bwoc. As previously described, values higher than that result in decreasing performance. Given these aspects and the content of n-SiO_2 and MWCNTs present in the manufactured hybrid, the pozzolanic evaluation tests were performed considering the proportions of 2, 4, and 6% of hybrid bwoc. These amounts were used considering a silica fume replacement. The content of 6 % bwoc was considered to evaluate an excess of material. The sample denominations and definitions are presented in Table 4.4.

Table 4.4 – Proportions definitions to the samples in the pozzolanic evaluations.

Sample	Hybrid content* (%)	n-SiO_2** (%)	MWCNTs** (%)
REF	0	0	0
H2%	2	1.32	0.68
H4%	4	2.64	1.36
H6%	6	3.96	2.04

* bwoc

** according to the MWCNTs yield presented in topic 5.5.3.

4.4.1. Chemical method

The method based on the electrical conductivity in solution was employed by Payá *et al*. (2001), Sinthaworn and Nimityongsul (2009), Velázquez *et al*. (2014), and Carneiro *et al*. (2018). The results show the efficiency of the process. Based on these works and after previous tests, to carry out the analyses, an apparatus according to Figure 4.5 was assembled. It consisted of a magnetic stirrer with heating, where a plastic Erlenmeyer (600 mL) with the test solution has the electric resistivity constantly monitored by an automatic measurement system controlled by the computer (using a specific software).

Based mainly on Carneiro *et al*. (2018), the following procedure was used: in the Erlenmeyer, 320 mL of deionized water, and 0.64 g of calcium hydroxide (Synth, 95%) were mixed to obtain a saturated solution (0.2 g . $100mL^{-1}$). This solution was heated up to 80°C under constant stirring (300 rpm) and after the resistivity reading stabilization, 0.53 g of the pozzolanic material was added, becoming the solution test. During 6 hours, resistivity readings were collected every 60 s. This procedure was performed in each pozzolanic sample described in Table 4.5. The conductivities were obtained considering the inverse of the measured resistivity.

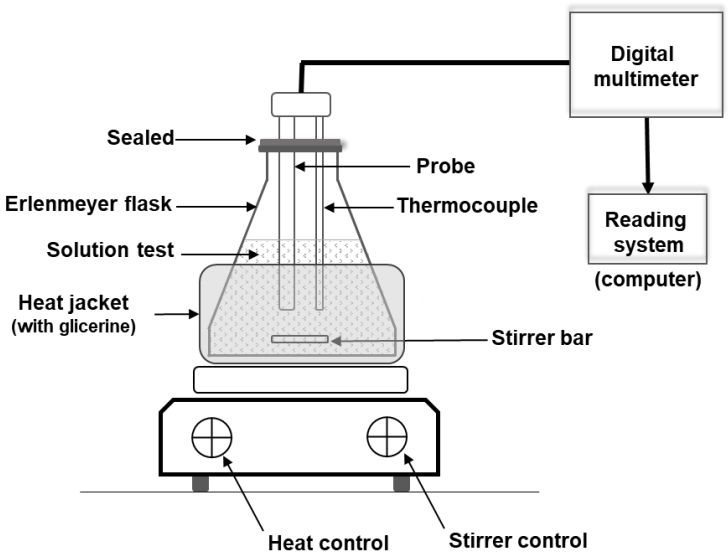

Figure 4.5 – Schematic diagram of the pozzolanic test setup by electrical conduction (chemical method).

Table 4.5 – Samples evaluated by the chemical method.

Pozzolanic material	Amount / Description
silica fume	530 mg silica fume
n-SiO_2	530 mg nanostructured sol-gel silica
hybrid	530 mg hybrid (n-SiO_2/CNTs)
H2%*	487 mg sílica fume + 42.4 mg hybrid
H4% *	445 mg sílica fume + 84.8 mg hybrid
H6% *	403 mg sílica fume + 127 mg hybrid

* Percentage relative to the amount of hybrid concerning the weight of cement, keeping the ratio (silica fume + hybrid)/cement equal to 0.25.

4.4.2. Analysis of the hydrated cement paste

Concerning the possible effects of the hybrid in the amounts of portlandite and calcium silicate hydrate, the thermogravimetric analysis, XRD analysis, N_2 adsorption analysis, and EDS-SEM evaluation were carried out. Cement pastes were prepared to keep the proportions of the materials (cement, silica fume, water, and superplasticizer) that were defined to standard RPC. No sand was used since it could interfere with the results. When used the hybrid (n-SiO_2/CNTs), the mass of the silica fume was discounted to keep constant the adopted binder ratios. Table 4.6 shows the materials and proportions used.

Table 4.6 – Cement pastes samples evaluated – Description and proportions.

Sample paste	Cement	Silica Fume	Water	Superplasticizer	hybrid
REF	1	0.25	0.18	0.016	-
H2%	1	0.23	0.18	0.016	0.02
H4%	1	0.21	0.18	0.016	0.04
H6%	1	0.19	0.18	0.016	0.06

To promote the mixing, a vertical mixer with an iron propeller was used. To prepare the pastes, cement and silica fume were previously mixed and homogenized manually in a plastic beaker (300 mL). In another beaker, the superplasticizer was dissolved in the water, and later slowly dropped into the first beaker, containing cement/silica fume, under constant mixing (2000 rpm) for 5 min. After these procedures, the pastes were cast in silicone molds to cure. In the first 24 h, the samples were kept under controlled ambient with relative humidity (95%) and then keep in submerse curing during 48 hours in saturated lime water at the temperature of 25°C. After that, each sample was carefully sawn and the dust resulting from this process was quartered and the remaining powder sieved at 75 μm and reserved for the analyses. Thus, to evaluate the effects of the hybrid in the hydration process at the age of 3 days, the hydration process was interrupted. For this, the samples were immersed in isopropanol (NEON, 99.5%) for 15 min, dried (in a muffle) for 24 hours at 40 °C, and then placed in a vacuum chamber for another 3 hours. This procedure is described by Scrivener; Snellings; Lothenbach (2016).

4.4.2.1. Thermogravimetric analysis

Considering that the hydration products can be evaluated indirectly through the bound water of various hydrated phases and the $Ca(OH)_2$ content can be expressed as a percentage of the dry sample weight, the DTA and dDTA curves were used to identify the exact boundary of phases or groups of phases present in the hydrated samples.

This procedure was adopted by Roychand *et al.* (2016), and according to them, the observed endotherms and their corresponding mass losses are:

- ≈60 – 250°C: C–S–H, C_2ASH_8, Ettringite, AFm, mono-carbonate (Mc): Group 1 (HP_{G1});
- ≈250 – 450°C: aluminate phases (C_2AH_8, C_3AH_6): Group 2 (HP_{G2});
- ≈400 – 500°C: Calcium hydroxide (CH): Group 3 (HP_{G3}).

Using thermogravimetric analysis, the powders, after the hydration process was interrupted, were analyzed following the heating program: 30°C to 900°C, 10°C.min^{-1}, and N_2 atmosphere with a flow of 50 cm³.min^{-1}. The amount of $Ca(OH)_2$ and hydrated phase groups were related to the amount of water evaporated, mass loss, at the first derivate of the TGA curves. The temperature boundaries were established according to Monteagudo *et al*. (2014), using the 2nd derivative (dDTA).

Equations 4.3 to 4.5 were used to measure the hydration products (HP) in each group. The indices b, c, e, f, and g correspond to the temperature boundaries, specific of each sample, and are presented in Table 5.10. The ratio 74/18 converts the CH bound water into the CH mass, where 74 is the molar mass of CH and 18 is the molar mass of H_2O. The value 1/C is related to normalization according to cement mass.

$$HP_{G1} = \frac{m_b - m_c}{m_g} \,.\, 100\% \tag{4.3}$$

$$HP_{G2} = \frac{m_c - m_e}{m_g} \,.\, 100\% \tag{4.4}$$

$$HP_{G3} = \frac{(m_e - m_f) \,.\, (74/18)}{m_g} \,.\, 100\% \,.\, 1/C \tag{4.5}$$

4.4.2.2. Phase analysis by XRD

To XRD evaluations, the adopted sample preparation was: initially, about 5 mg sample was deposited in a glass holder and approximately 3 mL of isopropyl alcohol (NEON, 99.8%) was dropped over.

After the evaporation, the glass holder was inserted in the Philips-Panalytical X-ray diffractometer, model PW 1710. The adopted analysis parameters were:

Using CuKα radiation (λ_1 = 1.5406Å) source and an accelerator detector operating at 50 kV and 35 mA. The 2θ scan range was set for 10-70° using a step size of 0.06° with a time per step of 1 s. The obtained profiles were compared with the portlandite pattern (00-900-9098).

4.4.2.3. N_2 adsorption and condensation analysis

Belsorp (MicroBel Corp) apparatus was used in the N_2 adsorption analyses carried out in the cement pastes. The adopted procedures were the same described in topic 4.2.1. However, to minimize changes in the microstructure of the hydrated paste, in the sample preparation, the time on degassed under vacuum was 12 h and the temperature 40°C.

4.4.2.4. EDS-SEM analysis

The EDS-SEM analyses were performed in hydrated cement pastes to verify the calcium/silicon ratio and investigate the influence of the hybrid in the C-S-H formation. This analysis was performed, firstly, in a representative sample region to measure the initial calcium/silicon (Ca/Si) ratio. Later, the analysis was performed in representative C-S-H regions at each sample to evaluate the Ca/Si ratio. According to Kunther; Ferreiro; Skibsted (2017) and Li *et al*. (2020), the EDS-SEM analysis is an important tool to also evaluate the cement hydration process in terms of C-S-H. The evaluations were performed using, again, the Electron Microscope, model SEM-FIB - Quanta FEG 3D FEI, at the voltage 5 kV, at the EDS mode. To make the analysis more significant, they were performed in form of maps, not in specific points in the samples.

The samples consisted of fragments of dry hydrated cement paste impregnated in resin, polished, and later metalized with carbon. The same interrupted hydration procedure was employed. The images were obtained by scanning electron microscopy in the back-scattered electron (BSE) mode.

4.5. APPLICATION OF THE HYBRID IN REACTIVE POWDER CONCRETE

Starting from the selected material and its adequate content, after the results and analyses from pozzolanic tests 5.6.4.6, the hybrid n-SiO_2/CNTs was applied in reactive powder concretes (RPCs). To verify these effects comparatively, samples with and without the hybrid material were produced. The control group, without the hybrid, was denominated REF. The group corresponding to the proportion of 2wt% (bwoc) of hybrid replacing silica fume was denominated H2R, and the group with the addition of 2wt% (bwoc) of the hybrid H2A. As mentioned in the introduction of Chapter 4, a sample group with proportional 0.25% (bwoc) MWCNTs also was considered in the study: it was denominated as H07R.

4.5.1. Mixing design

Based on the typic composition of the RPC type 200, according to Richard and Cheyrezy (1995), a numerical study was performed, using the open-source software EMMA Elkem Material Mix Analyzer - Elkem™, to evaluate the particle packing effect (particle size distribution) in the concrete, as mentioned in the topic 4.1. The information used in the study was the particle granulometric distribution and proportions of the cement, silica fume, and sand. Furthermore, the water-cement ratio (w/c) and the density of the materials were also informed. The concrete composition used, still according to Richard and Cheyrezy (1995), was of the type “non-fibered”, without pressure and heat treatment during the curing period. The w/c ratio was equal to 0.18.

Mix compositions were simulated, considering the Modified Andreassen model with the coefficient q = 0.37, followed by mixing and molding practical tests. Adequate proportion and composition are presented in Table 4.7.

Table 4.7 – Composition of RPC manufactured, by weight of cement.

Material	Proportion
Cement	1
Sand	
# 150 (56%)	0.616
# 300 (31%)	0.341
# 600 (13%)	0.143
Silica Fume	0.25
Superplasticizer	0.016
Water	0.18

4.5.2. Mixing procedure

A suitable mixing procedure is very important in RPC production. Aspects as the number of stage mix, mixing speed and duration are key according to Hiremath and Yaragal (2017). These authors indicate as ideal: four stages in the RPC mix process, a minimum mix speed of 50 rpm and an ideal duration close to 15 min.

Having this in the account and the specifics materials employed, after the practical tests, the adopted mixing procedure is presented in the sequence. A mechanical mixer (capacity of 5 L), with a planetary movement, 62 ± 5, and 125 ± 10 rpm, low and high rotation respectively, was used. The adequate total time was around 30 min. Using an amount of cement equal to 624 g, to each mix, the steps were:

i. Place cement and silica fume after a physical mixture between them;
ii. Add the three fractions of the sands, already mixed between them;
iii. Mix 5 min in low rotation (140 ± 5 rpm);
iv. Mix 3 min in low rotation, while adding 1/3 of the water;
v. Mix 5 min in low rotation, while adding more 1/3 of the water and 1/2 of the superplasticizer;
vi. Mix 10 min in low rotation, while adding the remaining of the water and superplasticizer;
vii. Mix by 2 min in high rotation (285 ± 10 rpm).

When the hybrid was used, it was previously mixed with sand using a rotary mill (50 rpm), without grinding elements. The remaining procedures were the same.

RPC was cast in steel molds, with approximated dimensions of 25 mm x 25 mm x 140 mm. These were kept at 95% relative humidity during the first 24 hours. Then they were stripped from the molds and placed to cure in lime-saturated water at 25 ± 2 °C until the day of testing.

4.5.3. Mechanical property tests

Three-point bending test (TPBT) and the direct compressive strength test were employed to verify mechanical properties.

The first mentioned test provides information about the Flexural Tensile Strength capacity (σ_F) and the fracture parameters, like Fracture Energy (G_F), the Tensile toughness areas (E_1 and E_2), and the tensile strain corresponded to the peak load (ε_T). TPBT were performed in notched (≈ 5 mm) beams with a span (S) of 120 mm, using a servo-hydraulic testing machine (DL 10000 – EMIC® - Load cell 5 kN), according to the scheme illustrated in Figure 4.6a-b. These tests were carried out at a constant displacement of 0.10 mm.min^{-1} in the machine force (F) application system, and the middle-span deflection was obtained by a Deflection Measurement System (DMS) connected in the machine and computer software. For each RPC group, six samples were evaluated at the age of 3 days after casting.

After the TPBTs, the remaining ends of the specimens had the dimensions of the broken cross-sections collected to be considered in the calculations of the parameters (σ_F, G_F, E_1, and E_2, ε_T). Three measurements were taken in height (h) and width (b) of the sample, Figure 4.6c.

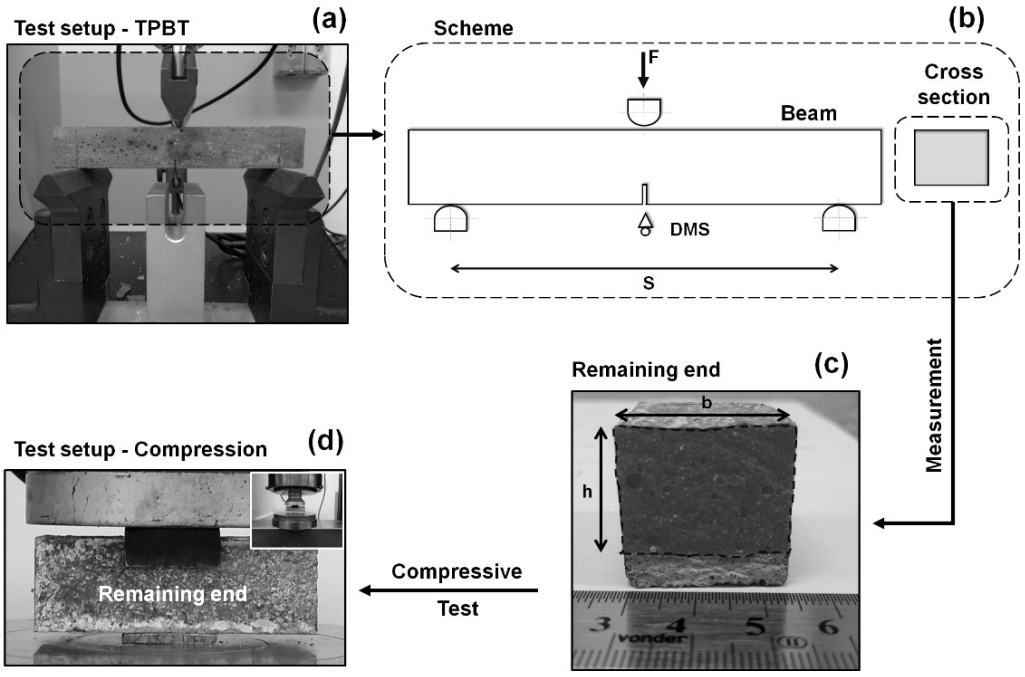

Figure 4.6 – Setup to mechanical tests. Schemes and dimensions.

The load-deflection data was recorded and used to obtain the load-deflection curves and the parameters E_1 and E_2, considering the areas delimited under the curves between the deflection (δ_f) in the F_{fmax}, and maximum deflection measured (δ_u), as used by Liu *et al.* (2019). This is illustrated in Figure 4.7.

After this, using a servo-hydraulic testing machine (DL 20000 – EMIC® - Load cell 20 kN), the remaining ends of these specimens were used for compressive strength evaluation. Steel plates, with contact area b_s x d_s, were placed at the top and bottom surfaces of the samples, Figure 4.6d. The load (F_c) was applied at a constant displacement rate of 0.5 mm.min^{-1}.

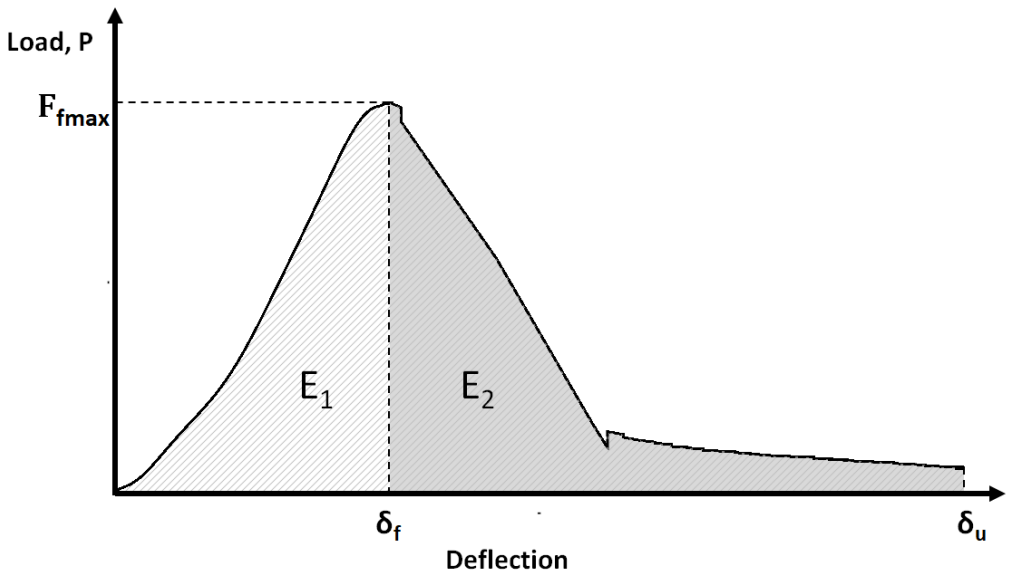

Figure 4.7 – Load-deflection curve – Toughness parameter definition.

Equations 4.6 to 4.10 were used to calculate the Flexural Tensile Strength capacity (σ_F) and the fracture parameters, like the Tensile Toughness areas (E_1 and E_2), the Fracture Energy (G_F), and the tensile strain corresponded to the peak load (ε_T), respectively.

$$\sigma_F = \frac{1.5\,(F_{fmax})S}{bh^2} \tag{4.6}$$

$$E_1 = \int_0^{\delta_f} P(\delta)d\delta \tag{4.7}$$

$$E_2 = \int_{\delta_f}^{\delta_u} P(\delta)d\delta \tag{4.8}$$

$$G_F = \int_{\delta_f}^{\delta_u} \frac{P(\delta)d\delta}{bh} \tag{4.9}$$

$$\varepsilon_T = \frac{6h\delta_f}{S^2} \tag{4.10}$$

The compressive strength (σ_c) was calculated according to Equation 4.11, where F_{cmax} was the maximum applied load to each sample, and product *bd* the contact area of the steel plates (b = 26.05 and d = 25.22 mm).

$$\sigma_c = \frac{F_{cmax}}{bd} \tag{4.11}$$

5. RESULTS AND DISCUSSION

In this chapter, results are presented at each stage of the study. First, the results of the syntheses and characterization of the silica, catalyst, and hybrid are presented and discussed (at the end of each topic) until the proper definition of production and application. Later, this material was evaluated in terms of the pozzolanic effect and influence in the cement hydration process. Lastly, the macro evaluation was performed to verify the effect of the hybrid in mechanical performance, particularly concerning toughness behavior.

5.1. SOL-GEL n-SiO_2 SUPPORTS

5.1.1. N_2 adsorption analysis

The N_2 adsorption isotherms obtained for the five synthesized sol-gel n-SiO_2 samples are shown in Figure 5.1, as well as the cumulative pore volume, representative of the pore size distribution (by BJH model), for each sample. Then, a summary of the results obtained by N_2 adsorption analysis is given in Table 5.1.

Table 5.1 – Morphological parameters assessed from N_2 adsorption for the n-SiO_2 supports synthesized by the sol-gel method with different pH.

Approximate pH	Specific surface area ($m^2.g^{-1}$)	Mesoporous volume ($cm^3.g^{-1}$)	Mean pore diameter (nm)
2	918 ± 46	0.76 ± 0.04	3.3 ± 0.2
3	679 ± 34	0.36 ± 0.02	2.1 ± 0.1
4	400 ± 20	0.83 ± 0.04	8.3 ± 0.4
6.5	239 ± 12	0.76 ± 0.04	12.8 ± 0.6
10	212 ± 11	0.19 ± 0.01	3.7 ± 0.2

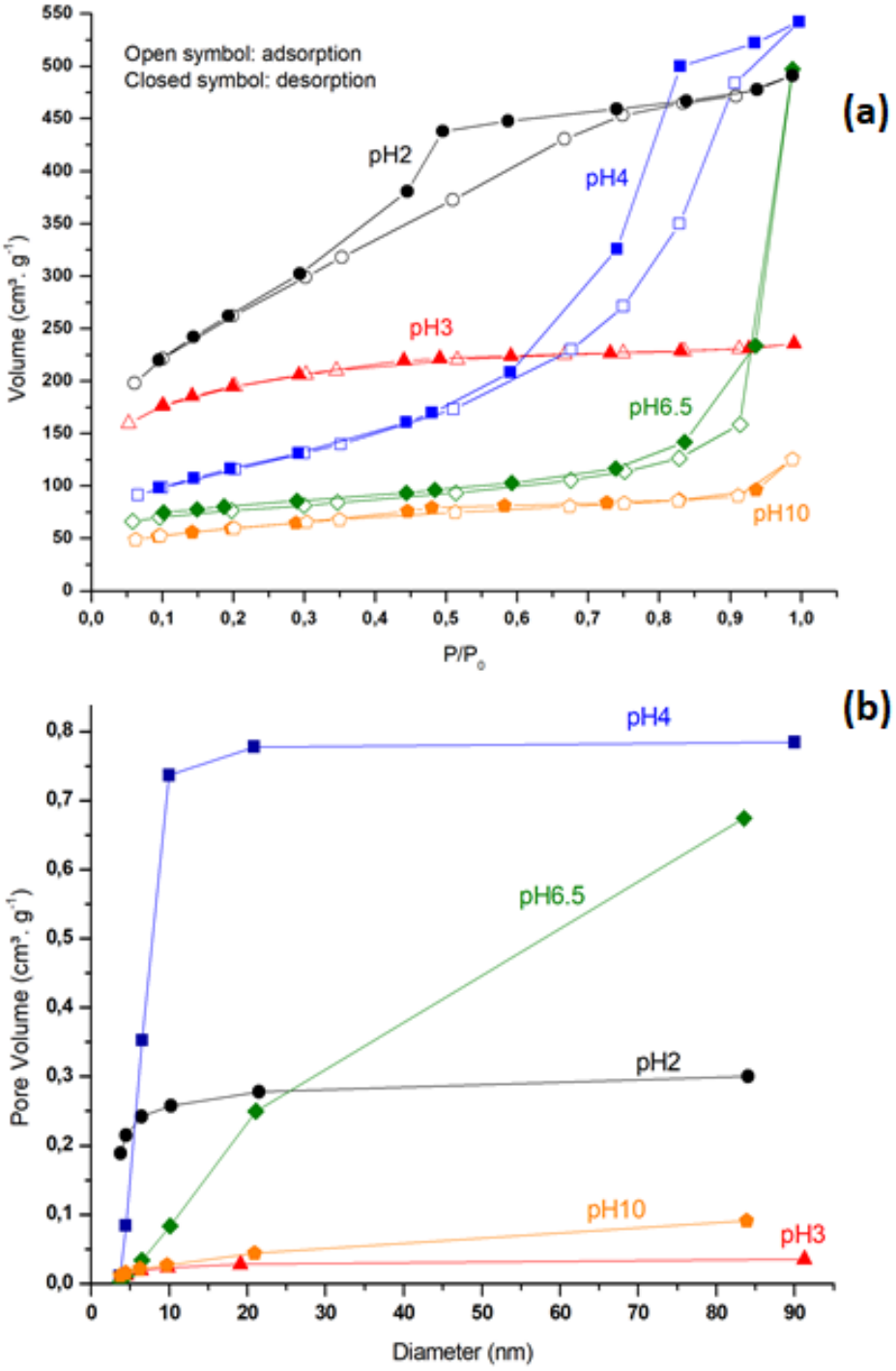

Figure 5.1 – n-SiO_2 supports synthesized by sol-gel method at different pH - N_2 adsorption analyses: (a) isotherms, and (b) cumulative pore volumes as a function of the pore diameter.

For the samples prepared with the acidic catalyst (pH 2, 3, and 4), the results showed that specific surface areas (SSA) decreased gradually with the pH increase. Regarding V_{mes} and d_p, the smaller values were obtained for the material synthesized at pH 3. This may be related to the slow kinetics of the

condensation reactions during the sol-gel process. Indeed, when the solution pH is around 3, the gelation time of the silica sol was increased due to the difficulty of contact between adjacent -Si-O-Si polymeric chains. This process was also observed by Pope and Mackenzie (1986), Tomita; Kawasaki; Okada (2004), and Castricum *et al.* (2014). This slower condensation rate results in the formation of a more organized and compact silica network, resulting in less porous structures (MOTA *et al.*, 2017). It is important to mention that the pH 3 is a theoretical value (calculated), with a possible deviation around the silica isoelectric point (pH ≈ 2), value considered in the literature according to Brinker and Scherer (1990). Concerning this deviation, Alothman (2012) shows, indirectly, with acidic catalyst and during the condensation process, that the isoelectric point can be closer to pH 3, which is in agreement with our results. Furthermore, similar changes related to the kinetics of the condensation reactions during the sol-gel process were also observed by HOUMARD *et al*., 2014, using HNO_3 as catalyst similarly to this work.

For higher acid concentrations (pH 2), the fast hydrolysis and condensation reactions seem to lead to a high concentration of small pores, which in turn favor a high SSA. For lower acid concentration (pH 4), the condensation is easier due to the higher attraction between -Si-O-Si- chains, but the hydrolysis rate is decreased, which could generate a condensation around non-hydrolyzed ethoxy groups from the TEOS precursor. Such behavior leads to pores with larger diameters and consequently high pore volume.

For the sample without catalyst (pH ≈ 6.5), SSA decreased even more, with a value close to a quarter of the pH 2 sample. Also, as shown in Table 5.1, the value of d_p evaluated for this sample (12.8 ± 0.6 nm) is even higher than the obtained for samples prepared with acidic catalyst, which is justified by the assumptions aforementioned. Indeed, when the pH is even higher and there is no catalyst to increase the hydrolyze rate, the condensation occurred favorably around non-hydrolyzed ethoxy groups leading to larger pores.

In the case of the pH 10 sample synthesized with a basic catalyst, SSA (212 ± 11 $m^2.g^{-1}$) is slightly lower than the other ones, with lower V_{mes} and smaller d_p. According to its isotherm (Figure 5.1), the lack of hysteresis between the

adsorption and desorption curves could be associated with a compact microstructure, with superficial and unconnected mesopores. Such results are consequences of the use of a basic catalyst modifying the way the sol-gel reactions occurred, leading to the formation of silica clusters that precipitate without gelation of the sol. This behavior was also observed by Silva and Airoldi (1997).

Concerning the capillary condensation of N_2 in the mesoporous structures, the samples synthesized with pH 3 and pH 10 did not present a clear hysteresis loop in the isotherms (Figure 5.1a). This is reflected by the low mesoporous volume values in Table 5.1. However, hysteresis loops are observed in the other samples, reflecting the mesoporous structure. The pH 2 sample presents a hysteresis loop type IV(a), and the pH 4 and pH 6.5 samples type V, according to Thommes *et al.*, 2015.

5.1.2. Infrared analysis

Figure 5.2a shows a typical FTIR spectrum of the samples obtained. All samples have absorption bands close to 798 cm^{-1}, which is associated with the bending mode of Si-O-Si bonds, as well as the peaks at about 1060 cm^{-1} (Figure 5.2b), (PRIMEAU; VAUTEY; LANGLET, 1997; JUNG *et al*., 2005; AGUIAR *et al*., 2009).

Another absorption band close to 950 cm^{-1} is associated with symmetric and asymmetric stretching modes of Si-OH bonds, according to Jung *et al*. (2005) and Aguiar *et al*. (2009). In Figure 5.2a, it is possible to see the presence of a small peak at about 3000 cm^{-1} associated with CH_2 bands, according to Jung *et al*. (2005), indicating the presence of unreacted ethoxy groups from the TEOS precursor. Besides, a large shoulder representative of OH bands from absorbed molecular water is observed between 2800 and 3700 cm^{-1}, (AGUIAR *et al*., 2009).

Based on the analysis presented by the IR spectra, the silica support samples did not present significant chemical differences in their compositions regardless of the pH used during the synthesis step.

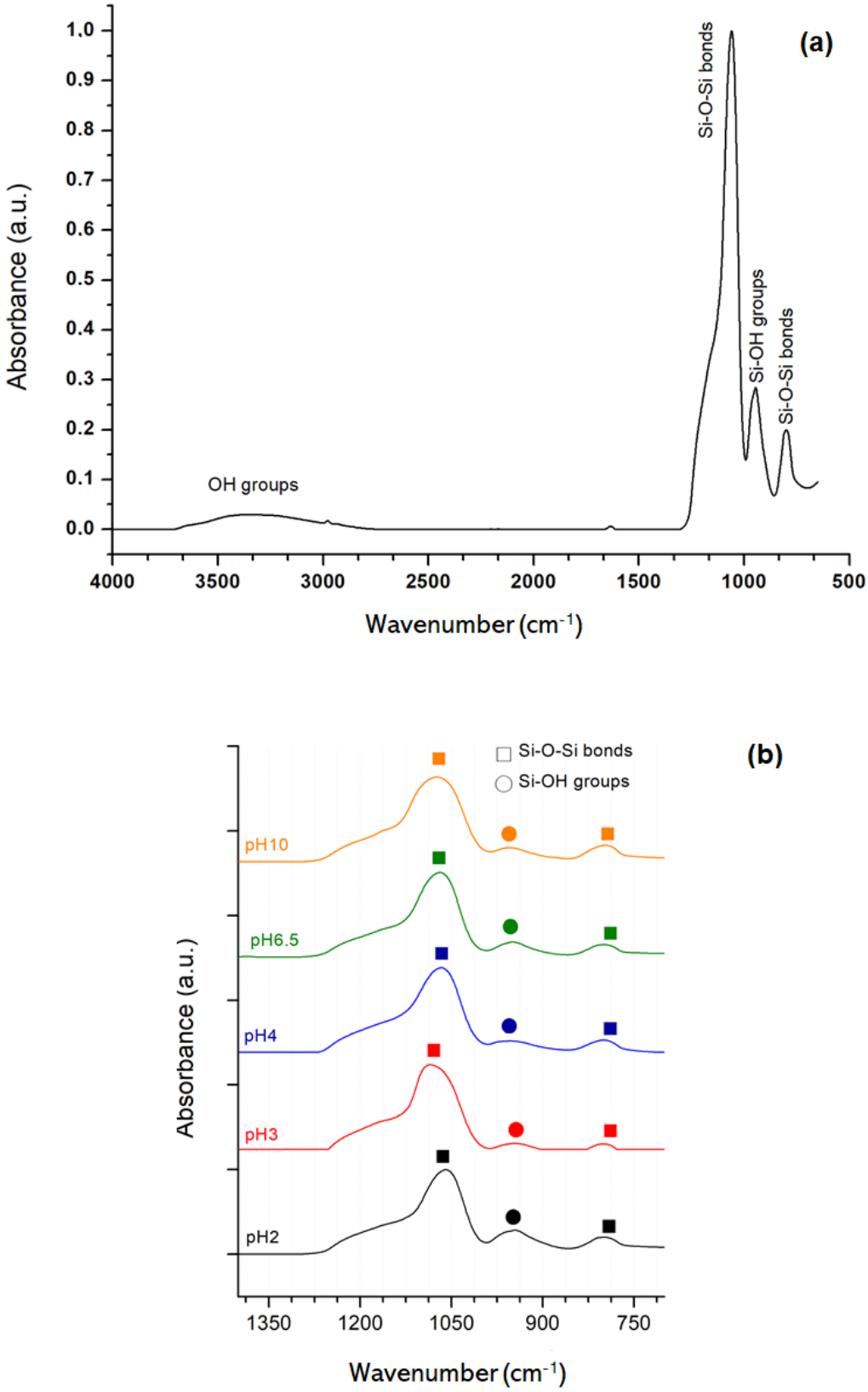

Figure 5.2 – FTIR spectrum of the silica samples. (a) typical full spectrum; (b) spectrum of all samples in the range focuses on the peaks corresponding to the Si-O-Si bonds and Si-OH groups.

5.1.3. Particle distribution by DLS analysis

Figure 5.3 shows the distribution curves with their respective relative frequency for the particle sizes of the five n-SiO_2 samples.

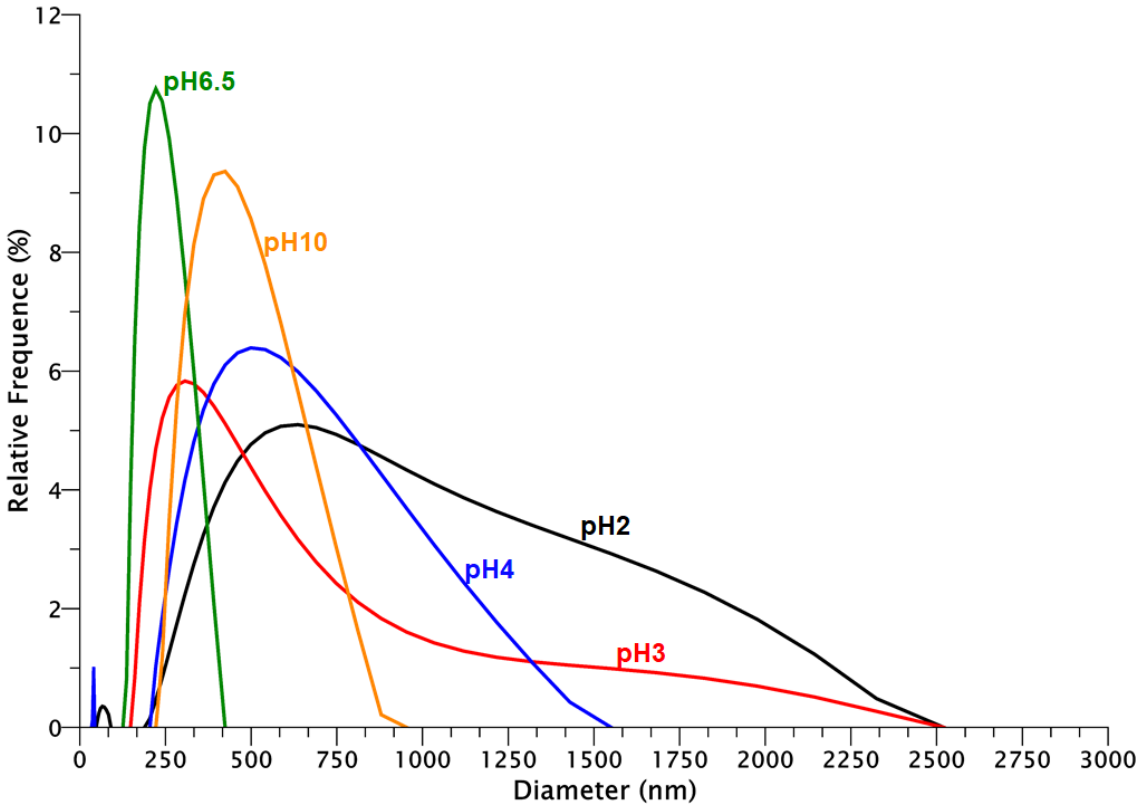

Figure 5.3 – Diameter distribution of n-SiO_2 evaluated in suspensions characterized by DLS.

It is verified that the samples pH2, pH3, and pH4 have distributions in shoulder peak form, containing a wide range of diameters. However, the samples pH6.5 and pH10 have distributions with better-defined peaks. In particular, the sample pH6.5 presents a particle distribution range more closed. These results may be well related to the kinetics of the condensation reactions during the sol-gel process, as previously mentioned.

5.1.4. Morphological evaluation

The morphology of the n-SiO_2 particles can be seen in Figure 5.4. Illustrated SEM images of particles of each sample with lower magnification are inset. The

samples synthesized with acidic catalysts (pH 2, 3, and 4) presented more compact particles, composed of nanoparticles agglomerated in blocks as can be seen in Figure 5.4a-c. The pH6.5 sample (Figure 5.4d) presents a rough surface, while in the pH10 sample (Figure 5.4e), small spheres of n-SiO_2 are agglomerated.

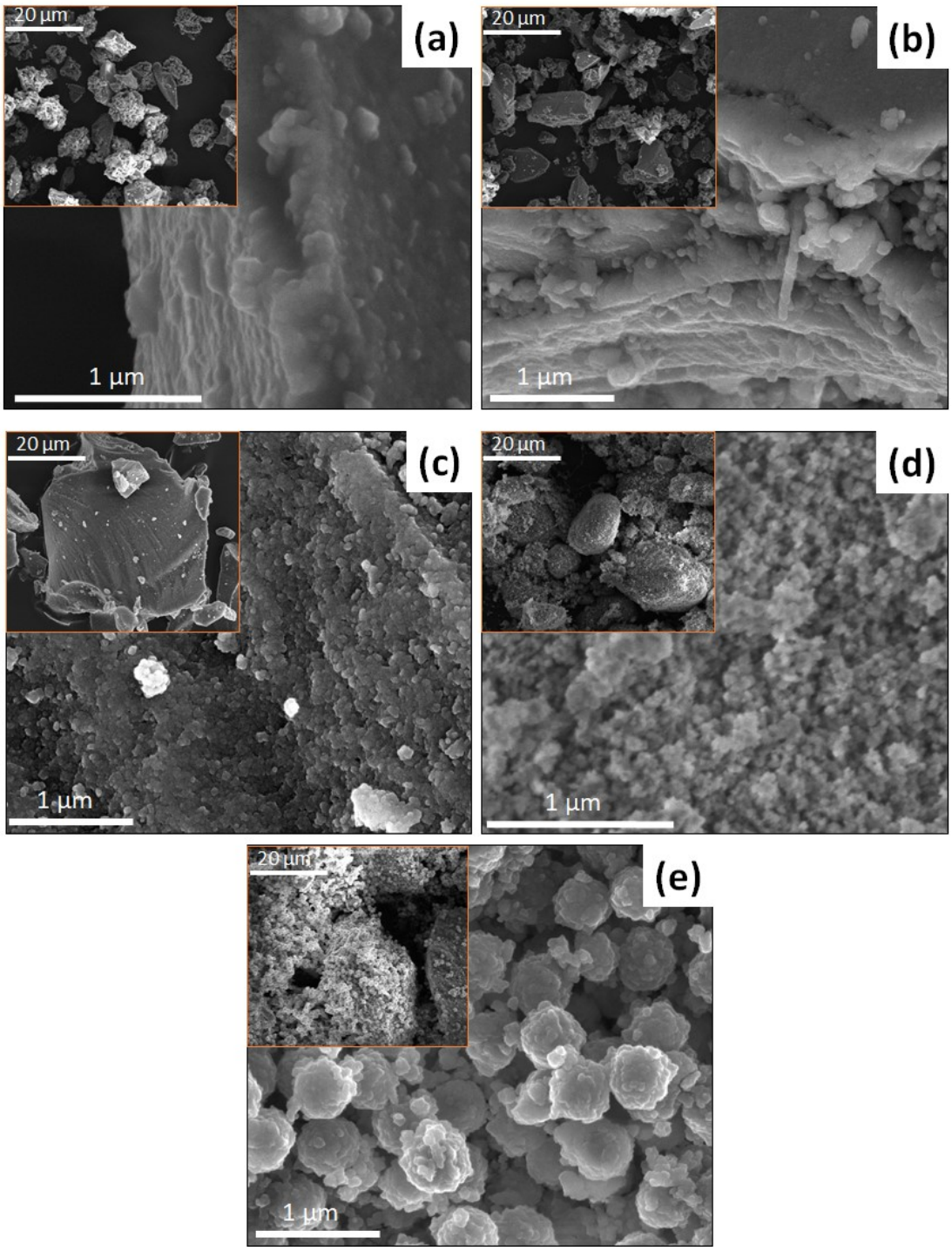

Figure 5.4 – SEM images of n-SiO_2 supports synthesized with different pH values: (a) 2; (b) 3; (c) 4; (d) 6.5; and (e) 10.

5.2. SOL-GEL Fe_2O_3 CATALYST

The N_2 adsorption results showed that the SSA of the prepared Fe_2O_3 powder is around 16.6 ± 8 $m^2.g^{-1}$ and mesoporous volume equal to 0.1 ± 0.01 $cm^3.g^{-1}$.

A typical X-ray diffraction pattern is presented in Figure 5.5. The main peaks fitted well to the crystalline structures of pure α-Fe_2O_3 according to the cataloged sheet RRUFF cod. R110013, (MASLEN *et al*., 1994). Using the Debye–Scherrer equation and considering K=0.89, λ=1.54443 Å, β=0.3° (measured in 2θ equal 32.97°) and θ = 32.97° - plane (104), the smaller crystallite size was calculated: the value was approximately 3.13 Å (0.313 nm).

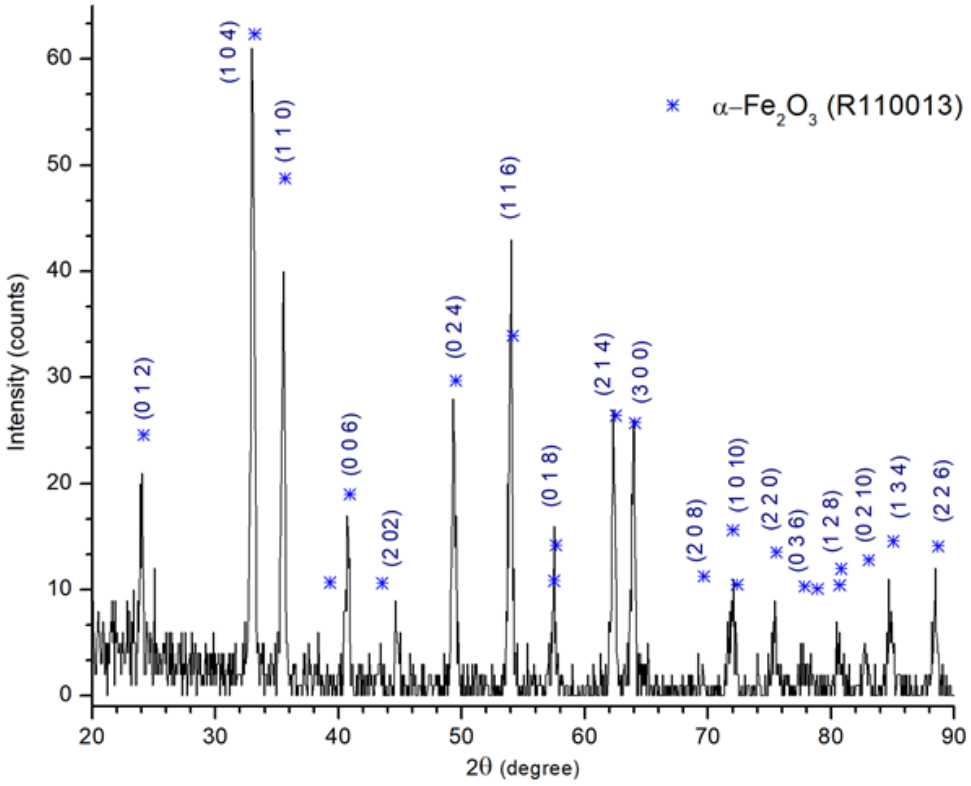

Figure 5.5 – XRD pattern of the Fe_2O_3 powder obtained from the catalyst.

About the morphology of the iron-catalyst synthesized, Figure 5.6 shows the features of the synthesized Fe_2O_3. Figure 5.6a shows the TEM image of the Fe_2O_3 particles, dispersed on the top of a copper (Cu) grid. This is a typical TEM image used to measure the α-Fe_2O_3 nano-particle (NPs) size.

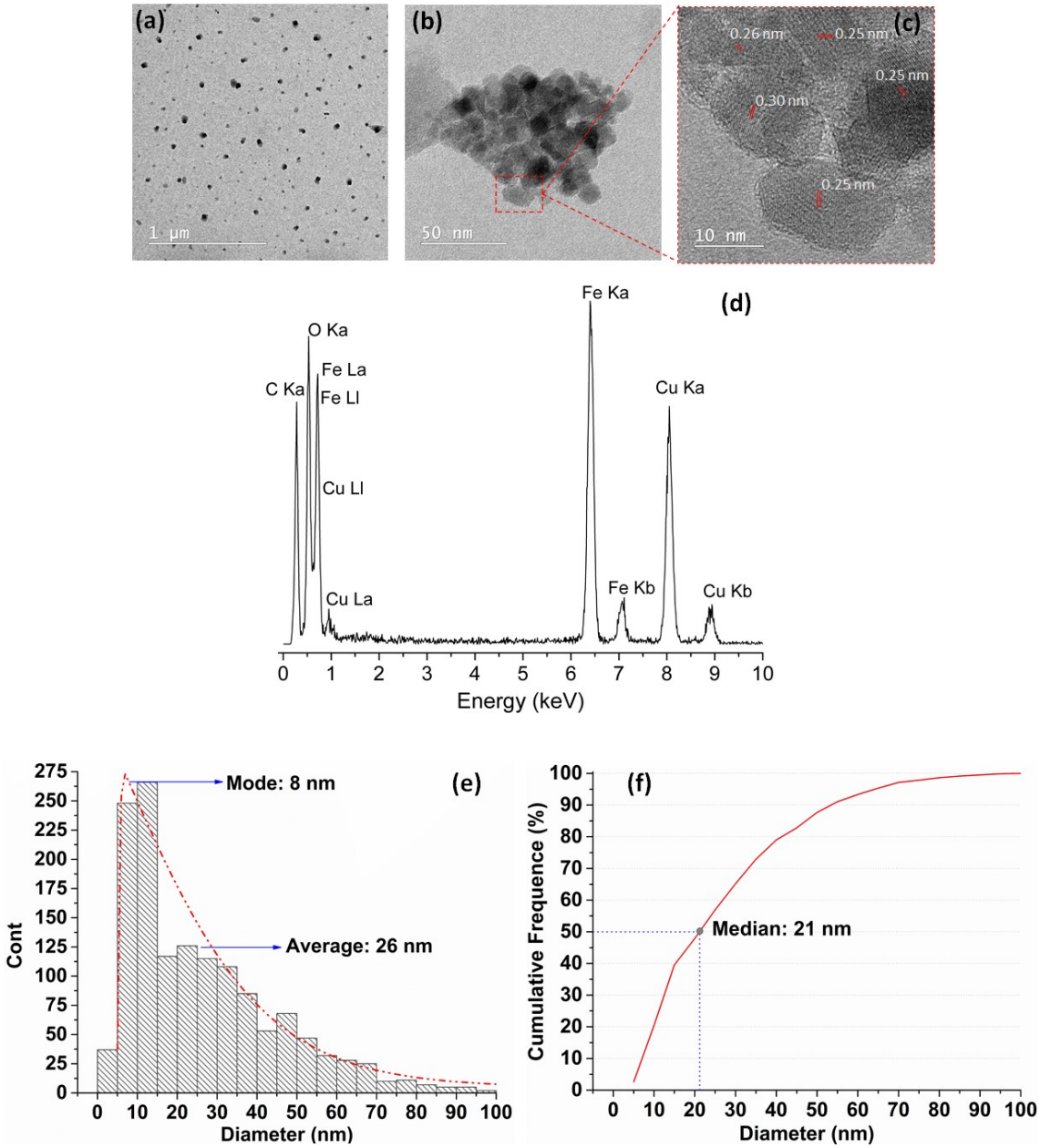

Figure 5.6 – Features of synthesized Fe_2O_3: (a) Typical TEM image. (b) TEM image with high magnification. (c) HRTEM image. (d) EDS spectrum. (e) Distribution of the particle size. (f) Cumulative particle size distribution curve.

Ten images were used to measure the particle size, using the ImageJ software considering the Feret´s diameter[2] to draw the distribution curve. Figure 5.6b shows a TEM image with high magnification of the as-synthesized α-Fe_2O_3 NPs and Figure 5.6c the high-resolution TEM (HRTEM) image of the NPs indicating the high crystallinity and lattice fringes of the nanoparticles, with a distance

[2] Correspond to the measurement of an object size along a specified direction. It is defined as the distance between two parallel planes tangent to the object in perpendicular directions.

around 0.25 nm. By the EDS spectrum (Figure 5.6d) it is possible verify that the chemistry of the catalyst particles synthesized consists only of iron (Fe) and oxygen (O) atoms. The presence of Cu is due to the composition of the TEM grid. This indicates that the used synthesis process produced material of good quality, without impurities.

The distribution of the particle size (equivalent diameter) measured from TEM images, mode, and average are indicated in Figure 5.6e, and the cumulative particle size distribution curve measured, with the mean value, is indicated in Figure 5.6f.

Considering a statistical analysis and distribution, most particles presented an equivalent diameter of around 10 nm. The mode value is 8 nm, but a considerable number of particles presented a size ranging from 15 to 55 nm with a mean value of about 26 nm (Figure 5.6e). Considering the diameter size distribution, the median size value is around 21 nm (Figure 5.6f).

5.3. INFLUENCE OF THE SILICA SUPPORTS ON THE CNTs STRUCTURE – First stage

Considering the desirable features of the hybrid n-SiO_2/CNTs, the results and the analyses presented in this topic are ordered to discuss the effect of the silica supports in the morphology of synthesized CNTs by the CCVD method. These results are related to the CNTs synthesis method described in topic 4.1.1 and characterization methods described in topic 4.2.

5.3.1. Raman spectroscopy analysis

Figure 5.7 shows the Raman spectra of n-SiO_2/CNTs samples synthesized. For each sample, six spectra were taken to be representative of the results.

According to Gupta *et al.* (2013), a typical Raman spectrum of CNTs can be divided into four regions: the RBM (radial breathing mode), associated with CNT

of few walls and typically around 100–400 cm^{-1}; the D band, associated with disordered carbon or structural defects, at 1280–1320 cm^{-1}; the graphene or G band (tangential mode) around 1500–1600 cm^{-1} and the G′ (or D*) band at 2700 cm^{-1}, present when a double-resonance Raman feature is induced by disorder, defects or ion intercalated between the graphitic walls, (OSSWALD; HAVEL; GOGOTSI, 2007).

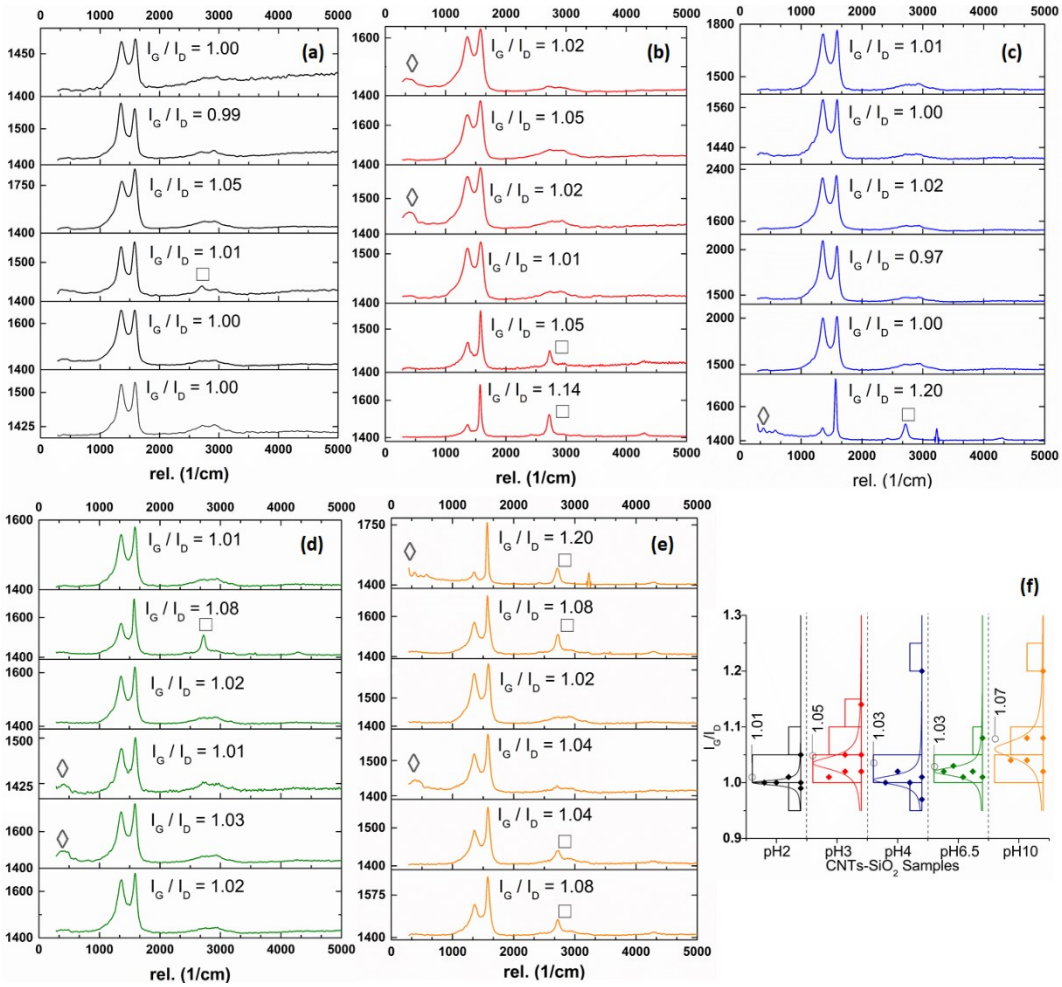

Figure 5.7 – Raman spectra with I_G/I_D ratios of the CNTs/n-SiO_2 composites obtained from sol-gel synthesis using pH: (a) 2; (b) 3; (c) 4; (d) 6.5 (e) 10; and (f) statistical variation of I_G/I_D values – First stage.
Symbols: (□) G´ band; (◊) RBM.

Thus, in Figure 5.7a-e, in general, it is possible to identify two main peaks in all the samples; the first associated with the D band (I_D) and the second with the G band (I_G). Taking into consideration that the ratio I_G/I_D is an indication of the graphitization degree of the material, as discussed by Dunens; Mackenzie; Harris (2009), Figure 5.7f shows the variation of these values for each sample, as well

as a distribution of probabilities, according to the I_G/I_D values calculated for each spectrum.

It is verified that the n-SiO_2/CNTs sample derived from synthesis with pH 2 has the lowest I_G/I_D average value, while the one derived from pH 10 has the highest average value. The samples derived from pH 4 and pH 6.5 presented mean values in the same order of magnitude and slightly lower than the sample derived from pH 3, respectively. Thus, a tendency to vary the degree of graphitization depending on the substrate structure is verified.

In the sample derived from pH 10, it is also possible to verify in four points (out of six) the presence of G´ band, which is also indicative of a higher degree of graphitization of the MWCNTs and corroborates with its high I_G/I_D values.

The presence of RBM in the spectra is not a usual result in MWCNTs since the RBM signal in large diameter tubes is generally too weak to be observable. Thus, this signal may be associated with the vibration of inner tubes, inside the MWCNTs, with a very small diameter, (MURPHY; PAPAKONSTANTINOU; OKPALUGO, 2006).

5.3.2. Thermogravimetric analysis

The results of thermogravimetric analysis (TGA) performed on the hybrids samples are presented in Figure 5.8.

The mass loss, Figure 5.8a, is related to the amount of oxidized carbon, which can be considered as the yield of CNTs in the sample, according to Trigueiro *et al.* (2007) and also Porwal *et al*. (2007). Thus, the samples derived from pH 4 and pH 6.5 showed the highest values (~21%), followed by the ones derived from pH 2 (17%), pH 10 (~14%), and pH 3 (~10%). These values were calculated considering the mass loss between the onset (T_i) and final (T_f) points of oxidation in each curve.

The derivative thermogravimetric (DTG) curve (Figure 5.8b) shows important information about the oxidation (degradation) events of the carbon structures.

The full half-maximum width (W) is directly related to the homogeneity of carbon structures and the peak temperature (T_p) related to its characteristics. Table 5.2 summarizes the information about the oxidation events for the different hybrids synthesized.

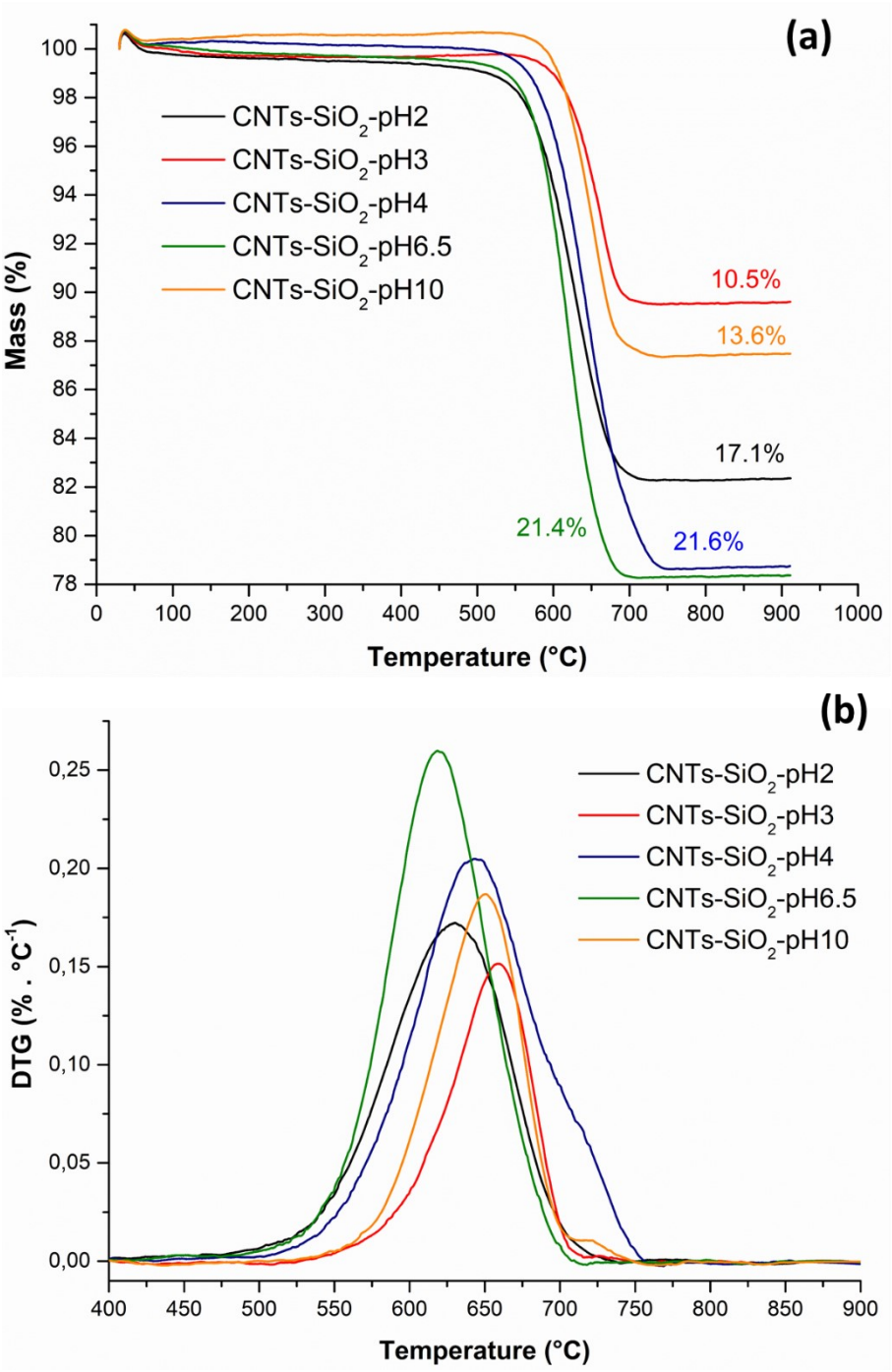

Figure 5.8 – Thermogravimetric analysis: (a) TGA and (b) DTG curves of the n-SiO_2/CNTs samples – First stage.

Table 5.2 – TGA results for the hybrids n-SiO_2 /CNTs – First stage.

Sample	T_i (°C)	T_f (°C)	T_p (°C)	W (°C)	Mass Loss (%)
n-SiO_2 /CNTs-pH2	500	730	628	673 – 578 = 95	17.1
n-SiO_2 /CNTs-pH3	528	741	663	685 – 622 = 63	10.5
n-SiO_2 /CNTs-pH4	500	760	644	690 – 596 = 94	21.6
n-SiO_2 /CNTs-pH6.5	500	730	618	657 – 581 = 76	21.4
n-SiO_2 /CNTs-pH10	500	740	654	677 – 611 = 66	13.6

5.3.3. Morphological evaluation of the hybrids n-SiO_2/CNTs

The micrographs presented in Figure 5.9 present SEM images with different magnifications of the as-grown carbon nanotubes using the silica materials as support. Independent of the sample synthesized, CNTs are dispersed randomly, without alignment, and with different morphologies. Tubular structures with large diameters and without hollow structures, which are usually carbon nanofibers (CNFs), similar to those presented by Gao *et al.* (2014), are also present. In some samples, metal catalyst particles encapsulated by amorphous carbon (noted E in the micrographs) can also be observed. Representative MWCNTs can be seen in detail in TEM images exhibited in Figure 5.10.

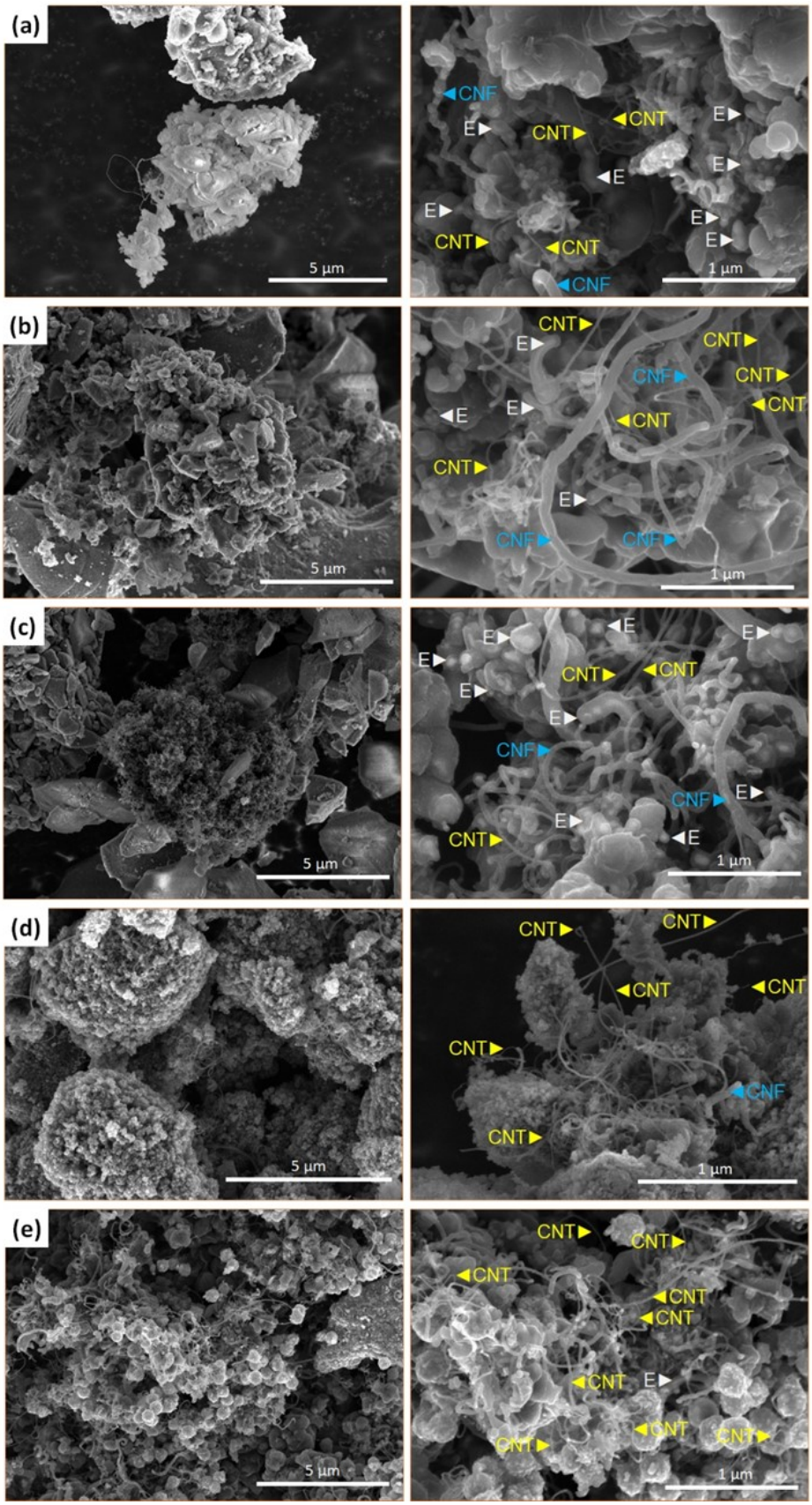

Figure 5.9 – SEM images of the as-grown MWCNTs on the n-SiO_2 supports synthesized from solution with pH: (a) 2; (b) 3; (c) 4; (d) 6.5 and (e) 10 – First stage.

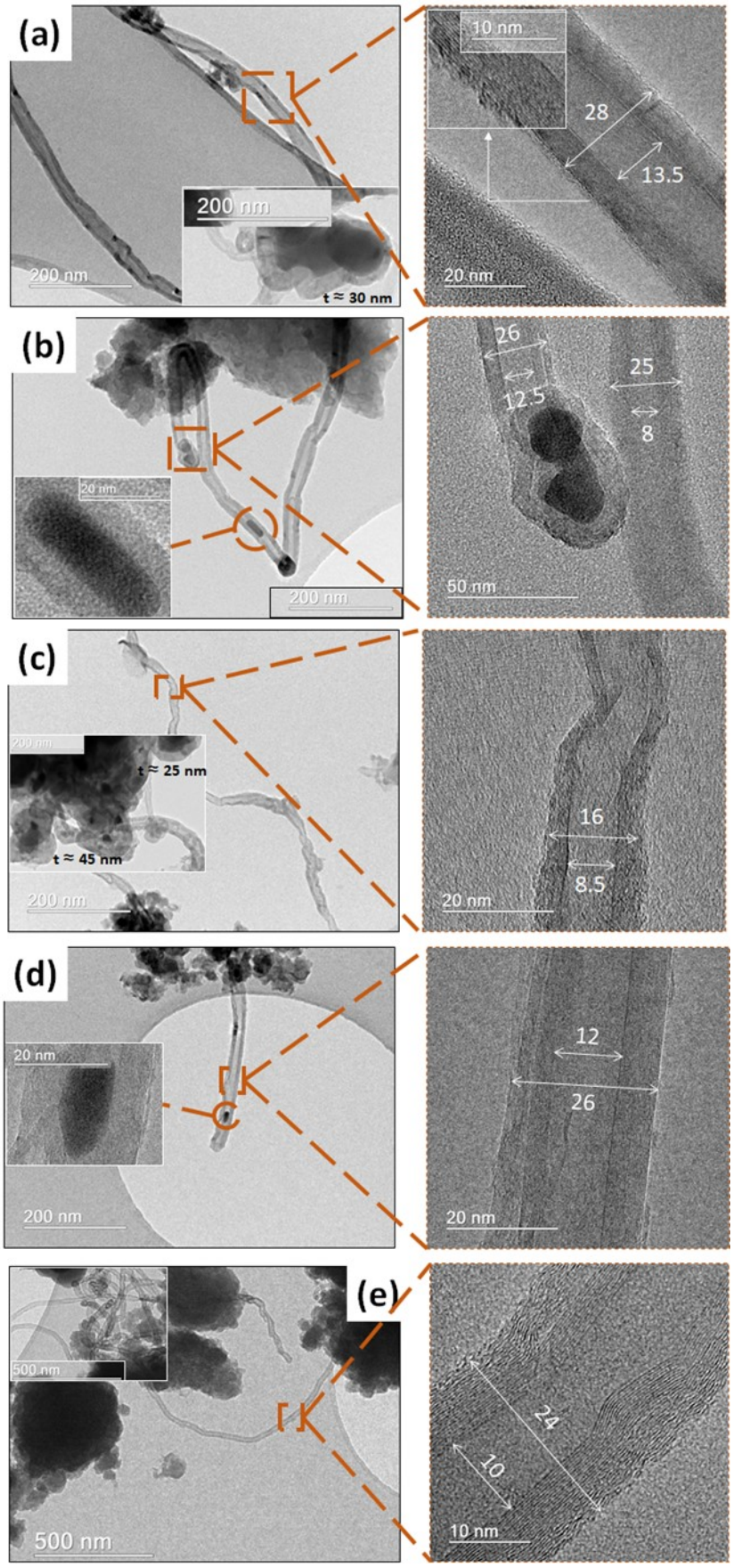

Figure 5.10 – TEM images of the as-grown MWCNTs on the n-SiO_2 supports synthesized from solution with pH: (a) 2; (b) 3; (c) 4; (d) 6.5; and (e) 10 – First stage.

5.3.4. Discussion of the first stage results

It can be identified from Raman, TGA, SEM, and TEM acquisitions that the structural variation of the silica supports resulted in morphological differences of the synthesized MWCNTs.

Despite its silica support present the lowest SSA value, according to Table 5.1, the composite n-SiO_2/CNTs derived from pH 10 showed the highest I_G/I_D ratio. On the other hand, the material with the highest SSA, i.e. n-SiO_2/CNTs derived from pH 2, presents the lowest I_G/I_D mean value. n-SiO_2/CNTs samples from pH 4 and pH 6.5 showed I_G/I_D ratio very close, and also mass loss values, even though they present different SSA values.

Correlating the information of Table 5.2 with the quality information of the CNTs by Raman spectra, the samples with the lowest I_G/I_D ratio are those with the highest mass loss and the highest W parameter (full half-maximum width) values. On the other hand, the samples with the highest degree of crystallinity, n-SiO_2/CNTs from pH 3 and pH 10, are those with lower values of mass loss and W parameter.

The oxidation temperature can be affected by characteristics of the material structure, such as diameter, the number of walls and, degree of graphitization, according to Cunha *et al.* (2018). From this point of view, it can be seen that the deposited carbon was not only in the form of MWCNTs, but also other byproducts such as amorphous carbon on CNF surface, or encapsulated metal catalyst particles.

The micrographs presented in Figure 5.9 indicate MWCNTs, CNFs, and metal catalyst particles encapsulated by carbon structures (E) present in the hybrid structures. It is possible to verify that the n-SiO_2/CNTs samples derived from pH 2 and pH 4, which have high pore volume, present plenty of these amorphous structures.

In the insets of Figure 5.10, catalyst particles (dark spots in the images) surrounded by thick (25 to 45 nm thickness) amorphous carbon structures are

identified. These factors could justify the larger mass loss and W parameter of these two samples.

Regarding the n-SiO_2/CNTs hybrid prepared at pH 3, the I_G/I_D ratio is higher than the n-SiO_2/CNTs hybrid from pH 2 and pH 4, with lower mass loss and W parameter. Once again, the higher degree of crystallinity corresponds to the lesser amount of amorphous or carbon with a low crystalline degree. Besides, Figure 5.10b evidences the presence of MWCNTs with well-defined internal and external walls, as well as the detection of catalyst particles with low interaction with the support (tip-growth mode).

The evaluation of the I_G/I_D ratio for the sample n-SiO_2/CNTs from pH 6.5 shows a mean value of 1.03. This result may be associated with the presence of by-products synthesized together with the MWCNTs. Indeed, several points are indicated in Figure 5.9d where CNFs structures are present. As mentioned above, these are structures that oxidize at lower temperatures, which is validated by the lowest peak temperature (T_p), shown in Table 5.2 and illustrated in the DTG curve of Figure 5.8b. The mass loss of approximately 21% involves the MWCNTs oxidation in addition to the other deposited carbon structures.

Concerning the n-SiO_2/CNTs hybrid derived from pH 10, its higher I_G/I_D ratio can be related to the high peak temperature and the second-lowest W parameter. As already mentioned, a low value of W relates to a small variety of types of deposited carbon structures. Through the images of Figure 5.9e, it is verified that there is a higher dispersion of the deposited MWCNTs among the spherical particles of n-SiO_2. In the images presented in Figure 5.10e, it is possible to see MWCNTs with a small internal diameter and well-defined walls.

As it can be observed in the high magnification TEM images shown in Figure 5.10, all samples exhibited MWCNTs with well-defined outer walls covered by layers of amorphous carbon (“rough layers”). The presence of amorphous carbon covering the MWCNTs can also act as preferential sites for lower temperature oxidation. This was also observed by Trigueiro *et al*. (2007) and Porwal *et al*. (2007).

This fact analyzed together with the degree of crystallinity, i.e. I_G/I_D ratio, and W parameter of MWCNTs, leads to the conclusion that the samples with lower peak temperature (T_p) are those presenting a higher incidence of amorphous structures, in this case, samples derived from synthesis with pHs 2, 4 and 6.5. On the other hand, samples derived from synthesis with pH 3 and pH 10 presented higher T_p and smaller W parameter, which may be associated with less amorphous structures or defect-free nanotubes, since defect-free nanotubes display higher oxidation temperatures. A similar result was obtained by Cunha *et al*. (2018).

Following this concept, the carbon mass loss obtained from TGA and the W parameter, for example, parameters of quantity and quality of the MWCNTs respectively, were correlated with the mesoporous characteristics of the silica supports. No relation about the effect of the SSA on the quantity or quality of the as-grown MWCNTs was observed in this case. This is different from reported in the literature by Ramesh *et al*. (2005), Magrez *et al*. (2010), Othman; Kinloch; Wilkinson (2013), and also Osorio and Bergmann (2013).

However, using a morphological parameter calculated from the multiplication of the mesoporous volume (Vmes) and the mean pore size (dp) of each silica assessed by nitrogen adsorption, a correlation can be discussed. Figure 5.11 presents this correlation.

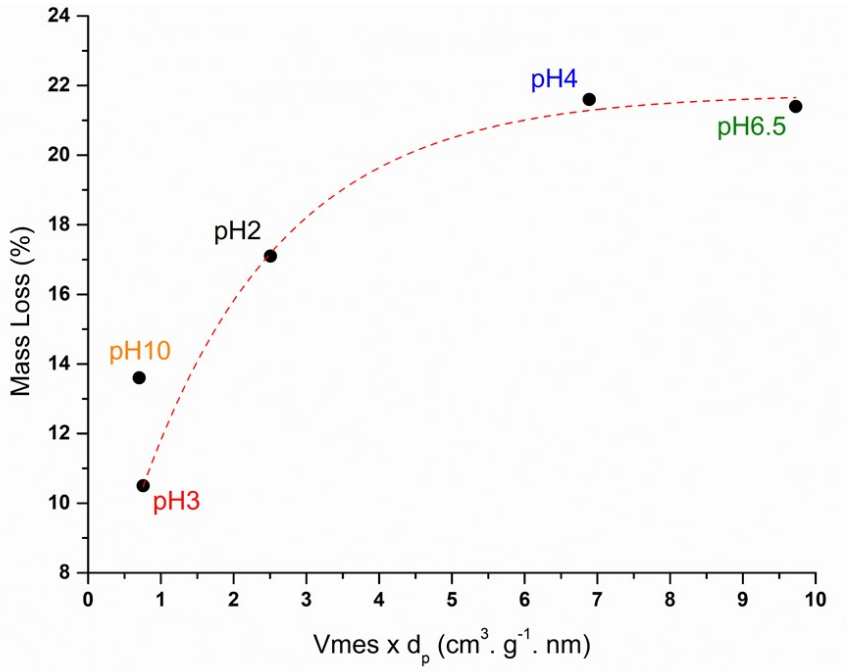

Figure 5.11 – Correlations between carbon mass loss from TGA as a function of (V_{mes} x d_p) parameter of the silica support – First stage.

Indeed, according to presented in Figure 5.11, silica supports with high mesopore volume and high mean pore size seem to favor an important growth of carbon nanostructures formed on the surface of the silica support. Such mesoporous features seem to improve the catalyst/support interaction and its chemical reactions with the methane gas during the CCVD process. However, it is important to remember that such formed carbon structures are not necessarily grown as MWCNTs with good quality.

Thus, using the same morphological parameter of the silica (V_{mes} x d_p), Figure 5.12 illustrates the inverse variation of the W parameter. In agreement with previous discussions, it is worth remembering that the lower 1/W parameter, the better the MWCNTs quality.

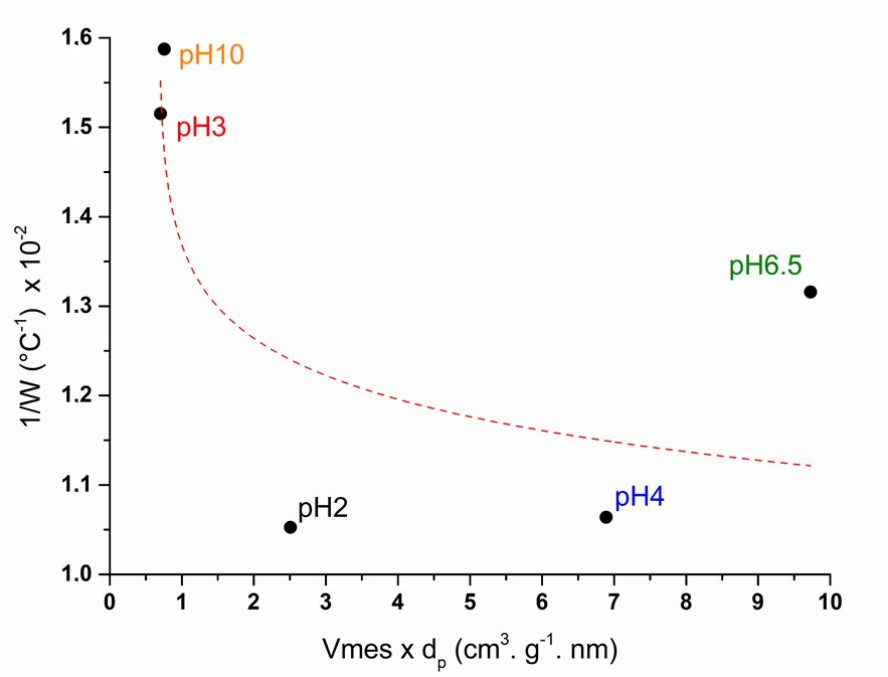

Figure 5.12 – Correlations between (1/W) parameter of MWCNTs as a function of the (V_{mes} x d_p) parameter of the silica support – First stage.

Based on this correlation, it is possible to show that the quality of the MWCNTs seems to be higher when "V_{mes} x d_p" is low. Indeed, according to obtained results, the highly mesoporous structure seems to decrease the quality of the as-grown MWCNTs. This result is probably due to inadequate pore size, much smaller than the catalyst particles, disfavoring its anchorage on the silica surface to grow MWCNTs with good quality. As a result, the macroscopic features of the silicas with very low mesoporosity seem to be more efficient to fix the catalyst on its surface to grow MWCNTs with high quality. Nevertheless, when the pore size of the silica structure gets closer to the size of the catalyst nanoparticles, the quality of the MWCNTs appears to improve again.

To elucidate more the correlations between the parameters, the 1/W parameter was plotted together with the graphitization parameter I_G/I_D. According to Figure 5.13, the parameter I_G/I_D seems directly proportional to the 1/W parameter.

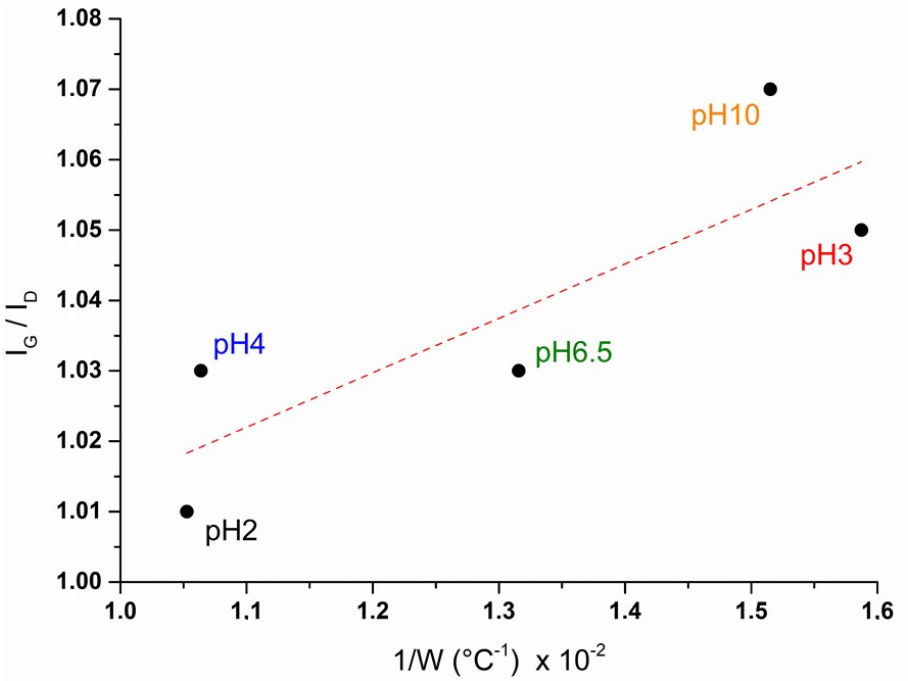

Figure 5.13 – Correlations between MWCNTs I_G/I_D as a function of the (1/W) parameter of the as-grown MWCNTs – First stage.

Figure 5.14 shows a correlation between the parameter representative of the quality and the quantity of the as-grown MWCNTs (Mass Loss / W), as a function of the morphological parameter of the silica supports (V_{mes} x d_p).

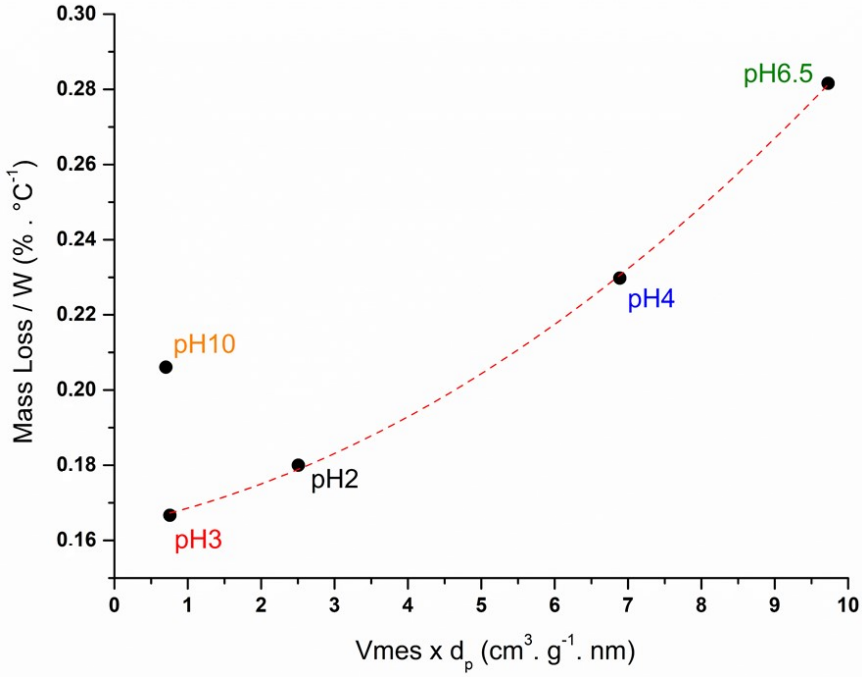

Figure 5.14 – Correlations between MWCNTs (Mass loss/W) parameter as a function of the (V_{mes} x d_p) parameter of the silica support – First stage.

It is possible to verify that the silicas synthesized with the acidic catalyst (pH 2, 3, 4, and 6.5) follow the same tendency (dotted line). Such tendency suggests that for the acidic sol-gel synthesis of n-SiO_2, the formed mesoporous structure disfavors the quality of the as-grown MWCNTs when producing a high volume of carbon nanostructures. Moreover, it is possible to observe that the sample synthesized over the silica produced with the basic catalyst (pH 10) presents a different behavior, which is probably a consequence of different sol-gel mechanisms occurring to form the support material.

Indeed, and in agreement with Brinker and Scherer (1990), the sol-gel reactions in the acidic medium led to the gelation of the silica support before the drying step, whereas the reactions in the basic medium led to the precipitation of silica particles. In this case, due to the nanotubes production with higher quality for the same quantity of carbon structures than the composite derived from pH 3, the n-SiO_2/CNTs composite derived from basic sol-gel (pH10) synthesis presents a higher quantity-quality. From an interesting perspective, such a sol-gel method in the basic medium could show a tendency to produce more CNTs with better quality, when following the employed synthesis conditions.

Contrary to various works (Magrez *et al*. (2010) and Osorio and Bergmann (2013)), the results presented herein indicate that the specific surface area of the substrate is not a predominant parameter to affect the quality of the as-grown MWCNTs. Besides, in agreement with some authors, De Los Arcos *et al*. (2002), Wang *et al*. (2006), and Esconjauregui *et al*. (2011), silica supports for CNTs synthesis seem to have not a good chemical interaction with metal-based catalysts.

Such observation could justify the high occurrence of amorphous carbon structures in the obtained results. Thus, according to phenomena already observed by Homma *et al*. (2003) and Ramesh *et al*. (2005), it is possible that the iron-based particles agglomerated and sintered during the CCVD process, due to the high temperature, leading to catalyst clusters, and favoring the deposition of amorphous carbon or MWCNTs with large diameters.

In agreement with some results previously described in the literature, silica supports did not show a good chemical interaction with iron-based catalyst, when used as support for CNTs growth by CCVD process.

The morphology of n-SiO_2 affected the interaction between the support and the catalyst, and consequently, the quality of MWCNTs that were synthesized. The mesoporous silica with pore size distribution smaller than the catalyst particles were inefficient to anchor the catalyst particle and maybe caused the formation of catalyst clusters during the CCVD process. The catalyst in cluster form should promote the formation of amorphous carbon, encapsulated metal catalyst particles, and carbon nanotubes with low quality.

Regardless of the quality of the carbon structure grown during the CCVD synthesis, silica supports with a combination of high mesopore volume and high mean pore size favor an important volume of carbon nanostructures formed on the surface of the silica support.

Thus, silica supports in this condition, mainly pH 6.5, were more adequate to the MWCNTs synthesis, in terms of quality of the as-grown material. The presence of macroscopic pores with compatible sizes for the catalyst particles may have allowed a better anchorage. Thus, the cluster formation of catalyst particles does not occur (or was reduced), inducing consequently a better quality of the as-grown MWCNTs.

Taking all this into account, the silica support sample pH 6.5 can be considered more suitable for the CNTs synthesis considering the employed conditions.

5.4. INFLUENCE OF THE CATALYST INCORPORATION METHOD ON THE CNTs STRUCTURE – Second stage

Considering the desirable features of the hybrid n-SiO_2/CNTs, the results and analyses presented in this topic are ordered to discuss the effect of the catalyst incorporation method on the morphology of synthesized CNTs. These results are

related to the CNTs synthesis procedure described in topic 4.1.2 and characterization methods described in topic 4.2.

5.4.1. Support and catalyst analyses

5.4.1.1. FTIR characterization

Figure 5.15 shows the FTIR spectra of SiO_2-dep, SiO_2-imp, and SiO_2-msg samples in the absorbance mode, before and after the calcination process (named with the suffix -cal). All samples have absorption bands close to 460 and 800 cm^{-1}, which are associated with the bending mode of Si-O-Si bonds, as well as the peaks at about 1060 cm^{-1} (PRIMEAU; VAUTEY; LANGLET, 1997; JUNG *et al.*, 2005; AGUIAR *et al*., 2009).

The absorption band close to 950 cm^{-1} is associated with symmetric and asymmetric stretching modes of Si-OH bonds, as mentioned by Jung *et al.* (2005) and also Aguiar *et al*. (2009). Still, according to these authors, the peaks around 1620-1640 cm^{-1}, indicate the H-O-H bending mode vibration of free or absorbed molecular water, and around the range of 2800 and 3700 cm^{-1}, the large shoulders represent the OH bands. For better observation, a spectrum region between 500 and 750 cm^{-1} (hatched area in blue) is magnified and presented on the right side of the figure. It is possible to see in all samples, shoulders around in the range of 550-600 cm^{-1}, which is associated with the iron-based catalysts present in the samples. According to Savii *et al.,* (2002) and Ahangaran; Hassanzadeh; Nouri (2013), this range is characteristic of stretching vibrations of Fe-O bonds. In the same region of the spectrum, a small peak is observed around 670 cm^{-1} which could be associated with residual TEOS, from SiO_4 symmetric stretching mode, Innocenzi (2003). Based on the presented IR spectra, no significant chemical differences are observed for the different preparation methods used. The iron oxide presence was confirmed in the samples, and it was not possible to verify the presence of Fe-O-Si bonds.

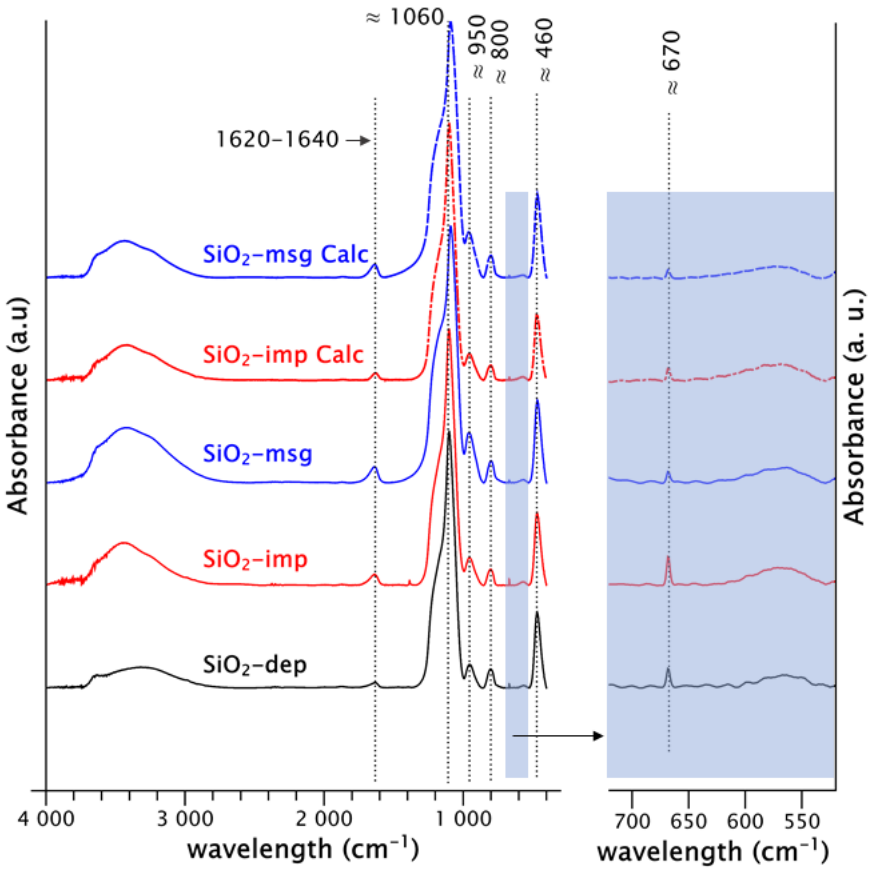

Figure 5.15 – FTIR spectrum of all n-SiO_2/catalyst samples – Second stage.

5.4.1.2. XRD characterization

Figure 5.16 shows the XRD profiles of SiO_2, SiO_2-dep, SiO_2-imp, and SiO_2-msg samples, before and after the calcination process (named with the suffix -cal). Unfortunately, due to a low amount of catalyst (1 wt%) present in the materials and the X-ray equipment detection limit (2%), it was not possible to verify the crystalline structure of the catalyst in the samples. Only the SiO_2-msg after the calcination process presented small peaks corresponding to the hematite phase. In all samples, the presence of amorphous silica was predominant, as expected, with a profile similar to the pure SiO_2 sample (Figure 5.16a). The two samples treated with the calcination process after the catalyst incorporation, SiO_2-imp, and SiO_2-msg, are featured in detail in Figure 5.16b.

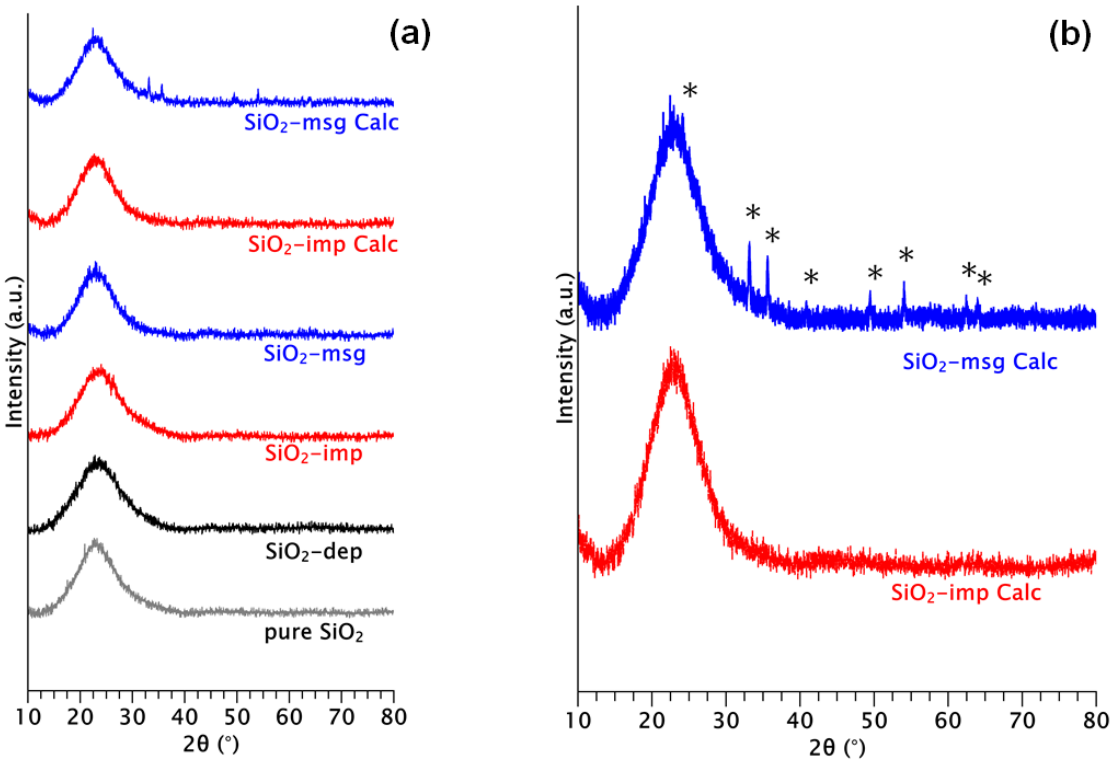

Figure 5.16 – XRD profiles of (a) n-SiO_2 and all n-SiO_2/catalyst samples. (b) calcined SiO_2-imp and SiO_2-msg samples, profiles magnification – Second stage.
(*) α-Fe_2O_3 - RRUFF pattern cod. R110013, Maslen *et al.* (1994).

In this case, the differences in the profiles are easily verified, specifically the presence of hematite in the sample SiO_2-msg, indicating the crystallization of the iron catalyst. A similar profile was obtained by Uma *et al.* (2018) which also used the sol-gel method to produce SiO_2-αFe_2O_3 materials. Most likely this can be related to the diffusion of the iron particles in the nanostructured silica during the calcination process, providing the formation of an iron oxide cluster. Thus, the presence of bigger concentrated iron particles could allow the detection of such crystalline phases by the equipment. It is important to mention that it was neither possible to identify the presence of crystalline phases containing Fe, Si, and O atoms from the X-ray analysis, which corroborates the FTIR results.

5.4.2. Morphological evaluation of the hybrid n-SiO_2/CNTs

The synthesized CNTs over the n-SiO_2 supports present the morphologies illustrated in the SEM images shown in Figure 5.17. On the left side of the figure, images with low magnification are presented to show the carbon structures dispersed over the n-SiO_2 particles. On the right side, the magnifications of each sample are presented to illustrate more details of the CNTs structure. In all samples, the carbon structures are dispersed randomly, without orientation, and with different morphologies. Evaluating the images, the SiO_2-dep (Figure 5.17a) and SiO_2-imp (Figure 5.17b) support samples produced similar structures, with fiber appearance, and similar lengths. The resulting deposited material on the SiO_2-msg support (Figure 5.17c) also shows, in low magnification image, fiber appearance. However, evaluating the images with greater magnification, it is observed amorphous structures (A), and structures similar to platelet carbon nanofibers (PCNF), as identified by the arrows. Such platelet structures are similar to the ones reported by Zheng *et al.* (2006) and Natewong *et al.* (2018), for example. This kind of carbon structure is more clearly illustrated in additional SEM images of the SiO_2-msg/CNTs sample shown in Figure 5.18. In these micrographs, the left image shows nanostructures covering the silica support and the presence of PCNFs in the right image (higher magnification).

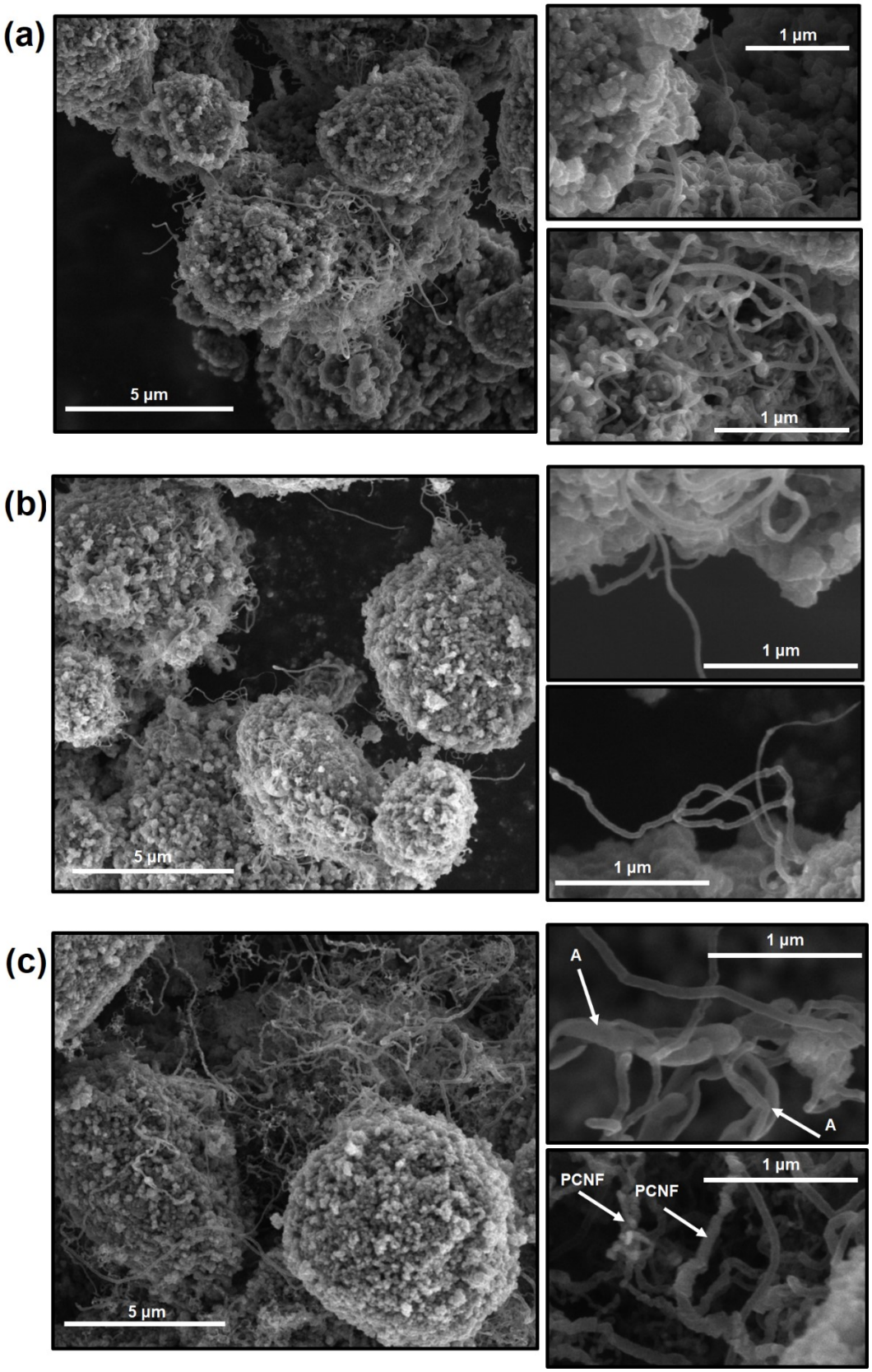

Figure 5.17 – SEM images of the carbon structures deposited over the different n-SiO_2/catalyst: (a) SiO_2-dep; (b) SiO_2-imp; (c) SiO_2-msg – Second stage.

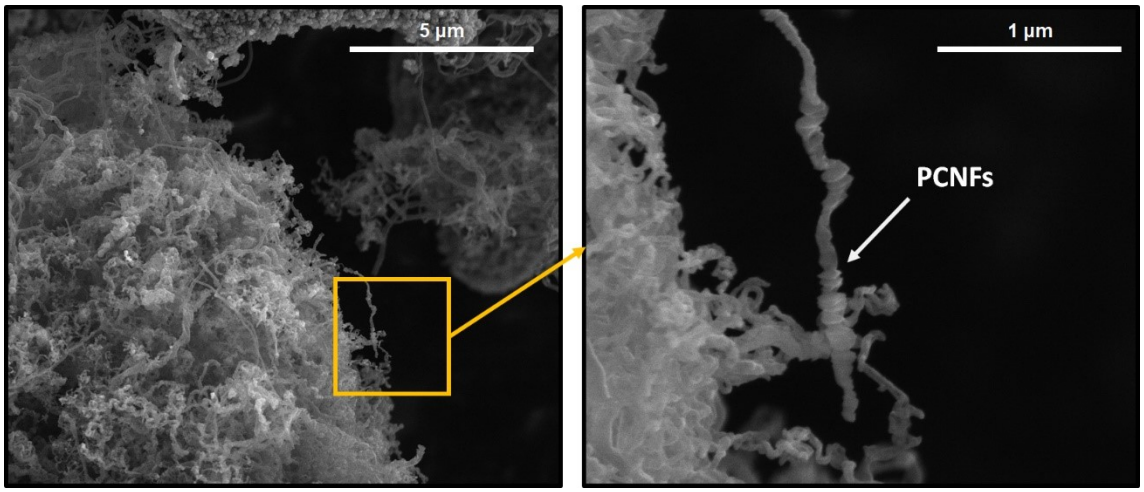

Figure 5.18 – SEM images of the SiO_2-msg/CNTs sample. PCNFs indication – Second stage.

Figure 5.19 and Figure 5.20 shows representatives TEM images of the hybrid samples.

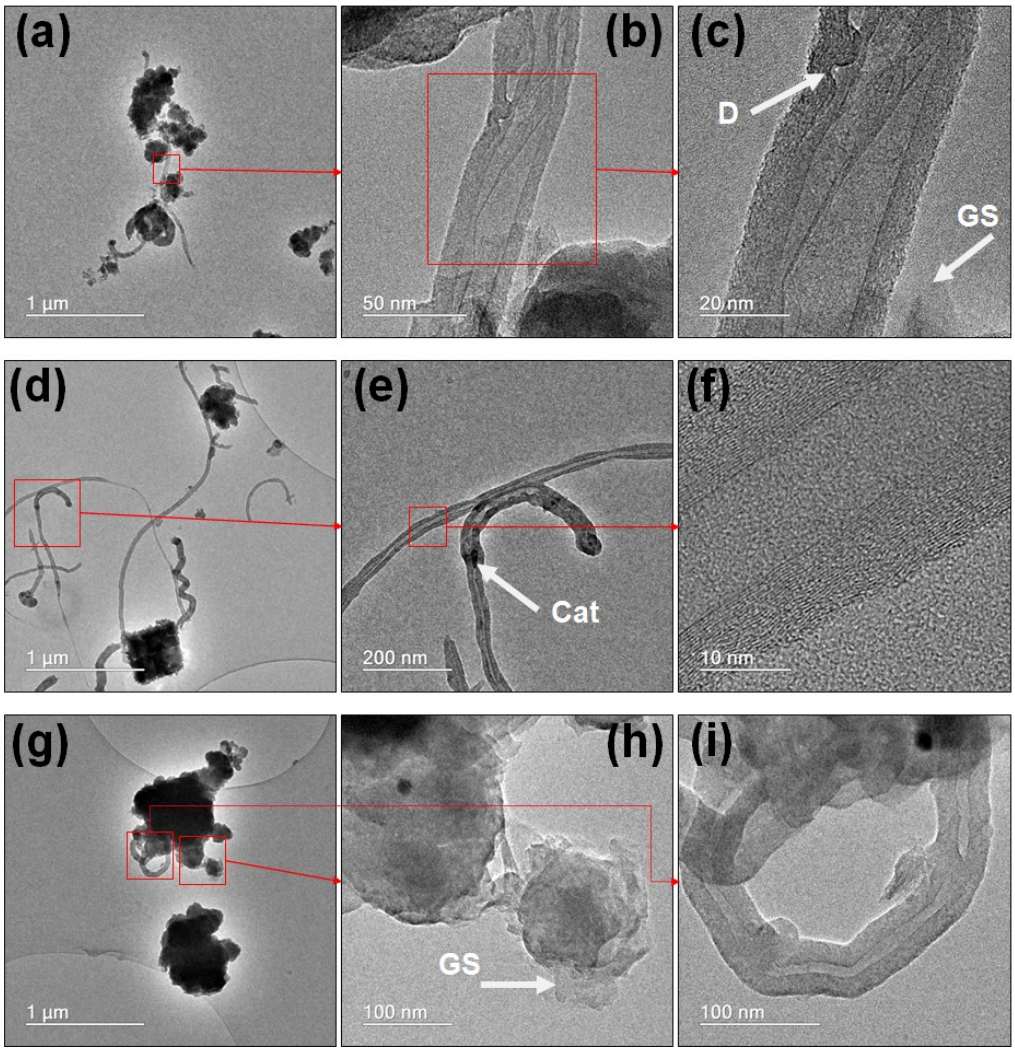

Figure 5.19 – SiO_2/CNTs hybrids TEM images and magnifications: (a-c) SiO_2-dep/CNTs; (d-f) SiO_2-imp/CNTs; (g-i) SiO_2-msg/CNTs – Second stage.

In Figure 5.19a, d, g, the nanostructured particles can be seen, with low magnification, of the SiO_2-dep/CNTs, SiO_2-imp/CNTs, and SiO_2-msg/CNTs hybrids, respectively. Corroborating with the SEM images, the presence of fiber structures is also verified with hollow sections and defined concentric internal and external walls of multi-walled CNTs (MWCNTs). However, some differences in the MWCNTs and other carbon structures deposited between the samples appear more evident when using higher magnification.

Figure 5.19b and c (SiO_2-dep/CNTs) show MWCNTs with defects in the internal walls and with asymmetric geometry. It is also possible to see laminar structures, like graphite sheets (GS) close to the catalyst (dark regions). These structures are identified by arrows in Figure 5.19c. Figure 5.20a-c presented carbon nanotubes with a bamboo-like type, similar to the obtained by Wang *et al.* (2007), as well as external and internal defects (D) in the walls. Concerning the SiO_2-imp/CNTs sample, Figure 5.19d, as well as Figure 5.20d, show carbon fibrillar structures with different diameters and lengths. Figure 5.19e-f and Figure 5.20e-f show, with greater magnification, the well-defined internal and external walls of MWCNTs. The presence of an iron oxide-catalyst particle (Cat) inside the MWCNTs structure is indicated by an arrow in Figure 5.19e. Finally, about the SiO_2-msg/CNTs sample, it can be seen, in Figure 5.19g-i, laminar structures, graphite-like sheets (arrow in Figure 5.19h) over the n-SiO_2 particle, as well as large diameter MWCNTs. In Figure 5.20g-i, it is possible to see a tubular carbon structure without well-defined internal walls and with a thick external layer of amorphous (A) carbon.

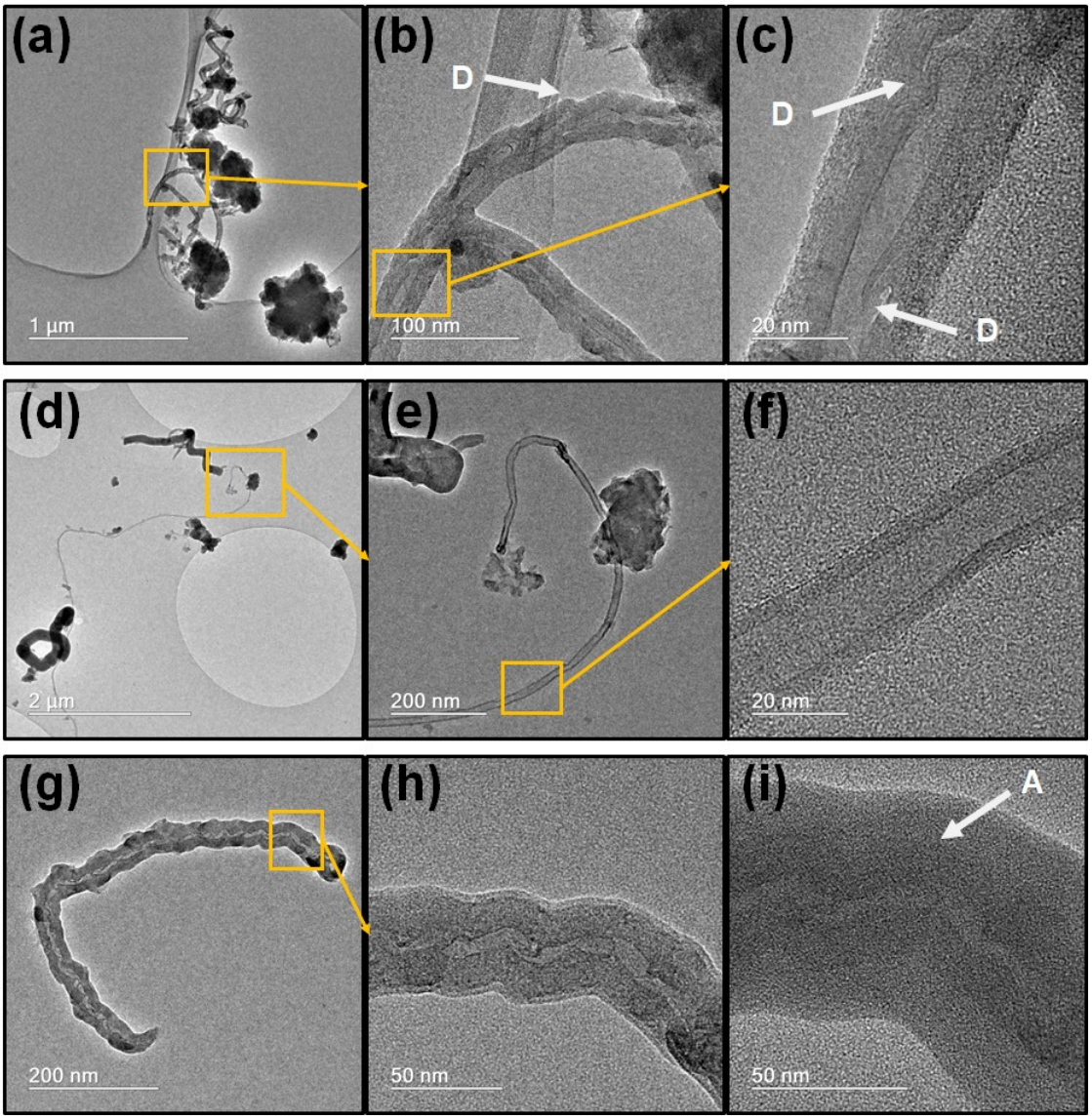

Figure 5.20 – Additional TEM images with different magnifications of the SiO_2/CNTs hybrids: (a-c) SiO_2-dep/CNTs; (d-f) SiO_2-imp/CNTs; (g-i) SiO_2-msg/CNTs – Second stage.

For the diameter evaluation, 190 measurements were made using images not presented in the text for the SiO_2-dep/CNTs and SiO_2-imp/CNTs samples. For the SiO_2-msg/CNTs sample, due to the difficulty to identify fibers structures in the images, only 65 measurements were made. Figure 5.21 presents the results. Considering the distributions, the MWCNTs of the SiO_2-dep/CNTs and SiO_2-imp/CNTs samples have very closed mean values: 59.9 ± 24.5 and 57.2 ± 19.3 nm, respectively. However, the fibers of the SiO_2-msg/CNTs sample presented a much larger mean diameter (104.0 ± 40.3 nm). Evaluating the MWCNT lengths from the SEM images (Figure 5.17), their range is around 0.5 to 30 µm regardless of the catalyst used.

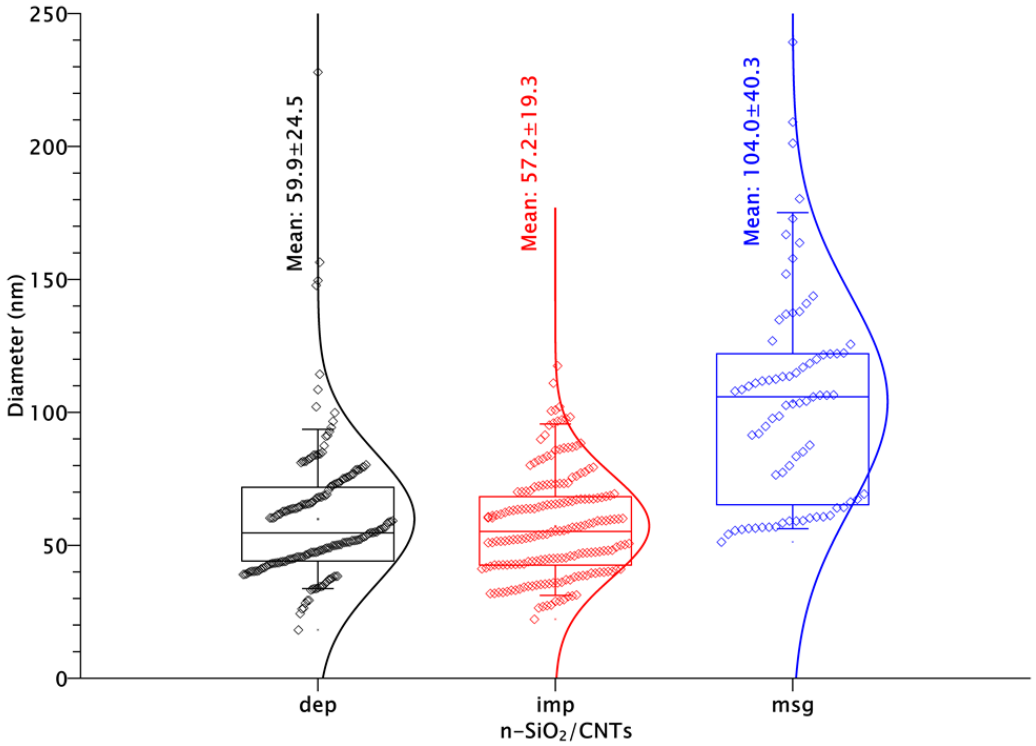

Figure 5.21 – MWCNTs diameter distribution from each sample – Second stage.

5.4.3. Raman spectroscopy analysis

As mentioned in the experimental section (topic 4.2.8), fourteen Raman spectra were recorded from each sample to have representative results for the analysis. The obtained spectra data were fitted and normalized with the intensity of the G band (I_G). Figure 5.22 shows the Raman spectra of the hybrid samples.

As mentioned in topic 5.3.1, the main peaks associated with CNTs quality are the D band, associated with disordered carbon or structural defects, at 1280–1320 $cm^{-1,}$ and the G band (tangential mode) around 1500–1600 cm^{-1} related to the tangential mode of the sp^2 carbon bonds in a hexagonal lattice. Another important band is the G′ (or D*) band present around 2700 cm^{-1} attributed to the overtone of the D band.

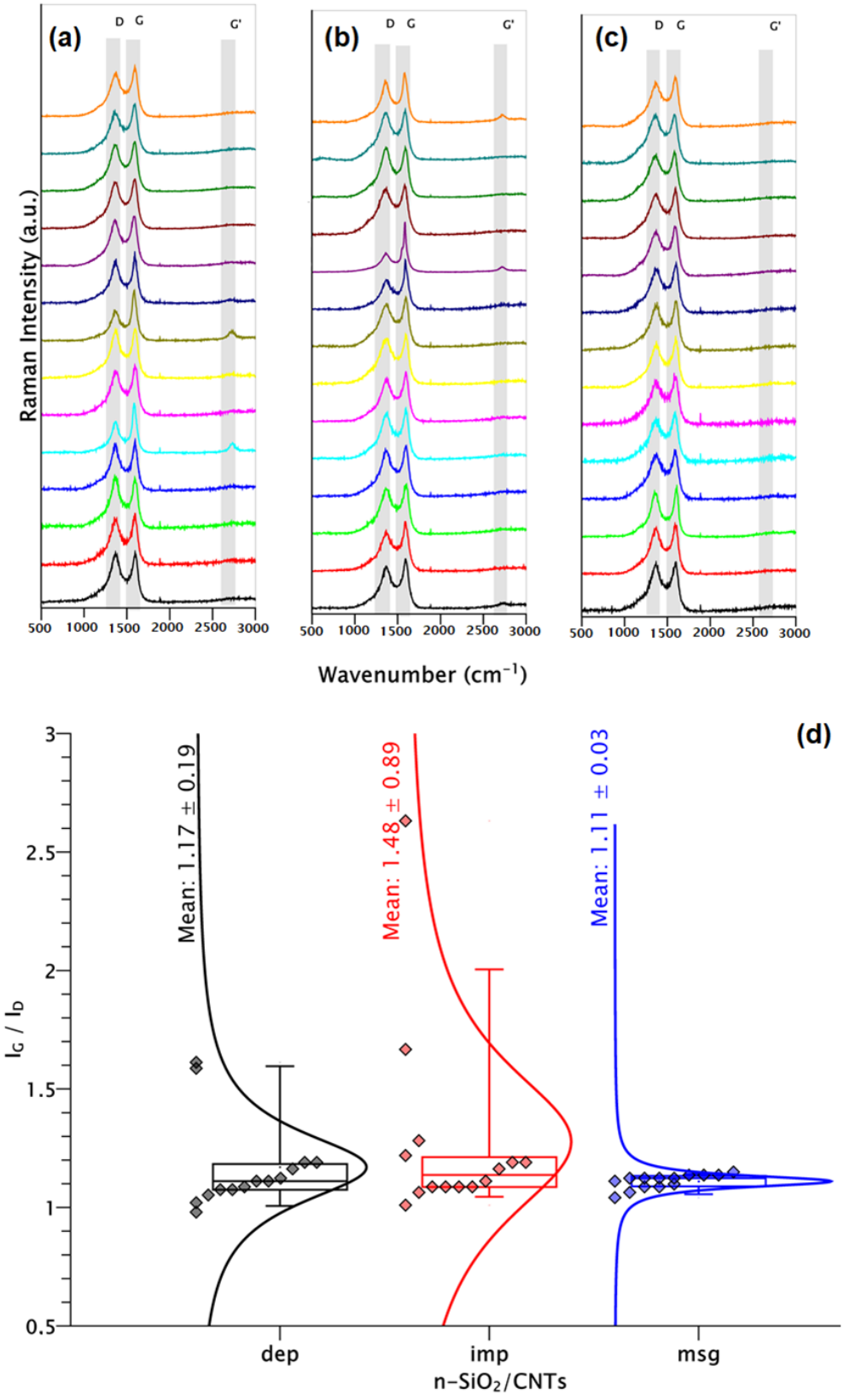

Figure 5.22 – Raman spectra of the hybrids. (a) SiO_2-dep/CNTs; (b) SiO_2-imp/CNTs; (c) SiO_2-msg/CNTs; and (d) statistical variation of I_G/I_D ratios with averages and standard deviations – Second stage.

In Figure 5.22a-c, the Raman spectra of the SiO_2-dep/CNTs, SiO_2-imp/CNTs, and SiO_2-msg/CNTs samples are presented, respectively. The position of the main peaks (I_D, I_G, and $I_{G'}$) is delimited by gray hatched regions. The first region is associated with the D band (I_D) and the second with the G band (I_G). Considering these peaks, the ratio of their intensities (I_G/I_D) is an indication of the graphitization degree of carbon nanotubes (DUNENS; MACKENZIE; HARRIS, 2009).

The I_G/I_D ratio was calculated for each of the fourteen spectra. Figure 5.22d shows the variation of these values, as well as the probability distribution following the Lorentz model[3]. Considering the calculated ratios and a statistical evaluation, the mean values of the I_G/I_D ratio, with its standard deviation, for the SiO_2-dep/CNTs, SiO_2-imp/CNTs, and SiO_2-msg/CNTs are respectively 1.17 ± 0.19, 1.48 ± 0.89, and 1.11 ± 0.03.

5.4.4. XRD analysis

Figure 5.23 shows the XRD spectra profiles registered for all hybrids synthesized, as well as the one for the pure silica support. The MWCNT diffraction planes, according to the PDF card number 00-058-1638, are identified and correspond to the 2θ position of 25.9, 42.9, 53.3, and 78.7°, planes (002), (100), (004) and (110), respectively. The SiO_2-dep/CNTs and SiO_2-imp/CNTs samples exhibit similar profiles with peaks located at 2θ close to 26 and 43°. These peaks were observed for graphitic structures by Ratkovic *et al.* (2014) and Awadallah *et al.* (2016), which confirms the MWCNT presence in these samples. It is worth noting that the main peak (002) characteristic of the graphitic structure is partially superposed with the large shoulder located near 2θ equal to 22° corresponded to the amorphous silica of the support.

Considering the Bragg's equation ($d = \lambda/2.\sin\theta$) for the graphitic peaks close to (002), the distance (d_{002}) of two graphite layers for the SiO_2-dep/CNTs and SiO_2-imp/CNTs samples are 0.364 nm (2θ = 24.41) and 0.355 nm (2θ = 25.06),

[3] Also called the Cauchy distribution, is a statistical continuous probability distribution that is the ratio of two independent normally distributed random variables if the denominator distribution has mean zero.

respectively. Such interlayer distance has been reported to be close to 0.32-0.35 nm for MWCNTs produced through a similar CCVD process (KHARISSOVA; KHARISOV, 2014).

However, the SiO_2-msg/CNTs sample shows a profile without well-defined peaks, which can reflect a graphitic disorder and a variety of carbon structures, as shown in Figure 5.19g-i, and Figure 5.20g-i.

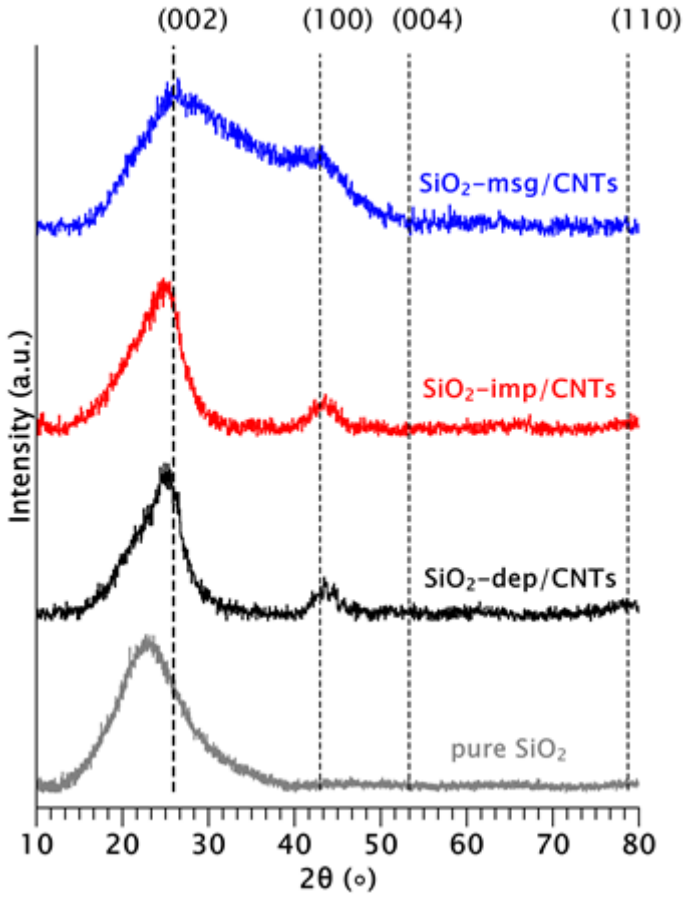

Figure 5.23 – XRD profiles of the n-SiO_2/CNTs hybrids and pure SiO_2 – Second stage.

5.4.5. Thermogravimetric analysis

The carbon nanotube resistance against oxidation was evaluated by thermogravimetric analysis (TGA) as a parameter indicating its quality. As mentioned by Lehman *et al.* (2011), TGA can be used to evaluate the thermal stability of one material as well as its purity. Moreover, in TGA analysis, the mass loss is related to the amount of oxidized carbon, which can be considered as the

yield of CNTs in the sample (TRIGUEIRO *et al.;* 2007, PORWAL *et al.;* 2007). In this case, the yield is calculated using the total mass loss between the onset (T_i), passing by the peak (T_p), and final (T_f) points of oxidation observed in the thermogram.

Figure 5.24a shows the total mass loss as a function of the temperature of the hybrid samples measured by TGA. In Figure 5.24b, the differential thermogravimetric (DTG) profile of each sample is also presented to identify the main peak of mass loss for each sample and its approximate temperature.

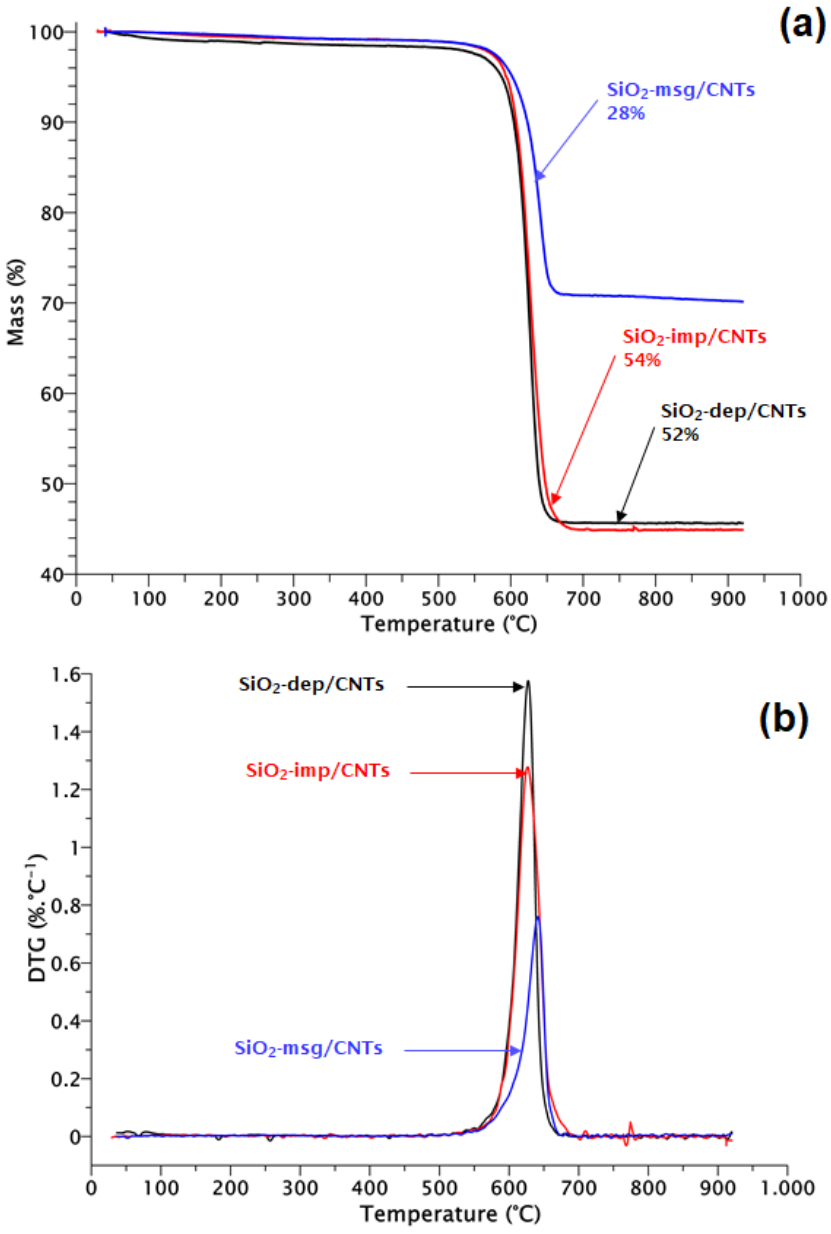

Figure 5.24 – (a) TGA and (b) DTG curves registered for the hybrid samples – Second stage.

The SiO_2-dep/CNTs and SiO_2-imp/CNTs samples practically present the same mass loss percentual (yield), 52%, and 54% respectively. However, the SiO_2-msg/CNTs sample presents a yield well below the other samples, about 28%. From the DTG profile (Figure 5.24b), important information about the oxidation (degradation) events of carbon structures was obtained. Indeed, the full half-maximum width (W), is directly related to the homogeneity of the synthesized carbon structures, and the peak temperature (T_p) is related to their physical characteristics. Table 5.3 summarizes the information about the oxidation events.

Table 5.3 – TGA results for hybrids – Second stage.

Sample	T_i (°C)	T_f (°C)	T_p (°C)	W (°C)	Mass Loss (%)
SiO_2-dep/CNTs	560	675	628	27	52
SiO_2-imp/CNTs	560	685	627	39	54
SiO_2-msg/CNTs	540	665	641	30	28

It is possible to verify that the samples SiO_2-dep/CNTs and SiO_2-imp/CNTs, in addition to similar mass loss, also have T_i and T_p with very close values. However, this is not valid for the W parameter measured values. The higher W parameter value obtained for the impregnated (SiO_2-imp/CNTs sample) method due to oxidation occurring at higher temperatures would reveal the presence of some CNTs with higher thermal stability among the synthesized carbon structures. Such observation could induce higher performances of the synthesized hybrid materials for some applications when using such a catalyst incorporation method. On the other hand, the SiO_2-msg/CNTs sample presents oxidation events occurring for other temperature ranges, indicating that different carbon structures have been deposited during the CCVD synthesis.

Considering all differences presented between the samples, as identified in the SEM and TEM images, as well as in the XRD, Raman, and TGA analysis, it is evident that the iron catalyst incorporation when using the co-condensation sol-gel method modified significantly the carbon deposited structures in term of morphology and quality. These variations are presented according to their characteristics associated with the graphitization degree and thermal stability.

To investigate better the variation in thermal stability of the synthesized MWCNTs using the different catalyst incorporation methods, a thermal analysis study was carried out. Several works already employed such thermal analysis as a tool to evaluate the quality and integrity of deposited carbon materials synthesized by CCVD. As mentioned by Lehman *et al.* (2011), highly crystalline MWCNTs are more resistant to oxidation compared to other forms of carbon. Bom *et al.* (2002) and Ratkovic *et al.* (2014), in turn, mention that different defects in the MWCNT structure, have different reactivity at a higher temperature in the oxygen atmosphere compared with MWCNTs without (or with few) defects.

First, the DTG curve in the range from 540 to 685°C was deconvoluted for each sample, to identify possible differences in the oxidation profile. The deconvolutions were performed with two sub-peaks represented by Gaussian functions with position and W parameter numerically optimized to minimize the difference between the experimental curves and the sum of the simulated peaks. Figure 5.25 shows the results of these deconvolutions for each sample, considering the adjustments with and their residual values. Peak 1, at lower temperatures, would represent carbon nanotubes with a low degree of graphitization and a high number of defects, as well as amorphous carbon. On the other hand, Peak 2, at higher temperature values, would be associated with carbon nanotubes with a high graphitization degree and low amount of structural defects, due to its greater resistance to oxidation according to Lehman *et al.* (2011) and Gallego; Batiot-Dupeyat; Mondragón (2013). The curve “sum” represents the sum of the peak 1 and peak 2 curves.

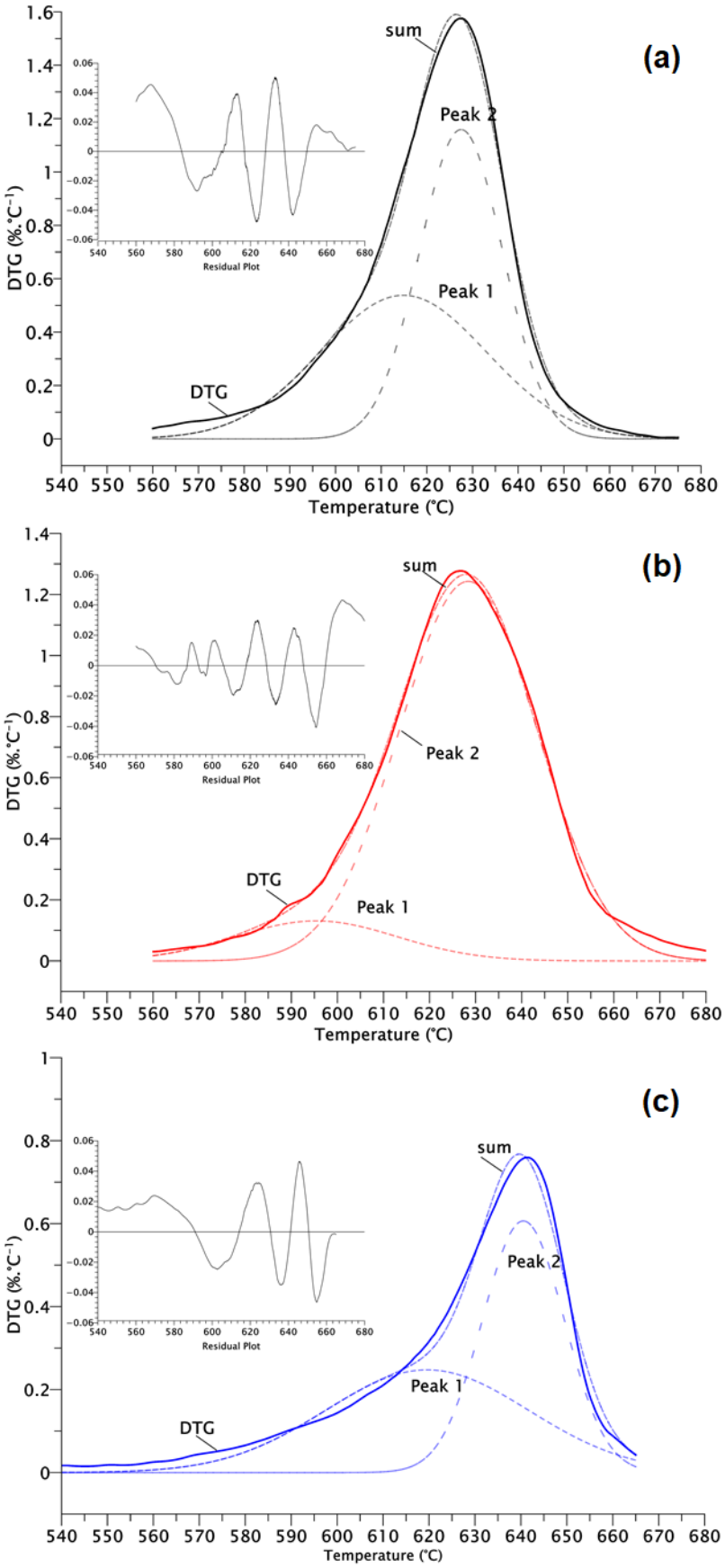

Figure 5.25 – DTG profiles and their Gaussian deconvolutions in two peaks for the (a) SiO_2-dep/CNTs, (b) SiO_2-imp/CNTs, and (c) SiO_2-msg/CNTs samples – Second stage.
Legend: Original DTG profile (—); Deconvolution curves (- - -); Sum of the two peaks (---).

According to Figure 5.25, it is possible to see that the sample SiO_2-imp/CNTs (Figure 5.25b) present a deconvolution where Peak 1 has the smallest area under the curve. As mentioned previously, this peak at a lower temperature would correspond to the presence of carbon structures with more defects or amorphous carbon materials. Still concerning the SiO_2-imp/CNTs sample, it is also possible to verify a better adjustment of the Gaussian related to Peak 2 with the original DTG profile. Such behavior would mean that the sample has a greater homogeneity. For the SiO_2-dep/CNTs and SiO_2-msg/CNTs samples, it seems evident that Peak 1 has a more significant area under the curves. This fact suggests the presence of higher proportions of defectives MWCNTs, MWCNTs with big diameters, and carbon structures with a low graphitization degree, or amorphous carbon materials. Table 5.4 summarizes the data extracted from the DTG deconvolution curves.

Table 5.4 – Summary of data related to the deconvolution analysis performed on the DTG curves obtained for the SiO_2/CNTs samples – Second stage.

Sample	Mass Loss* (%)	after the DTA deconvolution			
		Peak	T_p (°C)	Mass Loss** (%)	Percentage*** (%)
SiO_2-dep/CNTs	52	1	615	18	34.6
		2	627	34	65.4
SiO_2-imp/CNTs	54	1	595	11.5	21.3
		2	628	42.5	78.7
SiO_2-msg/CNTs	28	1	620	13	46.4
		2	640	15	53.6

* Full mass loss registered by TGA
** Data obtained through the sinusoid deconvolution of the TGA profile, considering the T_p values of each sub-peak.
*** Percentage relative to the mass loss after the deconvolution, in the function of mass loss obtained from TGA.

The literature reports that the combustion process of MWCNTs in the ambient atmosphere is a first-order reaction, as cited by Gallego; Batiot-Dupeyat; Mondragón (2013). Thus, an Arrhenius analysis can be conducted for this kind of material. According to Santangelo *et al.* (2011), MWCNTs possess higher thermal stability when higher energy (Activation Energy - E_a) is necessary for its oxidation. Moreover, the crystalline arrangement influences the kinetics of the oxidation

reaction. Besides, Gallego; Batiot-Dupeyat; Mondragón (2013) mention that the E_a increases for MWCNTs with a small number of defects. Thus, such evaluation was made to corroborate the results obtained from the SEM and TEM analyses with the Raman and TGA characterizations. For each sample, the apparent oxidation energy (E_a) of the deposited carbon structures was calculated from the Arrhenius *plots*, considering a linear fit of the experimental data. The E_a calculations were performed using the Pyris Kinetics software (Perkin Elmer), in the temperature range from 500 to 585°C.

Figure 5.26 exhibits the graphical results of the Arrhenius kinetic analysis. Considering that the E_a is proportional to the line slope, it is possible to verify that the E_a for each sample decreases in the following order: SiO_2-imp/CNTs, SiO_2-dep/CNTs, and SiO_2-msg/CNTs. Literature references present E_a values in order of 200-300 kJ.mol^{-1} for MWCNTs and graphitized carbon materials, as shown by Muradov; Smith; T-raissi (2005), and Santangelo *et al.* (2011), while in this work all materials present values close or higher than 400 kJ.mol^{-1}. Such a response could result from the massive presence of mesoporous silica used as support, which would improve the oxidation resistance of the carbon materials, increasing the activation energy, as reported by Shayed *et al.* (2016).

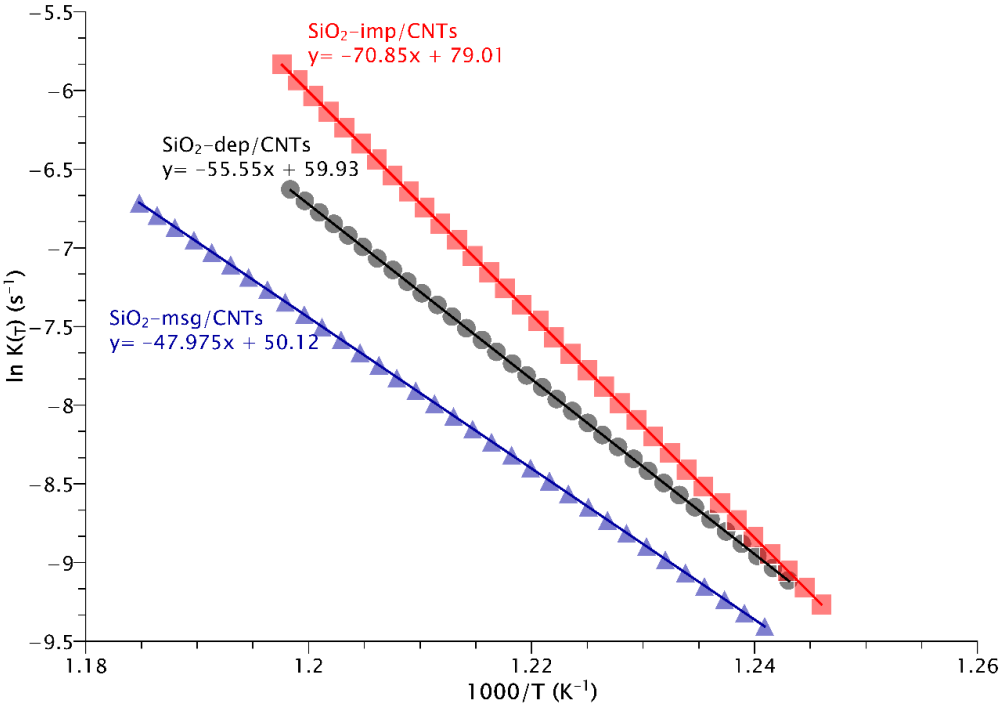

Figure 5.26 – Arrhenius plot of the thermal degradation kinetic analysis – Second stage.

5.4.6. Discussion of the second stage results

Table 5.5 summarizes the results related to the characterizations carried out in this stage.

Table 5.5 – Summary of the most relevant data extracted from all characterizations performed on the hybrid composite materials – Second stage.

Sample	SEM or TEM	Raman	TGA	DTG deconvolution		Arrhenius analysis
	Mean diameter (nm)	I_G/I_D ratio	Mass Loss (%)	Peak	Relative mass loss (%)	Ea ($kJ.mol^{-1}$)
SiO_2-**dep**/CNTs	59.9 ± 24.5	1.17 ± 0.19	52	1	34.6	461.79 ± 20.14
				2	65.4	
SiO_2-**imp**/CNTs	57.2 ± 19.3	1.48 ± 0.89	54	1	21.3	588.47 ± 26.85
				2	78.7	
SiO_2-**msg**/CNTs	104.0 ± 40.3	1.11 ± 0.03	28	1	46.4	398.81 ± 11.04
				2	53.6	

Considering all performed analyses, the results, and the considerations presented, some aspects can be imputed about the influence of the catalyst incorporation method used in the synthesis of n-SiO_2/carbon nanotube hybrid.

The co-condensation sol-gel method (msg) to incorporate the iron catalyst in the silica support resulted in different deposited carbon structures. Besides, carbon nanotube (with a mean diameter of about 104 ± 40.3 nm), graphite sheets, and platelet carbon nanofibers (PCNFs) were observed in TEM and SEM images. These carbon structures have a low graphitization degree, which is in agreement with the Raman analyses suggesting a low I_G/I_D ratio (about 1.11). The mass loss of this sample indicates that the yield of deposited carbon was much lower than the other hybrid materials synthesized. The TGA analyses also indicate a higher amount of deposited carbon structures with low thermal resistance for this sample (46.4%), as indicated by the percentage corresponding to Peak 1 of the deconvolution. The presence of carbon structures with low thermal resistance is corroborated by a low E_a value (398.81 ± 11.04 $kJ.mol^{-1}$) when compared to the values obtained for the other samples.

According to Santangelo *et al.* (2011), the energy necessary for the oxidation reaction always decreases with a decreasing aromatic ordering of the carbon network. The iron oxide cluster formation decurrent to the co-condensation sol-gel catalyst incorporation method adopted and the calcination performed should be responsible for the deposition of different structures like graphite sheets and PCNFs. As shown in Figure 5.16b, a Fe agglomeration by diffusion process seems to lead to the large hematite particle formation which in turn could impair the growth of CNTs with good quality. Similar behavior was reported by Martin-Gullon *et al*. (2006) and Awadallah *et al.* (2016).

About the SiO_2-dep/CNTs and SiO_2-imp/CNTs samples, the morphology of the carbon structures seems initially similar when taken into count the MWCNT mean diameter (around 60 nm) measured from the SEM images, and the carbon yield (mass loss around 52-54%). But, evaluating the TEM images, it is possible to identify different carbon structures deposited over the n-SiO_2 (support). Indeed, the SiO_2-dep/CNTs sample presents MWCNTs with defects in their structure and the incidence of laminar structures, like graphite sheets.

In the case of the SiO_2-imp/CNTs sample, these occurrences are less frequent, and the MWCNT structures seem better defined. By X-ray analysis, the interplanar distance of the graphitic sheets is close to the ideal value of graphite structures (0.335 nm). The small difference between SiO_2-dep/CNTs (0.364 nm) and SiO_2-imp/CNTs (0.355 nm) values with the literature (0.335 nm) may be related to a geometric artifact due to the curvature of the crystalline MWCNT structures, as reported by Ci *et al.* (2001).

Wang *et al.* (2007) discuss that the Fe-based catalyst has a weak interaction with the SiO_2 support, and this would favor the formation of catalyst clusters and their reshaping during the CNT synthesis. Considering this hypothesis, and in agreement with the results obtained, it is considered that the catalyst incorporation method employed influences the support-catalyst interaction, resulting in various deposited carbon structures of the final silica/CNT hybrid material. Such differences are more evident when comparing the I_G/I_D ratio and the percentage of carbon structures with higher thermal stability. Even with equivalent MWCNT diameters, the SiO_2-imp/CNT sample tends to have a higher

I_G/I_D ratio and activation energy than the ones of the SiO_2-dep/CNT sample. This can be explained by a better graphitization degree and lower defect density of the synthesized CNTs when using the impregnation method to fix the catalyst on the silica support.

Indeed, an increase in I_G/I_D ratio could result from an increase in the number of sp^2 bonds, as reported by Sekhar *et al*. (2014). Moreover, carbon nanotubes, and carbon structures in general, with better graphitization present more resistance towards thermal oxidation, as discussed previously, which is related to the graphitic ordering.

Corroborating all aspects discussed, Figure 5.27 presents an illustration of the physical events that occurred from the iron-based catalyst incorporation up until the produced hybrids with different features, before and after the CCVD process, and the consequent variations in MWCNT growth mode and deposition of other carbon structures.

Before the CCVD process, it is possible to verify, from the EDS-SEM maps, differences in the iron (from catalyst) distribution over the silica particles. In the SiO_2-dep sample, it is observed a iron atoms concentration in specific points, which is related to the trapping of the synthesized hematite particles on the mesoporous silica support. Concerning the SiO_2-imp and SiO_2-msg samples, the iron atoms are well distributed over the silica. These aspects are illustrated in the models of Figure 5.27, with the catalyst represented by the different red dots, with different sizes and positions over the silica supports. In agreement with the different methodologies used, the iron atoms should be located on the surface of the support for the impregnation method, and in the bulk of the silica particles when the sol-gel method was used.

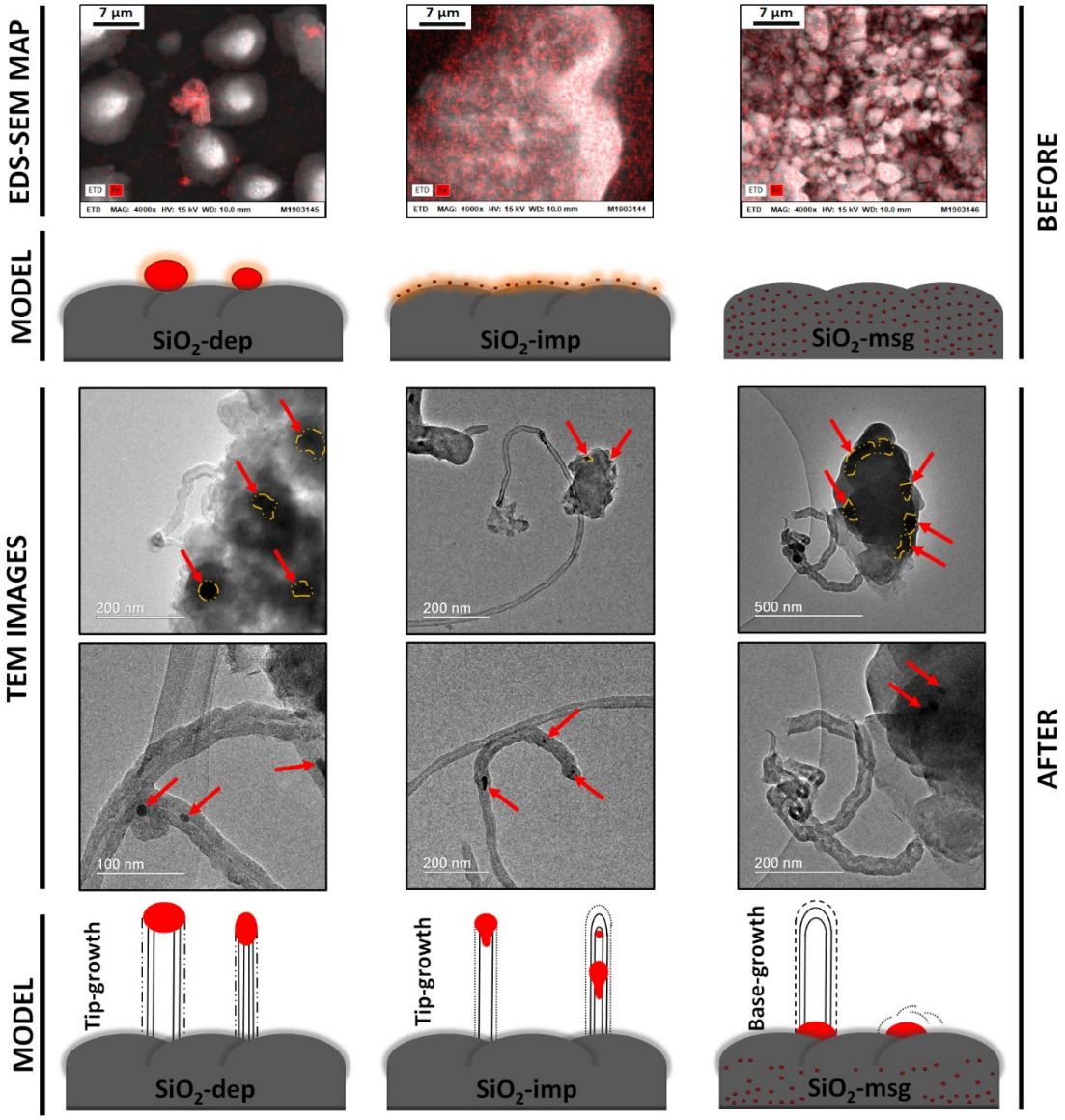

Figure 5.27 – Influence of the catalyst incorporation method on the support (n-SiO_2) /catalyst interactions before and after the CCVD process – Second stage.

Corresponding to the stage after the CCVD process, TEM images show the catalyst positions and concentration over the silica (dark regions indicated by the arrows), as well as some catalysts, present inner carbon nanotubes. For the SiO_2-dep sample, it is possible to see “big” particles over the support and inside some CNTs, with circular and elliptical shapes. This was observed by Ratkovic *et al*. (2014), which mentioned that the metal particles embedded in the interior of the tubes are probably part of the original metal clusters attached to the support where the growth process began. Based on this, it is reasonable to propose that the tip-growth mode occurred preferably.

For the SiO_2-imp sample, small catalyst particles were formed over the silica, and later, after the CNTs grows, the tip-growth mode also occurred, with changes in the catalyst shape. In both cases, the catalyst in the form of hematite must have prevented the iron cluster formation. Homma *et al*. (2003) discuss that during the CCVD process, hematite nanoparticles are reduced to Fe, but their particle diameter is different because Fe_2O_3 nanoparticles do not agglomerate, while Fe nanoparticles tend to form clusters. It is possible to infer that, after the catalyst reduction, in the SiO_2-dep and SiO_2-imp samples, the support-catalyst (Fe) interaction was weak and the tip-growth mode prevailed, as reported by Kutteri *et al*. (2018), with different catalyst sizes and shapes due to the previous different hematite particles size.

However, in the SiO_2-msg sample, initially, the catalyst particles were inside the silica matrix, and later, during the CCVD process at high temperature, the Fe atoms probably diffused providing the formation of iron clusters. Since such diffusion phenomenon is kinetically difficult, superficial diffusion must have been predominant (WANG *et al*., 2007), forming such cluster preferentially at the surface of the sílica support, but keeping a high interaction with the sílica. Therefore, a favorable condition to the base-growth mode, with CNTs with large diameters, and the deposition of other carbon structures, occurred. Considering the cluster formation, these conditions are in agreement with Yeoh *et al*. (2013), which mentioned that in a reduced atmosphere, a catalyst with a strong metal-support interaction can have an adverse effect due to the low reducibility of oxide species, obstructing the carbon nucleation and continuous growth of CNTs.

Thus, these results would suggest a better quality of the CNTs for the synthesized hybrid when the impregnation (imp) catalyst incorporation was used. Consequently, possible better performances of such hybrid composites can be achieved when they are added to reactive powder concrete.

5.5. LARGE SCALE HYBRID (n-SiO_2/CNTs) PRODUCTION – Third stage

With the chosen suitable support and with the defined catalyst incorporation method, the characterization of the hybrid synthesized on a large-scale is presented in this topic. In the large-scale process, a reactor with a greater capacity was used and the characteristics of the hybrid were different from the produced in the second stage. The results are related to the CNT synthesis procedure described in topic 4.1.3 and characterization methods described in topic 4.2. Corroborating the results presented in topics 5.3 and 5.4, nanostructured silica denominated n-SiO_2/pH6.5 was also chosen as support because of its particle size distribution, which compounds its structure, (according to topic 5.1.3) is in the nanometer order, in a well-distributed form. This is an important aspect concerning the particles stacking and pozzolanic reaction for the development of RPC with high performance.

5.5.1. Morphological evaluation of the hybrid

For the hybrid n-SiO_2/CNTs synthesized in the third stage, Figure 5.28 and Figure **5.29** present some SEM micrographs. In the first, it is possible to see MWCNTs randomly distributed over the silica particles, without orientation, and with different morphologies, as illustrated in Figure 5.28a and d with low magnification. Such observation can be seen better in Figure 5.28b and e with higher magnification. During the analysis, it was possible to verify that in the silica surface, some narrow CNTs were present almost in the same particle plane. A similar result was obtained by Barreca *et al.* (2007), who also used the iron oxide impregnation over the silica to grow carbon nanotubes. This detail is showed in Figure 5.28c and f, as indicated by the arrows.

In Figure 5.29 the lengths of the MWCNTs are evidenced by the SEM micrographs. Different tubular carbon structures, like carbon nano springs, can be seen as indicated by the arrow in Figure 5.29b. In Figure 5.29c, the arrow indicates a CNT with a great aspect ratio (length/diameter). Better detail about such long CNT can be observed in Figure 5.29d.

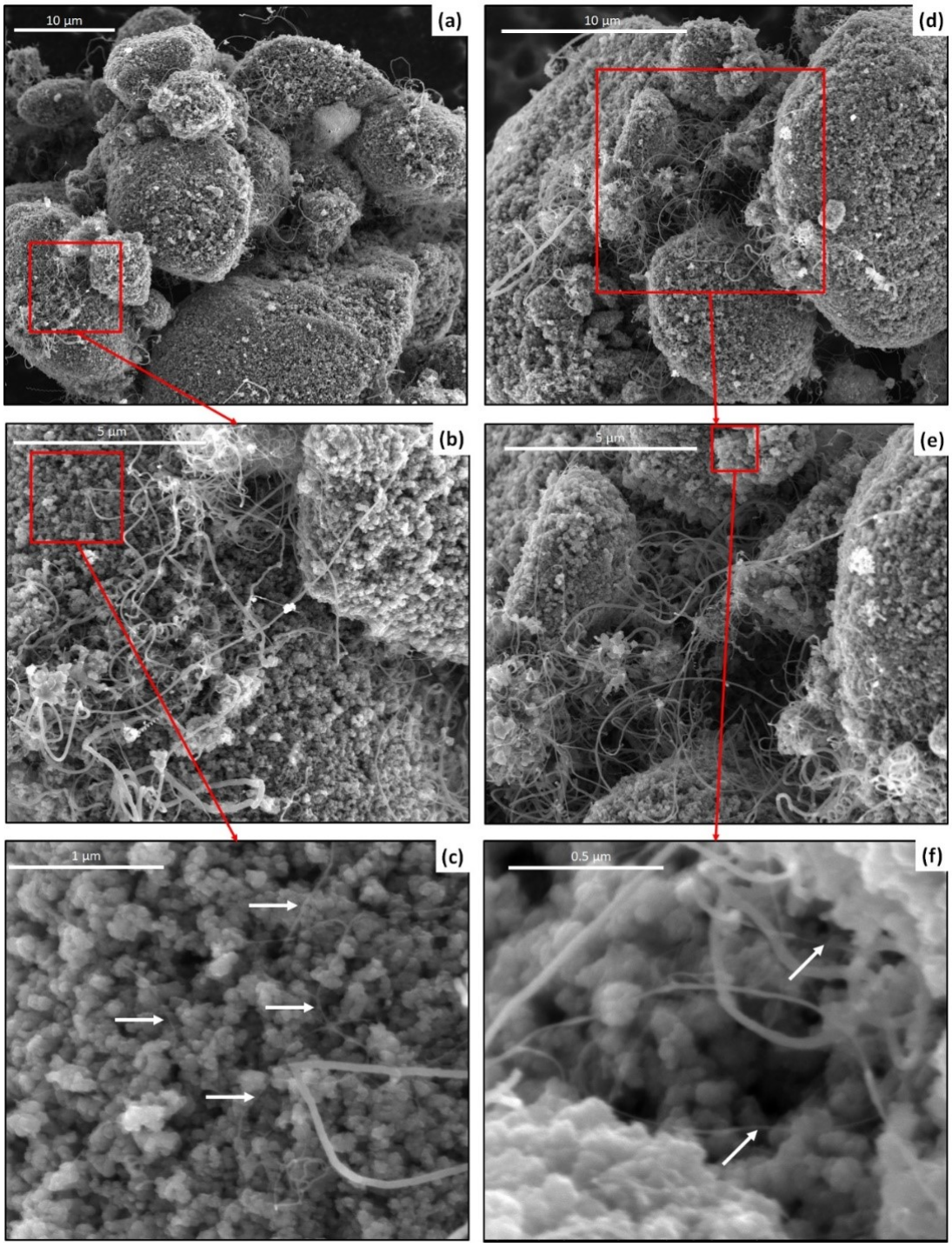

Figure 5.28 – SEM images. Hybrid produced – MWCNTs distribution over the n-SiO_2, details, and magnifications – Third stage.

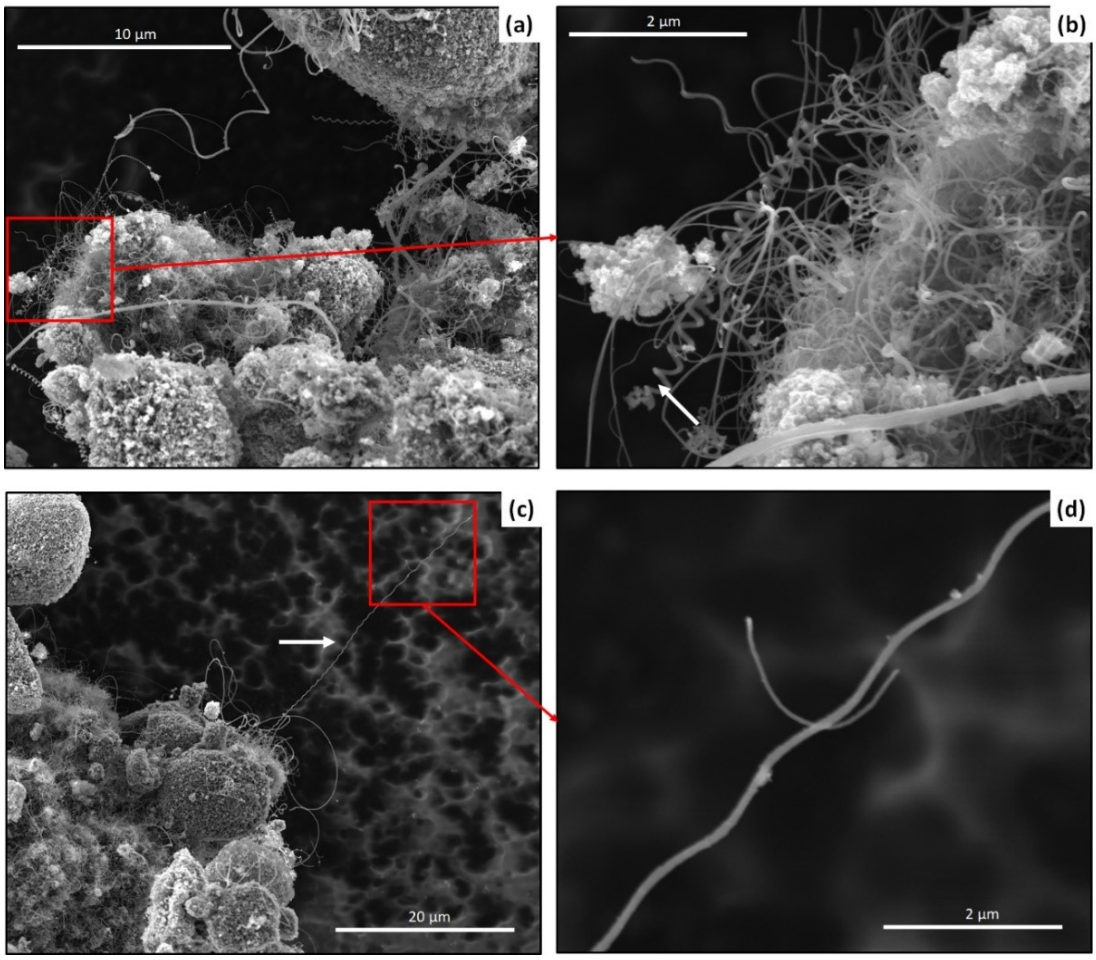

Figure 5.29 – SEM images. Hybrid produced – Morphology details of MWCNTs, details, and magnifications – Third stage.

Figure 5.30 shows with more details the carbon nanotubes structures of the hybrid using TEM microscopy. In the micrographs presented in Figure 5.30a-d, the link between the MWCNTs and the nanostructured silica is evident as well as its dispersion. In Figure 5.30e-f, CNTs with different morphologies are presented. Beyond the MWCNTs with inner and out well-defined walls (arrow and indications in Figure 5.30g-h), MWCNTs with defective walls (as shown in e) and nano springs (indicated by the arrow in f) can be seen. Also stands out the iron-based catalyst particles, which are the darker points in the micrographies.

The TEM images were used to evaluate the MWCNTs diameter distribution. As mentioned in topic 4.2.5, the measurements were performed using the software ImageJ, from images not presented in the manuscript. A total of 99 MWCNTs were measured considering their cross-section. Structures like nano springs were not used in the statistical analysis.

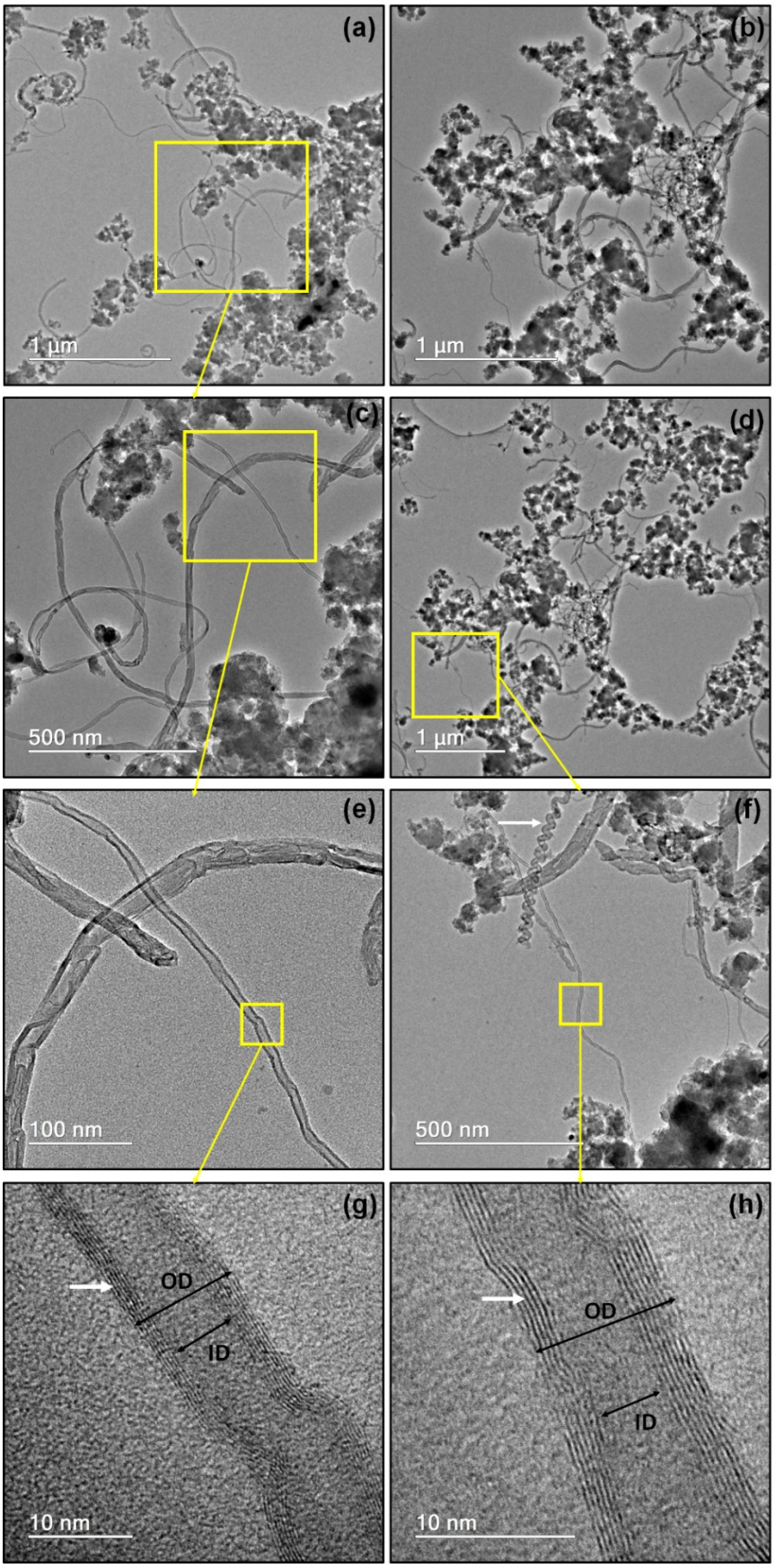

Figure 5.30 – TEM images representative of the hybrid produced in the third stage – Morphology details. (ID) inner diameter; (OD) out diameter.

The results showed a distribution of diameter with variations, but with values predominantly between 10 and 40 nm. Figure 5.31 illustrates the obtained results indicating a Lognormal[4] profile distribution (black line curve). Applying a statistical analysis, the mean diameter was found around 21 nm and the median about 17 nm. The box-plot inset in the figure shows the diameter dispersion considering the out-lines values.

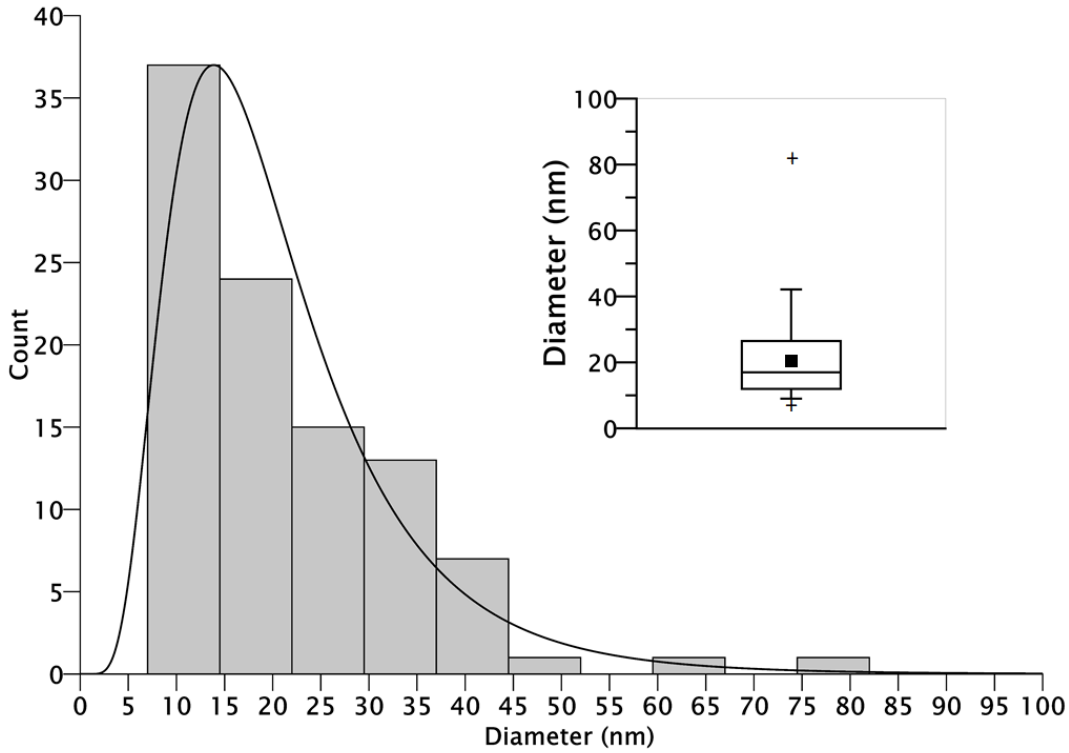

Figure 5.31 – MWCNTs diameter distribution measured from TEM images – Third stage. (■) mean; (__) median; (+) outlines

5.5.2. Raman spectroscopy analysis

As mentioned in topic 4.2.8, six Raman spectra were recorded in a sample to have representative results. Again, the obtained spectra data were fitted and normalized with the intensity of the G band (I_G). Figure 5.32 shows the Raman spectra of the hybrid sample produced on large scale. The results show well-defined peaks (around the delimited grey regions) in the range associated with

[4] A Lognormal distribution is a statistical distribution of logarithmic values from a related normal distribution.

disordered carbon or structural defects (D band), at 1280-1320 cm^{-1} and also in the G band, around 1500-1600 cm^{-1}. The peak around 2700 cm^{-1}, attributed to the overtone of the D band is evident in all spectra and is a CNT quality indication. The I_G/I_D ratio in each spectrum was calculated and the results indicate a good graphitization degree (I_G/I_D > 1) of the produced MWCNTs: in this case around 1.76 ± 0.58. This value is slightly higher than the one obtained in topic 5.4.3 (1.48 ± 0.49). This point will be discussed later. It is also noteworthy that there was an increase in the G´ band, compared to the hybrids synthesized in the first and second stages. The presence of the G´ band is indicative of MWCNTs quality and purity, according to Dileo; Landi; Raffaelle (2007).

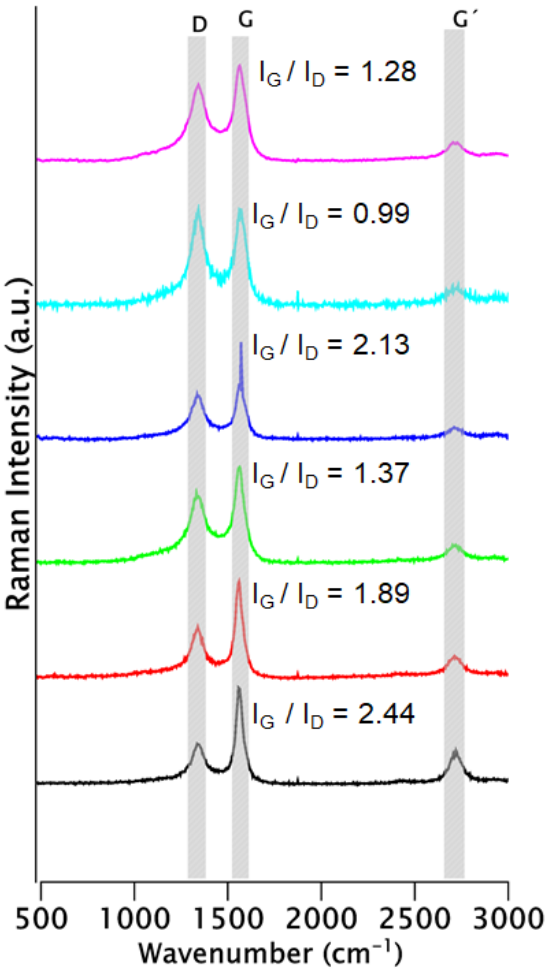

Figure 5.32 – Raman spectra of the hybrid produced – The third stage.

5.5.3. Thermogravimetric analysis

Concerning the thermal profile of the hybrid synthesized in the third stage, Figure 5.33a shows the total mass loss as a function of the temperature of the hybrid measured by thermal gravimetric analysis (TGA). In Figure 5.33b the differential thermogravimetric (DTG) profile was deconvoluted, as previously performed in topic 5.4.5. Having as a reference the mass loss profile and considering the DTG profile shown by peak 2 in Figure 5.33b, the MWCNTs yield (mass loss) was calculated considering the onset (T_i) and final (T_f) points of oxidation.

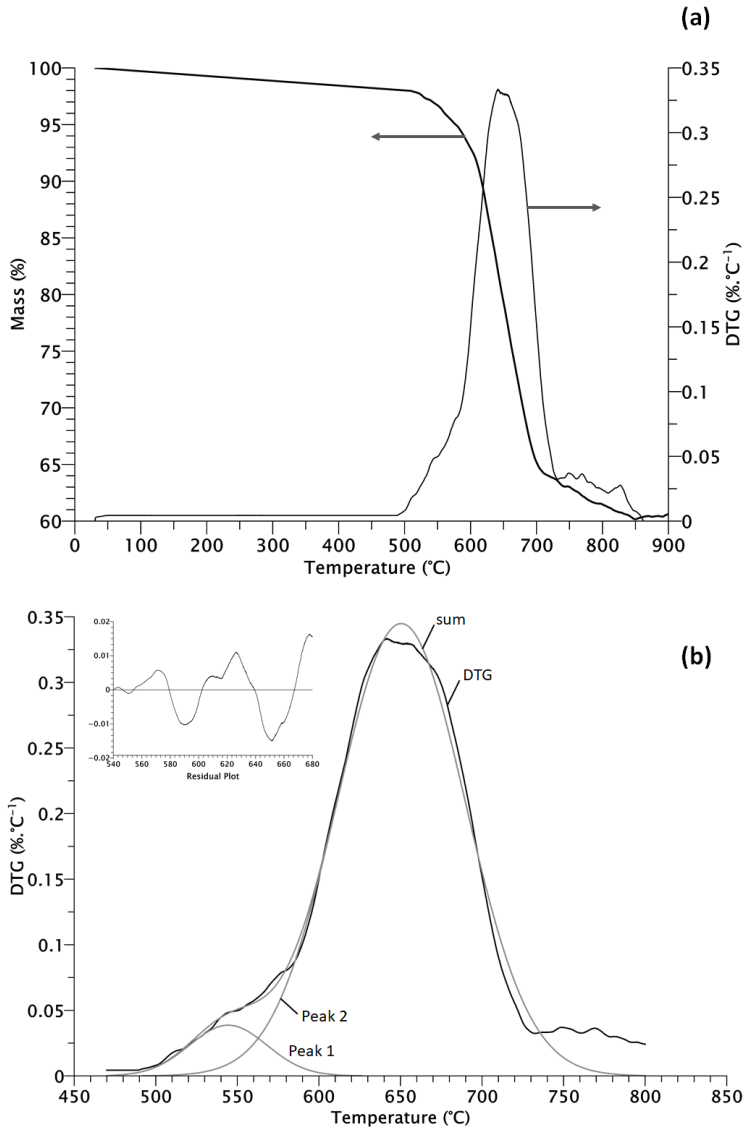

Figure 5.33 – (a) TGA and DTG profiles (b) DTG profiles and their Gaussian deconvolutions in two peaks of the hybrid produced in the third stage.

Table 5.6 summarizes the information about the oxidation events. These values will be discussed later in topic 5.5.5.

Table 5.6 – TGA results of the hybrid produced in the third stage considering peak 2 of the deconvolution – Third stage.

T_i (°C)	T_f (°C)	T_p (°C)	W (°C)	Mass Loss (%)
580	712	651	690-612 = 78	34

5.5.4. Specific surface area

As additional information, it was found, by N_2 gas adsorption analysis and applying the BET theory, that the specific surface area (SSA) of the hybrid is around 43.6 $m^2.g^{-1}$. According to the Review paper of Lehman *et al*. (2011), SSA is strongly dependent on the number of walls and the diameter of the nanotube. In general, still according to these authors, the measured surface areas for as-produced MWCNTs generally range from ≈ 10 to 500 $m^2.g^{-1}$.

It is important to highlight that these references concern pure carbon nanotubes, sometimes with catalyst impurity. But, in the case of the material in question, it is a hybrid with nanostructured silica and multi-walled carbon nanotubes.

Reduction in the SSA of silica after CNT synthesis also was observed by Othman; Kinloch; Wilkinson (2013), and can be related to the catalyst and nanotubes filling up the pores of the silica.

5.5.5. Discussion of the third stage results

The SEM and TEM images show that the MWCNTs synthesized over the nanostructure silica, developing the hybrid, in this third stage present variations in the morphology in terms of length, diameter, and form. This is an important aspect taking into account that in many composites, the CNT aspect ratio has different effects in terms of performance when the CNTs are employed in

cementitious composites, as discussed in the Literature Review (topic 3.2). Another important point that can be seen in the micrographies is the good MWCNT distribution over the nanostructured silica. This indicates that there were no preferred points to CNT growth and that the iron-based catalyst was probably well dispersed over the silica before the CCVD process.

A good graphitization degree was achieved, considering the Raman spectra showed in Figure 5.32. With the presented values, the mean I_G/I_D ratio is 1.76 ± 0.58. This variation can be associated with different morphologies, as already mentioned. Comparing this value with the presented in the topic 5.4.3 from the SiO_2-imp/CNTs sample (1.48 ± 0.89) no significant difference can be seen, but it can be an indicator of the production of CNTs with better graphitization quality.

The thermal analysis also represents well this variation. The presence of the two peaks after the deconvolution of the main peak shows different oxidations events similar to those profiles observed in Figure 5.25b. Different from the SiO_2-imp/CNT sample (topic 5.4), the hybrid produced according to topic 5.5 has a different MWCNT diameter distribution (Lognormal) with a tendency to lower values, as can be seen in Figure 5.31. In their Review paper, Lehman *et al*. (2011) present results that discuss how the CNTs morphology (diameter, length, and defects) influences the oxidation events and point out that the oxidation temperature is associated with the thermal stability of the material. In turn, this thermal stability is associated with the CNT graphitization degree, as already discussed. On the other hand, an increase in the oxidation temperature was observed when the CNT synthesis temperature was also increased, as reported by Rabbani *et al.* (2016), who worked with synthesis temperature next to the utilized in this work, around 900°C.

Thus, concerning characterizations of the hybrid produced in the third stage, a clear tendency to reduce the MWCNT diameter was observed, besides an indication of improvement in the graphitization degree due to the I_G/I_D ratio (>1) and the G´ band presence. The thermal stability may have increased due to this change. Concerning the decrease in the MWCNT yield, this can be explained by the MWCNT diameter reduction, because in a large-scale method, using a rotative reactor, the number of exposed catalyst particles is higher, and the

carbon nucleation will occur in more points. Considering the same carbon rate, the result was CNTs with smaller diameters, fewer walls, and a reduced amount of amorphous carbon deposited, which resulted in a lower carbon mass deposited over the support/catalyst.

Considering all these aspects, it is observed that the hybrid produced in this third stage has suitable features to be used in RPC.

5.6. REACTIVE POWDER CONCRETE

5.6.1. Materials employed

5.6.1.1. Cement

The chemical and physical characteristics of the Brazilian type CP-V cement, provided by the company InterCement, are summarized in Table 5.7. These are commonly presented in cement characterizations, considering the specified methods in the codes NBR 16697, NBR 7215, NBR 16372, NBR 16606, NBR 16607, NBR NM 14, NBR NM 16, NBR NM 18, and NBR NM 19 from Associação Brasileira de Normas Técnicas (ABNT).

Table 5.7 – Chemical and physical characteristics of used cement type CP-V.

Parameter	Cement sample	Brazillian codes specification
MgO	2.16 wt%	≤ 6.5 wt%
SO_3	4.07 wt%	≤ 4.5 wt%
Water content for normal consistency	34.2 wt%	-
Initial setting time	140 min	≥ 60 min
Final setting time	250 min	≤ 600 min
Blaine fineness	5,200 $cm^2.g^{-1}$	-
Loss ignition	3.42 wt%	≤ 6.5 wt%
Compressive strength		
3 days	41.5 MPa	≥ 14 MPa
7 days	45.0 MPa	≥ 34 MPa
28 days	52.9 MPa	-

Cement crystalline phases, by XRD, are presented in Figure 5.34, where the four main cement phases are identified: C3S, C2S, C3A, and C4AF. Using the software Qualx 2.0, Altomare *et al.* (2015), these phases and gypsum ($CaSO_4$) were quantified semi-quantitatively. The percentages found are presented in Table 5.8, considering the Rietveld X-ray diffraction analysis.

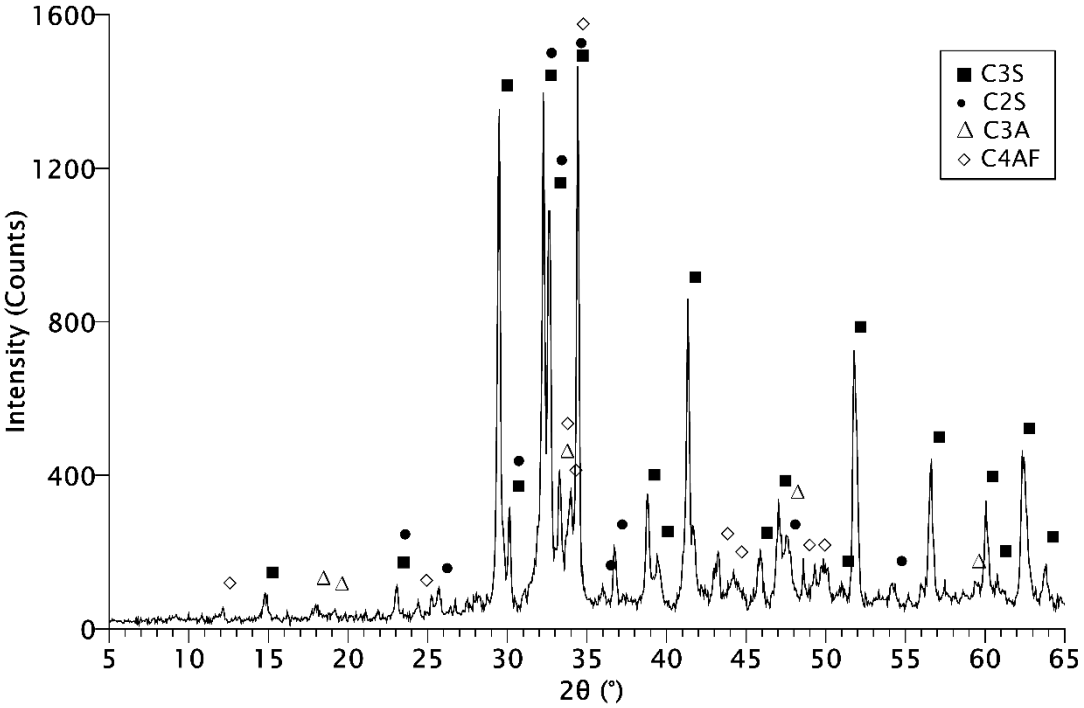

Figure 5.34 – XRD spectra cement CP-V and identification of the main phase identifications.

Table 5.8 – Semi-quantitative cement quantification phases.

Crystalline phase	Quantity (%)	Pattern reference[(a)]
C3S	54.5	00-154-0704
C2S	34.7	00-901-2789
C3A	4.1	00-901-5966
C4AF	5.2	00-100-8124
$CaSO_4$	1.5	00-153-7315

(a) Available at: https://www.crystallography.net

Concerning the cement granulometry, Figure 5.35 shows the cumulative curve for the particle size distribution in the logarithmic scale. The grain size range is between 0.1 to 50 μm, and the D10, D50, and D90 are 2.1, 10.7, and 25.4 μm respectively.

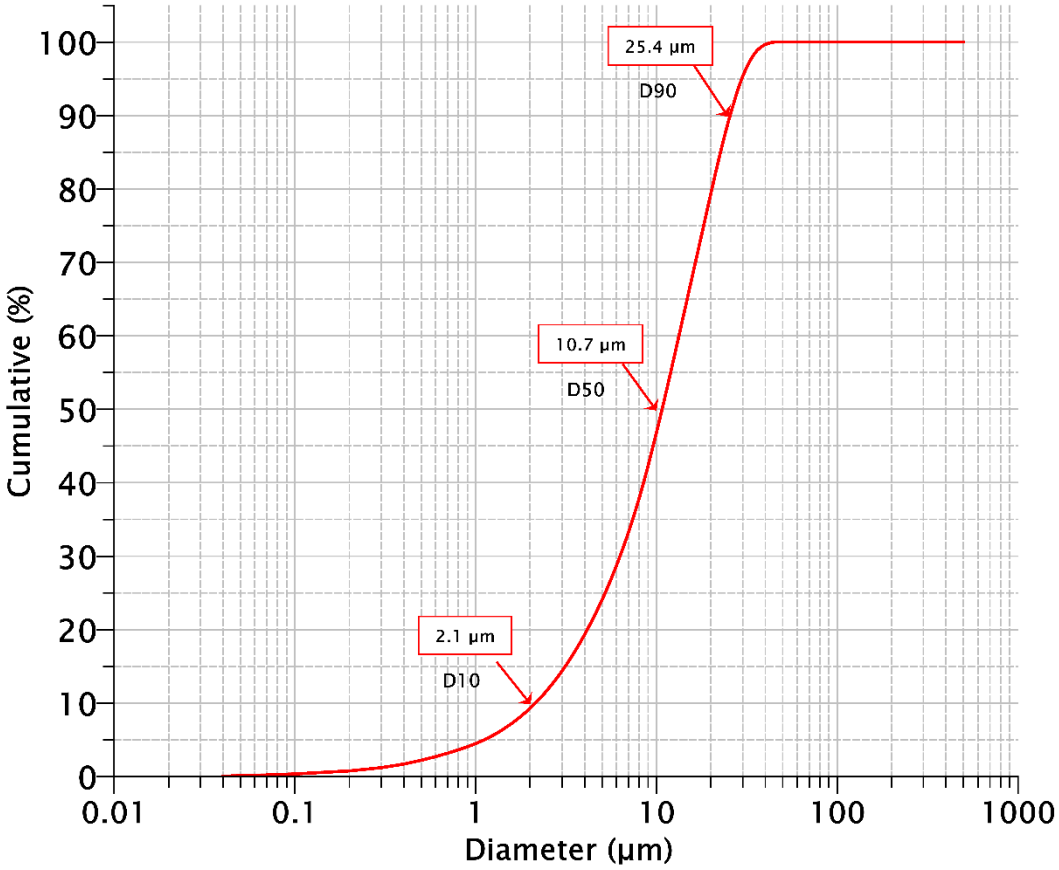

Figure 5.35 – Particle size distribution curve of the cement.

5.6.1.2. Silica Fume

According to the supplier, the commercial silica fume ("silica ativa") is an amorphous and fine powder resulting from the metal silicon manufacturing process. Their particles are spherical, amorphous, and with a diameter of around 10 µm. Their purity is more than 85%, the superficial surface area around 20 $m^2.g^{-1}$, and specific gravity equal to 2.22 $g.cm^{-3}$.

Figure 5.36 shows the cumulative curve for the silica fume particle size distribution in the logarithmic scale. The grain size range is between 0.4 to 50 µm, and the D10, D50, and D90 are 6.1, 17.1, and 29.5 µm respectively.

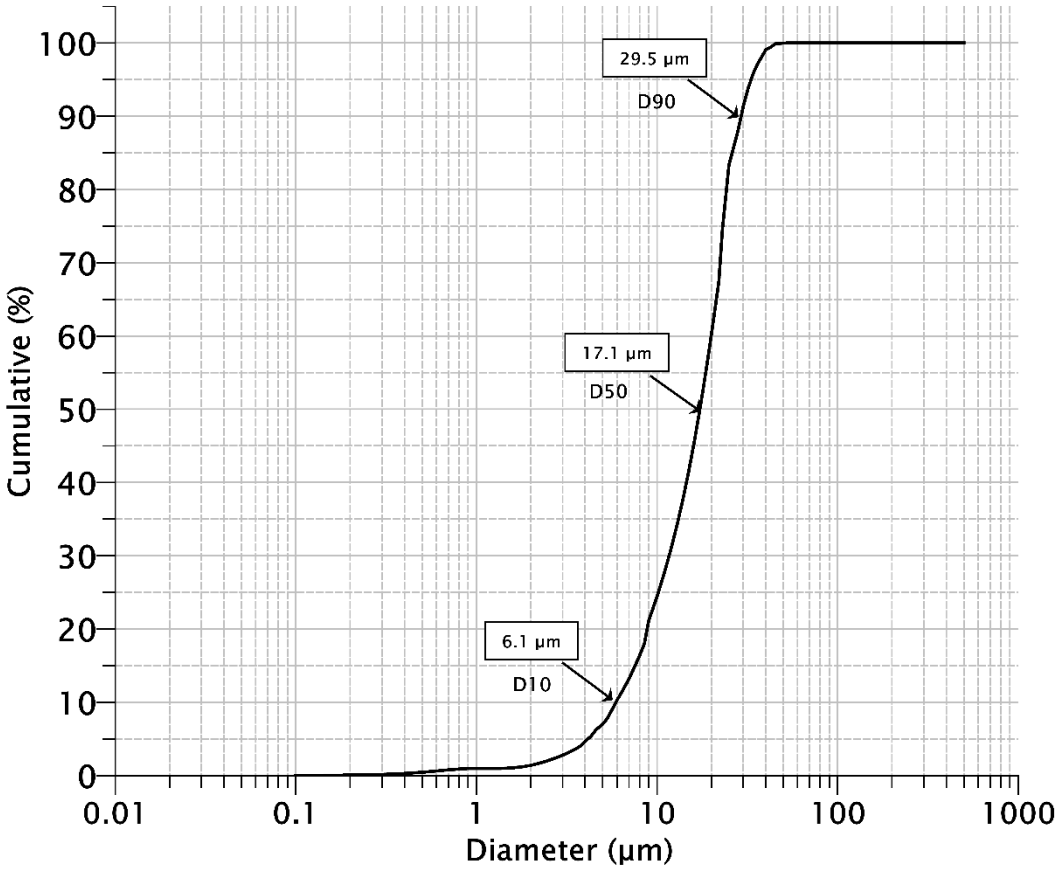

Figure 5.36 – Particle size distribution curve of the silica fume.

5.6.1.3. Superplasticizer

The ADVA 518 is a commercial superplasticizer, manufactured by GCP Applied Technologies™ and its specifications agree with the Brazilian Code ABNT NBR 11768 (2011), in the category "Tipo SP II / N/A/R". According to the provider, it is an orange liquid with a density in the range of 1.06 – 1.08 $g.cm^{-3}$.

Figure 5.37 shows representative TGA and DTG profiles of the superplasticizer where two main peaks can be seen. The first (starting at 35°C and finish close to 120°C) with a maximum of around 90°C represents the liquid mass loss with a total of around 65% (100 - 35%). From 120°C up to 334°C, a little mass loss of around 5% (35 - 30%) is present and can represent some volatile compounds. In the last mass loss stage, the peak which starts around 334°C and finishes next to 430°C is relative to the polymeric additive solids, which promote efficiently the plasticizer effects in the cementitious composites. The quantity is around 27% (30 - 3%). The final value of 3% would represent a residual

mass of some impurities. Thus, the additive solid content can be considered as 27% in mass.

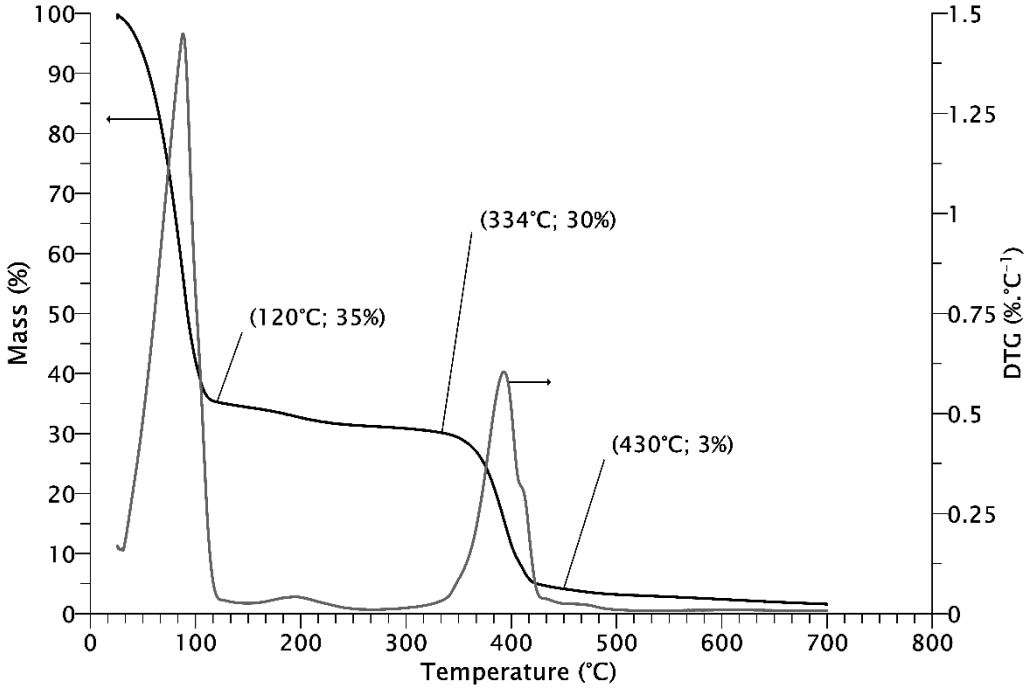

Figure 5.37 – Representative TGA and DTG of the superplasticizer ADVA 518.

5.6.1.4. Sand

The sand, provided by the “Instituto de Pesquisas Tecnológicas” (IPT) de São Paulo (lot number 45/2017), has specifications following the Brazilian Code ABNT NBR 7214 (2015). According to the supplier's technical specifications, the silica content is about 96.6 wt%, humidity equal to zero, and organic matter content inferior to 100 ppm. Table 5.9 shows the granulometric distribution of material.

Table 5.9 – Granulometric distribution of the as-provided sand.

Fraction	Retained material	Mass (%)	
		Result	Request
#16	2.4 and 2.0 mm	6	≤ 10
	2.0 and 1.2 mm	91	≥ 90
#30	1.2 and 0.6 mm	98	≥ 95
#50	0.6 and 0.3 mm	98	≥ 95
#100	0.3 and 0.15 mm	96	≥ 95

5.6.2. RPC composition and proportions

Figure 5.38 shows the particle size distribution (PSD) of each material used in the RPC composition and the optimized grading curves considering the packing model obtained from the mixed proportion of the RPC. The curves with continuous lines represent the raw materials and the dashed curves the final developed RPC (theoretical and obtained). In the figure, the left Y-axes represent the percentage of pass material, and the right Y-axes the percentage in volume composition of each material. The cumulative percentage curve (PD), considering the fraction of the total solids being smaller than size D (see equation 3.1), indicates the result of the composition using the raw materials according to its proportions, and the RPC curve the target to achieve the theoretical and optimum dense matrix.

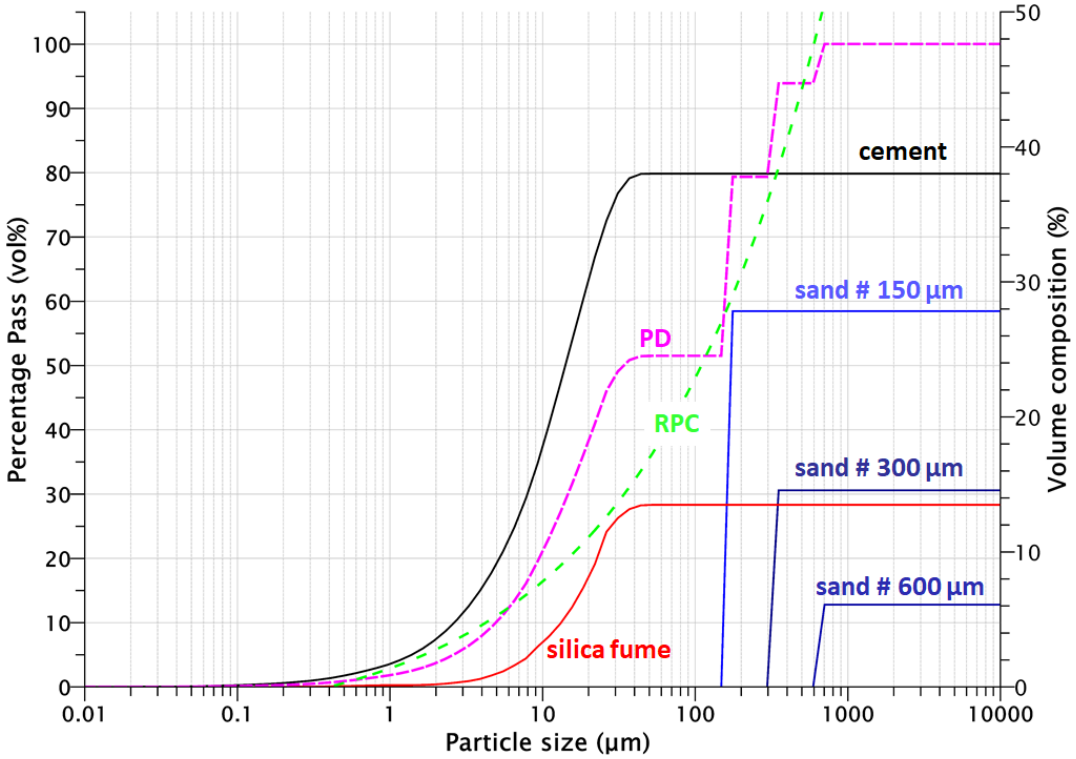

Figure 5.38 – PSDs of the materials, the target, and optimized grading curves of the RPC.

It is observed that the PD curve does not have a complete adjustment on the (theoretical) RPC curve, as expected in an optimal situation. This condition was obtained due to the real particle distribution of each raw material. For example, the fractions and the granulometric distribution of the sands are well-defined and

because of this, step curves are presented. Despite this aspect, the resultant curve (PD) presents an acceptable fit.

5.6.3. Pozzolanic effect evaluations

This topic presents the results relative to the methods employed to evaluate the pozzolanic behavior promoted by the hybrid, considering three different concentrations. As discussed in topic 4.4, the objective is to evaluate the adequate hybrid content to promote this pozzolanic effect with the generation of additional C-S-H around the n-SiO_2 particles and involving the CNTs, without harming the cement hydration process.

In the sequence, the results of the analyses are presented and discussed. For the analysis by chemical method, the definitions of the samples are presented in Table 4.5. Concerning the evaluations in cement pastes, the definitions of the samples are presented in Table 4.6.

5.6.3.1. By chemical method

Figure 5.39 shows the results of the conductivity decrease as a function of time. In Figure 5.39a, it is possible to see a conductivity decrease related to the initial ions (Ca^{2+}) adsorption over the pozzolanic material. Thus, the pure n-SiO_2 has an initial conductivity loss, a little more significant compared to other materials, which can be related to its large specific surface area (239 ± 12 $m^2.g^{-1}$) promoting greater adsorption of the ions. In the sequence, the H4% and H2% samples present an intermediary conductivity decrease, smaller than for the pure silica fume (SF), pure n-SiO_2/CNT, and H6% samples.

During the tests, it was possible to observe the agglomeration of the n-SiO_2/CNT and H6% materials, which migth have influenced directly the conductivity decrease.

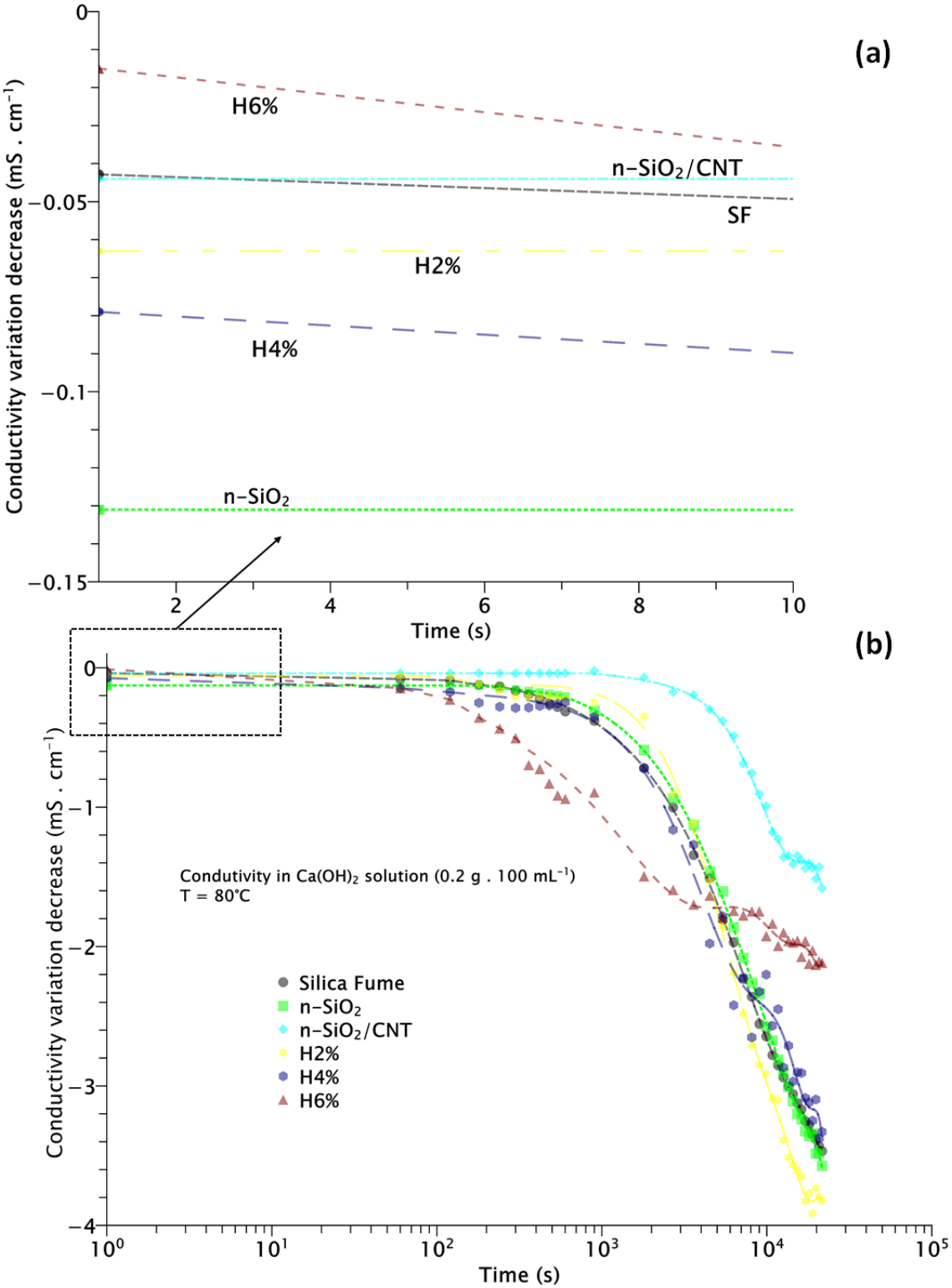

Figure 5.39 – Pozzollanic evaluation by the conductivity variation decrease in time.

Following the conductivity decrease up to around 6 h (≈ 21,600 s), the final profiles of each sample (as defined in Table 4.5) are presented in Figure 5.39b. After the initial decrease, the plateau stage represents the time necessary to diffuse the calcium ions through the superficial C-S-H layer formed initially. Then,

the events after 100 or 1000 s are due to the pozzolanic reaction occurring with the defused compounds. It is possible to see similar behavior between the samples SF, n-SiO_2, H4%, and H2% samples. This last with a final conductivity decrease slightly bigger than the others, which draw attention because at 10,000 s this sample had presented lower conductivity loss. The explanation can be related to more equilibrated Ca^{2+} adsorption and diffusion processes. Also evaluating the profiles, it is possible to see that the samples H6% and n-SiO_2/CNT presented a lower consumption of calcium ions, compared with the other samples. This indicates a lower pozzolanic effect.

5.6.3.2. By thermal analysis

Figure 5.40. shows the thermogravimetric analysis (TGA) profiles of the cement paste samples. It is possible to see that the REF sample (paste with silica fume and without the hybrid) presents greater final mass loss, followed by the H6%, H4%, and H2% samples, respectively.

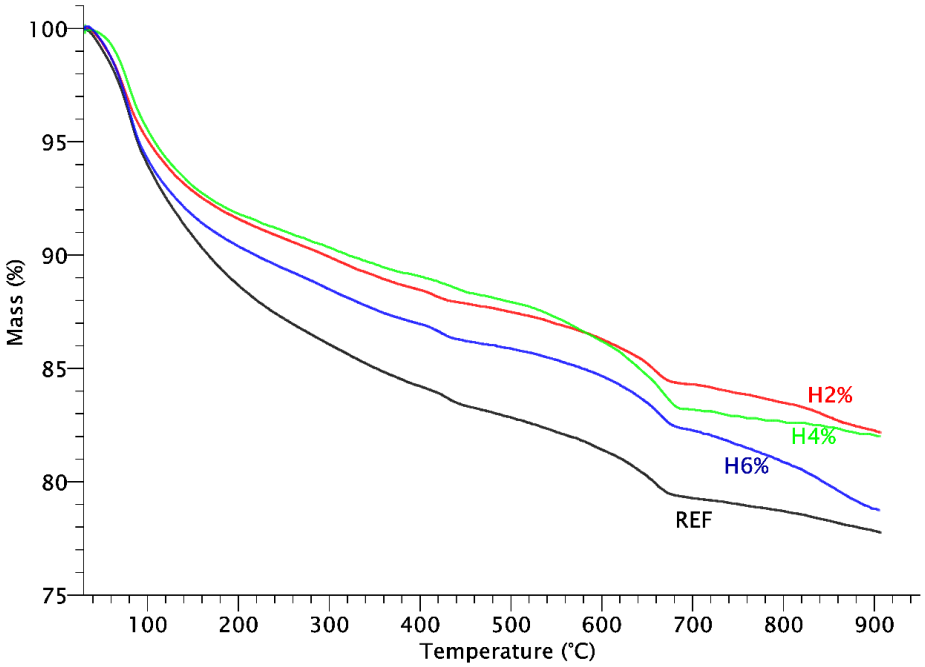

Figure 5.40 – TGA curves of the samples to pozzolanic evaluation.

For a better pozzolanic evaluation, Figures 5.41 – 5.44 show the derivative thermal analysis (DTA), and second derivative thermal analysis (dDTA) profiles

for each sample, together with their TGA curve. Considering the procedure and limits adopted by Roychand *et al.* (2016) (dotted line and values identified in the figures), Table 5.10 shows the mass loss values for each temperature. The temperatures of 30, 105, and 550°C were fixed to be considered as the initial temperature, the end of the water evaporation, and the end of the MWCNTs oxidation, respectively. As previously mentioned, the temperature ranges corresponding to the hydrated phases defined as group 1 (HP_{G1}) and group 2 (HP_{G2}) are about 60 – 250°C and 250 – 450°C, respectively. For the degradation of the calcium hydroxide (CH), the temperature range is about 400 – 500°C.

Table 5.10 – Mass loss from TGA to cement pastes in each temperature limits.

Samples	Boundaries													
	1st		2nd		3rd		4th		5th		6th		7th	
	T_a	m_a	T_b	m_b	T_c	m_c	T_d	m_d	T_e	m_e	T_f	m_f	T_g	m_g
REF	30	7.01	65	6.86	105	6.56	217	6.17	430	5.87	443	5.85	550	5.76
H2%	30	7.30	60	7.21	105	6.92	200	6.69	412	6.45	426	6.43	550	6.35
H4%	30	7.51	58	7.47	105	7.15	232	6.86	400	6.69	423	6.67	550	6.34
H6%	30	7.36	55	7.29	105	6.91	235	6.60	420	6.37	435	6.35	550	6.28

T – temperature (°C)
m – mass (mg)

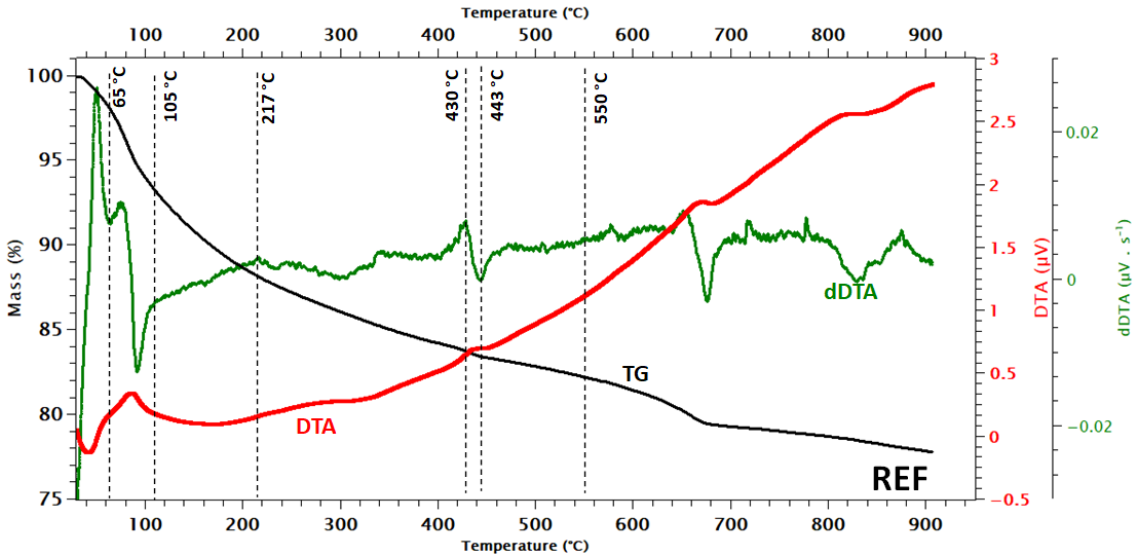

Figure 5.41 – TGA, DTA, and dDTA curves of the REF sample.

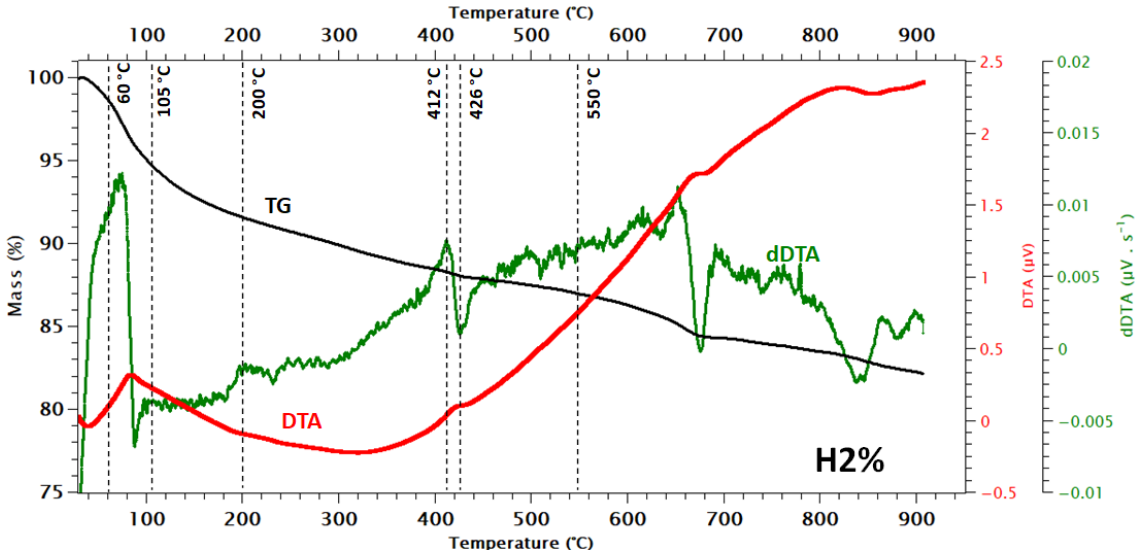

Figure 5.42 – TGA, DTA, and dDTA curves of the H2% sample.

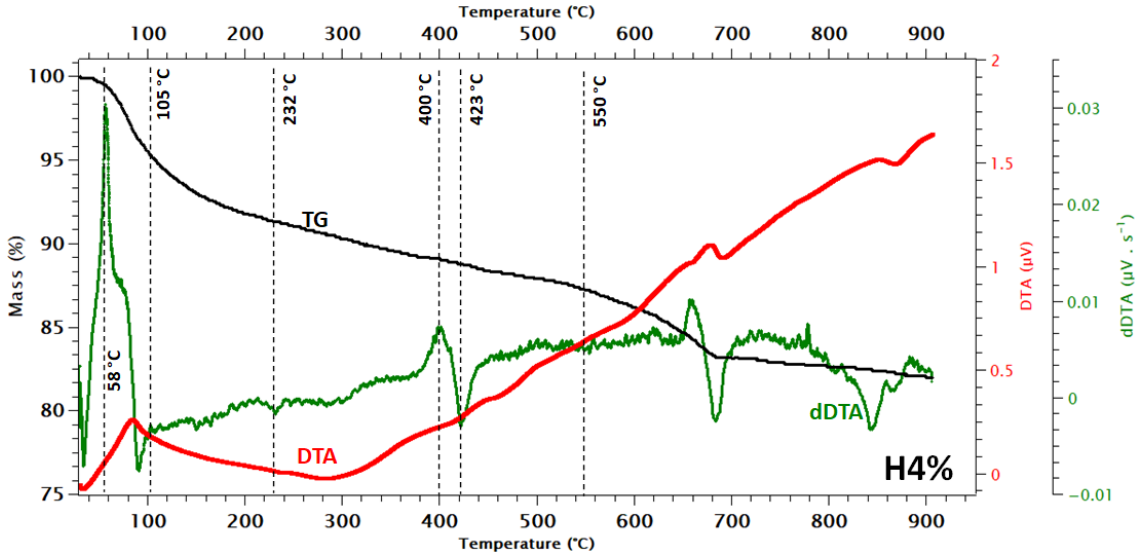

Figure 5.43 – TGA, DTA, and dDTA curves of the H4% sample.

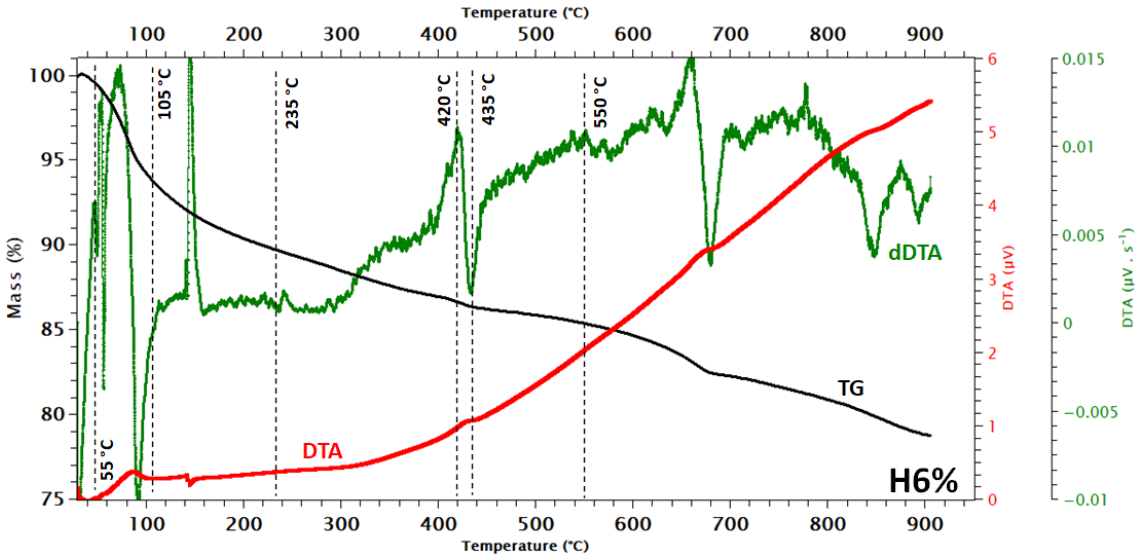

Figure 5.44 – TGA, DTA, and dDTA curves of the H6% sample.

Considering Equations 4.3 – 4.5 and the data of Table 5.10, Table 5.11 shows the percentage of hydration products in each group.

Table 5.11 – Percentage in mass, of the cement hydration products for each group considering the respective temperature range.

Samples	HP_{G1} (T_a until T_c)	HP_{G2} (T_c until T_e)	CH (T_e until T_f)
REF	12.0	5.2	1.8
H2%	8.2	3.8	1.6
H4%	9.6	2.7	1.6
H6%	11.0	3.7	1.6

It is possible to see that the sample REF presented a greater amount of hydration products (HP_{G1} + HP_{G2}) than the other samples, indicating better hydration of the paste without the hybrid.

Concerning this aspect, evaluating the influence of colloidal nano-SiO_2 (CNS – 2.5 and 5%) on the cement hydration process, Hou *et al*. (2013) based their study on the non-evaporated water (NEW) analysis to evaluate quantitatively the cement hydration. This is the same process employed in the performed analysis here, associating the mass loss at specific temperature ranges with the water present in the hydrated phases. These authors observed, an increase in the NEW content of cement paste, during the first 24 h of hydration. However, after 3 days, NEW content of the paste with CNS becomes lower than that of the control

(without CNS). The explanation, still according to these authors, was the changes in the gel (C-S-H) structure. During the polymerization process, combined water in silica chains can be released, resulting in a decrease in NEW. At an early age, this lower NEW content, compared to the control, must be due to a previous occurrence of the silicate chain elongation.

The CH content was slightly larger in the REF sample. Although the difference may not be relevant, it is important to take into account that even with less amount of silica fume, due to the replacement by an amount of hybrid, the samples with the hybrid presented a tendency to have a higher pozzolanic effect.

5.6.3.3. By XRD analysis

XRD analysis results were used to verify some aspects of the cement hydration process and calcium hydroxide (CH) formation. Figure 5.45 shows the XRD patterns obtained for the sample REF, as well as the cement pastes H2%, H4%, and H6%. It is observed that the profiles do not show significant differences and indicate that the hybrid does not produce new phases.

For comparison, the spectra of cement, and the portlandite (CH) are presented in the same figure. The main peaks of the portlandite, according to the pattern (00-900-9098), are the correspondent to the crystalline planes (001) and (101), 2θ around 18° and 34° respectively. Concerning the peaks at 18°, they cannot be identified clearly in all samples. On the other hand, the peaks at around 34° can be identified.

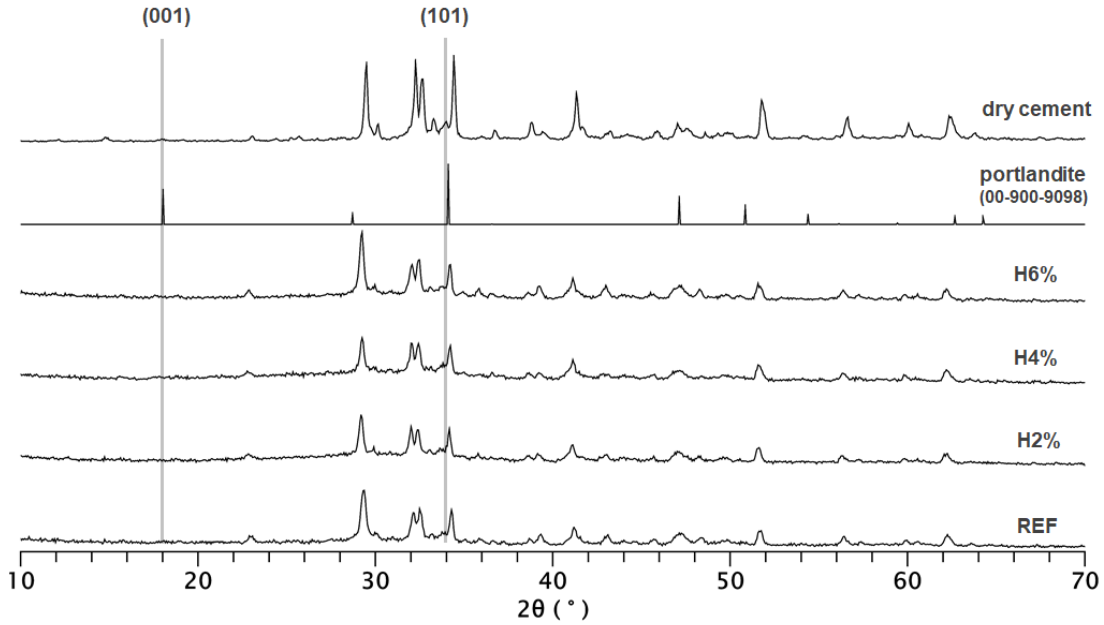

Figure 5.45 – XRD spectra of the samples and comparative with cement and portlandite.

Concerning the spectra of the hydrated cement pastes, the corresponding peaks appear to be overlapped with the ones of the anhydrous cement phases and thus, the REF spectrum is very similar to the dry cement one. This may have happened due to the low water-cement (w/c) ratio used (0.18). The hydrated cement pastes have a low hydration degree and the water necessary to promote an effective dissociation of the ions (mainly Ca^{+2} and OH^{-}) was not completely available. Anyway, this is an inherent condition to the reactive powder concretes, due to the low w/c ratio.

The results regarding the thermogravimetric analysis (topic 5.6.4.2) indicate the formation of CH. Thus, to try evaluating its structure, the crystalline orientation of CH was evaluated. This procedure was used by Qing *et al.* (2007), Cui *et al.* (2017), and Han *et al.* (2017a), and consist to obtain the index CH orientation (R), which is calculated according to Equation 5.1.

$$R = 1.35\frac{I_{(001)}}{I_{(101)}} \quad (5.1)$$

where $I_{(001)}$ and $I_{(101)}$ are the (001) and (101) crystal face peak intensities, corresponding to 2θ equal to 18° and 34°, respectively. To take into account the difference of intensities as a function of the 2θ displacement around the reference (pattern 00-900-9098) values, three values of intensity corresponding to each

plane (2θ) were obtained for each sample (spectrum) and the averages were calculated. The results are shown in Table 5.12.

Table 5.12 – Diffraction intensities and CH orientation crystal.

Sample	$I_{(001)}$		$I_{(101)}$		R
	considered values	average	considered values	average	
REF	166	179	289	367	0.67 ± 0.11
	182		357		
	188		454		
H2%	149	164	404	567	0.41 ± 0.09
	174		595		
	169		702		
H4%	180	175	424	551	0.45 ± 0.12
	180		557		
	166		671		
H6%	154	155	380	532	0.42 ± 0.12
	154		515		
	156		702		

The orientation indexes (R) show that despite the standard deviation, it is possible to verify that the REF sample presents a larger crystal CH orientation, and there is a trend to a lower CH crystallization in the samples with the hybrid, mainly in the sample H2%. These results indicate, even if modestly, that the presence of the hybrid can promote a decrease in the CH crystals, which can be directly related to the pozzolanic effect. Low intensities of these analyzed planes (at 2θ of 18° and 34°) in RPC were also observed by Zhang *et al.* (2018). This is discussed in topic 5.6.3.6.

To investigate better the hydration process, qualitatively, the magnitude of the main peaks on the unhydrated cement phase (C3S and C2S) were also evaluated. These main peaks have 2θ around 29.5, 32.2, and 32.7 °, according to the cement XRD pattern. Figure 5.46 shows these peaks in the cement and the samples, and Table 5.13 exhibits a comparison of the intensities.

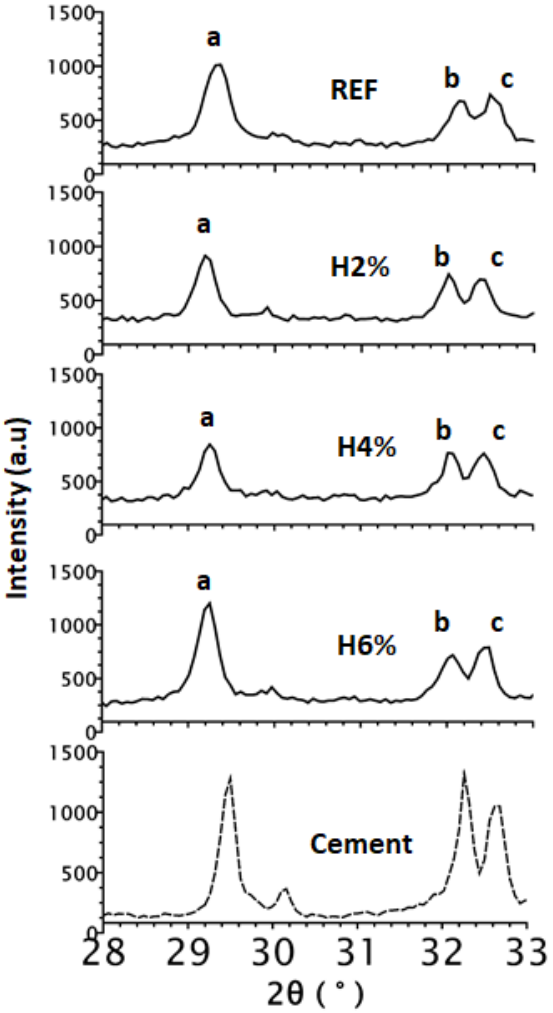

Figure 5.46 – XRD patterns of the samples and cement in the corresponding main peaks range to C3S and C2S.

Table 5.13 – Intensities of the main peaks in the range 29-33° (2θ).

Sample	Intensities		
	a (≈29.5°)	b (≈32.2°)	c (≈32.7°)
REF	1050	666	734
H2%	936	740	686
H4%	858	767	762
H6%	1267	713	795

Studying the effect of carbon nanofibers in mortars, the results presented by Fehervari *et al*. (2020) indicate that peaks in the range at 28–32° 2θ are indicative of the presence of calcium silicate hydrates (C-S-H) phases. This corroborates with the results presented in the spectra and Table 5.13.

It is observed that H2% and H4% samples present a decrease in the intensity of the 29.5° peak in comparison to the REF, indicating a better dissolution of C3S. The opposite is observed in the H6% sample, with an increase in the intensity. For the peak "c", the H2% sample presented a reduction of the intensity compared with the other samples.

The hydration process at an early age was investigated by Singh *et al*. (2015) considering the incorporation of silica nanoparticles (by sol-gel method). According to the authors, the characteristic peak of the unhydrated C3S ($2\theta \approx 32°$) gets overlapped with the C–S–H peak in hydrated samples. Still according to these authors, normally, due to the dissolution of C3S, in hydrated samples the intensity of this peak decrease in function of the hydration process. But, in the case of nano-silica incorporation, the intensity of this peak increases, indicating the formation of additional C–S–H, which is not observed in the hydrated C3S samples. Thus, compared with the REF sample, the samples with hybrid (n-SiO_2/CNT) resulted in a better answer in terms of C-S-H formation, due to the increase in the intensities of the "b" peaks.

5.6.3.4. By N_2 adsorption analysis

For the N_2 adsorption evaluations in the samples, Figure 5.47 shows the pore size (d_p) distribution, on a logarithmic scale, as a function of the volume fraction. This analysis allows verifying, indirectly, the effect of the variation of the amount of hybrid (n-SiO_2/CNT) in the cement hydration. According to Sun *et al.* (2017), changes in the pore structure were observed in cement paste due to the filling effect of nano-SiO_2, which promoted the formation of additional C–S–H due to an increased nucleation effect, and the pozzolanic reaction between nano-SiO_2 and CH. However, Mendonza, Sierra, and Tobón (2014) indicate that the synergic effect of nanosílica and MWCNTs (in excess) cannot be beneficial to the cement hydration process, and changes the dynamics of the CH formation. The MWCNT presence can absorb Ca^{2+} ions, changing the microstructure in terms of capillary pores (LI *et al*., 2020). In the curves presented in the inset of Figure 5.47, it is possible to see that the pore volume in the range 1 – 10 nm is greater in the

samples with the hybrid. This indicates a tendency to a pore refinement in the scale of the interlayer pores (< 2 nm) and gel pores (2-10 nm) due to the presence of the hybrid.

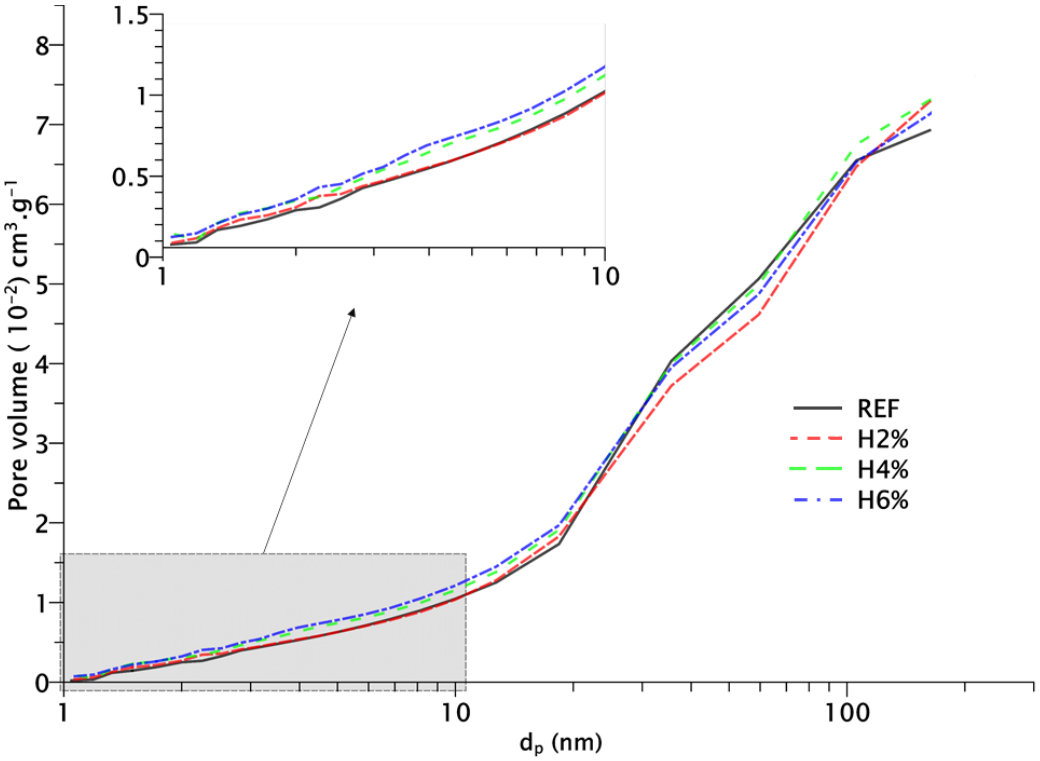

Figure 5.47 – Cumulative pore volume as a function of the pore diameter obtained by N_2 condensation for the hydrated cement pastes samples.

Figure 5.48 shows the cumulative pore volume of the samples as a function of the pore size. Concerning the interlayer pores (< 2 nm), REF and H2% samples presented the same amount of pore volume, and H4% and H6% samples presented a slightly greater quantity of pores in this range. For the gel pores (2-10 nm), no significant difference can be imputed between REF and H2% samples, and again, H4% and H6% samples presented a slightly higher quantity of pores in this range. Finally, about the capillary pores (>10 nm) no significant differences were observed.

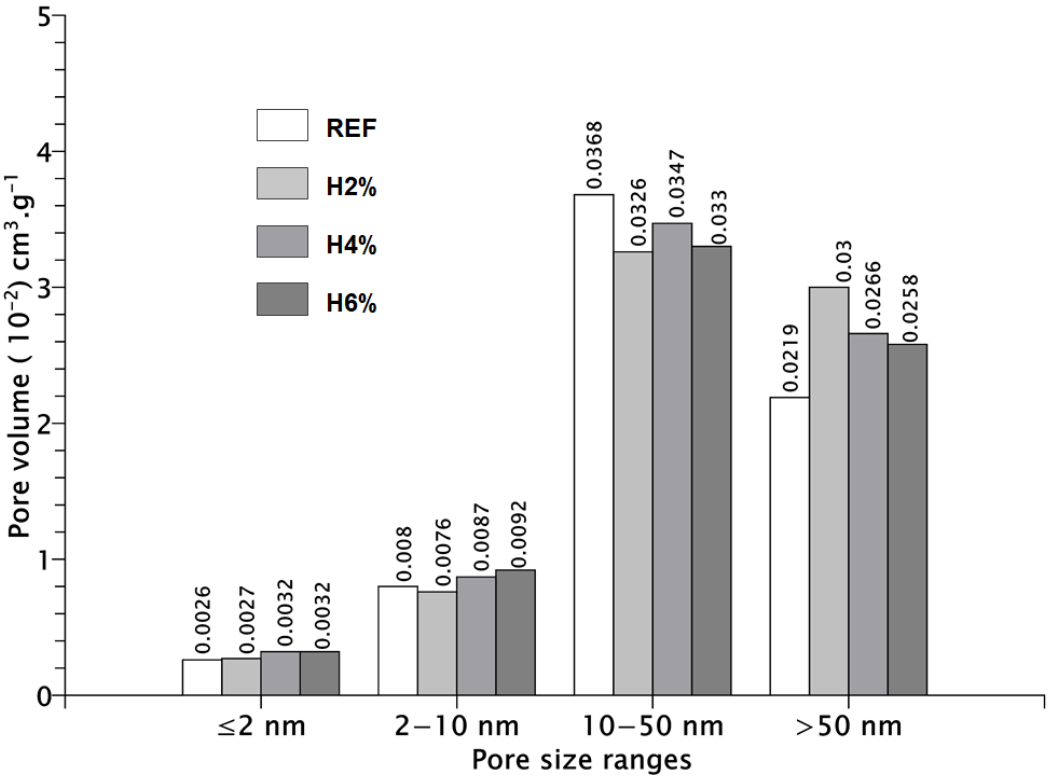

Figure 5.48 – Pore volume for each pore size range obtained by N_2 adsorption for the hydrated cement pastes samples.

5.6.3.5. By EDS analysis

For the EDS analysis, images in BSE mode were firstly performed for each hardened cement paste sample at low magnification to obtain the map in a wide region. Figures 5.49 – 5.52 show the results of the REF, H2%, H4%, and H6% samples, respectively.

From the BSE images, it is possible to see at low magnification, the aspect of the hydrated paste. In the REF and H2% samples, it is possible to see voids (dark points) and cracks with different lengths and propagation forms. These cracks may be due to the shrinkage of the cement paste during the hydration process, a common phenomenon occurring during the hydration of the cement, mainly for a high amount of cement, as mentioned by Aydin and Baradan (2013).

For the H4% and H6% samples, the cracks also are present but with lower incidence and length. The presence of voids is not significant, but in these two samples, there are large bubbles (well-defined spherical regions).

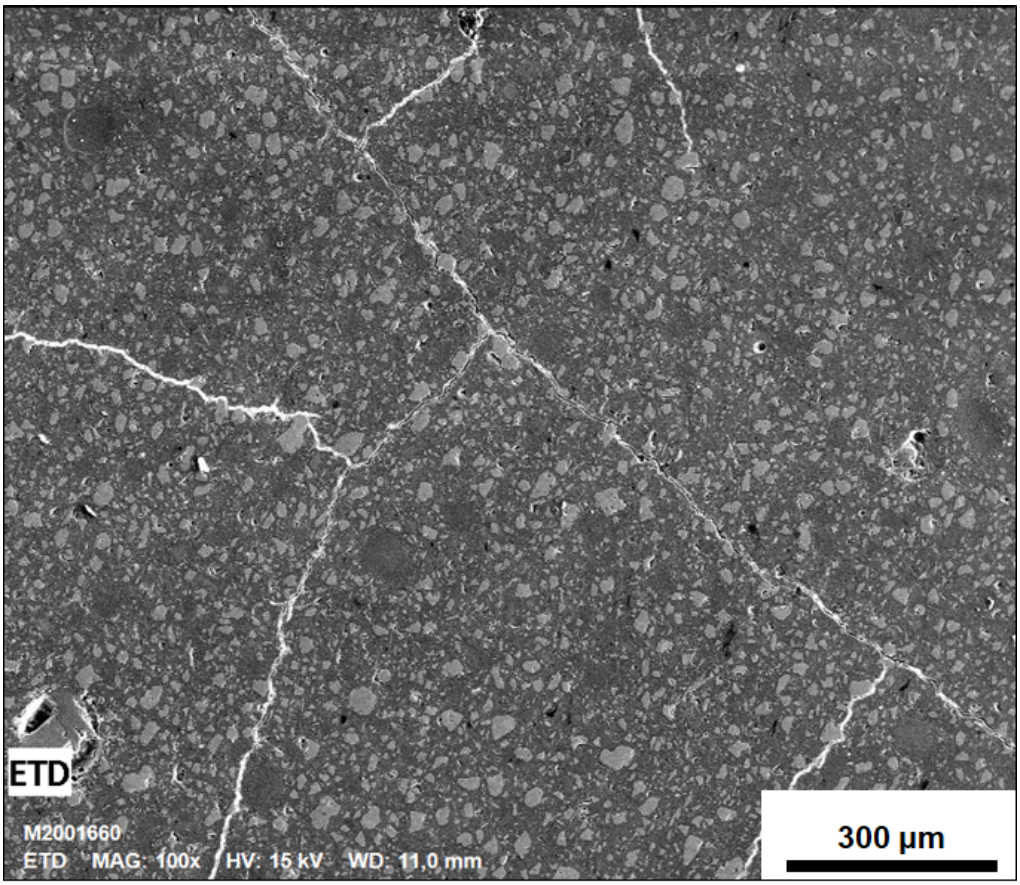

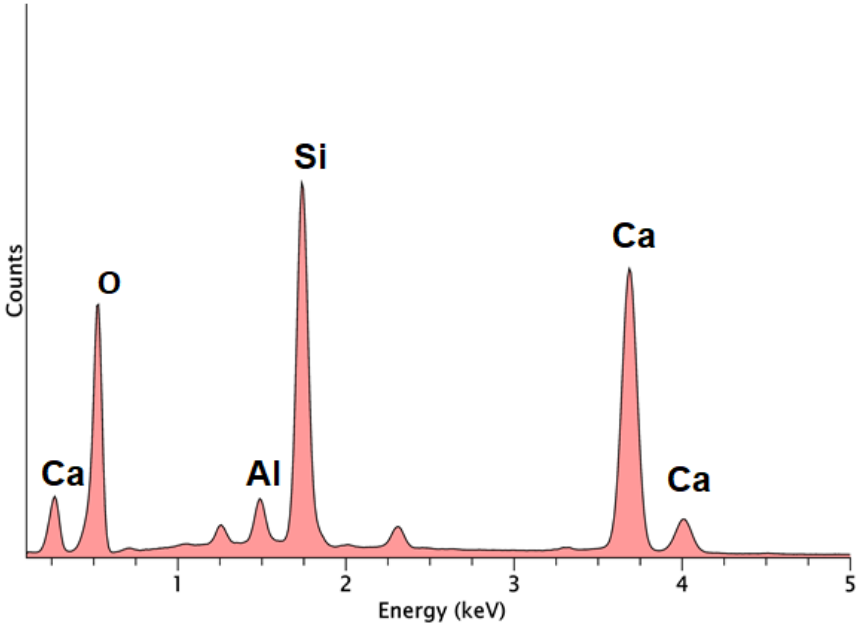

Quantitative EDS Map

Ca		Si		Al	
Atom	Std Dev	Atom	Std Dev	Atom	Std Dev
55.93	2.33	39.09	1.61	4.98	0.26

Figure 5.49 – EDS Map – REF sample.

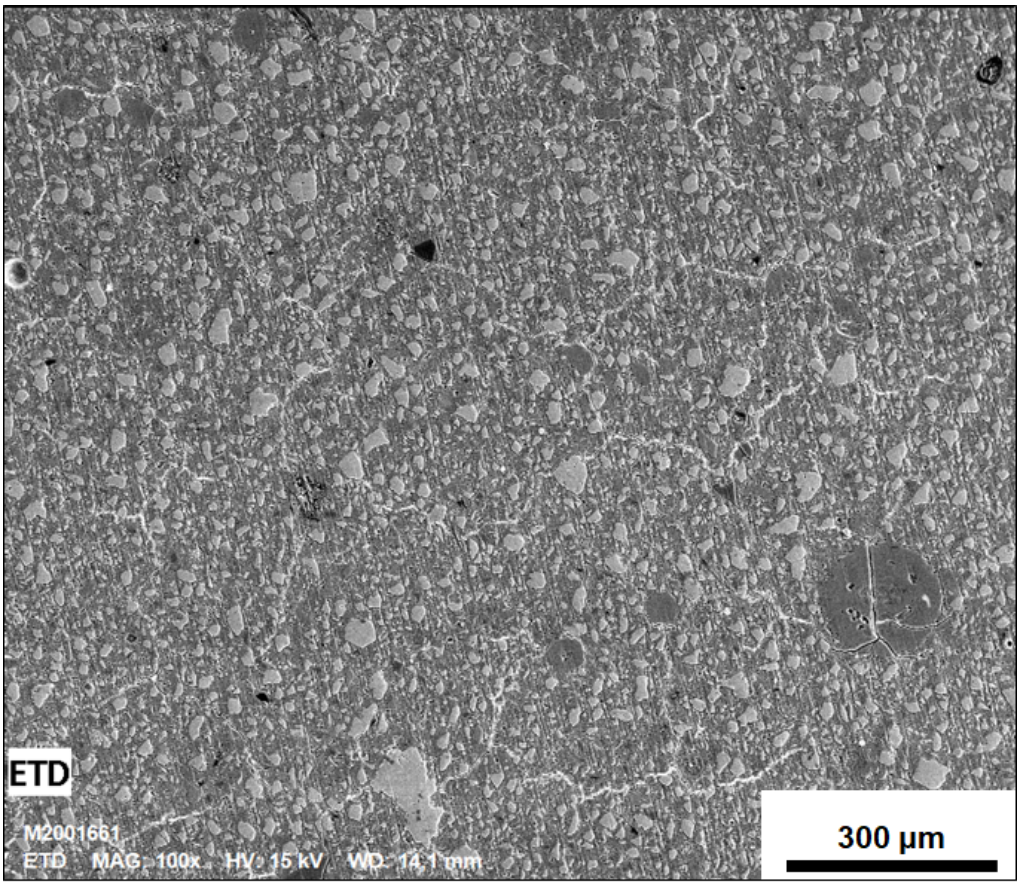

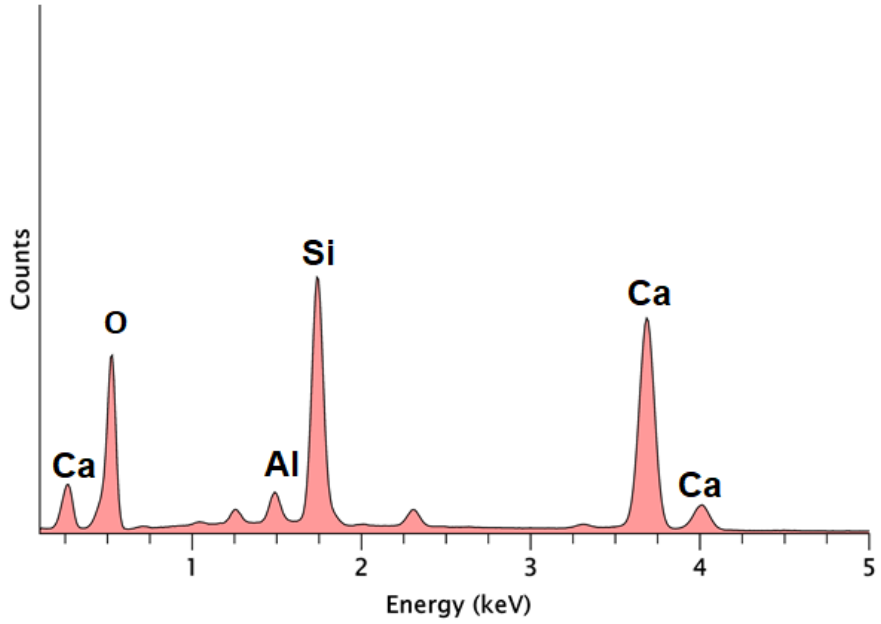

Quantitative EDS Map

Ca		Si		Al	
Atom	Std Dev	Atom	Std Dev	Atom	Std Dev
57.78	2.38	37.39	1.53	4.83	0.26

Figure 5.50 – EDS Map – H2% sample.

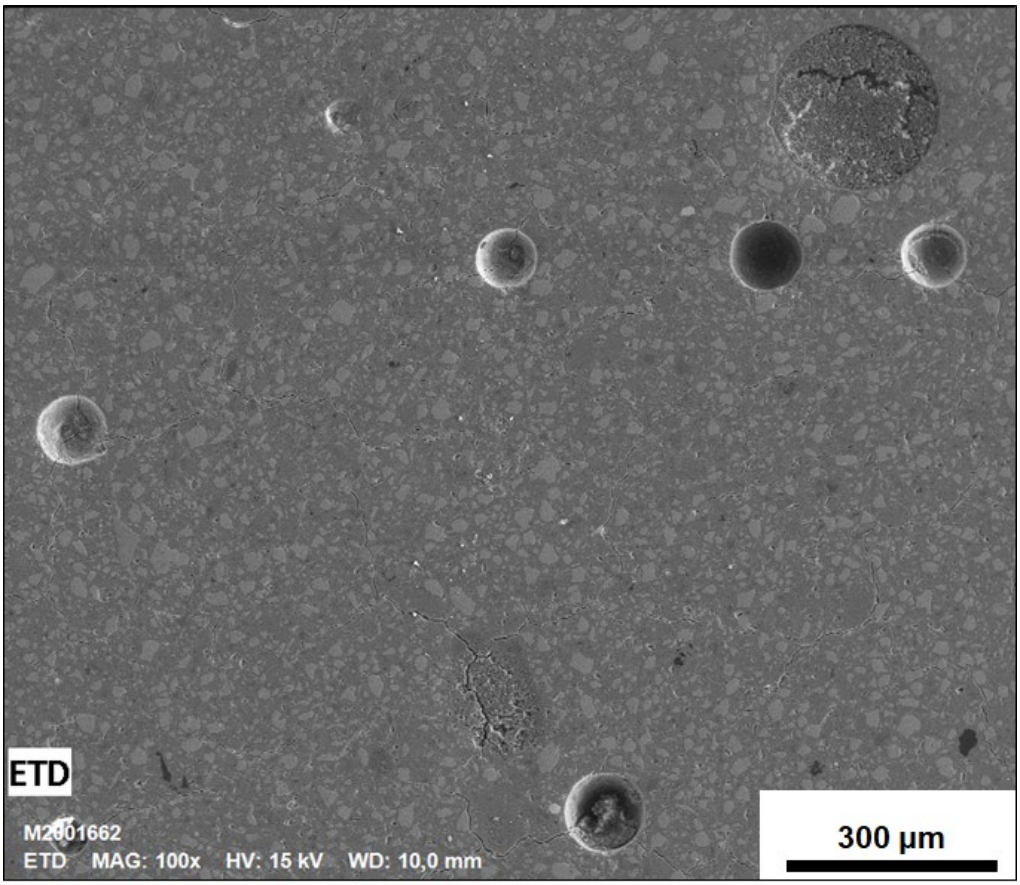

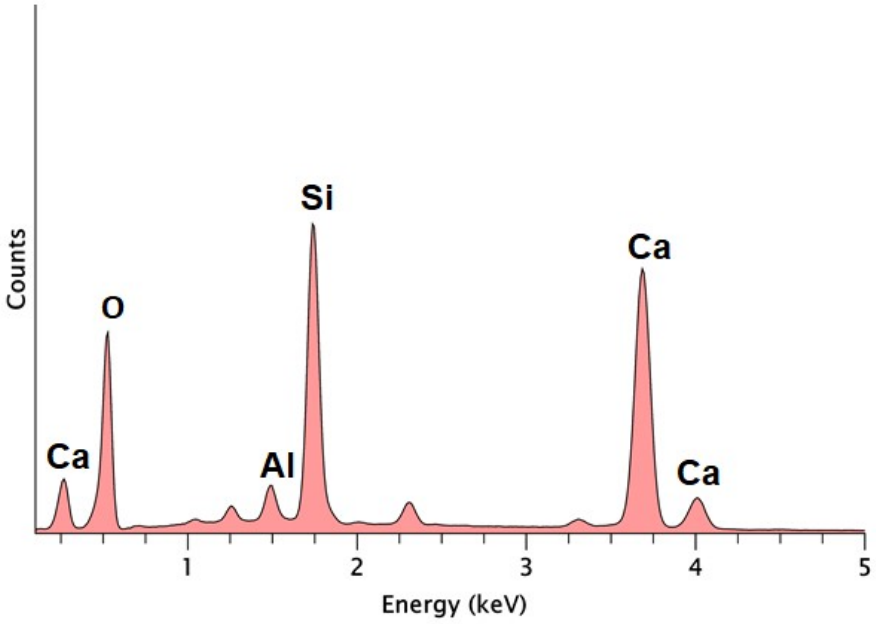

Quantitative EDS Map

Ca		Si		Al	
Atom	Std Dev	Atom	Std Dev	Atom	Std Dev
58.15	2.39	37.22	1.51	4.63	0.26

Figure 5.51 – EDS Map – H4% sample.

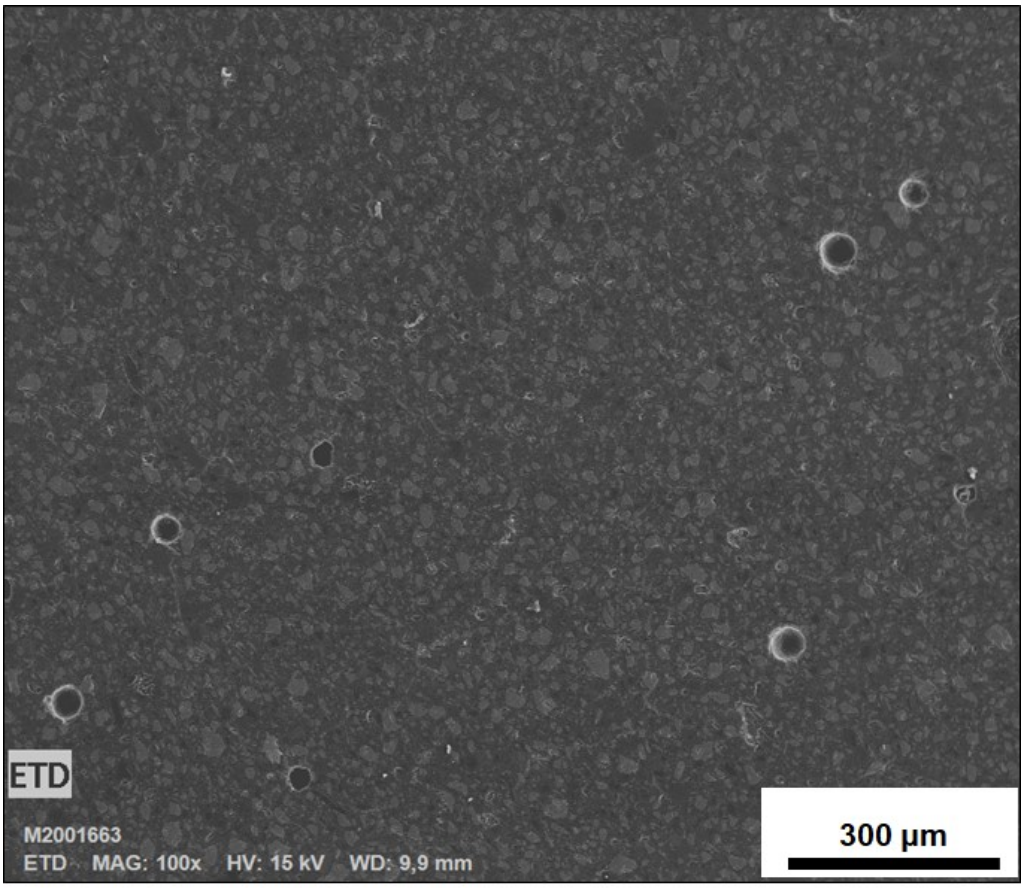

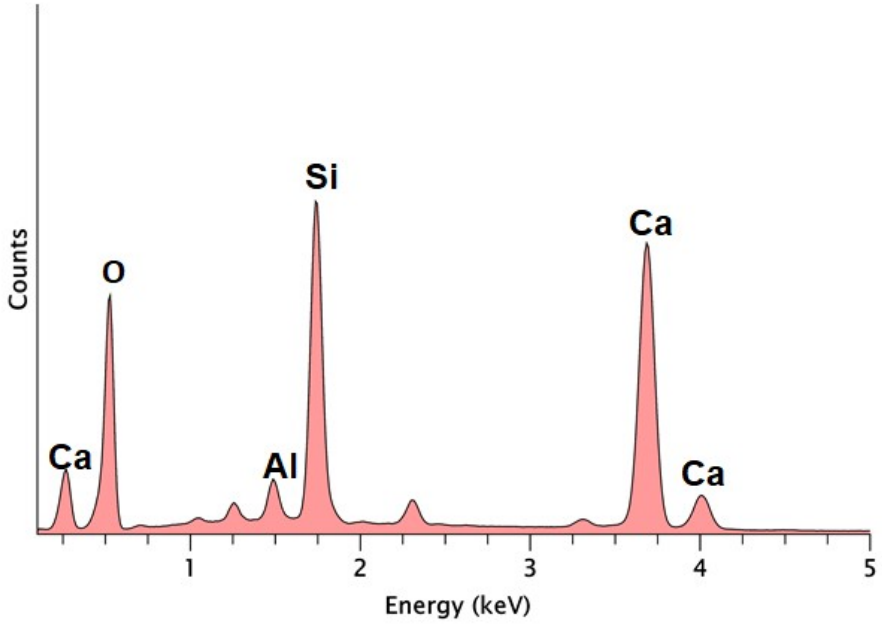

Quantitative EDS Map

Ca		Si		Al	
Atom	Std Dev	Atom	Std Dev	Atom	Std Dev
58.49	2.37	36.69	1.47	4.82	0.25

Figure 5.52 – EDS Map – H6% sample.

Considering that the presence of cracks in cement-based composites is a relevant aspect in terms of performance, a map of the cracks of each sample was created using the color contrast with the assistance of the ImageJ software. These maps can be seen in Figure 5.53.

A visual analysis of Figure 5.53 allows observing that the sample without the hybrid (REF) presents large and connected cracks. However, the samples with the hybrid show more spaced and not well-connected cracks, indicating that their propagation ways were smaller.

Figure 5.53 – Embedded RPC samples. Shrinkage cracks maps from SEM images in BSE mode treated using ImageJ software.

Then, as mentioned in topic 4.4.2.4, considering that the Ca/Si ratio is an indicator of the C-S-H quality, the presence of calcium, silicon, and aluminum was quantified to be the elements present in greater quantity in the cement hydrated phase. Considering the measured values, the means (with respective standard deviation) are presented in Figure 5.54a, and the Ca/Si ratio of each sample showed in Figure 5.54b.

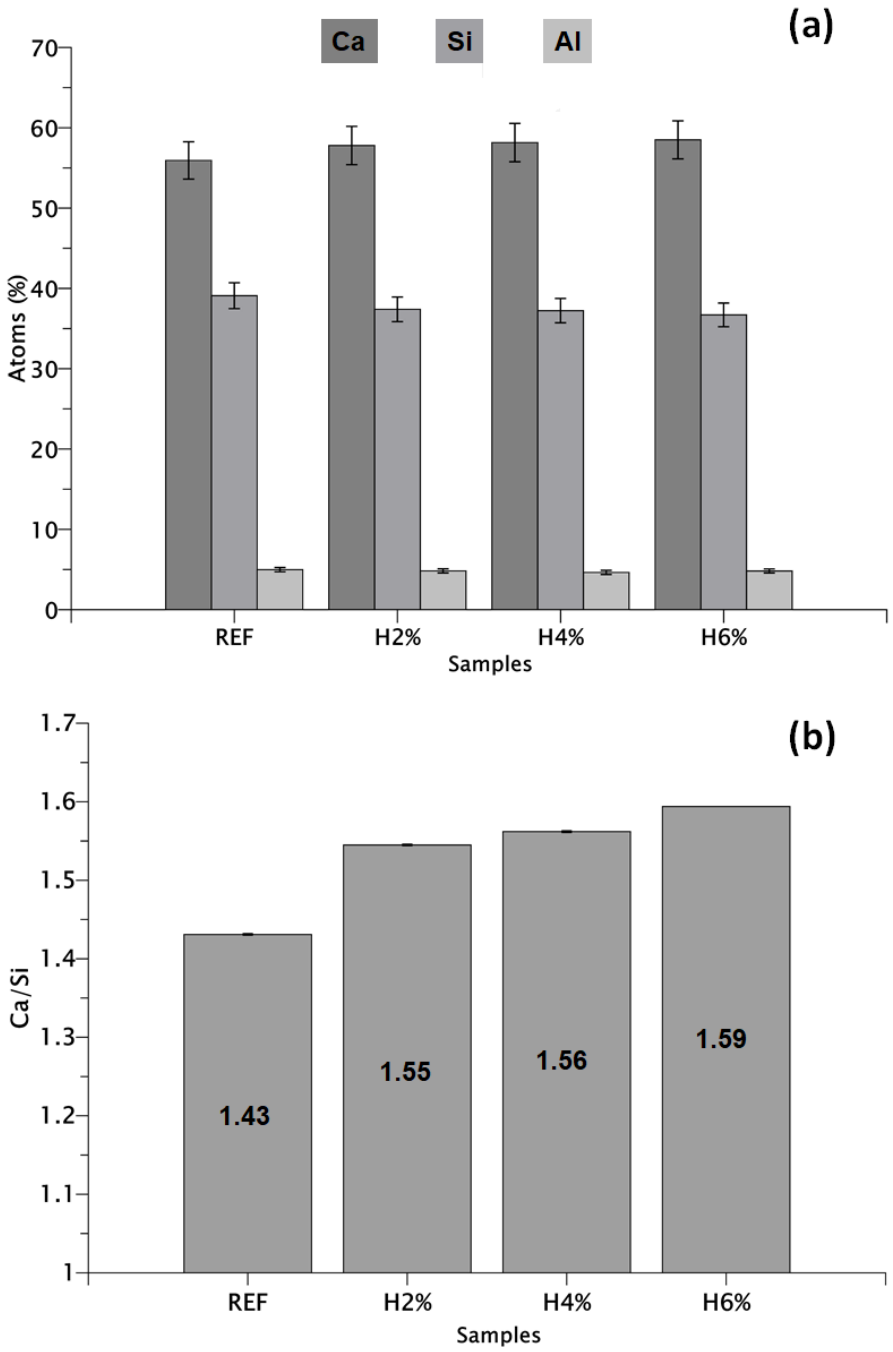

Figure 5.54 – Summary of the atomic composition and Ca/Si ratio measured from EDS-SEM analysis. (a) Ca, Si and Al percentage; (b) Ca/Si ratios.

For the Ca/Si ratios shown in Figure 5.54b, the sample REF would present a tendency to form more C-S-H, considering that a low Ca/Si ratio is characteristic of this. A decrease in the Ca/Si ratio, indicates an increase of the C-S-H formation (KUNTHER; FERREIRO; SKIBSTED, 2017).

These ratios are coherent with the proportion of compounds (cement and silica fume) present in each sample during its preparation, according to the proportions

presented in Table 4.6. It must be remembered that part of the silica fume (silicon source) was replaced in each sample with the incorporation of the hybrid, which naturally causes changes in the Ca/Si ratio.

In agreement with the objectives, specifically with the hypothesis of the formation of additional C-S-H involving the carbon nanotubes present in the hybrid, Figures 5.55 – 5.58 shows a local EDS map for the REF, H2%, H4%, and H6% samples, considering regions where it was possible to identify, morphologically, the presence of C-S-H structures in the hydrated paste.

Figure 5.55a shows a typical region in the sample REF, with the presence of hydrated structures in the cement paste. Laminar structures are present and can be identified as calcium hydroxide (CH). Studying the developed microstructure of cement-silica fume system and the C-S-H composition in RPC (w/c ratio equal to 0.4), Rossen, Lothenbach and Scrivener (2015) observed similar morphology of the CH also with a cure of 3 days. These authors mentioned that in a plain cement system, the morphology of CH is mostly as masses of CH, like in blocks, with few platelets. However, in the presence of silica fume, there is a majority of platelets. Thus, the CH morphology presented in Figure 5.55a is coherent and indicates that even if the lesser quantity, n-SiO_2 proved to more reactive in terms of pozzolanic effect.

In the inset detached (Figure 5.55b), the same platelets of CH are indicated, as well as the “mass of CH with few platelets”, C-S-H, and silica fume (SF) particle covered by some hydrated products. This region was analyzed by EDS to measure the Ca/Si ratio. The map is presented in Figure 5.55c and the atoms percentage indicated in the table in the figure. Considering the values, the ratio Ca/Si = 3.26.

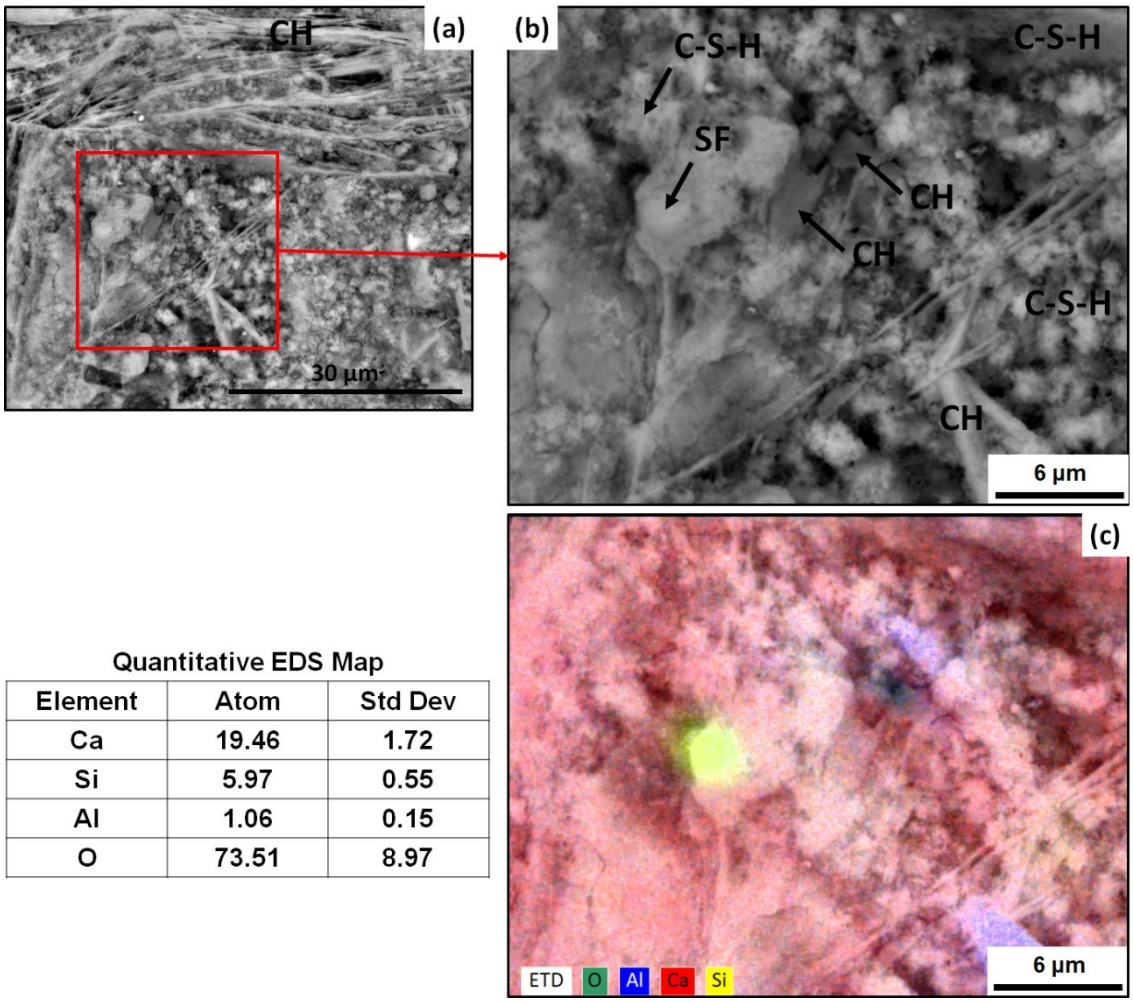

Quantitative EDS Map

Element	Atom	Std Dev
Ca	19.46	1.72
Si	5.97	0.55
Al	1.06	0.15
O	73.51	8.97

Figure 5.55 – EDS-SEM analysis from BSE image - REF sample.

For the H2% sample, Figure 5.56a shows a typical region presents in the obtained SEM images. Unreacted alite (C3S) particles can be seen, indicating that at an early age, cement systems with a low w/c ratio (as occurring in RPC) present deficiencies in the hydration process. The condition of cement particles without complete hydration at the age of 3 days was also reported by Rossen, Lothenbach and Scrivener (2015). These authors mentioned that the SF particles act as nucleation sites, resulting in the formation of more hydration products “outer” the cement grain (alite) and less “inner”. The result is the presence of a “hollow shell” around the alite, as also observed in Figure 5.56a.

In the inset detached (Figure 5.56b), morphologies consistent with C-S-H can be seen, beyond CH and silica dioxide particles from the hybrid (SiO_2/CNT), which are identified due to their shape and size. This region was analyzed by EDS to measure the Ca/Si ratio. The map is presented in Figure 5.56c and the

atoms percentage indicated in the table in the figure. Considering the values, the ratio Ca/Si = 1.48.

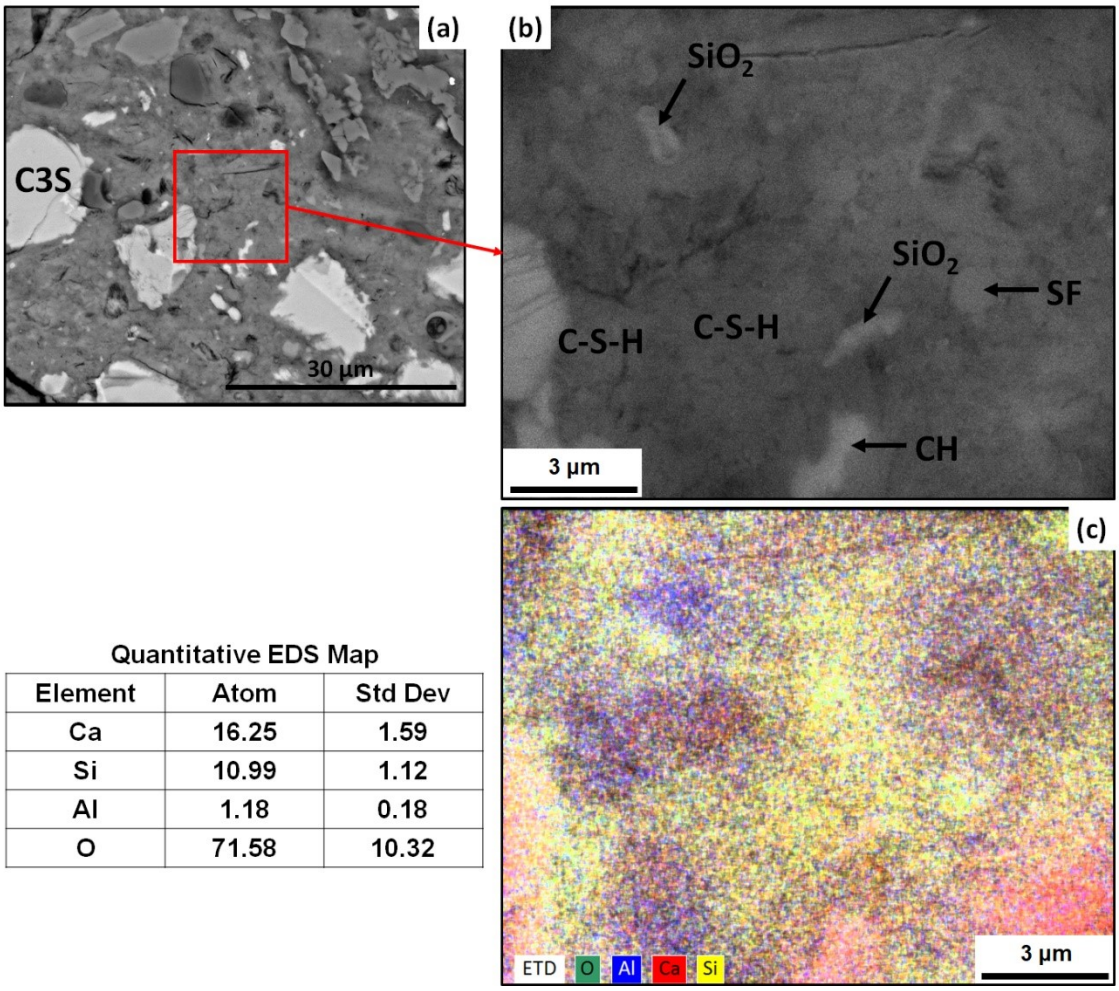

Quantitative EDS Map

Element	Atom	Std Dev
Ca	16.25	1.59
Si	10.99	1.12
Al	1.18	0.18
O	71.58	10.32

Figure 5.56 – EDS-SEM analysis from BSE image - H2% sample.

With the increase of the hybrid content to 4wt%, H4% sample, it is also possible to identify unreacted C3S particles, with “hollow shell” around them, and white dots disperse around the analysis region (Figure 5.57a). With higher magnification (Figure 5.57b), it is possible to better identify these white dots and see that they also are SiO_2 particles. The dense region in light gray is C-S-H formed and the spherical particle characteristic to the SF.

This region shown in Figure 5.57b, was analyzed by EDS to measure the Ca/Si ratio. The map is presented in Figure 5.57c and the atoms percentage indicated in the table in the figure. Considering the values, the ratio Ca/Si = 0.44. This low ratio can be related to the excess of silica particles, whether from the hybrid or

silica fume. Low Ca/Si ratio is typical of systems with largely unreacted silica (KUNTHER; FERREIRO; SKIBSTED, 2017).

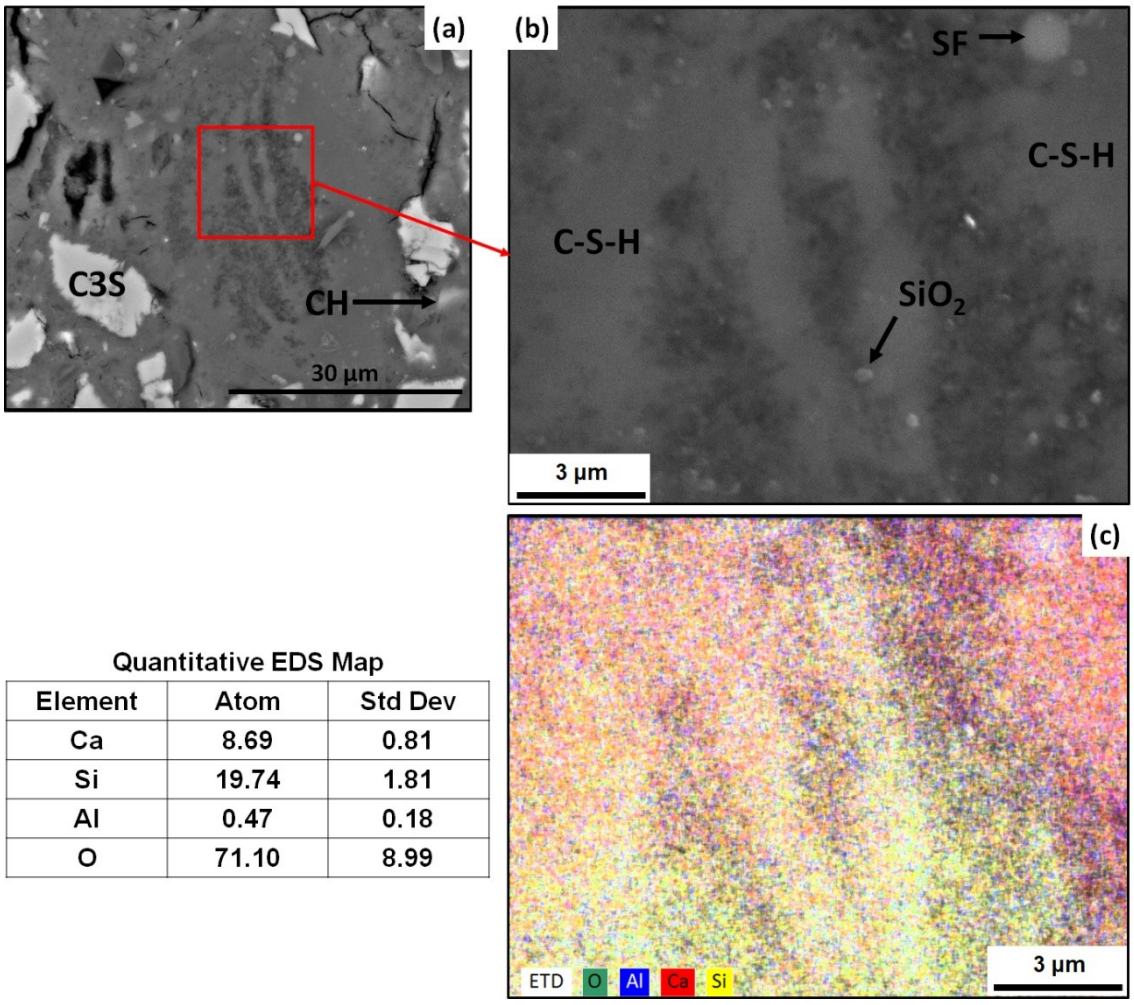

Quantitative EDS Map

Element	Atom	Std Dev
Ca	8.69	0.81
Si	19.74	1.81
Al	0.47	0.18
O	71.10	8.99

Figure 5.57 – EDS-SEM analysis from BSE image - H4% sample.

Finally, for the H6% sample, the presence of unreacted C3S particles can also be seen, beyond the silica fume (SF) particle (Figure 5.58a). In the inset detached (Figure 5.58b), despite the voids (dark points), the C-S-H structure is compact and without a clear presence of CH morphology. Figure 5.58b shows the region where was realized the EDS map to measure the Ca/Si ratio. The map is presented in Figure 5.58c and the atoms percentage indicated in the table in the figure. Considering the values, the ratio Ca/Si = 0.93.

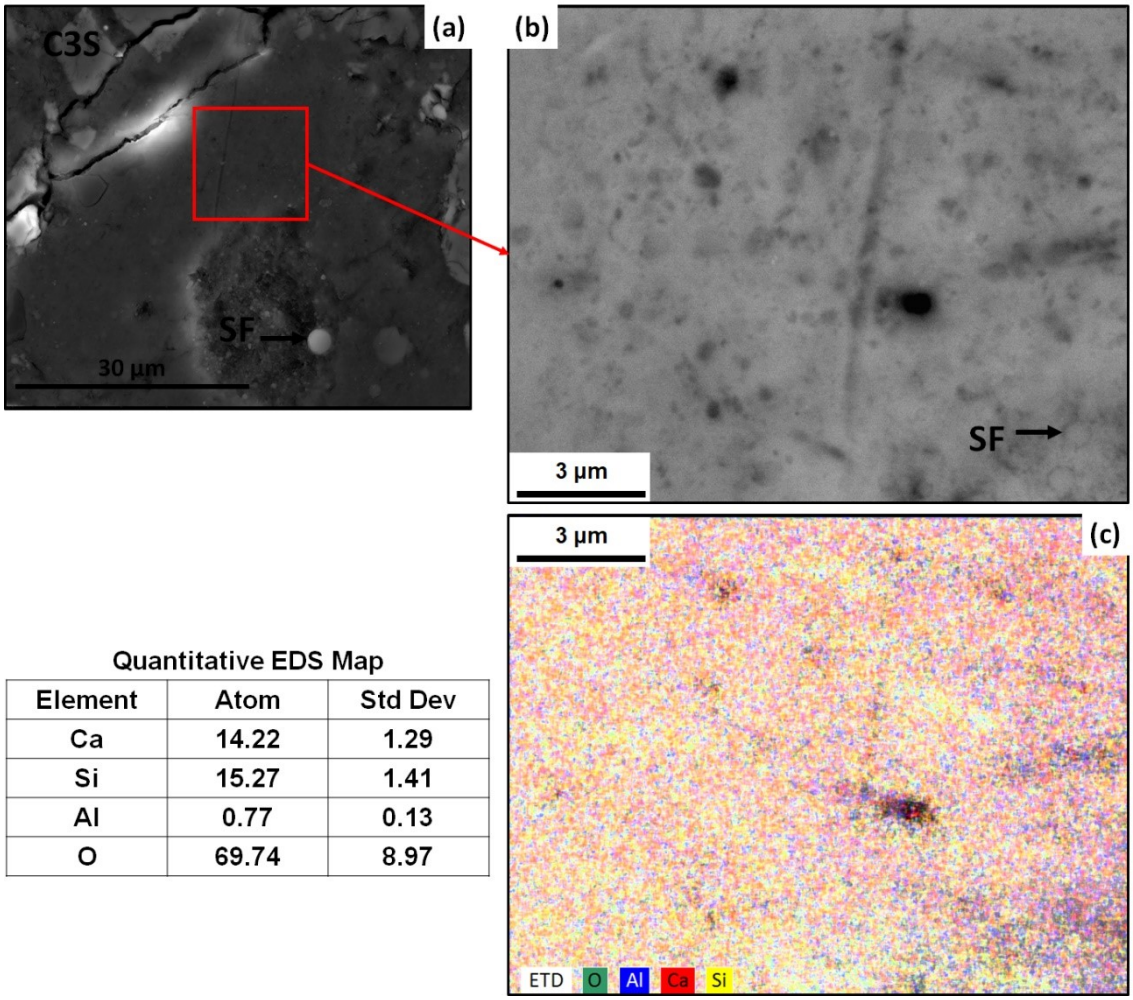

Quantitative EDS Map

Element	Atom	Std Dev
Ca	14.22	1.29
Si	15.27	1.41
Al	0.77	0.13
O	69.74	8.97

Figure 5.58 – EDS-SEM analysis from BSE image - sample H6%.

5.6.3.6. Discussion of the pozzolanic evaluation results

As previously mentioned, nanomaterials can promote significant changes in the cement hydration products, impacting mainly on mechanical performance and durability (PAUL *et al*., 2018). Thus, to evaluate these changes the use of different analysis technics contributes to a better interpretation of the results.

Based on this consideration, the hypothesis that the hybrid (n-SiO_2/CNT) promotes the pozzolanic effect and contributes positively to the microstructure of the cementitious matrices was evaluated.

As defined at the beginning of Chapter 4, variations in the hybrid amount were adopted (2%, 4%, and 6% by weight of cement), replacing a part of the silica

fume. The global and localized effects due to the pozzolanic activity explain the obtained results.

The influence of the hybrid and variations in its quantity and combination, in terms of Ca^{2+} adsorption, were evaluated in the called chemical method. From this analysis, the results indicated that the amount of material influenced the ion adsorption and diffusion effects. The excess of the hybrid, pure n-SiO_2/CNT or H6%, promoted fast, but not complete, adsorption, and diffusion effects, which seems to lead to an adequate reaction time. For other samples, the test showed a similar tendency between them, but the H2% sample presented a better behavior over time.

Considering the macro effect of the hybrid in the cement hydration process and the pozzolanic activity, the analyses in the cement/silica fume pastes showed structural variations between the different samples.

Initially, the results of the thermogravimetric analysis indicate a tendency that the REF sample formed more hydration products, either hydrates or CH. As previously mentioned, the presence of nano-silica can change the structure of the C-S-H gel, and the response in terms of non-evaporated water is altered. More specifically concerning the CH formation and its characteristics, the thermal analysis allowed observing two points:

(i) between the samples, the onset temperature of CH degradation was altered according to the hybrid content. The REF sample presented onset temperature equal to 430°C, and the H2%, H4%, and H6% samples, 412, 400, and 420°C respectively. This may be related to the degree of crystallinity of the CH.

(ii) the difference between the onset and final temperature (ΔT_{CH}). To the REF sample is equal to 13°C, and 14°C and 15°C for the H2% and H6% samples, respectively. However, for the H4% sample, the value was equal to 23°C, presenting a considerable difference.

Indeed, thermal analysis indicates some differences in the hydration products, and despite the low difference in the CH content, the samples with the hybrid showed more effectiveness in the pozzolanic effect.

About the XRD analysis, specifically concerning the portlandite, very low intensity on the peak (001) at 3 days curing age in RPC was also obtained by Zhang *et al.* (2018). The author discusses that such phenomenon is related to the CH crystal refinement process, due to the presence of the silica and also with the increased amount of the nanomaterial (nano boron nitride) employed. Again, despite the smaller amount of silica fume in the samples with the hybrid, the CH formation was different, modifying its morphology. This is observed in the index orientation (R) of the portlandite (Table 5.12) indicating a decrease in the value.

The results associated with the crystallinity of the CH appear to be directly related to the onset temperature degradation. The REF sample has a higher R index and the onset temperature suggesting that a more resistant CH has a higher temperature to start its degradation. In the contrast, the H2% sample had a lower onset temperature, ΔT_{CH}, and R index.

From the analysis and results of N_2 adsorption, the H2% sample showed more pores correspondent to the interlayer (<2 nm) and gel pores (2 – 10 nm), compared with the other samples with the presence of the hybrid. But values are similar to the REF sample. This can be associated with the CH presence, which is a compact structure with low porosity. However, the micrographs and the results presented in the EDS analysis topic showed that the H2% sample tends to form more C-S-H than CH.

Still, according to the EDS analysis, the general evaluation initially showed that the samples with the hybrid presented Ca/Si values greater than the REF sample. In cement-based systems, a lower Ca/Si ratio, is significant to higher C-S-H content up to a limit. However, according to the results obtained, the presence of the hybrid somehow supplied the local Si “deficit”, as mentioned in the discussion of the topic.

All these considerations indicate that the incorporation of the hybrid modifies the cement hydration process to promote, as indicated in the objectives of the

work, an additional formation of C-S-H around the hybrid n-SiO_2/CNT. As an adequate amount, the content of 2 % bwoc of the hybrid seemed to present better behavior. Thus, this content was used to evaluate the influence of the hybrid in reactive powder concrete.

5.6.4. Mechanical results

After the definition of the adequate amount of hybrid (2% bwoc) to be incorporated in reactive powder concrete (RPC) and the production of the samples, the mechanical performance results are presented in this topic. As previously mentioned, the evaluations were performed in concretes without the hybrid (REF) and also varying the form of incorporation and amount of the hybrid. Thus, the incorporation was by the addition (-A suffix) or by replacing (-R suffix) part of the silica fume. Beyond the amount of 2 % bwoc, 0.7 % bwoc was also used.

Initially, the three-point bending test (TPBT) results are presented. The load-midspan deflection curves, as illustrated in Figure 5.59, were obtained with measured values from the load-deflection system.

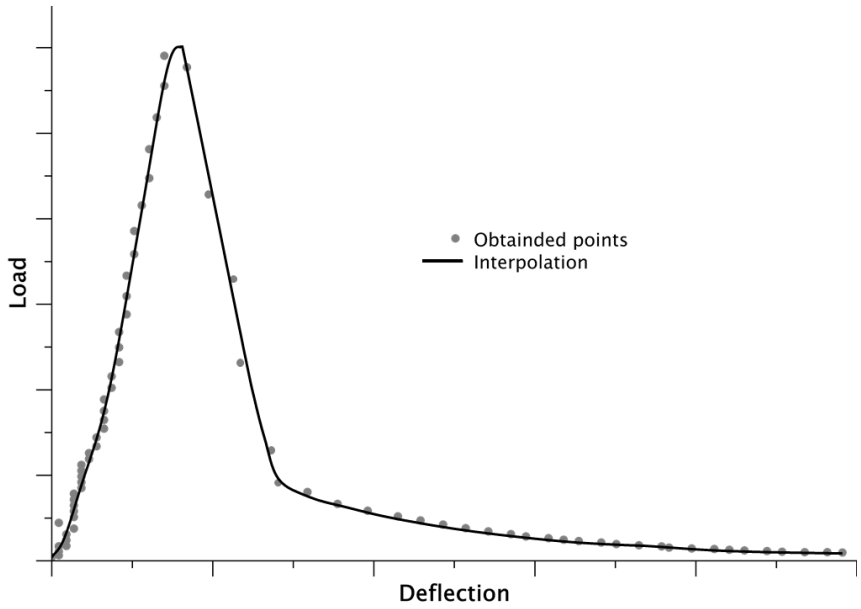

Figure 5.59 – Example of load-midspan deflection data points – Consideration for the interpolation.

For a better analysis of the results, curves with the data interpolation were obtained, as also illustrated in the figure. In some cases, the load-deflection curve shows differences at the initial range. The same behavior was already presented by Han *et al*. (2016), Dong *et al*. (2019), and Dong *et al*. (2020).

Figures 5.60 – 5.63 show the load-deflection curves for the groups of REF, H2R, H2A, and H07R samples, respectively. In the series corresponding to the REF and H2A, the curves of the six samples are presented. However, concerning the groups H2R and H07R, five curves are presented for each due to problems during the deflection data acquisition.

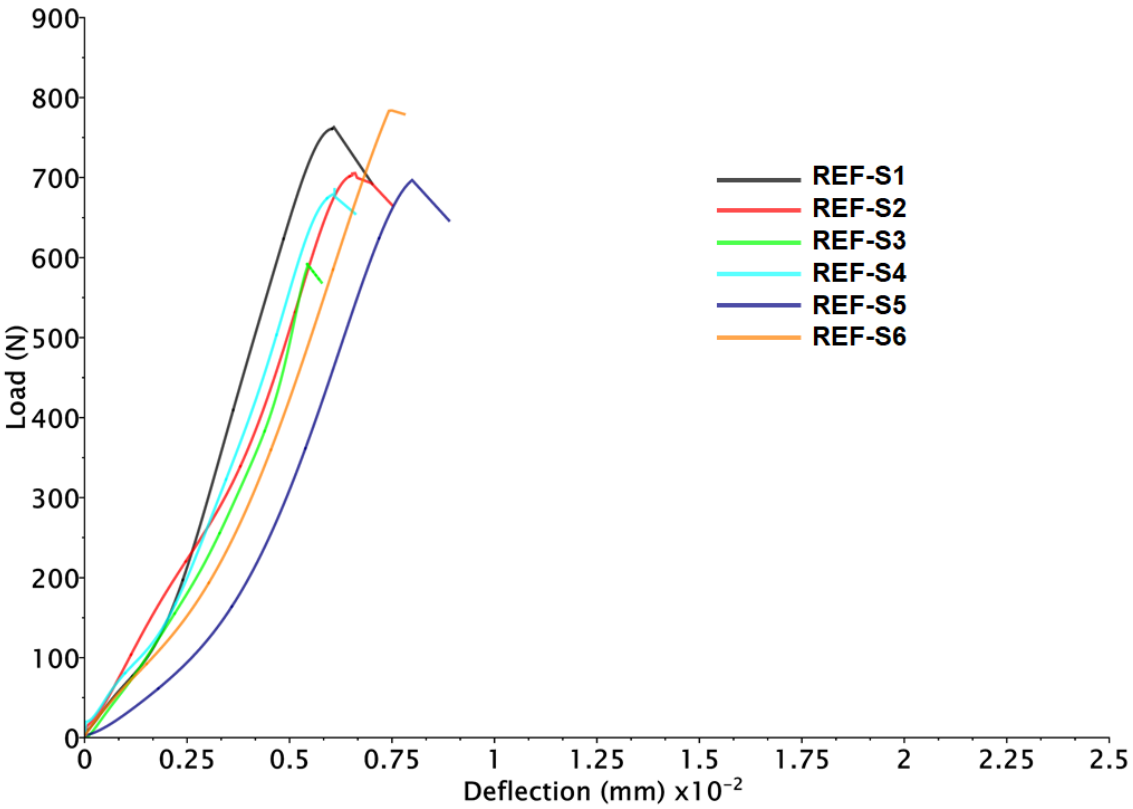

Figure 5.60 – Load-midspan deflection curve of the group of REF samples.

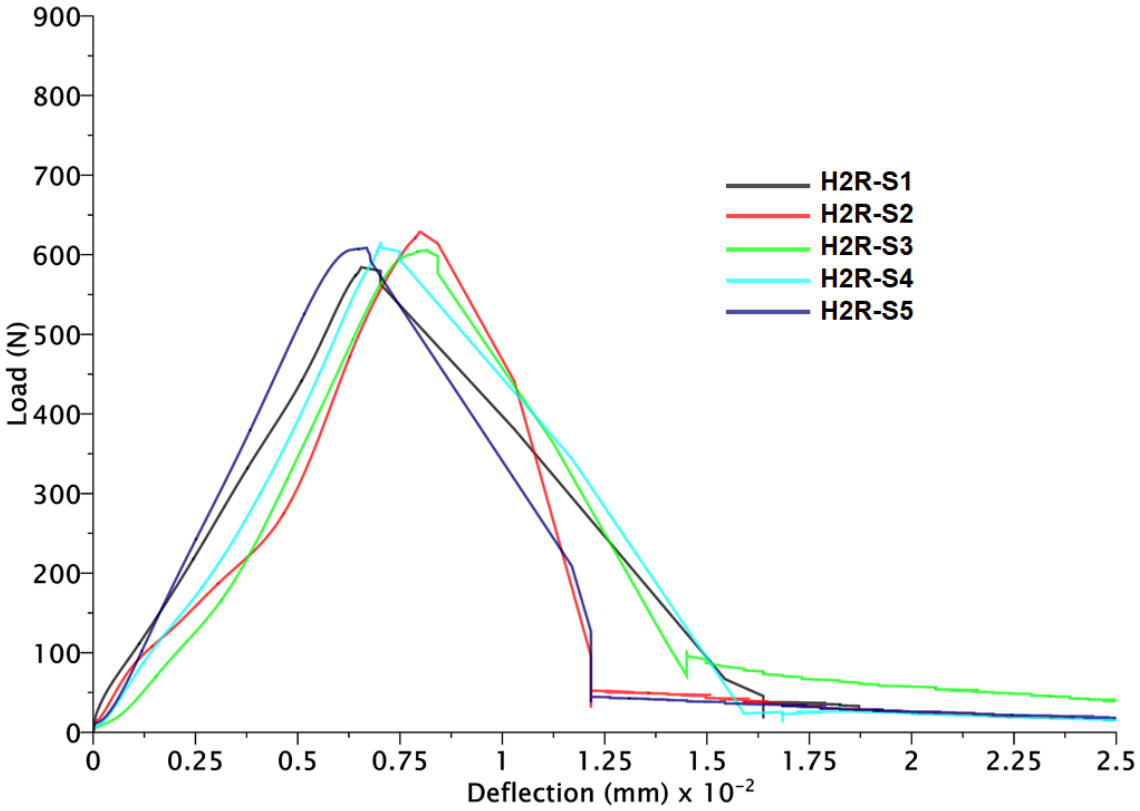

Figure 5.61 – Load-midspan deflection curve of the group of H2R samples.

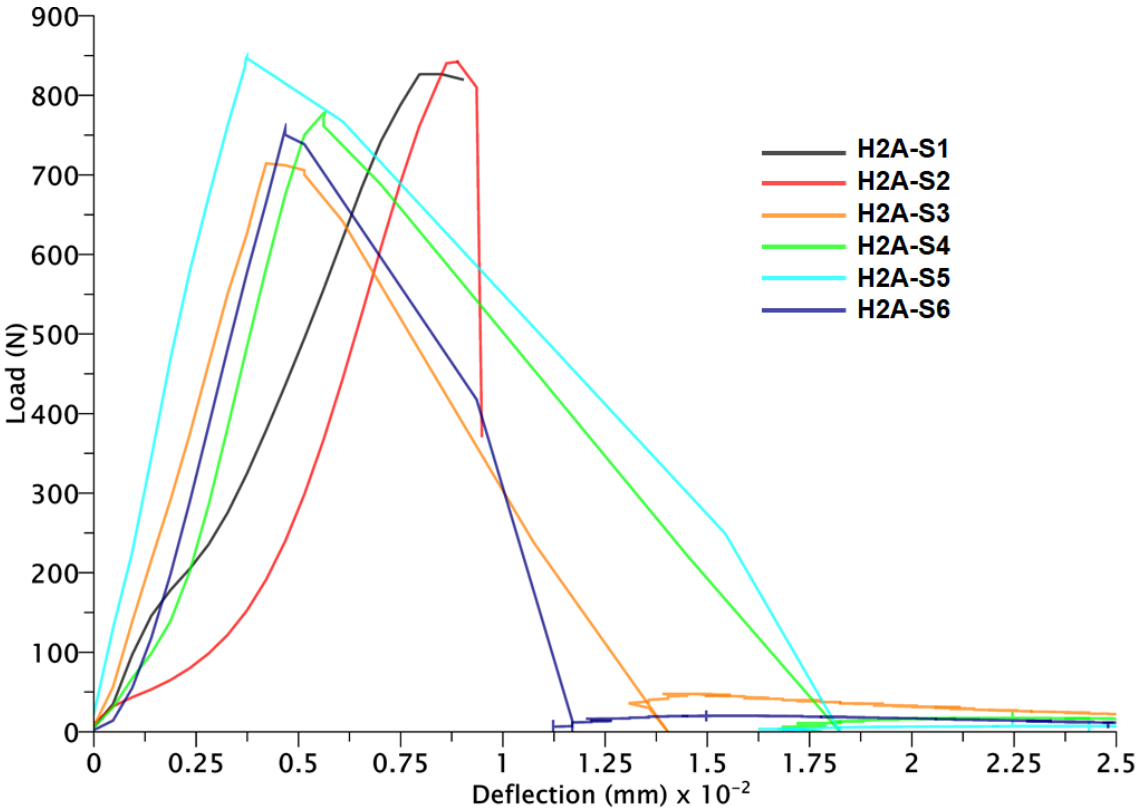

Figure 5.62 – Load-midspan deflection curve of the group of H2A samples.

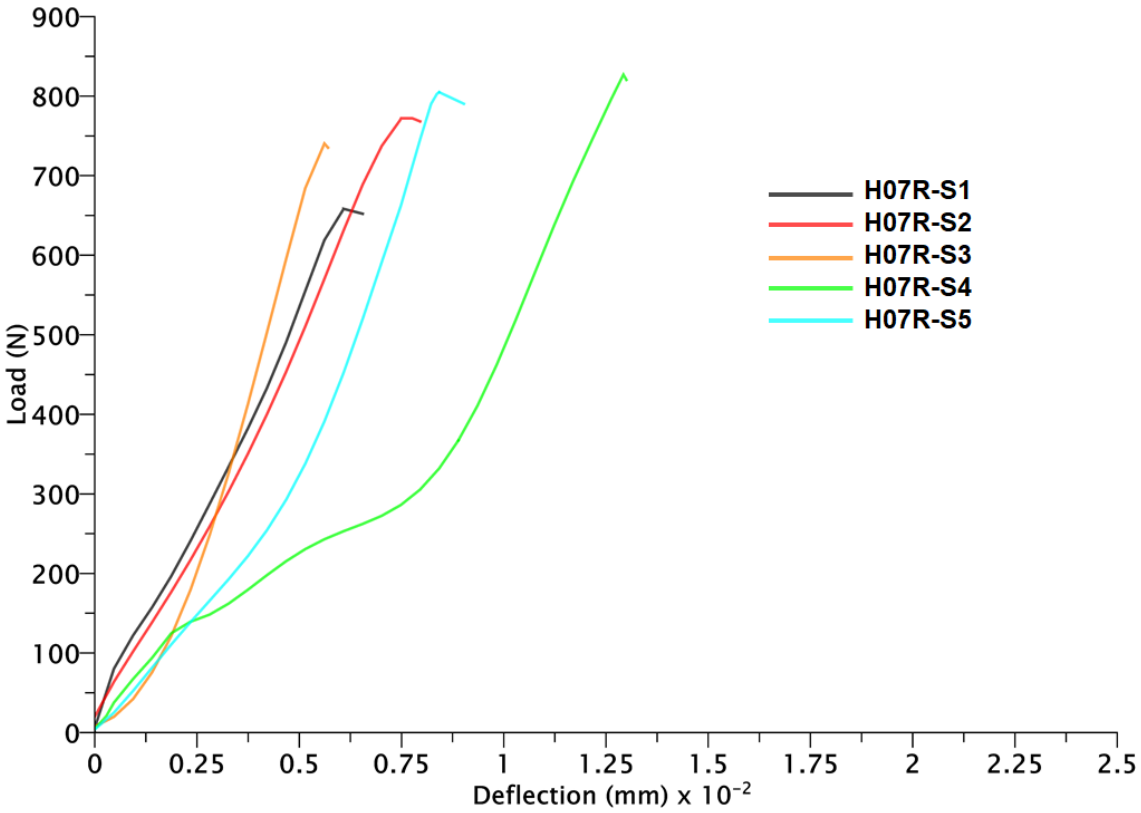

Figure 5.63 – Load-midspan deflection curve of the group of H07R samples.

As described in topic 4.5.3, after the three-point bending tests (TPBT), the results of the load-deflection curves and the dimensions of the broken cross-section in the samples were used to calculate the Flexural Tensile Strength (σ_F), Fracture Energy (G_F), Tensile toughness areas (E_1 and E_2), and Tensile strain corresponded to the peak load (ε_T).

Table 5.14 summarizes the information about the maximum peak loads (F_{fmax}) and the dimensions considered in each sample per group.

Table 5.14 – Maximum load-peaks and dimensions of the samples after the TPBTs.

Group	Sample	F_{fmax}	b1	b2	b3	h1	h2	h3	bm*	hm**
		(N)	mm							
REF	S1	763.19	25.78	25.69	25.52	20.77	20.99	21.23	25.7	21.0
	S2	705.50	26.24	26.16	25.85	19.49	20.86	19.75	26.1	20.0
	S3	591.81	26.57	26.47	26.41	18.54	19.09	18.44	26.5	18.7
	S4	680.12	25.56	25.25	25.07	20.35	20.72	19.51	25.3	20.2
	S5	696.19	25.68	25.64	25.46	19.74	20.51	20.00	25.6	20.1
	S6	783.83	25.83	25.55	25.56	20.15	21.08	20.84	25.6	20.7
H2R	S1	587.07	25.66	25.72	25.69	19.96	20.15	20.12	25.7	20.1
	S2	628.69	26.32	26.37	26.56	20.09	20.29	20.37	26.4	20.3
	S3	570.49	26.40	26.42	26.46	19.86	19.82	19.07	26.4	19.6
	S4	605.85	25.15	25.26	25.48	19.64	19.84	19.89	25.3	19.8
	S5	614.14	25.57	25.56	25.71	19.91	20.21	20.17	25.6	20.1
	S6	608.56	25.59	25.58	25.54	20.70	20.83	19.90	25.6	20.5
H2A	S1	826.63	25.61	25.58	25.63	22.04	22.99	22.76	25.6	22.6
	S2	842.20	25.23	25.15	24.99	22.88	22.27	22.49	25.1	22.5
	S3	714.47	25.50	25.47	25.70	21.91	22.07	21.15	25.6	21.7
	S4	778.25	25.44	25.41	25.71	22.47	22.77	22.96	25.5	22.7
	S5	848.80	25.60	25.49	25.58	22.29	22.84	22.65	25.6	22.6
	S6	757.95	25.88	25.51	25.58	22.90	21.88	22.37	25.7	22.4
H07R	S1	658.31	25.69	25.75	25.75	20.10	20.47	20.74	25.7	20.4
	S2	772.10	26.55	26.53	26.64	20.26	20.95	20.27	26.6	20.5
	S3	740.32	26.05	25.76	25.73	20.33	20.43	20.65	25.8	20.5
	S4	826.98	26.45	26.36	26.34	20.61	20.54	20.23	26.4	20.5
	S5	804.07	26.36	26.43	26.56	21.00	21.40	21.25	26.5	21.2
	S6	753.78	26.58	26.39	26.48	20.83	20.92	20.04	26.5	20.6

* bm – mean width.

** hm – mean height.

Figures 5.64 – 5.67 show using the curves, the identification of the toughness areas (E_1 and E_2), as well as the deflection (in mm) in the maximum load-peak for each sample per group. These parameters were used to calculate G_F, E_1, E_2, and ε_T. The results and the flexural tensile strength (σ_F) are summarized in Table 5.15; the values considered as outliers to the statistical analysis of the results are indicated. This procedure was adopted for the calculation of the average values of G_F, E_1, E_2, and ε_T, and their corresponding statistical parameters.

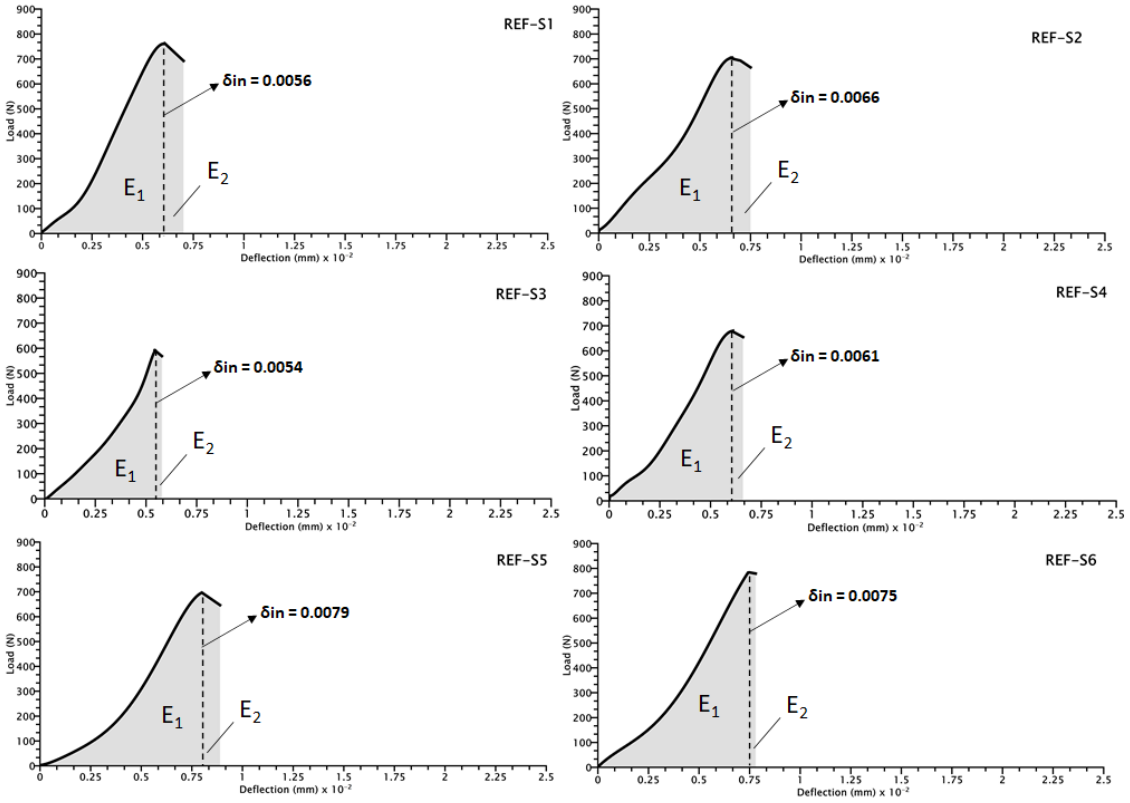

Figure 5.64 – Load-midspan deflection curves with toughness areas and deflection in the maximum load peak – group of samples REF.

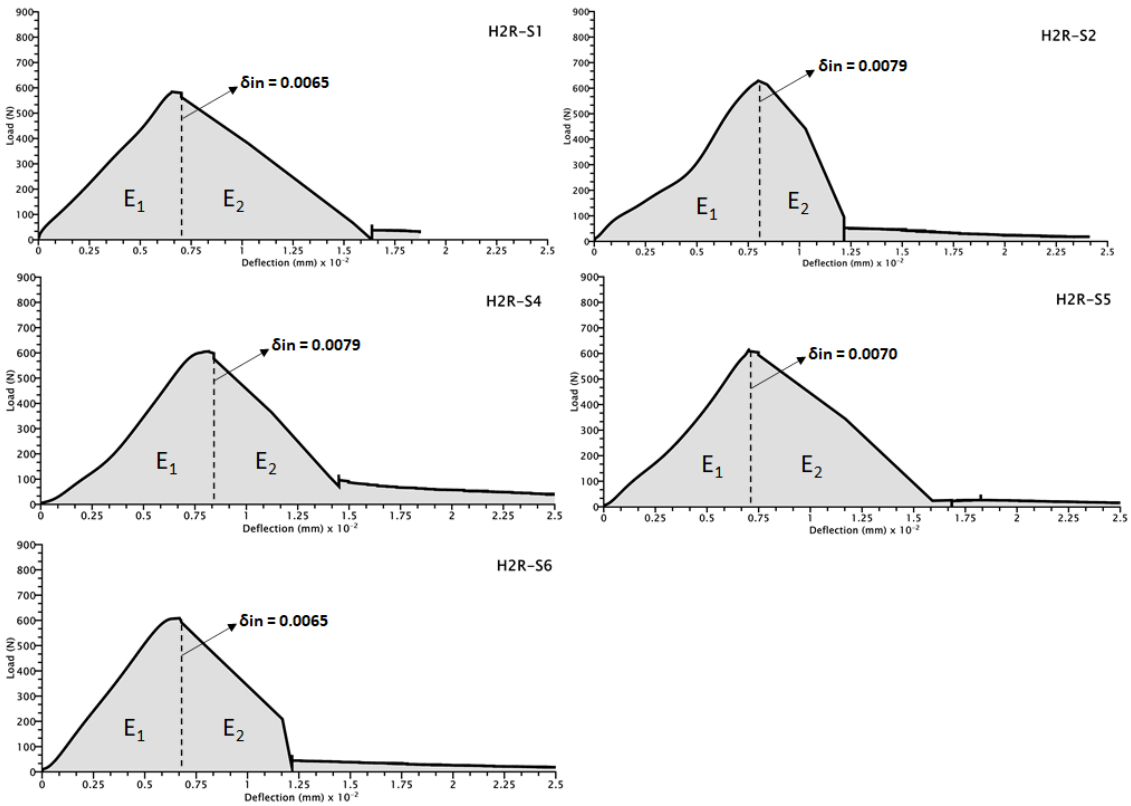

Figure 5.65 – Load-midspan deflection curves with toughness areas and deflection in the maximum load peak – group of samples H2R.

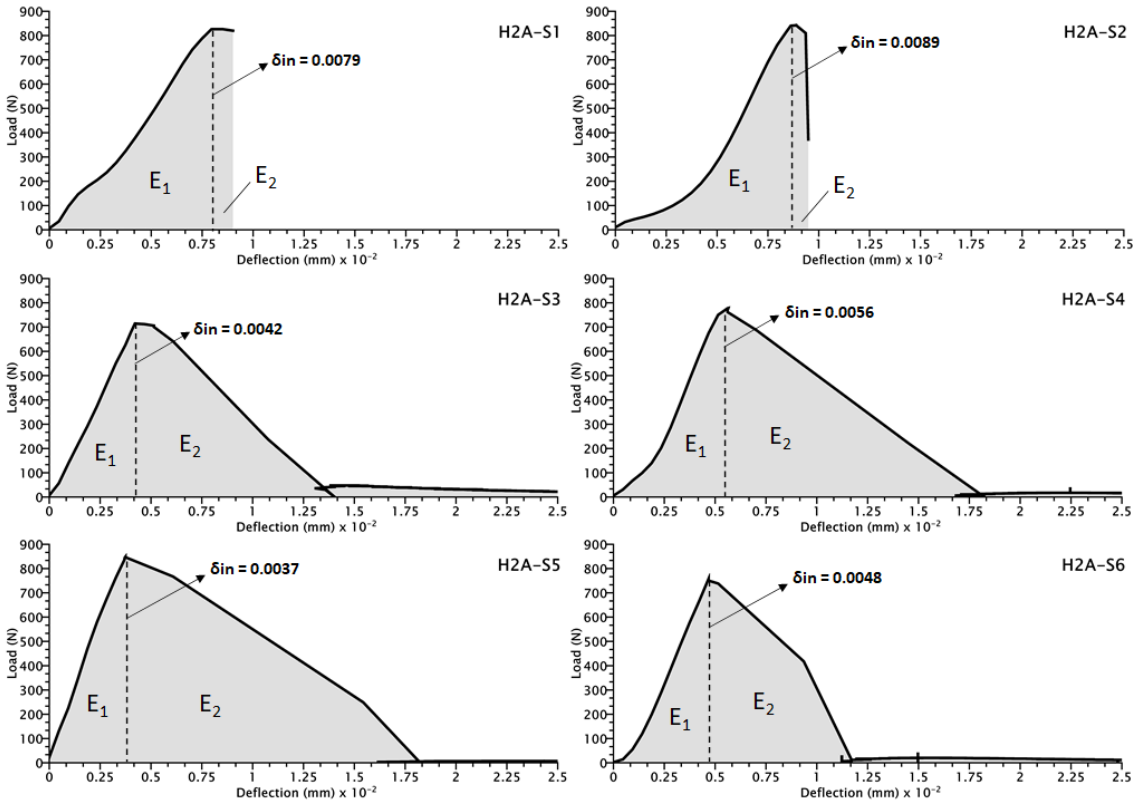

Figure 5.66 – Load-midspan deflection curves with toughness areas and deflection in the maximum load peak – group of samples H2A.

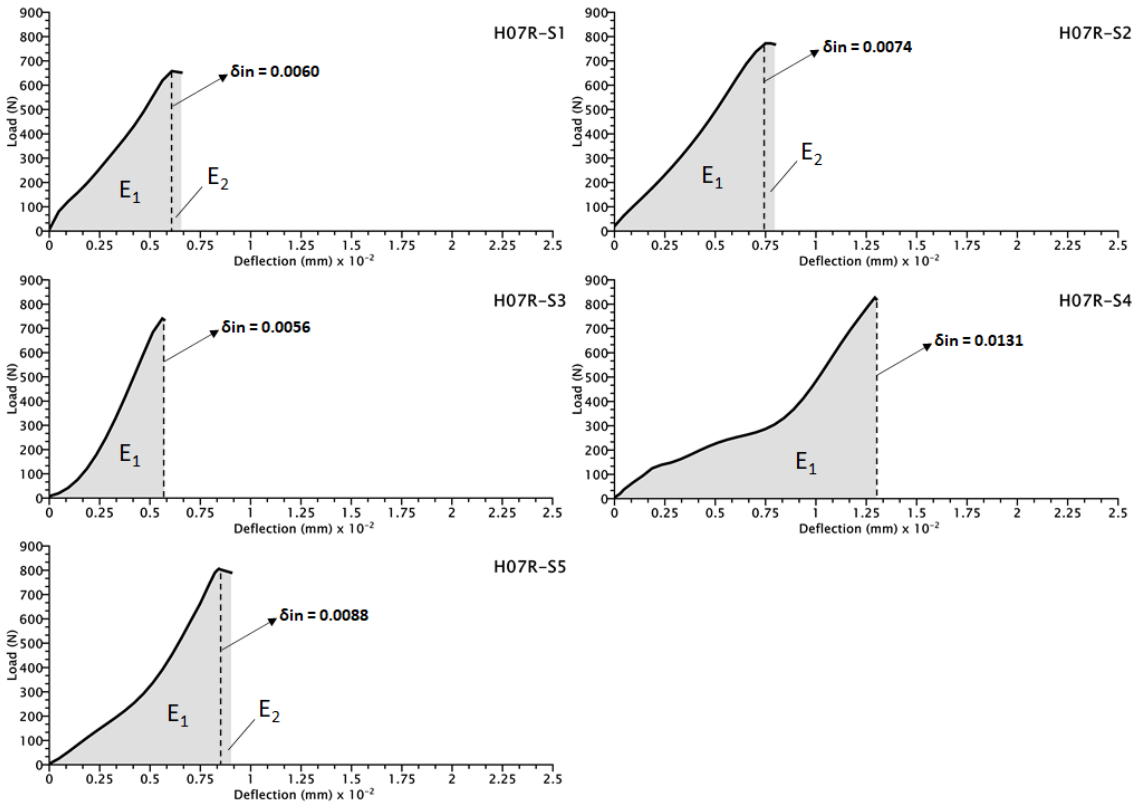

Figure 5.67 – Load-midspan deflection curves with toughness areas and deflection in the maximum load peak – group of samples H07R.

The profile of the load-deflection curves with the hybrid, in general, is similar to the one observed by Dong *et al.* (2020), with a tail after the peak load. These authors worked with super-fine stainless wire reinforcing reactive powder concrete, using the mix proportion proposed by Richard and Cheyrezy (1995), like in this work. In the case of the RPC of the group REF, the profile of the load-deflection curves are similar to the curves obtained for carbon nanotubes reinforced reactive powder concretes in a reported work by Ruan *et al.* (2018).

Table 5.15 – Calculated values to tensile strength, toughness parameters, tensile strain corresponded to the peak load, and fracture energy.

Group	Sample	σ_F	E1	E2	ε_T	G_F
		(MPa)	(N.mm)		(10^{-3})	($J.m^{-2}$)
REF	S1	12.1	2.08	0.68	0.049	5.13
	S2	12.1	2.16	0.62	0.055	5.31
	S3	11.5	1.23†	0.20†	0.042†	2.89†
	S4	11.9	1.86	0.33	0.051	4.30
	S5	12.1	2.13	0.60	0.066	5.31
	S6	12.9	2.34	0.29	0.065	4.97
H2R	S1	10.2	1.91	3.09	0.054	9.74
	S2	10.4	2.24	2.14	0.067	8.19
	S3	10.1	-	-	-	-
	S4	11.0	2.30	3.46	0.065	11.50
	S5	10.7	1.92	3.27	0.059	10.1
	S6	10.2	2.18	2.89	0.055	9.74
H2A	S1	11.4	3.13†	0.83†	0.074†	6.86†
	S2	11.9	2.81†	0.46†	0.084†	5.79†
	S3	10.7	1.44	4.36	0.034	10.45
	S4	10.6	1.94	5.07	0.053	12.08
	S5	11.7	1.69	7.07	0.035	15.17
	S6	10.6	1.48	3.67	0.045	8.97
H07R	S1	11.0	1.98	0.31	0.051	4.35
	S2	12.5	2.81	0.36	0.063	5.82
	S3	12.3	1.74†	0.00	0.048	3.29†
	S4	13.5	4.15	0.00	0.111†	7.80
	S5	12.2	2.64	0.48	0.078	5.56
	S6	12.1	-	-	-	-

† value not considered in the statistical analysis.

Concerning the compressive tests, the rupture load (F_{cmax}), and the compressive strength (σ_C) of each sample, per group, are presented in Table 5.16.

Table 5.16 – Compressive tests: rupture load and compressive strength.

Group	Sample	F_{cmax}	σ_C
		(N)	(MPa)
REF	S1	24.98	38.0
	S2	44.42	67.6
	S3	42.03	64.0
	S4	31.93	48.6
	S5	32.35	49.3
	S6	33.25	50.6
	S7	30.27	46.1
	S8	39.82	60.6
	S9	35.42	53.9
	S10	37.33	56.8
	S11	45.56	69.4
	S12	41.87	63.7
H2R	S1	31.46	47.9
	S2	35.93	54.7
	S3	43.46	66.2
	S4	40.39	61.5
	S5	31.89	48.5
	S6	29.88	45.5
	S7	39.85	60.7
	S8	39.16	59.6
	S9	37.59	57.2
	S10	33.00	50.2
	S11	28.42	43.3
	S12	27.22	41.4
H2A	S1	36.74	55.9
	S2	37.71	57.4
	S3	32.22	49.1
	S4	42.48	64.7
	S5	34.65	52.8
	S6	31.45	47.9
	S7	31.06	47.3
	S8	28.58	43.5
	S9	39.49	60.1
	S10	25.44	38.7
	S11	39.91	60.8
	S12	46.88	71.4

(continues)

(sequence of the previous page)

H07R	S1	28.92	44.0
	S2	35.72	54.4
	S3	40.97	62.4
	S4	37.08	56.5
	S5	35.55	54.1
	S6	38.56	58.7
	S7	31.04	47.3
	S8	29.56	45.0
	S9	38.08	58.0
	S10	42.58	64.8
	S11	42.90	65.3
	S12	33.65	51.5

Considering the mechanical tests, Figures 5.68 – 5.70 present the main results for a better interpretation and discussion.

Concerning the flexural tensile strength (Figure 5.68a), it is verified that no differences were observed between the mean values of REF, H2A, and H07R groups, considering the standard deviations. However, the tensile strength of the H2R shows a mean value slightly lower. The mean value in the order of 10-12 MPa is reasonable, comparing with Zhang *et al.* (2018). These authors also worked with the inclusion of a nanomaterial (boron nitride) in RPC. The mix proportion was also based on Richard and Cheyrezy (1995), but the w/c ratio equal to 0.38. At the age of 3 days of curing, the flexural strength was between 7 and 11 MPa. Also corroborating with these results, referencing the work of Han *et al.* (2017a), it is possible to verify that the flexural strength in RPC at the 3 days age was between 4 and 10 MPa, but with a w/c ratio equal to 0.30 and with a variation of the nano SiO_2-coated TiO_2 amount. Finally, in similar conditions in terms of mix proportion, Dong *et al.* (2020) show a range of flexural strength in RPC, even at the age of 28 days, between 5 and 13 MPa.

For the compressive strength (Figure 5.68b), considering the standard deviations, there is no difference between the average values of the groups. The magnitude of the compressive strengths obtained is also similar to the works of Han *et al.* (2017a) and Zhang *et al.* (2018), who evaluated RPC samples at the age of 3 days. According to Liu *et al.* (2019), independent of the MWCNT type (aspect ratio), the increase in the compressive strength on RPC was insignificant

with the increase of the nanomaterial content. The obtained results show a similar tendency, with no significant changes in the compressive strength.

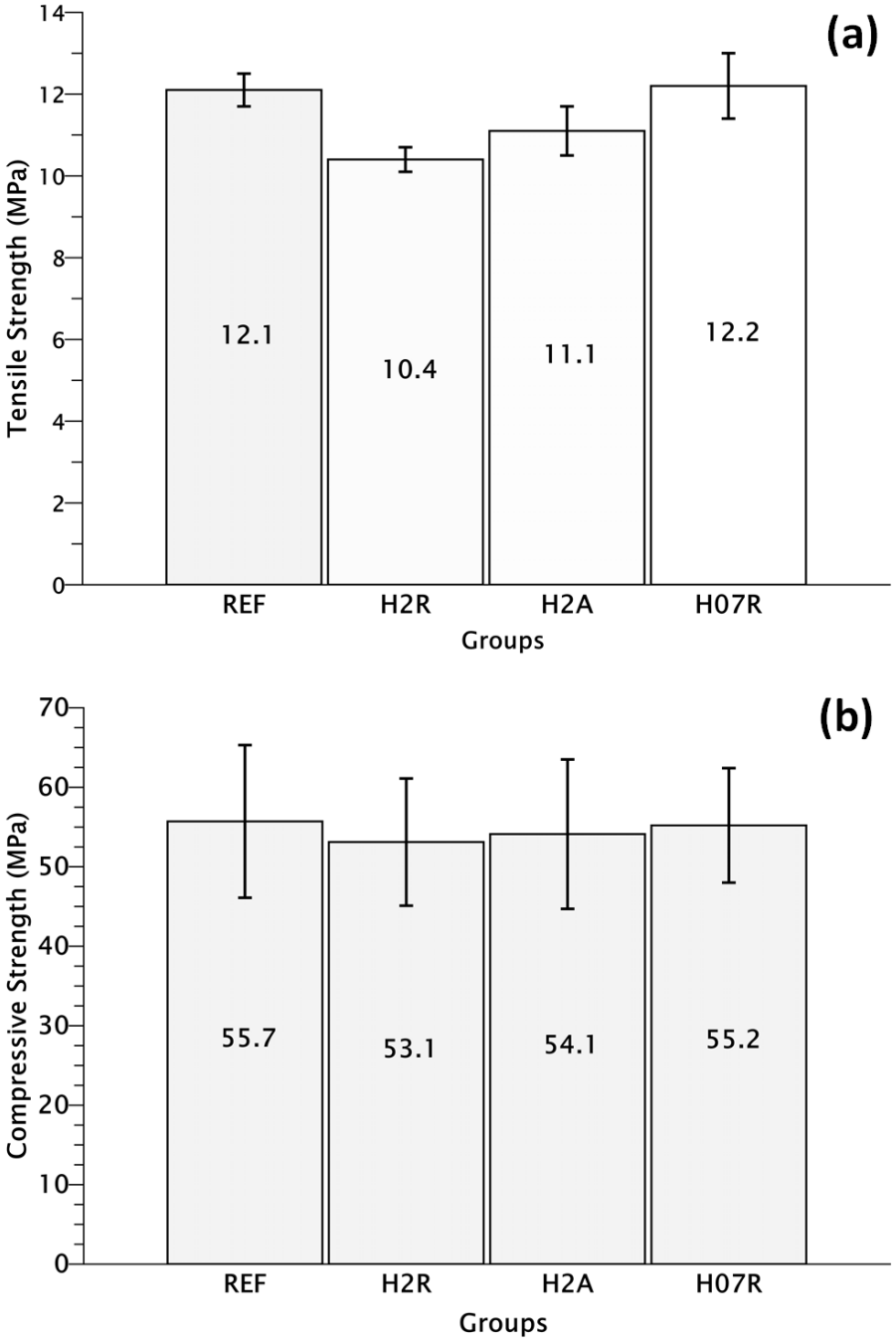

Figure 5.68 – Results of the mechanical tests. (a) Tensile strength; (b) Compressive strength.

Concerning the results (Figure 5.69) related to the toughness parameter (E_1 and E_2), two different behaviors can be observed.

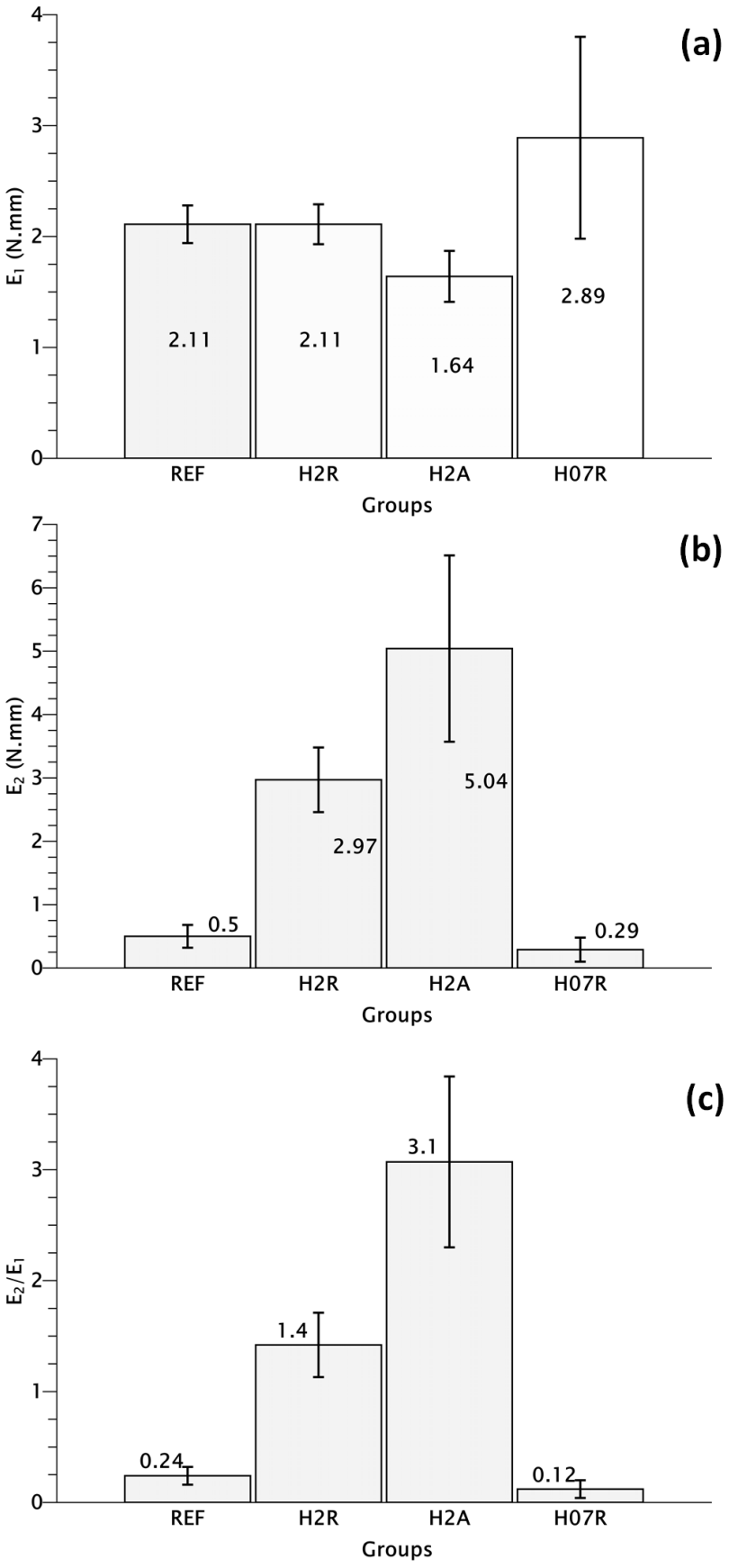

Figure 5.69 – Mean toughness parameters measured from the load-midspan deflection curves of the samples.

First, in the computed area below de curve between zero and the maximum load peak (E_1), the average values of the four groups are equivalent, considering the standard deviation (Figure 5.69a). This is coherent given since in the four groups, tensile strength was similar.

However, concerning the computed area below the curve (when existing) after the peak load (E_2 parameter) the average values have a significant difference (Figure 5.69b). Even considering the standard deviations, the groups with 2% of hybrid (H2A and H2R) presented values much higher than those REF and H07R. This indicates that the presence of the hybrid in the concentration of around 2% changes the crack propagation behavior after the peak load.

To a better comparison between the behavior before and after the peak load, Figure 5.69c shows the E_2/E_1 ratio. Considering the values, the groups with 2% of hybrid, either as substitution or addition, provided effective energy absorption capacity.

As shown in Figure 5.70a, no significant differences were observed in the tensile strain corresponded to the peak load, which is a function of deflection (δ_{in}) corresponding to that load.

Finally, Figure 5.70b shows the effect of the incorporation of the hybrid on the fracture energy of the reactive powder concrete matrix. No differences can be seen between the group REF and H07R, due to the standard deviation overlap. Between H2R and H2A groups, the values are equivalent, taking into account the standard deviation overlap. However, these values are about twice the values corresponding to the REF and H07R samples. It is important to mention that, according to Richard and Cheyrezy (1995), the behavior of RPC matrices (without fibers) is purely linear and elastic, and the fracture energy (in the age of 28 days) not exceeding 30 $J.m^{-2}$. Thus, the observed values, in the order of 5 $J.m^{-2}$ for example, can be considered reasonable for the age of 3 days.

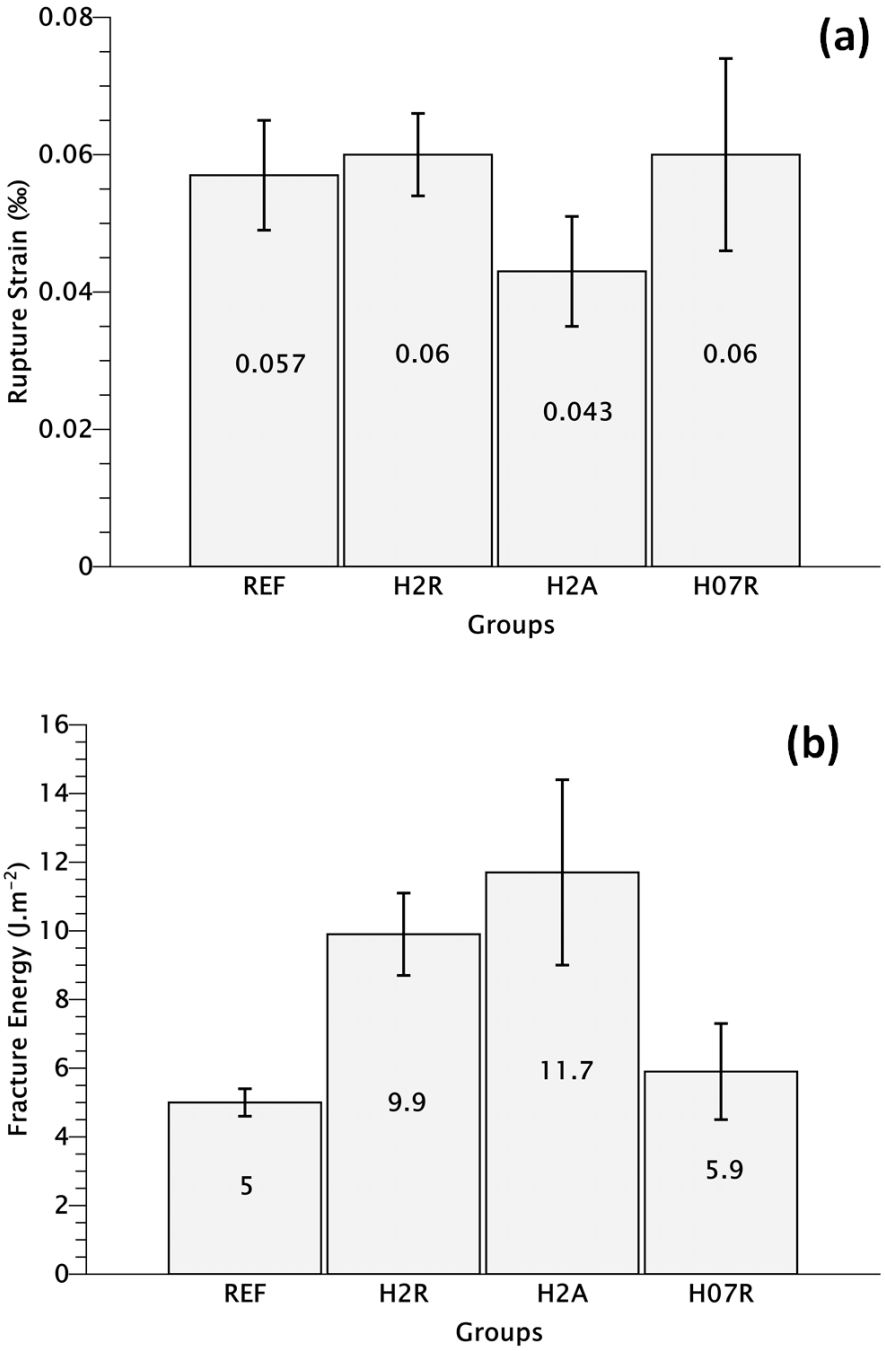

Figure 5.70 – Results of the mechanical tests. (a) Tensile strain at the peak load; (b) Fracture Energy.

Evaluating all results of the mechanical tests, some aspects can be discussed to understand the effect of the hybrid in the RPC matrix.

In general, considering the deviations of the values, no differences were observed between the groups, relative to compressive strength, flexural tensile strength, and tensile strain at the peak load. This may indicate that, despite the incorporation of the hybrid, the RPC matrix did not present significant changes in

its structure to improve directly the mechanical performance, at least for the curing age studied. In this line of thought, maybe the excess of n-SiO_2 was higher than the amount required to combine with the liberated lime during the hydration process impairing the development of the mechanical strength, as reported by Wang *et al*. (2016). On the other hand, this was not sufficient to decrease considerably the mechanical performance.

Considering the three-point bending test, as cited by Han *et al*. (2016), in the midspan region of the specimen, the micro-cracks initiate randomly and propagate quickly, generating a negative effect on the flexural strength. This brittle behavior was illustrated in Figure 3.1, topic 3.1. Thus, CNT incorporation improves the mechanical capacity in terms of toughness, mostly in the microcrack zone. This was demonstrated by the area under the load-deflection curve as verified in the H2R and H2A groups, after the peak load.

In this aspect, it is plausive to consider that with CNT present in the hybrid, the MWCNT capacity was effective in reinforcing the matrix. This behavior was discussed by Gdoutos; Konsta-Gdoutos; Danoglidis (2016), who worked with MWCNTs in cement mortar. They verified such improvement about the fracture properties, understanding that this was caused by the capacity of the MWCNTs to work against the localized stress concentration near the microcracks.

Carbon nanotubes could delay the initiation of microcracks development to macro cracks, as observed by Liu *et al*. (2019), who evaluated the synergy effect of MWCNTs and steel fibers in the improvement of the RPC. The carbon nanotubes present in the hybrid, in contact with the C-S-H, may have acted as a local reinforcement element, absorbing efficiently the crack propagation energy and presenting a relatively slow descending stage after the peak load in the curve. The mechanism of the local reinforcement, in the micro-cracks zone, is illustrated in Figure 5.71.

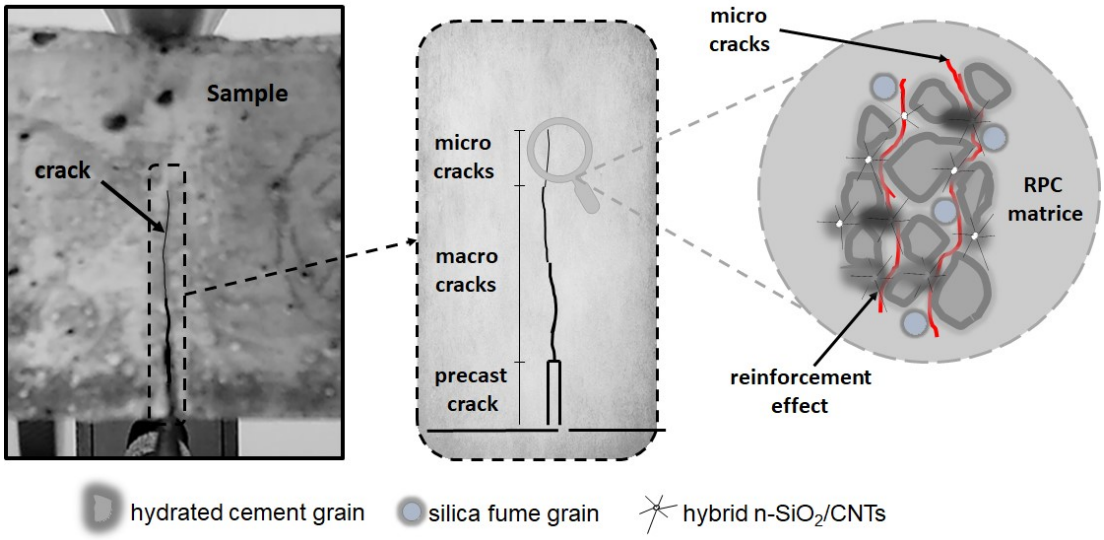

Figure 5.71 – Illustration of the crack propagation in the RPC sample and the reinforcement effect by the hybrid.

As reported by Gdoutos *et al.* (2016), flexural toughness represents the energy required for the material to fail. Working with carbon nanotubes and carbon nanofibers, these authors verified that the addition of these nanomaterials significantly increased the toughness in cement-based composite, and this was due to the controlled coalescing process of the cracks in the nano- and micro-scale, allowing the obtention of a matrix with higher toughness. The same effect was observed for the RPC samples produced in this work with 2% bwoc of the developed hybrid material. The flexural toughness and the energy needed by the material to fail were increased.

The greatest evidence of the hybrid capacity, in the amount of 2% bwoc, to minimize the crack propagation was the fact that, in the TPBT, the rupture did not occur abruptly, as in the samples of the REF and H07R groups. This means that the MWCNTs present in the hybrid promoted a reinforcement in the nano- and micro-scale which was enough to avoid an immediate rupture just after the peak load.

Still, regarding the rupture process of the samples during the mechanical tests, Figure 5.72 (without the hybrid) and Figure 5.73 (with the hybrid) show sequences of images during the TPBT test, moments immediately before and also after the initial crack. This sequence was obtained from a video footage performed during some tests. In these figures, beyond the image sequence and the time (in ms),

an inset indication of the respective moment in the force x displacement (F x δ) curve is illustrated and this position is represented by the red dot.

Figure 5.72 shows the sequence of images from a representative sample of the REF group. In Figure 5.72a the image shows the sample moments before the crack formation. Figure 5.72b shows the crack formation in a moment immediately before the peak load (as represented by the red dot in the inset). Then, rupture occurs due to the complete fracture, as shown in Figure 5.72c. In sequence, parts of the sample were separated (Figure 5.72d) and finally, two parts are observed (Figure 5.72e). All these events occurred in a small fraction of time, indicating that the process was very brittle.

With the incorporation of the hybrid, the sequence of images for a representative sample from the H2A group illustrates a different behavior during the rupture process. In Figure 5.73a, the first image shows the sample moments before the crack formation. In the sequence, it occurred a crack formation (Figure 5.73b) and at this moment, it did not fail. The application of the force (F) continued (Figure 5.73c-e) and the sample resisted the rupture, without the complete separation of the parts. It is observed that this whole process occurred for a relatively long time until the end of the curve (F x δ). This behavior is typical of a cementitious matrix with fiber reinforcement and indicates that the MWCNTs present in the hybrid worked in this way deaccelerating the crack propagation and inhibiting brittle failure.

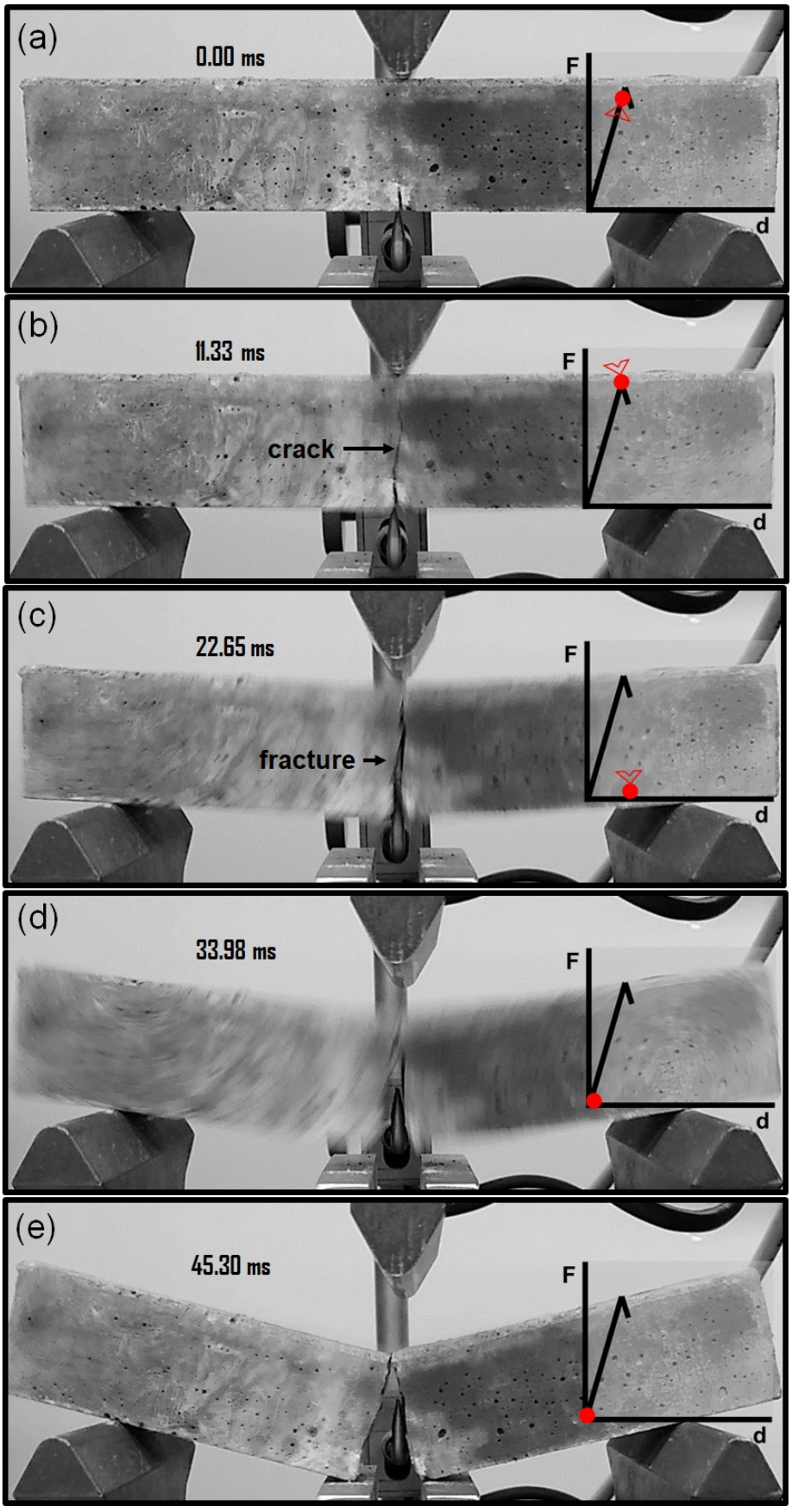

Figure 5.72 – Rupture process during the TPBT illustrated by a sequence of images. A representative sample of the REF group.

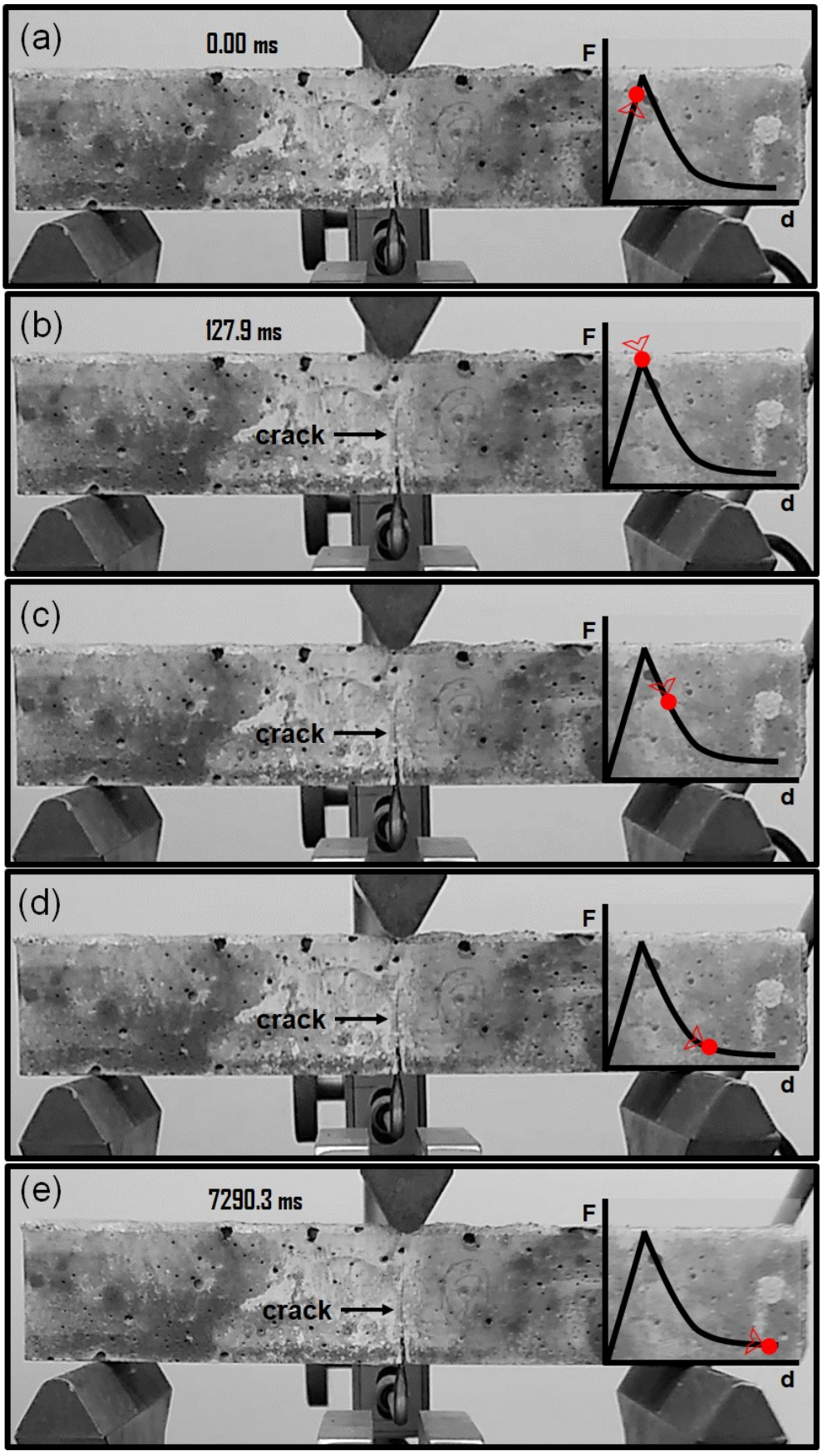

Figure 5.73 – Rupture process during the TPBT illustrated by a sequence of images. A representative sample of the H2A group.

Finally, to illustrate the capacity of the hybrid to promotes adhesion in the RPC matrix, Figure 5.74 shows an image obtained from another video, where one sample from the H2A group, was manually manipulated and secured by one end (like a cantilever beam). Even with a fissure and under agitation, the sample parts remained together. Again, this illustrates the effective capacity of the hybrid to promote reinforcement in the RPC cracked matrix in the region above the end of the crack. Considering the application of this material in real structures, this can be very important in terms of maintaining integrity after some damage and rupture process. Such behavior would also permit to apply a possible maintenance process to restore the structure before its collapse.

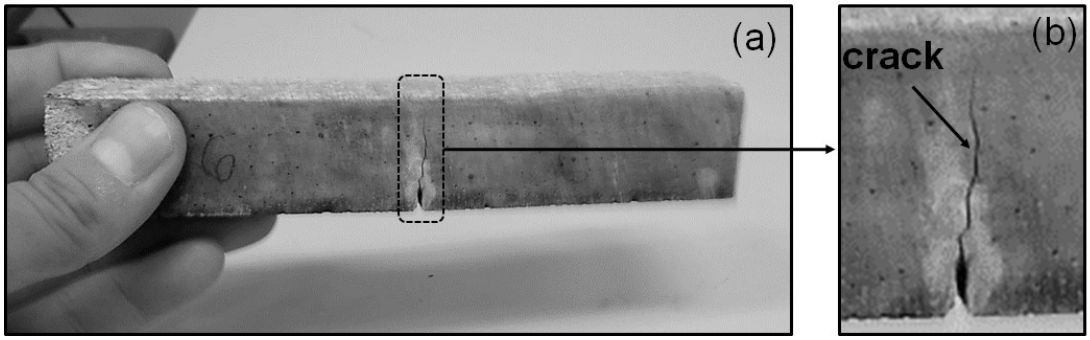

Figure 5.74 – H2A sample pos crack and in a cantilever beam condition after the TPBT.

The evidence of the nano- and micro-scale reinforcement can be seen in Figure 5.75, which shows SEM images of H2R (a-b) and H2A (c-d) samples after the mechanical tests. Figure 5.75a shows a region in the H2R RPC matrix where the cement hydrated phases are present. It is possible to see from the inset (Figure 5.75b) the presence of a CNT (arrow) connecting regions where the C-S-H phase is present. From the analysis of this figure, it is clear that occurred the proposed hypothesis of C-S-H formation over the CNTs in the RPC matrix due to the presence of the hybrid. In Figure 5.75c, a crack is shown in the matrix of a H2A sample. From these images, it is possible to identify a CNT acting as a reinforcement point (Figure 5.75d) in the microscale of the cementitious structure.

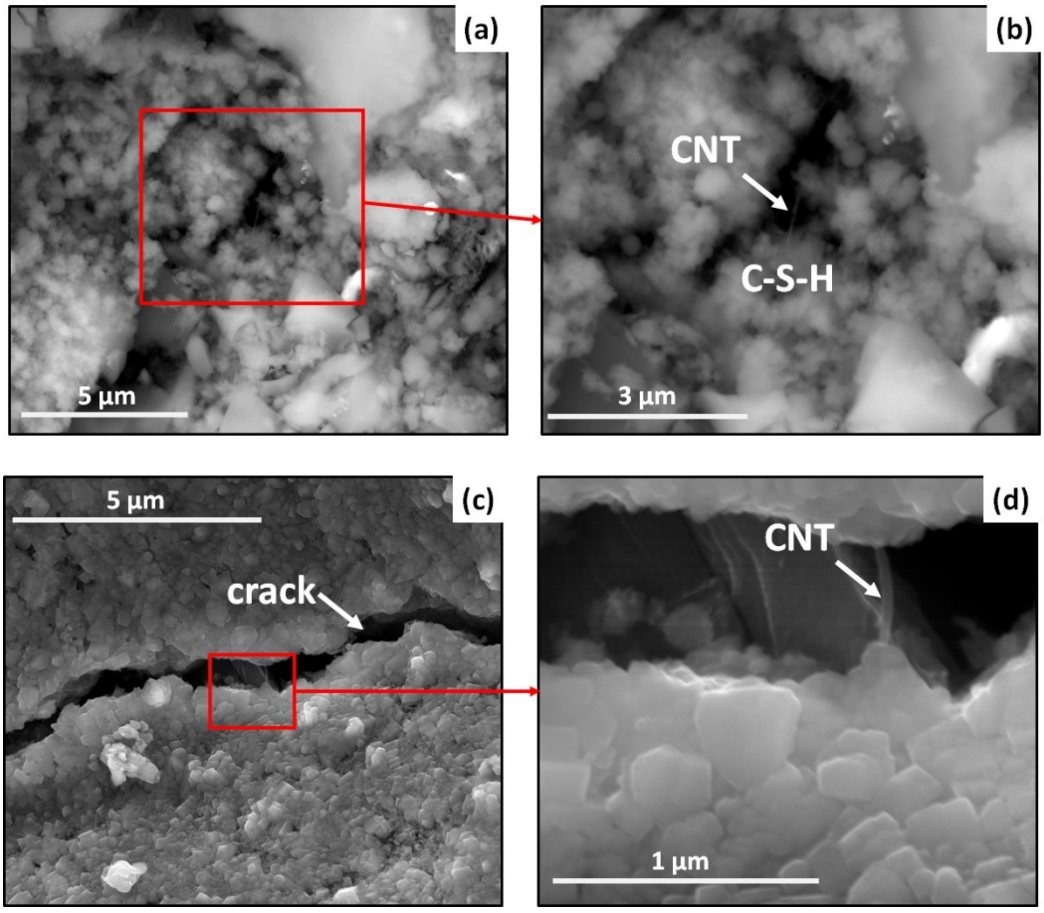

Figure 5.75 – Representative SEM images of RPC groups H2R (a and b) and H2A (c and d) after mechanical tests.

6. SUMMARY AND CONCLUSIONS

This study explored routes to produce carbon nanotubes and nanostructured silica with specific and desired features, to obtain a hybrid material. This concept was defined to solve a great problem relative to the use of CNTs in cementitious materials: the adequate dispersion of the nanomaterials. Considering the development of this hybrid, its application was made in RPC to verify, mainly, its effect in terms of toughness gains. Starting from the preliminary hypothesis, going through the development, and finishing with the evaluation of the results obtained with the material, the followed points are presented as conclusions.

Using the sol-gel method, nanostructured silicas with controlled physical features have been successfully synthesized. Variations in parameters of the process allowed obtaining five different silicas, with significant differences in specific surface area and porosity. It was verified that according to the bibliography, the use of an acidic catalyst in the sol-gel process led to a high superficial surface area (SSA ≈ 400 - 900 $m^2.g^{-1}$) and small pore diameters (≈ 2 - 8 nm). Also, when a basic catalyst was used or without catalyst, silicas with spherical morphology were obtained, with smaller SSA (≈ 220 $m^2.g^{-1}$).

By the catalytic chemical vapor deposition method (CCVD), and using these five nanostructured silicas (as support) and an iron-based catalyst, multi-walled carbon nanotubes were synthesized. Differences in terms of quality and quantity were observed, indicating a clear influence of the substrate (silicas) on the results. Using correlations between the physical parameters of the substrate and the quality and quantity of the produced MWCNTs, the silica synthesized without catalyst (in the sol-gel process) presented a better behavior. In this silica, the presence of macroscopic pores with compatible size for the catalyst particles may have allowed a better anchoring of them. Thus, the cluster formation of catalyst particles did not occur, inducing consequently the growth of MWCNTs with a good quantity and quality.

When the influence of the catalyst incorporation method was evaluated, the MWCNT features changed due to the interaction between the iron-catalyst and the silica supports. The method influenced the catalyst/support interaction and

consequently, different carbon structures were deposited during the CCVD process. Using the impregnation method, the carbon structures deposited after the CCVD method were mainly MWCNTs. Moreover, the synthesized hybrid material showed carbon nanotubes with higher graphitization degree and thermal stability.

Considering the adequate silica support and iron-catalyst incorporation method, it was possible to produce the hybrid material with MWCNTs, using a rotative reactor, with quality and aspect ratio adequate for the fabrication of functionalized RPC composite, with the desirable characteristics for micro-structural scale reinforcement.

The tests employed to evaluate the influence of the amount of the hybrid in the cement hydration process showed that 2% bwoc was an adequate quantity to promote the pozzolanic effect, without significantly impairing the hydration process. First, by the chemical method, it was verified that the hybrid influenced de Ca^{+2} adsorption and diffusion processes, an important condition to promote the pozzolanic effect. Later, by the other analyzes, it was also verified that the hybrid modified the cement hydration process, and the hypothesis of additional C-S-H generation around the CNTs was confirmed. This was evidenced by Figure 5.75b.

Considering the results of the mechanical tests in RPC samples, it was clear that independent of the amount of the hybrid, improvements in the compressive strength and flexural tensile strength did not occur. However, it is worth mentioning that these parameters are specifically related to the mechanical capacity of the cement hydrated matrix, before the cracks formation and propagation process. This can be verified from the statistically equivalent values of the tensile strain at the peak for all groups.

After the formation process and propagation of the cracks, the strength was no longer resisted by the matrix, but by the composite with the fiber elements, in this case, the MWCNTs. Thus, the mechanical reinforcement, now from the toughness behavior, was achieved by the addition of the hybrid, with an amount of 2% bwoc.

The RPC groups with 2% bwoc of the hybrid had improvements in the fracture energy from 98% up to 134%, comparing with the REF group (without the hybrid). This performance was possible with the significant improvement of toughness (E_2) after the peak load. In this case, the increases were in the order of 400 up to 1,000%, comparing with the REF group. These amounts prove the provision of gains in terms of toughness behavior.

It was verified that differently from the literature review, which indicates CNTs optimal upper limit concentrations around 0.15-0.2% bwoc using the physical mixture process, the use of the hybrid allowed the incorporation of much higher contents of MWCNTs (≈0.7%), solving the dispersion problem and resulting in the expressive gains mentioned previously.

7. SUGGESTIONS FOR FUTURE WORKS

Considering the development of this new material and the possibilities that it can provide the following topics are suggestions for future works:

- Produce the hybrid (n-SiO_2/CNTs) considering the catalyst incorporation method by impregnation and using the different silica supports synthesized. The influence in the CNT quality and quantity must be evaluated.

- Produce the hybrid (n-SiO_2/CNTs) considering the use of another carbon source in the CCVD process, as natural gas for example, and change (decrease) the temperature process. The influence in the CNT quality and quantity must be evaluated.

- Study the influence of the hybrid in reactive powder concretes (RPC), considering the amount used in this work and other variations, in terms of mechanical behavior in other cure ages (after 3 days), verifying possible changes in the performance.

- Study the synergy effect of the hybrid (n-SiO_2/CNTs) and fibers (polymeric or metallic) or MWCNTs synthesized directly over cement, in the mechanical performance of RPC and verified the contribution of the hybrid in crack propagation development. This study can be carried out using advanced methods to visualize the fracture behavior, like the technology of digital image correlate (DIC).

- Study the effect of the hybrid in cement pastes, mortars, and RPC used in retrofitting concrete structures.

8. INTELECTUAL AND SCIENTIFIC PRODUCTIONS

During the period that comprised the development of this Thesis, some scientific papers were published, and patents were deposited. These are listed below.

Articles in scientific journals:

SILVA, L. M.C.; GONÇALVES, B. S.; BRAGA, J. O.; **SOUZA, T. C. C**.; CASTRO, V. G.; SILVA, G. G.; LACERDA, G. R. B. S.; MATENCIO, T.; BARBOSA, T. C.; VIANA, C. M.; HOUMARD, M.; NUNES, E. H. M. *Preparation of titania-reduced graphene oxide composite coatings with electro- and photosensitive properties*. *APPLIED SURFACE SCIENCE*, v. 538, p. 148029, 2021.
DOI: 10.1016/j.apsusc.2020.148029.

SOUZA, T. C. C.; MELO, A. C. O.; BARBOSA, T. C.; MARTINS, C. V.; LADEIRA, L. O.; HOUMARD, M. *Influence of the Fe-based catalyst incorporation method on the carbon nanotube structure of hybrid composites synthesized by CCVD method using methane and without hydrogen reduction step*. CERAMICS INTERNATIONAL, v. In Pre, p. 1, 2020.
DOI: 10.1016/j.ceramint.2020.11.040

SOUZA, T. C. C.; PINTO, G.; CRUZ, V. S.; MOURA, M.; LADEIRA, L. O.; CALIXTO, J. M. *Evaluation of the rheological behavior, hydration process, and mechanical strength of Portland cement pastes produced with carbon nanotubes synthesized directly on clinker.* CONSTRUCTION AND BUILDING MATERIALS, v. 248, p. 118686, 2020.
DOI: 10.1016/j.conbuildmat.2020.118686

SOARES, P. A.; BENEDETTI, A. Z.; **SOUZA, T. C. C**.; CALIXTO, J. M. F.; LADEIRA, L. O. *Early-age behavior of blast-furnace slag cement pastes produced with carbon nanotubes grown directly on clinker*. REVISTA IBRACON DE ESTRUTURAS E MATERIAIS, v. 13, p. 603-612, 2020.
DOI: 10.1590/s1983-41952020000300010

SOUZA, T. C. C.; BRASIL, A.; LADEIRA, L. O.; HOUMARD, M. *Influence of the nanostructure of silica supports on the growth and morphology of MWCNTs synthesized by CCVD method.* CERAMICS INTERNATIONAL, v. 45, p. 13297-13307, 2019.
DOI: 10.1016/j.ceramint.2019.04.019

GONCALVES, B. S.; PALHARES, H. G.; **SOUZA, T. C. C.**; CASTRO, V. G.; SILVA, G. G.; SILVA, B. C.; KRAMBROCK, K.; SOARES, R. B.; LINS, V. S. C.; HOUMARD, M.; NUNES, E. H. M. *Effect of the carbon loading on the structural and photocatalytic properties of reduced graphene oxide-TiO2 nanocomposites prepared by hydrothermal synthesis*. JOURNAL OF MATERIALS RESEARCH AND TECHNOLOGY-JMR&T, v. 8, p. 1-13, 2019.
DOI: 10.1016/j.jmrt.2019.10.020

GONÇALVES, B. S.; SILVA, L. M.C.; **SOUZA, T. C. C**.; CASTRO, V. G.; SILVA, G. G.; SILVA, B.C.; KRAMBROCK, K.; SOARES, R. B.; LINS, V. F.C.; HOUMARD, M.; NUNES, E. H. M. *Solvent effect on the structure and photocatalytic behavior of TiO_2-RGO nanocomposites.* JOURNAL OF MATERIALS RESEARCH, v. 22, p. 1-13, 2019.
DOI: 10.1557/jmr.2019.342

PAULA, J. N.; CALIXTO, J. M.; LADEIRA, L. O.; LUDVIG, P.; **SOUZA, T. C. C**. *Tensile Strength of Oil-Well Cement Pastes Produced with Carbon Nanotubes Directly Synthesized on Clinker.* THE INTERNATIONAL JOURNAL OF ENGINEERING AND SCIENCE, v. 7, p. 57-62, 2018.
DOI: 10.9790/1813-0707015762

LUDVIG, P.; CALIXTO, J. M. F.; LADEIRA, L. O.; **SOUZA, T. C. C.**; Paula, J. N. *Analysis of Cementitious Composites Prepared with Carbon Nanotubes and Nanofibers Synthesized Directly on Clinker and Silica Fume*. JOURNAL OF MATERIALS IN CIVIL ENGINEERING, v. 29, p. 06017001, 2017.
DOI: 10.1061/(ASCE)MT.1943-5533.0001836

Conference:

SOUZA, T. C. C.; BRASIL, A.; CALIXTO, J. M. F.; LADEIRA, L. O.; HOUMARD, M. . *Synthesis and characterization of carbon nanotubes by CVD method supported in SiO_2 nanostructured to applied in cementitious matrix*. 2017 - 18th International Conference on the Science and Application of Nanotubes and Low dimensional Materials. Belo Horizonte-MG/Brazil.

Deposited patents:

Patente: Privilégio de Inovação. Número do registro: BR1020170113345, título: "PROCESSO PARA SÍNTESE DE NANOMATERIAIS DE CARBONO SOBRE ESCÓRIA DE ALTO-FORNO, PRODUTOS E USO", Brasil. Instituição de registro: INPI - Instituto Nacional da Propriedade Industrial. Depósito: 30/05/2017. LADEIRA, L.O; DIAS, A. E.; OLIVEIRA, S. ; CALIXTO, J. M. F. ; **SOUZA, T. C. C**.

Patente: Privilégio de Inovação. Número do registro: BR10201702103, título: "MÉTODO DE SÍNTESE DE GRAFENO 3D A PARTIR DO POLITEREFTALATO DE ETILENO (PET)", Brasil. Instituição de registro: INPI - Instituto Nacional da Propriedade Industrial. Depósito: 29/09/2017. LADEIRA, L. O.; VIANA, C. O.; **SOUZA, T. C. C**.; RAMOS, S. L. L. M.

Patente: Modelo de Utilidade. Número do registro: BR10201701985, título: "REATOR PARA SÍNTESE CONTÍNUA DE NANOTUBOS DE CARBONO SOBRE MATERIAIS CIMENTÍCIOS", Brasil. Instituição de registro: INPI - Instituto Nacional da Propriedade Industrial. Depósito: 15/09/2017. LADEIRA, L. O.; CALIXTO, J. M.; **SOUZA, T. C. C**.; LUDVIG, P.

Patente: Privilégio de Inovação. Número do registro: BR1020190143320, título: ”PROCESSO DE TRATAMENTO DA CAREPA DE LAMINAÇÃO E USO DE SEU PRODUTO COMO CATALISADOR NA SÍNTESE DE NANOTUBOS OU NANOFIBRAS DE CARBONO EM MATRIZES CIMENTÍCIAS”, Brasil. Instituição de registro: INPI - Instituto Nacional da Propriedade Industrial. Depósito: 10/07/2019. OLIVEIRA, R. Q. F. G.; LADEIRA, L. O.; CALIXTO, J. M. F.; **SOUZA, T. C. C.**

Patente: Privilégio de Inovação. Número do registro: BR10201901872, título: "PROCESSOS DE COBERTURA DE CARBONO NANOESTRUTURADO SOBRE SUBSTRATO CERÂMICO E/OU GRANULAR UTILIZANDO POLIETILENO TEREFTALATO (PET) COMO PRECURSOR DE CARBONO E USOS", Brasil. Instituição de registro: INPI - Instituto Nacional da Propriedade Industrial. Depósito: 10/09/2019. LADEIRA, L. O.; CALIXTO, J. M. F.; WILMER, A. M.; SANTOS, T. G.; OLIVEIRA, R. K. F. G.; **SOUZA, T. C. C**.

9. BIBLIOGRAPHICAL REFERENCES

ABNT – ASSOCIAÇÃO BRASILEIRA DE NORMAS TÉCNICAS - **NBR 7214** - Areia normal para ensaios de cimento – Especificação. Rio de Janeiro, 2015.

ABNT – ASSOCIAÇÃO BRASILEIRA DE NORMAS TÉCNICAS - **NBR 7215** - Cimento Portland - Determinação da resistência à compressão de corpos de prova cilíndricos. Rio de Janeiro, 2019.

ABNT – ASSOCIAÇÃO BRASILEIRA DE NORMAS TÉCNICAS - **NBR 11768** - Aditivos químicos para concreto de cimento Portland – Parte 1: Requisitos. Rio de Janeiro, 2019.

ABNT – ASSOCIAÇÃO BRASILEIRA DE NORMAS TÉCNICAS - **NBR 13956** - Sílica ativa para uso com cimento Portland em concreto, argamassa e pasta. Rio de Janeiro, 2012.

ABNT – ASSOCIAÇÃO BRASILEIRA DE NORMAS TÉCNICAS - **NBR 16372** - Cimento Portland e outros materiais em pó - Determinação da finura pelo método de permeabilidade ao ar (método de Blaine). Rio de Janeiro, 2015.

ABNT – ASSOCIAÇÃO BRASILEIRA DE NORMAS TÉCNICAS - **NBR 16606** - Cimento Portland - Determinação da pasta de consistência normal. Rio de Janeiro, 2018.

ABNT – ASSOCIAÇÃO BRASILEIRA DE NORMAS TÉCNICAS - **NBR 16607** - Cimento Portland — Determinação dos tempos de pega. Rio de Janeiro, 2018.

ABNT – ASSOCIAÇÃO BRASILEIRA DE NORMAS TÉCNICAS - **NBR 16697** - Cimento Portland – Requisitos. Rio de Janeiro, 2019.

ABNT – ASSOCIAÇÃO BRASILEIRA DE NORMAS TÉCNICAS - **NBR NM 14** - Cimento Portland - Análise química - Método de arbitragem para determinação de dióxido de silício, óxido férrico, óxido de alumínio, óxido de cálcio e óxido de magnésio. Rio de Janeiro, 2012.

ABNT – ASSOCIAÇÃO BRASILEIRA DE NORMAS TÉCNICAS - **NBR NM 16** - Cimento Portland - Análise química - Determinação de anidrido sulfúrico. Rio de Janeiro, 2012.

ABNT – ASSOCIAÇÃO BRASILEIRA DE NORMAS TÉCNICAS - **NBR NM 18** - Cimento Portland - Análise química - Determinação de perda ao fogo. Rio de Janeiro, 2012.

ABNT – ASSOCIAÇÃO BRASILEIRA DE NORMAS TÉCNICAS - **NBR NM 19** - Cimento Portand - Análise química - Determinação de enxofre na forma de sulfeto. Rio de Janeiro, 2012.

ABU AL-RUB, R. K.; ASHOUR, A. I.; TYSON, B. M. On the aspect ratio effect of multi-walled carbon nanotube reinforcements on the mechanical properties of cementitious nanocomposites. **Construction and Building Materials**, v. 35, p. 647–655, 2012.

AGUIAR, H.; SERRA, J.; GONZÁLEZ, P.; LEÓN, B. Structural study of sol-gel silicate glasses by IR and Raman spectroscopies. **Journal of Non-Crystalline Solids**, v. 355, n. 8, p. 475–480, 2009.

AHANGARAN, F.; HASSANZADEH, A.; NOURI, S. Surface modification of Fe_3O_4@SiO_2 microsphere by silane coupling agent. **International Nano Letters**, v. 3, n. 1, p. 1–5, 2013.

AKBAR, S.; HASANAIN, S. K.; AZMAT, N.; NADEEM, M. Synthesis of Fe_2O_3 nanoparticles by new Sol-Gel method and their structural and magnetic characterizations. **Condensed Matter**, p. 1–19, 2004.

ALOTHMAN, Z. A. A review: Fundamental aspects of silicate mesoporous materials. **Materials**, v. 5, n. 12, p. 2874–2902, 2012.

ALREKABI, S.; CUNDY, A.; WHITBY, R. L. D.; LAMPROPOULOS, A.; SAVINA, I. Effect of undensified silica fume on the dispersion of carbon nanotubes within a cementitious composite. In: APPLIED NANOTECHNOLOGY AND NANOSCIENCE INTERNATIONAL CONFERENCE, 829., 2016, Barcelona. **Anais…**Bristol: IOP PUBLISHING, 2017.

ALTOMARE, A.; CORRIERO, N.; CUOCCI, C.; FALCICCHIO, A.; MOLITERNI, A.; Rizzi, R. QUALX2.0: A qualitative phase analysis software using the freely available database POW_CODJ. **Journal of Applied Crystallography**, v. 48, p. 598–603, 2015.

ANDREASEN, A. H. M. Ueber die Beziehung zwischen Kornabstufung und Zwischenraum in Produkten aus losen Körnern (mit einigen Experimenten). **Kolloid-Zeitschrift**, v. 50, n. 3, p. 217–228, 1930.

AWADALLAH, A. E.; EL-DESOUKI, D. S.; ABOUL-GHEIT, N. A. K.; IBRAHIM, A. H.; ABOULT-GHEIT, A. K. Effect of crystalline structure and pore geometry of silica based supported materials on the catalytic behavior of metallic nickel particles during methane decomposition to CO_x-free hydrogen and carbon nanomaterials. **International Journal of Hydrogen Energy**, v. 41, n. 38, p. 16890–16902, 2016.

AYDIN, A. C.; NASL, V. J.; KOTAN, T. The synergic influence of nano-silica and carbon nanotube on self-compacting concrete. **Journal of Building Engineering**, v. 20, n. April, p. 467–475, 2018.

AYDIN, S.; BARADAN, B. Engineering properties of reactive powder concrete without Portland cement. **ACI Materials Journal**, v. 110, n. 6, p. 619–627, 2013.

BALAPOUR, M.; JOSHAGHANI, A.; ALTHOEY, F. Nano-SiO_2 contribution to mechanical, durability, fresh and microstructural characteristics of concrete: A review. **Construction and Building Materials**, v. 181, p. 27–41, 2018.

BARRECA, D; BLAU, W. J.; CROKE, G. M.; DEENEY, F. A.; DILLON, F. C.; HOLMES, J. D.; KUFAZVINEI, C.; MORRIS, M. A.; SPALDING, T. R.; TONDELLO, E. Iron oxide nanoparticle impregnated mesoporous silicas as platforms for the growth of carbon nanotubes. **Microporous and Mesoporous Materials**, v. 103, p. 142–149, 2007.

BARRET, E. P.; JOYNER, G.; HALENDA, P. **The determination of pore volume and area distributions in porous substances. I. Computations from nitrogen isotherms**. Report. v. 73, p. 373–380, 1951.

BERRA, M.; CARASSITI, F.; MANGIALARDI, T.; PAOLINI, A. E.; SEBASTIANI, M. Effects of nanosilica addition on workability and compressive strength of Portland cement pastes. **Construction and Building Materials**, v. 35, p. 666–675, 2012.

BHUSHAN, B. **Handbook Springer of Nanotechnology**. Springer-Verlag New York, LLC, 2007.

BJÖRNSTRÖM, J.; MARTINELLI, A.; MATIC, A.; BÖRJESSON, L.; PANAS, I. Accelerating effects of colloidal nano-silica for beneficial calcium-silicate-hydrate formation in cement. **Chemical Physics Letters**, v. 392, n. 1–3, p. 242–248, 2004.

BOM, D.; ANDREWS, R.; JACQUES, D.; ANTHONY, J.; CHEN, B.; MEIER, M. S.; SELEGUE, J. P. Thermogravimetric analysis of the oxidation of multiwalled carbon nanotubes: Evidence for the role of defect sites in carbon nanotube chemistry. **Nano Letters**, v. 2, n. 6, p. 615–619, 2002.

BOURLINOS, A. B.; GEORGAKILAS, V.; ZBORIL, R.; DALLAS, P. Preparation of a water-dispersible carbon nanotube–silica hybrid. **Carbon**, v. 45, n. 10, p. 2136–2139, 2007.

BRUNAUER, S.; EMMETT, P. H.; TELLER, E. **Adsorption of Gases in Multimolecular Layers**. Report. v. 60, p. 309–319, 1938.

BRINKER, C.J.; SCHERER, G. W. **Sol-Gel Science - The physics and chemistry of sol-gel processing**. New York, Academic Press, 1990.

CARNEIRO, L. R. S.; GARCIA, D. C. S.; COSTA, M. C. F.; HOUMARD, M.; FIGUEIREDO, R. B. Evaluation of the pozzolanicity of nanostructured sol-gel silica and silica fume by electrical conductivity measurement. **Construction and Building Materials**, v. 160, p. 252–257, 2018.

CASTRICUM, H. L.; PARADIS, G. G.; MITTELMEIJER-HAZELEGER, M. C.; BRAS, W.; EECKHAUT, G.; VENTE, J. F.; ROTHENBERG, G.; TEN ELSHOF, J. E. Tuning the nanopore structure and separation behavior of hybrid organosilica membranes. **Microporous and Mesoporous Materials**, v. 185, p. 224–234, 2014.

CASTRICUM, H. L.; QURESHI, H. F.; NIJMEIJER, A.; WINNUBST, L. Hybrid silica membranes with enhanced hydrogen and CO_2 separation properties. **Journal of Membrane Science**, v. 488, p. 121–128, 2015.

CI, L.; WEI, B.; XU, C.; LIANG, J.; WU, D.; XIE, S.; ZHOU, W.; LI, Y.; LIU, Z.; TANG, D. Crystallization behavior of the amorphous carbon nanotubes prepared by the CVD method. **Journal of Crystal Growth**, v. 233, n. 4, p. 823–828, 2001.

COLEMAN, J. N.; KHAN, U.; BLAU, W. J.; GUN'KO, Y. K. Small but strong: A review of the mechanical properties of carbon nanotube–polymer composites. **Carbon**, v. 44, n. 9, p. 1624–1652, 2006.

CUI, H.; YANG, S.; MEMON, S. A. Development of carbon nanotube modified cement paste with microencapsulated phase-change material for structural–functional integrated application. **International Journal of Molecular Sciences**, v. 16, n. 4, p. 8027–8039, 2015.

CUI, X.; HAN, B.; ZHENG, Q.; YU, X.; DONG, S.; ZHANG, L.; OU, J. Mechanical properties and reinforcing mechanisms of cementitious composites with different types of multiwalled carbon nanotubes. **Composites Part A**: **Applied Science and Manufacturing**, v. 103, p. 131–147, 2017.

CUNHA, T. H. R.; OLIVEIRA, S.; MARTINS, I. L.; GERALDO, V.; MIQUITA, D.; RAMOS, S. L. M.; LACERDA, R. G.; LADEIRA, L. O.; FERLAUTO, A. S. High-yield synthesis of bundles of double- and triple-walled carbon nanotubes on aluminum flakes. **Carbon**, v. 133, p. 53–61, 2018.

CWIRZEN, A.; PENTTALA, V.; VORNANEN, C. Reactive powder-based concretes: Mechanical properties, durability and hybrid use with OPC. **Cement and Concrete Research**, v. 38, n. 10, p. 1217–1226, 2008.

DE LOS ARCOS, T.; VONAU, F.; GARNIER, M. G.; THOMMEN, V.; BOYEN, H. G.; OELHAFEN, P.; DÜGGELIN, M.; MATHIS, D.; GUGGENHEIM, R. Influence of iron-silicon interaction on the growth of carbon nanotubes produced by chemical vapor deposition. **Applied Physics Letters**, v. 80, n. 13, p. 2383–2385, 2002.

DILEO, R. A.; LANDI, B. J.; RAFFAELLE, R. P. Purity assessment of multiwalled carbon nanotubes by Raman spectroscopy. **Journal of Applied Physics**, v. 101, n. 6, p. 1–6, 2007.

DONG, S.; ZHOU, D.; ASHOUR, A.; HAN, B. OU, J. Flexural toughness and calculation model of super-fine stainless wire reinforced reactive powder concrete. **Cement and Concrete Composites**, v. 104, n. July, p. 103367–103380, 2019.

DONG, S.; DONG, X.; ASHOUR, A.; HAN, B. OU, J. Fracture and self-sensing characteristics of super-fine stainless wire reinforced reactive powder concrete. **Cement and Concrete Composites**, v. 105, n. September 2019, p. 103427–103441, 2020.

DOUVEN, S.; PIRARD, S. L.; HEYEN, G.; TOYE, D.; PIRARD, J. P. Kinetic study of double-walled carbon nanotube synthesis by catalytic chemical vapor deposition over a Fe-Mo / MgO catalyst using methane as the carbon source. **Chemical Engineering Journal**, v. 175, p. 396–407, 2011.

DUBEY, R. S.; RAJESH, Y. B. R. D.; MORE, M. A. Synthesis and characterization of SiO_2 nanoparticles via sol-gel method for industrial applications. **Materials Today: Proceedings**, v. 2, n. 4–5, p. 3575–3579, 2015.

DUNENS, O. M.; MACKENZIE, K. J.; HARRIS, A. T. Synthesis of multiwalled carbon nanotubes on fly ash derived catalysts. **Environmental Science and Technology**, v. 43, n. 20, p. 7889–7894, 2009.

DUPUIS, A. C. The catalyst in the CCVD of carbon nanotubes – a review. **Progress in Materials Science**, v. 50, p. 929–961, 2005.

DWECK, J.; CHEREM DA CUNHA, A. L.; PINTO, C. A.; PEREIRA, J. G.; BÜCHLER, P. M. Thermogravimetry on calcined mass basis - Hydrated cement phases and pozzolanic activity quantitative analysis. **Journal of Thermal Analysis and Calorimetry**, v. 97, n. 1, p. 85–89, 2009.

ESCOBAR, M.; MORENO, M. S.; CANDAL, R. J.; MARCHI, M. C.; CASO, A.; POLOSECKI, P. I.; RUBIOLO, G. H.; GOYANES, S. Synthesis of carbon nanotubes by CVD: Effect of acetylene pressure on nanotubes characteristics. **Applied Surface Science**, v. 254, n. 1 SPEC. ISS., p. 251–256, 2007.

ESCONJAUREGUI, S.; FOUQUET, M.; BAYER, B. C.; ESLAVA, S.; KHACHADORIAN, S.; HOFMANN, S.; ROBERTSON, J. Manipulation of the catalyst-support interactions for inducing nanotube forest growth. **Journal of Applied Physics**, v. 109, n. 4, p. 1–7, 2011.

FEHERVARI, A.; MACLEOD, A. J. N.; GARCEZ, E. O.; ALDRIDGE, L.; GATES, W. P.; YANG, Y.; COLLINS, F. On the mechanisms for improved strengths of carbon nanofiber-enriched mortars. **Cement and Concrete Research**, v. 136, n. July, p. 106178–106189, 2020.

FERRO, G.; TULLIANI, J. M.; JAGDALE, P.; RESTUCCIA, L. New Concepts for Next Generation of High-Performance Concretes. **Procedia Materials Science**, v. 3, p. 1760–1766, 2014.

FRAGA, J. L.; MARÍA, J.; GARCÍA, J. Á. Carbon Nanotube-Cement Composites in the Construction Industry: 1952-2014. A State of the Art Review. In: 2nd INTERNATIONAL CONFERENCE ON EMERGING TRENDS IN ENGINEERING AND TECHNOLOGY (ICETET'2014), 2014, London. **Anais**... London, 2014.

GALLEGO, J.; BATIOT-DUPEYAT, C.; MONDRAGÓN, F. Activation energies and structural changes in carbon nanotubes during different acid treatments. **Journal of Thermal Analysis and Calorimetry**, v. 114, n. 2, p. 597–602, 2013.

GAO, J.; ZHONG, J.; BAI, L.; LIU, J.; ZHAO, G.; SUN, X. Revealing the role of catalysts in carbon nanotubes and nanofibers by scanning transmission X-Ray microscopy. **Scientific Reports**, v. 4, p. 1–6, 2014.

GDOUTOS, E. E.; KONSTA-GDOUTOS, M. S.; DANOGLIDIS, P. A.; SHAH, S. P. Advanced cement-based nanocomposites reinforced with MWCNTs and CNFs. **Frontiers of Structural and Civil Engineering**, v. 10, n. 2, p. 142–149, 2016.

GDOUTOS, E. E.; KONSTA-GDOUTOS, M. S.; DANOGLIDIS, P. A. Portland cement mortar nanocomposites at low carbon nanotube and carbon nanofiber content: A fracture mechanics experimental study. **Cement and Concrete Composites**, v. 70, p. 110–118, 2016.

GOHIER, A.; EWELS, C. P.; MINEA, T. M.; DJOUADI, M. A. Carbon nanotube growth mechanism switches from tip- to base-growth with decreasing catalyst particle size. **Carbon**, v. 46, n. 10, p. 1331–1338, 2008.

GUO, Q.; HUANG, D.; KOU, X.; CAO, W.; LI, L.; GE, L.; LI, J. Synthesis of disperse amorphous SiO_2 nanoparticles via sol-gel process. **Ceramics International**, v. 43, n. 1, p. 192–196, 2017.

GUPTA, D.; SINGH, N. B.; CHOUDHARY, B. P.; GAJBNIYE, N. S. Carbon nanotubes: an overview. **Emerging Materials Research**, v. 2, n. EMR6, p. 299–337, 2013.

HAMBACH, M.; MÖLLER, H.; NEUMANN, T.; VOLKMER, D. Portland cement paste with aligned carbon fibers exhibiting exceptionally high flexural strength (> 100 MPa). **Cement and Concrete Research**, v. 89, p. 80–86, 2016.

HAN, B.; SUN, S.; DING, S.; ZHANG, L.; YU, X.; OU, J. Review of nanocarbon-engineered multifunctional cementitious composites. **Composites Part A: Applied Science and Manufacturing**, v. 70, p. 69–81, 2015.

HAN, B.; DONG, S.; OU, J.; ZHANG, C.; WANG, Y.; YU, X.; DING, S. Microstructure related mechanical behaviors of short-cut super-fine stainless wire reinforced reactive powder concrete. **Materials and Design**, v. 96, p. 16–26, 2016.

HAN, B.; LI, Z.; ZHANG, L.; ZENG, S.; YU, X.; HAN, B.; OU, J. Reactive powder concrete reinforced with nano SiO_2 -coated TiO_2. **Construction and Building Materials**, v. 148, p. 104–112, 2017a.

HAN, B.; ZHANG, L.; ZENG, S.; DONG, S.; YU, X.; YANG, R.; OU, J. Nano-core effect in nano-engineered cementitious composites. **Composites Part A: Applied Science and Manufacturing**, v. 95, p. 100–109, 2017b.

HELMI, M.; HALL, M. R.; STEVENS, L. A.; RIGBY, S. P. Effects of high-pressure/temperature curing on reactive powder concrete microstructure formation. **Construction and Building Materials**, v. 105, p. 554–562, 2016.

HENCH, L.; VASCONCELOS, W. Gel-Silica Science. **Annual Review of Materials Science**, v. 20, n. Table 1, p. 269–298, 1990.

HIRATSUKA, R. S.; SANTILLI, C. V.; PULCINELLI, S. H. O processo sol-gel: uma visão físico-química - Revisão. **Química nova**, v. 18, n. 2, p. 171–180, 1995.

HIREMATH, P. N.; YARAGAL, S. C. Influence of mixing method, speed and duration on the fresh and hardened properties of Reactive Powder Concrete. **Construction and Building Materials**, v. 141, p. 271–288, 2017.

HOMMA, Y.; KOBAYASHI, Y.; OGINO, T.; TAKAGI, D.; ITO, R.; JUNG, Y. J.; AJAYAN, P. M. Role of transition metal catalysts in single-walled carbon nanotube growth in chemical vapor deposition. **The Journal of Physical Chemistry B**, v. 107, n. 44, p. 12161–12164, 2003.

HONG, G.; CHEN, Y.; LI, P.; ZHANG, J. Controlling the growth of single-walled carbon nanotubes on surfaces using metal and non-metal catalysts. **Carbon**, v. 50, p. 2067–2082, 2012.

HOU, P.; KAWASHIMA, S.; KONG, D.; COOR, D. J.; QIAN, J.; SHAH, S. P. Modification effects of colloidal nanoSiO_2 on cement hydration and its gel property. **Composites Part B: Engineering**, v. 45, n. 1, p. 440–448, 2013.

HOU, P.; QIAN, J.; CHENG, X.; SHAH, S. P. Effects of the pozzolanic reactivity of nanoSiO_2 on cement-based materials. **Cement & Concrete Composites**, v. 55, p. 250–258, 2015.

HOUMARD, M.; NUNES, E. H. M.; VASCONCELOS, D. C. L.; BERTHOMÉ, G.; JOUDd, J.-C.; LANGLET, M.; VASCONCELOS, W. L. Correlation between sol-gel reactivity and wettability of silica films deposited on stainless steel. **Applied Surface Science**, v. 289, p. 218–223, jan. 2014.

IIJIMA, S. Helical microtubules of graphitic carbon. **Nature**, v. 354, n. 6348, p. 56–58, 1991.

INNOCENZI, P. Infrared spectroscopy of sol-gel derived silica-based films: a spectra-microstructure overview. **Journal of Non-Crystalline Solids**, v. 316, p. 309–319, 2003.

JOURDAIN, V.; BICHARA, C. Current understanding of the growth of carbon nanotubes in catalytic chemical vapor deposition. **Carbon**, v. 58, p. 2–39, 2013.

JUNG, H. Y.; GUPTA, R. K.; OH, E. O.; KIM, Y. H.; WHANG, C. M. Vibrational spectroscopic studies of sol-gel derived physical and chemical bonded ORMOSILs. **Journal of Non-Crystalline Solids**, v. 351, n. 5, p. 372–379, 2005.

JUNG, S. H.; OH, S.; KIM, S. W.; MOON, J. H. Effects of CNT dosages in cement composites on the mechanical properties and hydration reaction with low water-to-binder ratio. **Applied Sciences**, v. 9, n. 21, p. 2–13, 2019.

KALRA, M.; SAXENA, S. K. Nanoscience of cement and concrete. **Materials Today: Proceedings**, v. 4, n. 4, p. 5478–5487, 2017.

KHALOO, A.; MOBINI, M. H.; HOSSEINI, P. Influence of different types of nano-SiO_2 particles on properties of high-performance concrete. **Construction and Building Materials**, v. 113, p. 188–201, 2016.

KHARISSOVA, O. V.; KHARISOV, B. I. Variations of interlayer spacing in carbon nanotubes. **RSC Advances**, v. 4, n. 58, p. 30807–30815, 2014.

KIM, G. M.; KIM, Y. K.; KIM, Y. J.; SEO, J. H.; YANG, B. J.; LEE, H. K. Enhancement of the modulus of compression of calcium silicate hydrates via covalent synthesis of CNT and silica fume. **Construction and Building Materials**, v. 198, p. 218–225, 2019.

KIM, Y. J.; SHIN, T. S.; CHOI, H. D.; KWON, J. H.; CHUNG, Y. C.; YOON, H. G. Electrical conductivity of chemically modified multiwalled carbon nanotube/epoxy composites. **Carbon**, v. 43, n. 1, p. 23–30, 2005.

KONG, D.; SU, Y.; DU, X. YANG, Y.; WEI, S.; SHAH, S. P. Influence of nano-silica agglomeration on fresh properties of cement pastes. **Construction and Building Materials**, v. 43, p. 557–562, 2013.

KORAYEM, A. H.; TOURANI, N.; ZAKERTABRIZI, M.; SABZIPARVAR, A. M.; DUAN, W. H. A review of dispersion of nanoparticles in cementitious matrices: Nanoparticle geometry perspective. **Construction and Building Materials**, v. 153, p. 346–357, 2017.

KUMAR, M. Carbon nanotube synthesis and growth mechanism. **In**: YELLAMPALLI, S. (Ed.). Carbon Nanotubes - Synthesis, Characterization, Applications. Shangai: INTECH, 2011. v. 6p. 147–170.

KUMAR, M.; ANDO, Y. Chemical Vapor Deposition of Carbon Nanotubes: A review on growth mechanism and mass production. **Journal of Nanoscience and Nanotechnology**, v. 10, n. 6, p. 3739–3758, 2010.

KUNTHER, W.; FERREIRO, S.; SKIBSTED, J. Influence of the Ca/Si ratio on the compressive strength of cementitious calcium-silicate-hydrate binders. **Journal of Materials Chemistry A**, v. 5, n. 33, p. 17401–17412, 2017.

KUTTERI, A. D.; WANG, I. W.; ANUPAM, S.; LI, L.; HU, J. Methane decomposition to tip and base grown carbon nanotubes and CO_x-free H_2 over mono- and bimetallic 3d transition metal catalysts. **Catalysis Science and Technology**, v. 8, n. 3, p. 858–869, 2018.

LAND, G.; STEPHAN, D. The influence of nano-silica on the hydration of ordinary Portland cement. **Journal of Materials Science**, v. 47, n. 2, p. 1011–1017, 2012.

LAVERGNE, F.; BELHADI, R.; CARRIAT, J.; FRAJ, A. B. Effect of nano-silica particles on the hydration, the rheology and the strength development of a blended cement paste. **Cement and Concrete Composites**, v. 95, n. May 2018, p. 42–55, 2019.

LEE, M. G.; WANG, Y. C.; CHIU, C. TE. A preliminary study of reactive powder concrete as a new repair material. **Construction and Building Materials**, v. 21, n. 1, p. 182–189, 2007.

LEHMAN, J. H.; TERRONES, M.; MANSFIELD, E.; HURST, K. E.; MEUNIER, V. Evaluating the characteristics of multiwall carbon nanotubes. **Carbon**, v. 49, n. 8, p. 2581–2602, 2011.

LI, W.; JI, W.; ISFAHANI, F. T.; WANG, Y.; LI, G.; LIU, Y.; XING, F. Nano-silica sol-gel and carbon nanotube coupling effect on the performance of cement-based materials. **Nanomaterials**, v. 7, n. 185, p. 1–15, 2017.

LI, Y.; LI, H.; WANG, Z.; JIN, C. Effect and mechanism analysis of functionalized multi-walled carbon nanotubes (MWCNTs) on C-S-H gel. **Cement and Concrete Research**, v. 128, p. 105955–105967, 2020.

LIN, J. H.; CHEN, C. S.; RÜMMELI, M. H.; BACHMATIUK, A.; ZENG, Z. Y.; MA, H. L.; BÜCHNER, B.; CHEN, H. W. Growth of carbon nanotubes catalyzed by defect-rich graphite surfaces. **Chemistry of Materials**, v. 23, n. 7, p. 1637–1639, 2011.

LIU, J.; JIN, H.; ZHAO, X.; WANG, C. Effect of multi-walled carbon nanotubes on improving the toughness of reactive powder concrete. **Materials**, v. 12, n. 16, 2019.

LIVAGE, J.; SANCHEZ, C.; HENRY, M.; DOEUFF, S. The chemistry of the sol-gel process. **Solid State Ionics**, v. 32–33, n. PART 2, p. 633–638, 1989.

LONG, G.; MA, K.; SHI, Y.; XIE, Y. Reactive powder concrete reinforced by nanoparticles. **Advances in Cement Research**, v. 28, n. 2, p. 99–109, 2016.

LU, L.; OUYANG, D.; XU, W. Mechanical properties and durability of ultra high strength concrete incorporating multi-walled. **Materials**, v. 9, n. 419, p. 1–11, 2016.

LUDVIG, P.; CALIXTO, J. M.; LADEIRA, L. O.; GASPAR, I. C. P. Using converter dust to produce low-cost cementitious composites by in situ carbon nanotube and nanofiber synthesis. **Materials**, v. 4, n. 12, p. 575–584, 2011.

LUXAN M. P.; MADRUGA F.; SAAVEDRA J. Rapid evaluation of pozzolanic activity of natural products. **Cement and Concrete Research**, v. 19, p. 63–68, 1989.

MAGREZ, A.; SEO, W. S.; SMAJDA, R.; MIONIĆ, M.; FORRÓ, L. Catalytic CVD synthesis of carbon nanotubes: Towards high yield and low-temperature growth. **Materials**, v. 3, p. 4871–4891, 2010.

MAKAR, J. M.; CHAN, G. W. Growth of cement hydration products on single-walled carbon nanotubes. **Journal of the American Ceramic Society**, v. 92, n. 6, p. 1303–1310, 2009.

MAKAR, J.; MARGESON, J.; LUH, J. **Carbon Nanotube / Cement Composites – Early Results and Potential Applications**. Report. NRCC-47643, Institute for Research in Construction, Ontario, p. 1–10, 2005.

MANZUR, T.; YAZDANI, N.; EMON, M. A. B. Effect of carbon nanotube size on compressive strengths of nanotube-reinforced cementitious composites. **Journal of Materials**, v. 2014, p. 1–8, 2014.

MARTIN-GULLON, I.; VERA, J.; CONESA, J. A.; GONZÁLEZ, J. L.; MERINO, C. Differences between carbon nanofibers produced using Fe and Ni catalysts in a floating catalyst reactor. **Carbon**, v. 44, n. 8, p. 1572–1580, 2006.

MASLEN, E. N.; STRELTSOV, V. A.; STRELTSOVA, N. R.; ISHIZAWA, N. Synchrotron X-ray study of the electron density in α-Fe_2O_3. **Acta Crystallographica Section B**, v. 50, n. 4, p. 435–441, 1994.

MENDOZA, O.; SIERRA, G.; TOBÓN, J. I. Effect of the reagglomeration process of multi-walled carbon nanotubes dispersions on the early activity of nano-silica in cement composites. **Construction and Building Materials**, v. 54, p. 550–557, 2014.

MENDOZA REALES, O. A.; PEARL Jr, W. C.; PAIVA, M. D. M.; MIRANDA, C. R.; TOLEDO FILHO, R. D. Effect of a commercial dispersion of multi-walled carbon nanotubes on the hydration of an oil well-cementing paste. **Front. Struct. Civ. Eng** v. 10, n. 2, p. 174–179, 2016.

MENDOZA REALES, O. A.; TOLEDO FILHO, R. D. A review on the chemical, mechanical and microstructural characterization of carbon nanotubes-cement based composites. **Construction and Building Materials**, v. 154, p. 697–710, 2017.

MENDOZA REALES, O. A.; JARAMILLO, Y. P. A.; BOTERO, J. C. O.; DELGADO, C. A.; QUINTERO, J. H.; TOLEDO FILHO, R. D. Influence of MWCNT/surfactant dispersions on the rheology of Portland cement pastes. **Cement and Concrete Research**, v. 107, p. 101–109, 2018.

MONTEAGUDO, S. M. MORAGUES, A.; GÁLVEZ, J. C.; CASATI, M. J. REYES, E. The degree of hydration assessment of blended cement pastes by differential thermal and thermogravimetric analysis. Morphological evolution of the solid phases. **Thermochimica Acta**, v. 592, p. 37–51, 2014.

MOTA, T. L. R.; OLIVEIRA, A. P. M.; NUNES, E. H. M.; HOUMARD, M. Simple process for preparing mesoporous sol-gel silica adsorbents with high water adsorption capacities. **Microporous and Mesoporous Materials**, v. 253, p. 177–182, 2017.

MOUNANGA, P.; CHERKAOUI, K.; KHELIDJ, A.; COURTIAL, M.; DE NOIRFONTAINE, M. N.; DUNSTETTER, F. Extrudable reactive powder concretes: Hydration, shrinkage and transfer properties. **European Journal of Environmental and Civil Engineering**, v. 16, n. SUPPL. 1, p. 1–21, 2012.

MUDIMELA, P. R.; NASIBULINA, L. I.; NASIBULIN, A. G.; CWIRZEN, A.; VALKEAP, M.; HABERMEHL-CWIRZEN, K.; MALM, J. E. M.; KARPPINEN, M. J.; PENTTALA, V.; KOLTSOVA, T. S.; TOLOCHKO, O. V.; KAUPPINEN, E. I. Synthesis of carbon nanotubes and nanofibers on silica and cement matrix materials. **Journal of Nanomaterials**, v. 2009, p. 1–4, 2009.

MURADOV, N.; SMITH, F.; T-RAISSI, A. Catalytic activity of carbons for methane decomposition reaction. **Catalysis Today**, v. 102–103, p. 225–233, 2005.

MURPHY, H.; PAPAKONSTANTINOU, P.; OKPALUGO, T. I. T. Raman study of multiwalled carbon nanotubes functionalized with oxygen groups. **Journal of Vacuum Science & Technology B: Microelectronics and Nanometer Structures**, v. 24, n. 2, p. 715, 2006.

NASIBULIN, A. G.; SHANDAKOV, S. D.; NASIBULINA, L. I.; CWIRZEN, A.; MUDIMELA, P. R.; HABERMEHL-CWIRZEN, K.; GRISHIN, D. A.; GAVRILOV, Y. V.; MALM, J. E. M. TAPPER, U.; TIAN, Y.; PENTTALA, V.; KARPPINEN, M. J.; KAUPPINEN, E. I. A novel cement-based hybrid material. **New Journal of Physics**, v. 11, p. 1–11, 2009.

NATEWONG, P.; PRASONGTHUM, N.; MHADMHAN, S.; REUBROYCHAROEN, P. Fibrous platelet carbon nanofibers-silica fiber composite supports for a Co-based catalyst in the steam reforming of acetic acid. **Applied Catalysis A: General**, v. 560, p. 215–224, 2018.

NORHASRI, M. S. M.; HAMIDAH, M. S.; FADZIL, A. M. Applications of using nanomaterial in concrete: A review. **Construction and Building Materials**, v. 133, p. 91–97, 2017.

PAULA, J. N.; CALIXTO, J. M. F.; LADEIRA, L. O.; LUDVIG, P.; SOUZA, T. C. C.; ROCHA, J. M.; MELO, A. V. Mechanical and rheological behavior of oil-well cement slurries produced with clinker containing carbon nanotubes. **Journal of Petroleum Science and Engineering**, v. 122, p. 274–279, 2014.

OERTEL, T.; HUTTER, F.; HELBIG, U.; SEXTEL, G. Amorphous silica on the hydration in ultra-high performance concrete: First hour of hydration. **Cement and Concrete Research**, v. 58, p. 121–130, 2014.

OSORIO, A. G.; BERGMANN, C. P. Effect of surface area of substrates aiming the optimization of carbon nanotube production from ferrocene. **Applied Surface Science**, v. 264, p. 794–800, 2013.

OSSWALD, S.; HAVEL, M.; GOGOTSI, Y. Monitoring oxidation of multiwalled carbon nanotubes by Raman spectroscopy. **Journal of Raman Spectroscopy**, v. 38, p. 728–736, 2007.

OTHMAN, R. N.; KINLOCH, I. A.; WILKINSON, A. N. Synthesis and characterization of silica–carbon nanotube hybrid microparticles and their effect on the electrical properties of poly(vinyl alcohol) composites. **Carbon**, v. 60, p. 461–470, 2013.

PALMER, R. E**. Nanostructured Materials**. 1. ed. Amsterdam: Elsevier, 2009.

PARVEEN, S.; RANA, S.; FANGUEIRO, R. A review on nanomaterial dispersion, microstructure, and mechanical properties of carbon nanotube and nanofiber reinforced cementitious composites. **Journal of Nanomaterials**, v. 2013, p. 1–19, 2013.

PARVEEN, S.; RANA, S.; FANGUEIRO, R.; PAIVA, M. C. Microstructure and mechanical properties of carbon nanotube reinforced cementitious composites developed using a novel dispersion technique. **Cement and Concrete Research**, v. 73, p. 215–227, 2015.

PAUL, S. C.; van ROOYEN, A. S.; van ZIJL, G. P. A. G.; PETRIK, L. F. Properties of cement-based composites using nanoparticles: A comprehensive review. **Construction and Building Materials**, v. 189, p. 1019–1034, 2018.

PAYÁ, J.; BORRACHERO, M. V.; MONZÓ, J.; PERIS-MORA, E.; AMAHJOUR, F. Enhanced conductivity measurement techniques for evaluation of fly ash pozzolanic activity. **Cement and Concrete Research**, v. 31, n. 1, p. 41–49, 2001.

PIÑERO, M.; MESA-DÍAZ, M. M.; DE LOS SANTOS, D.; REYES-PECES, M.V.; DÍAZ-FRAILLE, J. A.; DE LA ROSA-FOX, N.; ESQUIVIAS, L.; MORALES-FLOREZ, V. Reinforced silica-carbon nanotube monolithic aerogels synthesised by rapid controlled gelation. **Journal of Sol-Gel Science and Technology**, v. 86, p. 381–389, 2018.

POPE, E. J. A.; MACKENZIE, J. D. Sol-gel processing of silica. II. The role of the catalyst. **Journal of Non-Crystalline Solids**, v. 87, n. 1–2, p. 185–198, 1986.

PORWAL, D.; MUKHOPADHYAY, K.; RAM, K.; MATHUR, G. N. Investigation of the synthesis strategy of CNTs from CCVD by thermal analysis. **Thermochimica Acta**, v. 463, n. 1–2, p. 53–59, 2007.

PRIMEAU, N.; VAUTEY, C.; LANGLET, M. The effect of thermal annealing on aerosol-gel deposited SiO_2 films: a FTIR deconvolution study. **Thin Solid Films**, v. 310, n. 1–2, p. 47–56, 1997.

QING, Y.; ZENAN, Z.; KONG, D.; RONGSHEN, C. Influence of nano-SiO_2 addition on properties of hardened cement paste as compared with silica fume. **Construction and Building Materials**, v. 21, n. 3, p. 539–545, 2007.

RABBANI, F. A.; MALAIBARI, Z. O.; ATIEH, M. A.; JAMIE, A. Catalytic synthesis of substrate-free, aligned and tailored high aspect ratio multiwall carbon nanotubes in an ultrasonic atomization head CVD reactor. **Journal of Nanomaterials**, v. 2016, n. 2014, 2016.

RAHMAN, I. A.; PADAVETTAN, V. Synthesis of silica nanoparticles by sol-gel: Size-dependent properties, surface modification, and applications in silica-polymer nanocomposites - a review**. Journal of Nanomaterials**, V. 2012, p. 1–15, 2012.

RAMESH, P.; OKAZAKI, T.; TANIGUCHI, R.; KIMURA, J.; SUGAI, T.; SATO K.; OZEKI, Y.; SHINOHARA, H. Selective chemical vapor deposition synthesis of double-wall carbon nanotubes on mesoporous silica. **Journal of Physical Chemistry B**, v. 109, p. 1141–1147, 2005.

RAMEZANI, M.; KIM, Y. H.; SUN, Z. Mechanical properties of carbon nanotube reinforced cementitious materials: Database and statistical analysis. **Magazine of Concrete Research**, v. 72, n. 20, p. 1047–1071, 2020.

RAO, A. V.; BHAGAT, S. D. Synthesis and physical properties of TEOS-based silica aerogels prepared by two-step (acid-base) sol-gel process. **Solid State Sciences**, v. 6, n. 9, p. 945–952, 2004.

RASHAD, A. M. Effect of carbon nanotubes (CNTs) on the properties of traditional cementitious materials – Review. **Construction and Building Materials**, v. 153, p. 81–101, 2017.

RATKOVIC, S.; PEICA, N.; THOMSEN, C.; BUKUR, D. B.; BOSKOVIC, G. Thermal stability evolution of carbon nanotubes caused by liquid oxidation. **Journal of Thermal Analysis and Calorimetry**, v. 115, n. 2, p. 1477–1486, 2014.

RECHES, Y. Nanoparticles as concrete additives: Review and perspectives. **Construction and Building Materials**, v. 175, p. 483–495, 2018.

RICHARD, P.; CHEYREZY, M. Composition of reactive powder concretes. **Cement and Concrete Research**, v. 25, n. 7, p. 1501–1511, 1995.

ROSSEN, J. E.; LOTHENBACH, B.; SCRIVENER, K. L. Composition of C-S-H in pastes with increasing levels of silica fume addition. **Cement and Concrete Research**, v. 75, p. 14–22, 2015.

ROYCHAND, R.; DE SILVA, S.; LAW, D.; SETUNGE, S. High volume fly ash cement composite modified with nano-silica, hydrated lime and set accelerator. Materials and Structures/Materiaux et Constructions, v. 49, n. 5, p. 1997–2008, 2016.

RUAN, Y.; HAN, B.; YU, X.; ZHANG, W.; WANG, D. Carbon nanotubes reinforced reactive powder concrete. **Composites Part A: Applied Science and Manufacturing**, v. 112, p. 371–382, 2018.

RUEDEN, C. T.; SCHINDELIN, J.; HINER, M. C. **ImageJ2: ImageJ for the next generation of scientific image data**, 2017.

SAID, A. M.; ZEIDAN, M. S.; BASSUONI, M. T.; TIAN, Y. Properties of concrete incorporating nano-silica. **Construction and Building Materials**, v. 36, p. 838–844, 2012.

SANTANGELO, S.; MESSINA, G.; FAGGIO, G.; LANZA, M.; MILONE, C. Evaluation of crystalline perfection degree of multi-walled carbon nanotubes: Correlations between thermal kinetic analysis and micro-Raman spectroscopy. **Journal of Raman Spectroscopy**, v. 42, n. 4, p. 593–602, 2011.

SAVII, C.; POPOVICI, M.; ENACHE, C.; SUBRT, J.; NIZNANSKY, D.; BAKARDZIEVA, S.; CAIZER, C.; HRIANCA, I. Fe_2O_3-SiO_2 composites obtained by sol-gel synthesis. **Solid State Ionics**, v. 151, n. 1–4, p. 219–227, 2002.

SCRIVENER, K. L.; SNELLINGS, R.; LOTHENBACH, B. **A practical guide to microstructural analysis of cementitious materials**. Boca Raton, Taylor & Francis, 2016.

SEKHAR C. RAY, ZIKHONA N. TETANA, RUDOLPH ERASMUS, ASHISH MATHUR, N. J. C. Carbon spheres for energy applications: Raman and X-ray photoemission spectroscopy studies. **International Journal of Energy Research**, v. 38, p. 444–451, 2014.

SHAH, K. A.; TALI, B. A. Synthesis of carbon nanotubes by catalytic chemical vapor deposition: A review on carbon sources, catalysts and substrates. **Materials Science in Semiconductor Processing**, v. 41, p. 67–82, 2016.

SHAYED, M. A.; HUND, H.; HUND, R. D.; CHERIF, C. Thermal and oxidation-resistant barrier on carbon fiber with Si and Si–Ti based pre-ceramic coatings for high-temperature application. **Textile Research Journal**, v. 86, n. 18, p. 1901–1913, 2016.

SHI, C.; WU, Z.; XIAO, J.; WANG, D.; HUANG, Z.; FANG, Z. A review on ultra-high performance concrete: Part I. Raw materials and mixture design. **Construction and Building Materials**, v. 101, p. 741–751, 2015.

SHI, T.; LI, Z.; GUO, J.; GONG, H.; GU, C. Research progress on CNTs/CNFs-modified cement-based composites – A review. **Construction and Building Materials**, v. 202, p. 290–307, 2019.

SHIMOGAKI, T.; TOKORO, H.; TABUCHI, M.; KOIKE, N.; YAMASHINA, Y.; TAKAHASHI, M. Large-scale synthesis of monodisperse microporous silica nanoparticles by gradual injection of reactants. **Journal of Sol-Gel Science and Technology**, v. 74, n. 1, p. 109–113, 2015.

SHUKRULLAH, S.; MOHAMED, N. M.; SHAHARUN, M. S.; NAZ, M. Y. Parametric study on vapor-solid-solid growth mechanism of multiwalled carbon nanotubes. **Materials Chemistry and Physics**, v. 176, p. 32–43, 2016.

SIKORA, P.; ABD ELRAHMAN, M.; CHUNG, S. Y.; CENDROWSKI, K.; MIJPWSKA, E.; STEPHAN, D. Mechanical and microstructural properties of cement pastes containing carbon nanotubes and carbon nanotube-silica core-shell structures, exposed to elevated temperature. **Cement and Concrete Composites**, v. 95, n. 2018, p. 193–204, 2019.

SILVA, C.; AIROLDI, C. Acid and base catalysts in the hybrid silica sol-gel process. **Journal of colloid and interface science**, v. 195, n. 2, p. 381–7, 1997.

SINGH, L. P.; KARADE, S. R.; BHATTACHARYYA, S. K.; YOUSUF, M. M.; AHALAWAT, S. Beneficial role of nano-silica in cement-based materials – A review. **Construction and Building Materials**, v. 47, p. 1069–1077, 2013.

SINGH, L. P.; BHATTACHARYYA, S. K.; KUMAR, R.; MISHRA, G.; SHARMA, U.; SINGH, G.; AHALAWAT, S. Sol-Gel processing of silica nanoparticles and their applications. **Advances in Colloid and Interface Science**, v. 214, p. 17–37, 2014.

SINGH, L. P.; BHATTACHARYYA, S. K.; SHAH, S. P.; MISHRA, G.; AHALAWAT, S.; SHARMA, U. Studies on early-stage hydration of tricalcium silicate incorporating silica nanoparticles: Part I. **Construction and Building Materials**, v. 74, p. 278–286, 2015.

SINTHAWORN, S.; NIMITYONGSKUL, P. Quick monitoring of pozzolanic reactivity of waste ashes. **Waste Management,** v. 29, n. 5, p. 1526–1531, 2009.

SOBOLKINA, A.; MECHTCHERINE, V.; KHAVRUS, V.; MAIER, D.; MENDE, M.; RITSCHEL, M.; LEONHARDT, A. Dispersion of carbon nanotubes and its influence on the mechanical properties of the cement matrix. **Cement and Concrete Composites**, v. 34, n. 10, p. 1104–1113, 2012.

SONG, I.K.; CHO, Y.S.; CHOI, G.S.; PARK, J.B.; KIM, D.J. The growth mode change in carbon nanotube synthesis in plasma-enhanced chemical vapor deposition. **Diamond and Related Materials**, v. 13, n. 4–8, p. 1210–1213, 2004.

SOUZA, T. C. C; PINTO, G.; CRUZ, V. S.; MOURA, M.; LADEIRA, L. O.; CALIXTO, J. M. Evaluation of the rheological behavior, hydration process, and mechanical strength of Portland cement pastes produced with carbon nanotubes synthesized directly on clinker. Construction and Building Materials, v. 248, p. 118686–118698, 2020.

SUN, J.; XU, Z.; LI, W.; SHEN, X. Effect of nano-SiO_2 on the early hydration of alite-sulphoaluminate cement. **Nanomaterials**, v. 7, n. 5, p. 1–15, 2017.

SUN, S.; YU, X.; HAN, B.; OU, J. In situ growth of carbon nanotubes/carbon nanofibers on cement/mineral admixture particles: A review. **Construction and Building Materials**, v. 49, p. 835–840, 2013.

TAN, L.; ONG, W. J; CHAI, S. P.; MOHAMED, R. A. Growth of carbon nanotubes over non-metallic based catalysts: A review on the recent developments. **Catalysis Today**, v. 217, p. 1–12, 2013.

TOMITA, T.; KAWASAKI, S.; OKADA, K. A novel preparation method for foamed silica ceramics by sol-gel reaction and mechanical foaming. **Journal of Porous Materials**, v. 11, n. 2, p. 107–115, 2004.

THOMMES, M.; KANEKO, K.; NEIMARK, A. V.; OLIVIER, J. P.; RODRIGUEZ-REINOSO, F.; ROUQUEROL, J.; SING, K. S.W. Physisorption of gases, with special reference to the evaluation of surface area and pore size distribution (IUPAC Technical Report). **Pure and Applied Chemistry**, v. 87, n. 9–10, p. 1051–1069, 2015.

TRIGUEIRO, J. P. C.; SILVA, G. G.; LAVALL, R. L.; FURTADO, C. A.; OLIVEIRA, S.; FERLAUTO, A. S.; LACERDA, R. G.; LADEIRA, L. O.; LIU, J. W.; FROST, R. L.; GEORGE, G. A. Purity Evaluation of Carbon Nanotube Materials by Thermogravimetric, TEM, and SEM Methods. **Journal of Nanoscience and Nanotechnology**, v. 7, n. 10, p. 3477–3486, 2007.

TUTIKIAN, B. F.; ISAIA, G. C.; HELENE, P. **Concreto: Ciência e Tecnologia.** 1° ed. São Paulo, 2011.

UMA, K.; BALU, S.; PAN, G. T.; YANG, T. C. K. Assembly of ZnO nanoparticles on SiO_2@α-Fe_2O_3 nanocomposites for an efficient photo-Fenton reaction. **Inorganics**, v. 6, n. 3, 2018.

van DAMME, H. Concrete material science: Past, present, and future innovations. **Cement and Concrete Research**, v. 112, n. May, p. 5–24, 2018.

VANDER WAL, R. L.; TICICH, T. M.; CURTIS, V. E. Substrate–support interactions in metal-catalyzed carbon nanofiber growth. **Carbon**, v. 39, n. 15, p. 2277–2289, 2001.VELÁZQUEZ, S.; MONZÓ, J. M.; BORRACHERO, M. V.; PAYÁ, J. Assessment of the pozzolanic activity of a spent catalyst by conductivity measurement of aqueous suspensions with calcium hydroxide. **Materials**, v. 7, n. 4, p. 2561–2576, 2014.

WANG, D.; SHI, C.; WU, Z.; XIAO, J.; HUANG, Z.; FANG, Z. A review on ultra-high performance concrete: Part II. Hydration, microstructure and properties. **Construction and Building Materials**, v. 96, p. 368–377, 2015.

WANG, L.; ZHENG, D.; ZHANG, S.; CUI, H.; LI, D. Effect of nano-SiO_2 on the hydration and microstructure of Portland cement. **Nanomaterials**, v. 6, n. 12, 2016.

WANG, Y.; LI, B.; HO, P. S.; YAO, Z.; SHI, L. Effect of supporting layer on growth of carbon nanotubes by thermal chemical vapor deposition. **Applied Physics Letters**, v. 89, n. 18, p. 1–4, 2006.

WANG, Y.; LUO, Z.; LI, B.; HO, P. S.; YAO, Z.; SHI, L.; BRYAN, E. N.; NEMANICH, R. J. Comparison study of catalyst nanoparticle formation and carbon nanotube growth: Support effect. **Journal of Applied Physics**, v. 101, n. 12, p. 1–8, 2007.

WRIGHT, A. C.; XIONG, Y.; MAUNG, N.; EICHHORN, S. J.; YOUNG, R. J. The influence of the substrate on the growth of carbon nanotubes from nickel clusters-

an investigation using STM, FE-SEM, TEM and Raman spectroscopy. **Materials Science and Engineering C**, v. 23, n. 1–2, p. 279–283, 2003.

WU, Z.; HENRI, K.; SHI, C. Effect of nano-SiO_2 particles and curing time on development of fiber-matrix bond properties and microstructure of ultra-high-strength concrete. **Cement and Concrete Research**, v. 95, p. 247–256, 2017.

YAKOVLEV, G. I.; SKRIPKIUNAS, G.; POLIANSKICH, I. S.; LAHAYNE, O.; EBERHARDSTEINER, J.; URKHANOVA, L. A.; PUDOV, I. A.; SYCHUGOV, S. V.; KARPOVA, E. A.; SEN'KOV, S. A. Modification of cement matrix using carbon nanotube dispersions and nano-silica. **Procedia Engineering**, v. 172, p. 1261–1269, 2017.

YAZICI, H.; YIĞITER, H.; KARABULUT, A. Ş.; BARADAN, B. Utilization of fly ash and ground granulated blast furnace slag as an alternative silica source in reactive powder concrete. **Fuel**, v. 87, n. 12, p. 2401–2407, 2008.

YEOH, W. M.; LEE, K. Y.; CHAI, S. P.; LEE, K. T.; MOHAMED, A. R. Effective synthesis of carbon nanotubes via catalytic decomposition of methane: Influence of calcination temperature on metal-support interaction of Co-Mo/MgO catalyst. **Journal of Physics and Chemistry of Solids**, v. 74, n. 11, p. 1553–1559, 2013.

YU, R.; SPIESZ, P.; BROUWERS, H. J. H. Effect of nano-silica on the hydration and microstructure development of Ultra-High Performance Concrete (UHPC) with a low binder amount. **Construction and Building Materials**, v. 65, p. 140–150, 2014.

ZHANG, P.; WAN, J.; WANG, K.; LI, Q. Influence of nano-SiO_2 on properties of fresh and hardened high-performance concrete: A state-of-the-art review. **Construction and Building Materials**, v. 148, p. 648–658, 2017.

ZHANG, W.; HAN, B.; YU, X.; RUAN, Y.; OU, J. Nano boron nitride modified reactive powder concrete. **Construction and Building Materials**, v. 179, p. 186–197, ago. 2018.

ZHANG, Y. J.; SHEN, Y. F.; HAN, D. X.; WANG, Z. J.; SONG, J. X.; NIU, L. Reinforcement of silica with single-walled carbon nanotubes through covalent functionalization. **Journal of Materials Chemistry**, v. 16, n. 47, p. 4592–4597, 2006.

ZHENG, R.; ZHAO, Y.; LIU, H.; LIANG, C.; CHENG, G. Preparation, characterization and growth mechanism of platelet carbon nanofibers. **Carbon**, v. 44, n. 4, p. 742–746, 2006.

ZHOU, L.; ENAKONDA, L. R.; HARB, M.; SAIH, Y.; AGUILAR-TAPIA, A.; OULD-CHIKH, S.; HAZEMANN, J. L.; LI, J.; WEI, N.; GARY, D.; DEL-GALLO, P.; BASSET, J. M. Fe catalysts for methane decomposition to produce hydrogen and carbon nanomaterials. **Applied Catalysis B: Environmental**, v. 208, p. 44–59, 2017.